Preparation and Characterization of Catalysts for Efficient Hydrogen Production via the High Temperature Water Gas Shift Reaction

Zur Erlangung des akademischen Grades eines

DOKTORS DER NATURWISSENSCHAFTEN

(Dr. rer. nat.)

von der KIT-Fakultät für Chemie und Biowissenschaften

des Karlsruher Instituts für Technologie (KIT)

genehmigte

DISSERTATION

von

Dipl.-Chem. Gülperi Cavusoglu

aus

Solhan, Türkei

KIT-Dekan: Prof. Dr. Willem M. Klopper

Referent: Prof. Dr. Jan-Dierk Grunwaldt

Korreferent: Prof. Dr. Andreas Goldbach

Tag der mündlichen Prüfung: 10.02.2017

Acknowledgement

Finally I would like to express my gratitude to my lovely family, who believed in me, let me follow my own way, always support me and love me unconditionally as I love them. In loving memory of my parents; your life was a blessing, your memory a treasure you are loved beyond words and missed beyond measure.

Abstract

Worldwide growing population and higher living standards are causing increasing energy consumption. The largest amount of energy is consumed by the sectors of commerce, trade, transport and industry. In general, the fossil, non-renewable raw materials such as petroleum, natural gas, coal and brown coal are used for power generation and as carbon sources for the chemical industry. The production of energy from these materials leads to a particularly high emission of greenhouse gases, which contributes to global warming. In consequence, research activities towards more efficient and environmentally friendly energy technologies have been intensified with increasing global energy demands and growing concerns for the environment. Fuel cell technology which uses hydrogen as an energy source and produces water as the only byproduct is a promising energy conversion system for the future. Hydrogen is considered as a potential future replacement for gasoline, diesel fuel and natural gas. Therefore, there has been a large demand for hydrogen production, purification and separation technologies in the past decade.

The Water Gas Shift (WGS) reaction is an industrially important process for hydrogen production and purification. This reaction is well established for reducing CO levels in hydrogen stream, such as in hydrogen production for ammonia plants. CO is furthermore a well-known poison for fuel cell catalysts. The WGS reaction is a commercially well-established process occurring in two steps: High Temperature Shift (HTS) and Low Temperature Shift (LTS). The HTS reaction is typically performed in the temperature range between 320 and 450 °C using Fe/Cr catalysts and converts most of the CO in the stream. Further CO conversion requires the LTS reaction as a next step, which is operated in the temperature range between 200 and 250 °C using Cu/Zn catalysts. However, for fuel cell applications this two-step process using iron and copper catalysts is too complex. The development of a single-stage process – for example based on membrane reactors – requires new catalysts. In the literature, noble metal particles supported on redox active metal oxides are discussed as promising catalysts for such applications. Pt based catalysts are well-suited for high temperature WGS. They have been usually prepared by conventional preparation methods, such as precipitation, incipient wetness impregnation and sol-gel. As an alternative preparation method for catalysts, a rather new method known as Flame Spray Pyrolysis (FSP)

was used for the experiments described in this thesis. FSP is considered as a promising method for preparation of catalysts with highly dispersed active centers and high stability in a single step.

In the first part of this thesis, Rh and Pt particles supported on reducible oxides (CeO_2, ZrO_2, mixed oxide CeO_2/ZrO_2 and TiO_2) were prepared by Single Flame (SF) and Double Flame (DF) spray pyrolysis for high temperature WGS reactions. These catalysts were characterized by N_2 adsorption, CO chemisorption, ICP-OES, XRD, TEM and *in situ* XAS. They exhibited a high specific surface area and a high degree of nanocrystallinity. Moreover, the noble metal constituent was highly dispersed, typically as small nanoparticles. Single flame made catalysts showed higher dispersion, larger surface areas and higher reduction temperatures compared to double flame made catalysts. The catalytic performance of these catalysts was tested in two different reactors: A fixed bed reactor and a capillary microreactor, which was also applied at synchrotron radiation facilities for *in situ* XAS experiments under WGS reaction conditions. Furthermore, the influence of steam to CO (S/C) ratio and residence time (Gas Hourly Space Velocity, GHSV) on theses catalysts was studied. In general, platinum based catalysts showed a better performance than rhodium based catalysts, especially in terms of selectivity and activity. Furthermore, a strong influence of the support and preparation method on the selectivity and activity was observed.

The second part of this thesis focused on the use of the catalysts in membrane reactors and the characterization of both the membrane and catalysts under reaction conditions. Rh/ceria catalysts and an ultrathin hydrogen selective, commercially obtained membrane were used in a novel micro-structured membrane reactor specially designed for x-ray absorption spectroscopic measurements under WGS conditions. In this newly designed membrane reactor, 10.5 wt.% Rh/CeO_2 catalyst and a commercial available ultrathin hydrogen selective alloyed Pd based membrane foil were investigated under WGS reaction conditions at atmospheric pressure. The *in situ* XAS measurements could be combined both with the analysis of the product and permeate stream under the demanding conditions of the WGS reaction (up to 10% water). XAS spectra at the Pd K-edge were recorded *in situ* to correlate the structure of the membrane and the efficiency of *in situ* H_2 extraction. The results show that the membrane was stable and did not undergo any structural change during WGS. The combination of X-ray absorption spectroscopy and on-line catalytic data provided insight into the structure-performance relationships of the flame made 10.5 wt.% Rh/CeO_2 catalyst under different WGS reaction conditions and during reduction. The

WGS experiments showed that the Rh species are in a reduced state under WGS reaction conditions. These studies will be beneficial in the future as a benchmark, and the infrastructure established will allow further experiments for the development of new membranes and catalysts.

Kurzfassung

Die zunehmende Weltbevölkerung gepaart mit einem höheren Lebensstandard verursachen weltweit einen steigenden Energieverbrauch. Neben den privaten Haushalten verbrauchen die Bereiche Industrie, Gewerbe, Handel und Transport den größten Anteil an Energie. Trotz Kernenergie und regenerativer Energieerzeugung werden überwiegend die fossilen, nicht-erneuerbaren Rohstoffe Erdöl, Erdgas, Steinkohle und Braunkohle verwendet. Darüber hinaus werden diese Rohstoffe auch als Kohlenstoffquelle für die chemische Industrie eingesetzt. Bei der Energieerzeugung aus fossilen, nicht-erneuerbaren Rohstoffen ist die Emission an Treibhausgasen sehr hoch. Diese tragen entscheidend zur globalen Klimaerwärmung bei. Infolgedessen wurden die Forschungsaktivitäten im Hinblick auf effizientere und umweltfreundliche Energietechnologien vor dem Hintergrund zunehmender globaler Energiebedürfnisse und wachsender Bedenken für die Umwelt verstärkt. Wasserstoff gilt als vielsprechende Alternative zu Benzin, Dieselkraftstoff und Erdgas. Demzufolge hat die steigende Nachfrage nach effizienten Technologien für die Wasserstoffproduktion, -reinigung und -trennung in den letzten zehn Jahren großes Interesse hervorgerufen.

Die Wasser Gas Shift (WGS) Reaktion ist ein industriell wichtiges Verfahren zur Wasserstoffherstellung und -reinigung. Besondere Bedeutung hat die WGS-Reaktion bei der Verminderung der CO-Konzentration in der Wasserstoffherstellungskette. Da CO als Katalysatorgift wirkt, ist die WGS Reaktion zum Beispiel bei der Ammoniaksynthese oder Wasserstoffumsetzung in Brennstoffzellen sehr wichtig. Die heute industriell eingesetzte WGS Reaktion läuft in einem zweistufigen Prozess ab; dem Hochtemperatur-Shift und dem Tieftemperatur-Shift Prozess. Die Hochtemperature-Shift-Reaktion wird an Fe/Cr Katalysatoren bei ca. 320 °C bis 450 °C durchgeführt. Bei dieser Reaktion wird der Großteil des CO umgesetzt. Um das restliche CO umzusetzen wird die Tieftemperatur-Shift-Reaktion angewendet. Bei dieser Reaktion werden die CO und Wasser bei 200 °C bis 250 °C über Cu/Zn Katalysatoren umgesetzt. Jedoch ist dieses zweistufige Verfahren unter Verwendung von Eisen- und Kupferkatalysatoren für die Anwendung in Brennstoffzellen zu komplex. Für die angestrebte Umsetzung eines einstufigen Verfahrens – zum Beispiel basierend auf Membranreaktoren – werden daher neue Katalysatoren benötigt. Dafür haben sich in der Literatur Edelmetallkatalysatoren mit redox-

aktiven Trägern als vielversprechender Ansatz herauskristallisiert. Insbesondere Pt-basierte Katalysatoren wurden als alternative Katalysatoren für einstufige WGS-Reaktionen diskutiert. Diese wurden meist auf konventionelle Weise nasschemisch präpariert z. B. mittels Fällung, Nass- oder Trockenimprägnierung. Als Alternative zu klassischen Präparationsmethoden wurde die Flammen Sprüh Pyrolyse (FSP) als neuartige Synthesemethode für die Herstellung von WGS-Katalysatoren im Rahmen der vorliegenden Arbeit eingesetzt. Die mittels FSP in einem Schritt hergestellten Katalysatoren zeichnen sich generell durch eine hohe Dispersion aktiver Zentren und eine hohe Stabilität aus.

Im ersten Teil dieser Arbeit wurden Titandioxid, Cer-, Zirconium- und Cer/Zirconium-oxid geträgerte Platin- bzw. Rhodium-Hochtemperatur-WGS-Katalysatoren jeweils im Einflammen und Zweiflammen Sprüh Pyrolyse hergestellt. Diese Katalysatoren wurden mittels N_2-Physisorption, CO-Chemisorption, ICP-OES, XRD, TEM und *in situ* XAS charakterisiert. Sie wiesen eine hohe spezifische Oberfläche und einen hohen Grad an Kristallinität auf. Die geträgerten Edelmetalle lagen als hochdisperse Partikel im Nanometerbereich vor. Einflammensynthetisierte Katalysatoren zeigten hohe Edelmetal-Dispersion und spezifische Oberflächen, und zweiflammensynthetisierte Katalysatoren zeichneten sich durch niedrige Reduktionstemperaturen der Edelmetallkomponente aus. Die Aktivitätsmessungen wurden in zwei verschiedenen Reaktortypen durchgeführt: In einem Festbettreaktor und in einem Kapillar-Mikroreaktor. Der Vorteil der Experimente mit dem Kapillar-Mikroreaktor ist, dass *in situ* XAS-Messungen unter WGS Bedingungen an Synchrotronstrahlungsquellen durchgeführt werden können. Weiterhin wurden der Einfluss der S/C (Wasserdampf/CO) Verhältnisse untersucht und die Verweilzeit (Gas Hourly Space Velocity, GHSV) für die verschiedenen Katalysatoren optimiert. Die Platin-basierten Katalysatoren wiesen in der Regel eine höhere katalytische Aktivität und Selektivität auf als vergleichbare Rhodium-basierten Katalysatoren auf.

Der zweite Teil lag der Fokus auf den Einsatz von Membran-Reaktor sowie die Charakterisierung sowohl des Katalysators als auch der Membran unter Reaktionsbedingungen. Insbesondere wurden Rh/CeO_2 Katalysatoren und eine ultradünne H_2-selektive Membran *in situ* in einem mikrostrukturierten Membran-Reaktor, der speziell für röntgenabsorptionsspektroskopische Messungen entwickelt wurde, eingesetzt. In diesem Reaktor wurde der mittels FSP hergestellte 10.5 Gew.% Rh/CeO_2 Katalysator und eine ultradünne, im Handel erhältliche H_2-selektive Pd-Membranfolie unter WGS-Bedingungen bei Atmosphärendruck untersucht. Dabei gelang es, die

in situ XAS Messungen mit der Analyse sowohl des Trägergases als auch Produktgasstroms unter den herausfordernden Bedingungen der WGS Reaktion (bis zu 10% Wasser) zu kombinieren. *In situ* an der Pd K-Kante gemessene XAS Spektren zeigen direkte Zusammenhänge zwischen der Struktur der Membran und *in situ* H_2-Extraktion. Die Ergebnisse zeigen, dass die Pd-Membranfolie stabil war und keine strukturellen Veränderungen während der WGS Reaktion auftreten. Die Kombination von Röntgenabsorptionsspektroskopie und on-line katalytischen Messungen liefern einen Einblick in die Struktur-Leistungs-Korrelation des Rh/CeO_2 Katalysators bei verschiedenen WGS-Reaktionsbedingungen. Die Ergebnisse zeigen, dass die Rh-Spezies unter WGS-Reaktionsbedingungen in einem reduzierten Zustand vorliegen. Diese Messungen dienen als Machbarkeitsstudie (proof-of-concept) und als Referenz für zukünftige Experimente für die Entwicklung neuartiger Membranen und Katalysatoren.

CONTENTS

Part I: Background & Motivation

Part II: Experimental

Part III: Catalytic Studies

Part IV: Advanced Spectroscopic Studies

Part V: Final Remarks and Outlook

PART I: BACKGROUND & MOTIVATION

1 Introduction

Clean and alternative energy and its transportation has become a globally significant subject of research for sustainable energy development. Among these important developments are counted hydrogen production, purification and storage. Hydrogen has versatile application in chemical industry, food industry, and fuel cell systems. In particular, due to the high efficiency with essentially zero harmful emissions, hydrogen is a promising alternative energy carrier for fuel cells in mobile and stationary applications [1]. For the future, hydrogen is being considered as an environmentally benign replacement for gasoline, diesel fuel, natural gas, and other fuels in the transportation sector among others [2].

Hydrogen is the most common element in the environment and mostly occurs in water and in other compounds such as hydrocarbons [3]. The worldwide production of hydrogen is assessed as being 50 million tons per year [4]. For large-scale production of hydrogen the following primary energy sources are commonly applied (Eq. 1.1 – Eq. 1.5): steam reforming, partial oxidation, auto reforming, gasification of coal, and the water gas shift reaction [1, 4, 5]. Hydrogen can also be produced from non-hydrocarbon-based sources, such as water electrolysis and thermochemical water decomposition, or the conversion of alcohols (methanol, ethanol) [5, 6].

Steam reforming
$$C_mH_n + m\,H_2O \rightleftarrows m\,CO + \left(m + \frac{n}{2}\right)H_2$$
Eq. 1.1

Partial oxidation
$$C_mH_n + \frac{m}{2}\,O_2 \rightleftarrows m\,CO + \frac{n}{2}\,H_2$$
Eq. 1.2

Auto reforming
$$C_mH_n + \frac{m}{2}\,H_2O + \frac{m}{4}\,O_2 \rightleftarrows m\,CO + \left(\frac{m}{2} + \frac{n}{2}\right)H_2$$
Eq. 1.3

Gasification of carbon
$$C + H_2O \rightleftarrows CO + H_2$$
Eq. 1.4

Water gas shift
$$CO + H_2O \rightleftarrows CO_2 + H_2$$
Eq. 1.5
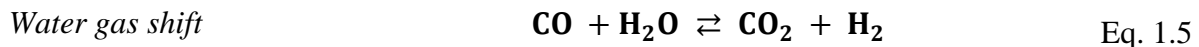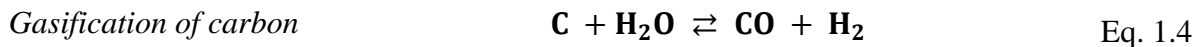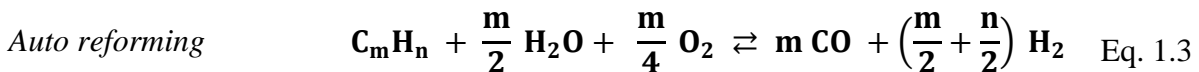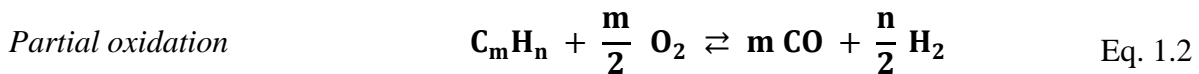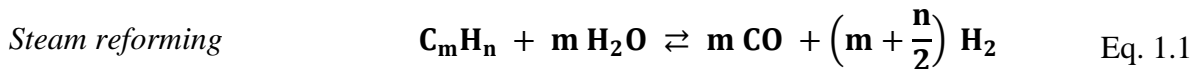
In many commercial hydrogen production plants syngas (H_2/CO) production and conversion are intermediate steps for enhancing the H_2 yield. Depending on carbonaceous materials and processes (Eq. 1.1 – Eq. 1.4) the appropriate H_2/CO (syngas) ratio is variable. The H_2/CO ratio can be adjusted by CO conversion via the water gas shift reaction (Eq. 1.5). As a consequence of this, the industrial water gas shift reaction is an essential process to increase the production of hydrogen and to achieve appropriate H_2/CO ratios during production. Following the water gas shift reaction H_2 can be further purified through caustic scrubbers for CO_2 removal.

In recent years H_2 production for fuel cell applications has become attractive due to growing concerns about environmental issues. All fuel cells directly utilize directly chemical energy instead of combusting fuel. A fuel cell is in principle much more efficient than a combustion engine at converting fuel to electricity [1]. There are five types of fuel cells, namely: proton exchange membrane fuel cells (PEMFC), alkali fuel cells (AFC), phosphoric acidic fuel cells (PAFC) molten carbonate fuel cells (MCFC) and solid oxide fuel cells (SOFC) [7]. For PEMFC Pt based catalysts are mostly used. Hydrogen is dissociated on the surface and subsequently oxidized forming a proton and electron. The electrons proceed through an external circuit where the energy can be used in the form of electricity. The protons diffuse through the PEM to the cathode where they react with oxygen to water as the only byproduct, which makes such fuel cells environmentally friendly. The Pt catalysts exhibit high activity, chemical stability and high exchange current [7]. However, Pt catalysts are extremely sensitive to CO which acts as a poison in PEM fuel cells. Therefore, the amount of residual CO in the feed gas must be reduced via the water gas shift reaction (Eq. 1.5) yielding CO_2 and additional H_2. As a consequence, the WGS reaction is a decisive reaction especially for hydrogen production.

1.1 Water Gas Shift Reaction

The water gas shift reaction was first observed in 1780 by the Italian physicist Felice Fontana when passing steam through a bed of incandescent coke. The experiment was reported in 1888 by Ludwig Mond and his assistant Carl Langer. Mond focused on the synthesis of ammonia from coal and coke and discovered a process for producing the "Mond-gas" (CO_2, CO, H_2 and N_2) via a reaction of air and steam on the coke or coal (the basis of coal gasification). The "Mond-gas" was used for the world´s first fuel cell. Feeding pure hydrogen to the "Mond battery" was a challenging step due to the presence of carbon monoxide which poisoned the Pt electrode. Mond

found a solution for this problem by passing the "Mond gas" mixture and steam over nickel at 400 °C to react the carbon monoxide and steam to carbon dioxide and additional hydrogen. In this way, a H_2 rich feed free from CO could be successfully obtained for fuel cell applications. [8, 9]

The water gas shift reaction received growing attention as a source of hydrogen for ammonia production via the Haber process. In the first ammonia synthesis plant, CO was removed by liquefaction and scrubbing with hot caustic soda solution. However, this procedure was not applicable to large scale plants. A catalytic process to remove CO was needed. Therefore, the water gas shift reaction was used to convert CO into CO_2 which is easier to remove. In this manner the WGS reaction was industrially applied in 1913 for Haber-Bosch process of ammonia production (Figure 1.1). [8, 10]
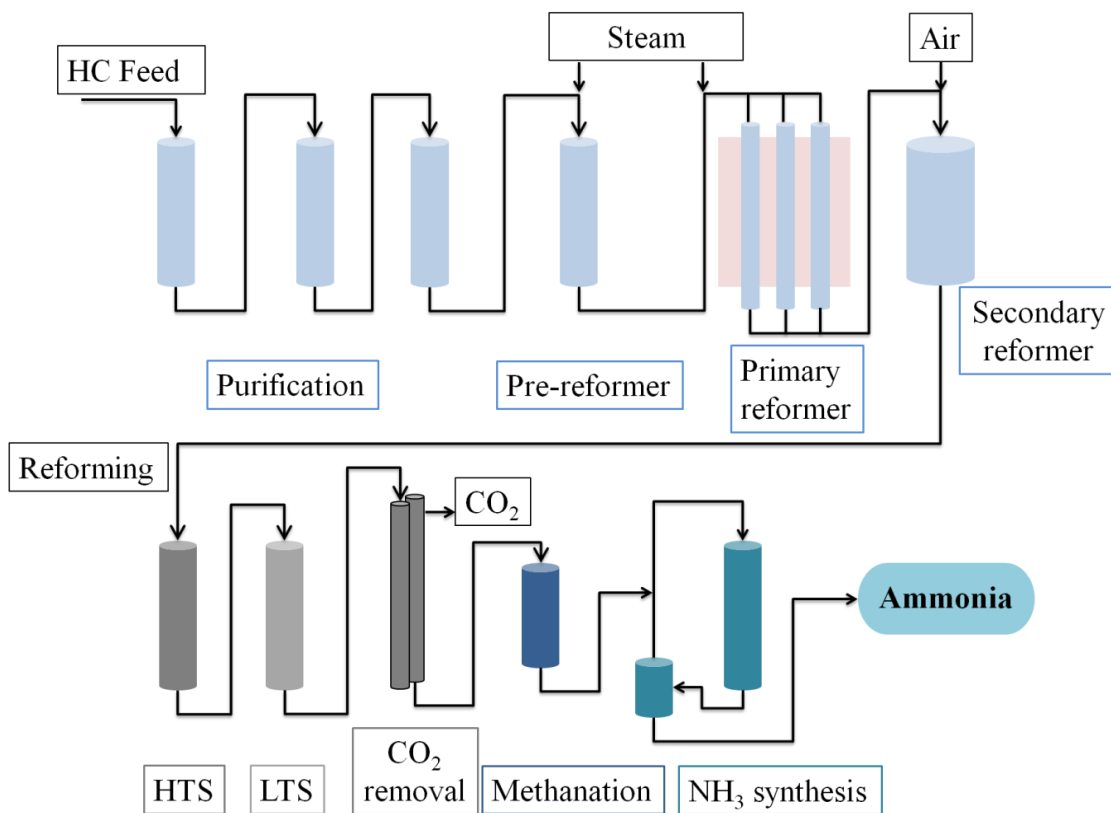
Figure 1.1: Industrial application of ammonia production for the Haber-Bosch process (adapted from [11]).

As shown in Figure 1.1, hydrogen is produced by methane from natural gas for ammonia production via the Haber-Bosch process. In the first step all sulfur compounds must be removed

from the natural gas to avoid catalyst poisoning (purification). Afterwards, the gas is sent to the primary reformer for steam reforming (Eq. 1.1) and then flows to the secondary reformer where the remaining methane reacts with oxygen, producing more H_2 (Eq. 1.2). In the next step carbon monoxide is converted to carbon dioxide via the high and low temperature WGS reaction (Figure 1.1). Before the gas is fed into the ammonia synthesis loop carbon dioxide is removed. Remaining carbon dioxide as well as carbon monoxide are converted to methane (methanation).

In 1914, BASF scientists Bosch and Wild discovered that iron oxide stabilized in chromium oxide could be used as a catalyst to convert a mixture of steam and CO into CO_2 at $400 – 500 °C$ in a single step reducing the residual CO concentration to ca. 2% [8, 12]. Since then, the iron-based catalysts were used in industrial applications for the high temperature WGS reaction. The next evolution of the process was the introduction of a second-stage converter in the temperature range between 320 and $360 °C$ to reduce the CO further. In the 1960s Cu-based catalysts were discovered and used at a second stage for low temperature WGS reactions $(190 – 250 °C)$ to achieve CO contents lower than 0.5% [10, 12]. From that time until today, the use of the WGS reaction followed the increasing industrial demand for hydrogen production, ammonia synthesis, hydrotreating of petroleum feedstocks, and coal processing by using the two stage high temperature (HT) and low temperature (LT) shift reaction (Figure 1.1).

1.1.1 Thermodynamic and Kinetic Consideration

$$\mathbf{CO + H_2O \rightleftarrows CO_2 + H_2} \qquad\qquad \Delta H = -40.6\ \frac{kJ}{mol} \qquad \text{Eq. 1.6}$$

The water gas shift reaction is a reversible, moderately exothermic chemical reaction (Eq. 1.6) and conversion is typically equilibrium controlled at high temperature. The equilibrium constant K_p decreases with increasing temperature and is given in the following Eq. 1.7 [13] :

$$K_p = e^{\left(\frac{4577.8}{T} - 4.33\right)} \qquad\qquad \text{Eq. 1.7}$$

where T is the temperature in Kelvin. Figure 1.2a shows the equilibrium constant K_p as a function of temperature and pointing that the equilibrium constant decreases with increasing temperature. Accordingly, high conversions are favored at low temperatures. At elevated temperature the CO

content at equilibrium can be 20 times lower at 200 °C than at 400 °C (K_p(T = 400 °C) = 11.8 while K_p(T = 200 °C) = 228) [13]. However, at low temperature reaction rates diminish and the reaction is controlled by the kinetics.
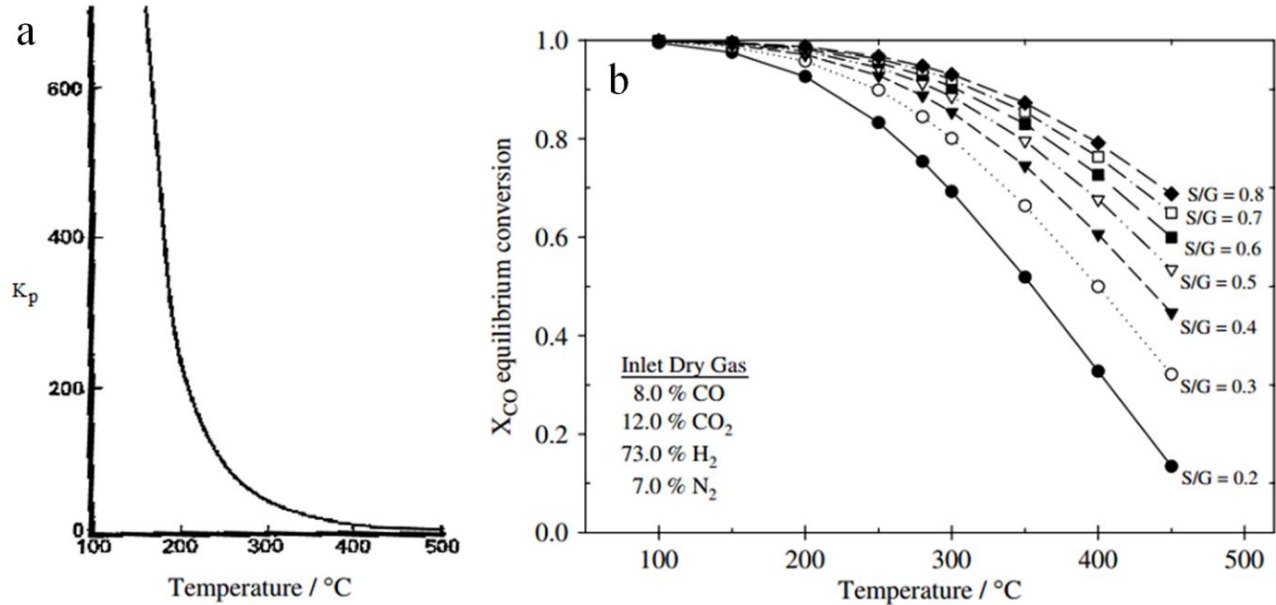
Figure 1.2: (a) Variation of equilibrium constant (Kp) for the water-gas shift reaction with temperature [10]. (b) CO equilibrium conversions of a typical reformate stream from a methane steam reforming process at various steam to dry gas (S/G) ratios reprinted with permission from ref. [9].

Figure 1.2b shows that CO conversion decreases with increasing temperature. Additionally, the steam to gas ratio clearly influences the equilibrium. As shown in Figure 1.2b, with a high amount of water present, i.e. at a higher S/C ratio, the equilibrium is shifted towards the product side, resulting in a lower CO concentration. Hence, from the point of view of steam economy, a lower reaction temperature is desirable. However, in order to achieve the required reaction rates higher temperature is often needed. The optimal WGS conditions were obtained in a multi-stage reactor for ammonia production. The first stage is worked at higher temperatures (favorable kinetics), favoring fast CO consumption and minimizing catalyst bed volume. In the second stage, the reaction occurs at a lower temperature (favorable thermodynamics) in order to obtain higher conversions.

1.1.2 Industrial Process and Catalysts

As a consequence of the kinetic and thermodynamic factors described in section 1.1.1, traditionally and in most industrial processes the WGS reaction is carried out in two steps with different catalysts to optimize the CO equilibrium conversion, as shown in Figure 1.3.
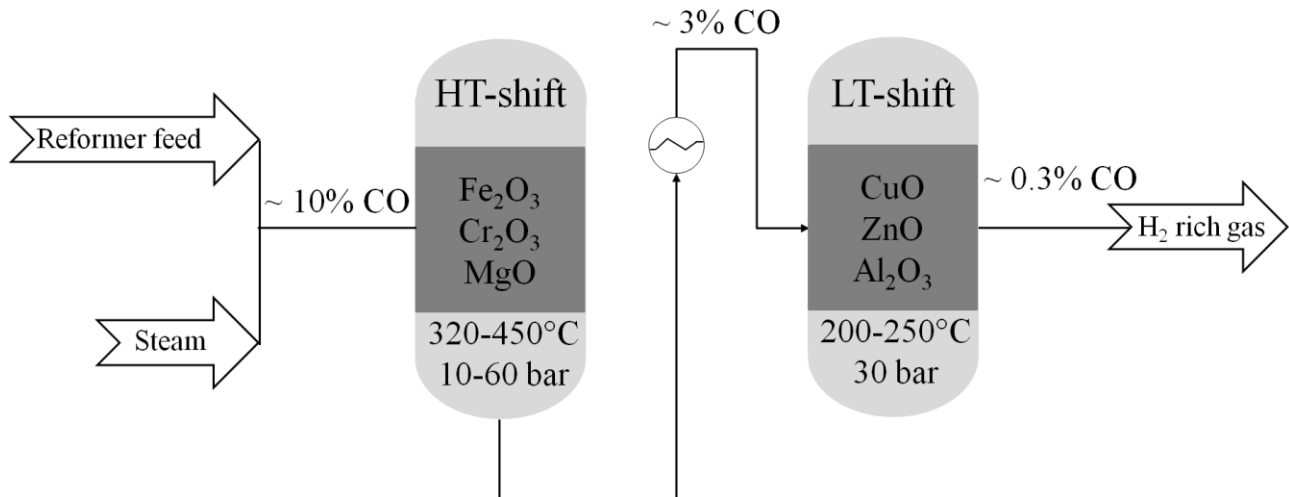
Figure 1.3: Two step industrial water-gas shift setup.

The first step, the so-called high temperature shift reaction (HT-shift), is performed at 320 – 450 °C over an iron oxide based catalyst [13]. The feed gas from the reformer with 10–13% CO content undergoes further processing to decrease residual CO and to increase H_2 yields at 10 – 60 bar with GHSV 400 – 1200 h^{-1} and the operating values depend on the feed composition and adjacent plant requirements [10, 14]. The outlet gas from the HT shift reactor contains ca. 3% CO. The CO concentration in the gas mixture can be further reduced by the so-called low temperature shift reaction (LT-shift). The feed gas for LT-shift is cooled to 200 °C by an inter-cooler system between the stages. The LT-shift reaction operates in the temperature range between 200 and 250 °C using copper oxide based catalysts. A typical operating pressure is 30 bar and GHSV of about 3600 h^{-1} [1, 13]. The resultant CO concentration in the outlet gas is typically less than 0.3%.

1.1.2.1 High Temperature Shift Catalysts

For high temperature operation (320 – 450 °C) ferrochrome catalysts based on an iron oxide structurally promoted with chromium oxide are used [15]. A typical composition of high temperature shift catalyst is 74.2% Fe_2O_3, 10.0% Cr_2O_3, 0.2% MgO and balance volatiles [13]. Cr_2O_3 acts as a stabilizer rather than structural promoter and prevents sintering of iron oxide and decrease in surface area, thus enhancing the activity and stability of the iron based catalysts [12]. Several studies have been performed to determine the optimal content of Cr_2O_3, which is about 14%. Before use, the ferrochrome catalysts need a special treatment in order to improve the activity since Fe_3O_4 is the active phase. The pretreatment of ferrochrome catalysts is carried out by reducing the Fe_2O_3 (Hematite) to Fe_3O_4 (Magnetite) (Eq. 1.8 and Eq. 1.9) using process gas mixtures of hydrogen, nitrogen, carbon monoxide, carbon dioxide and water vapor [10, 12, 15]:

$$3\ Fe_2O_3 + H_2 \rightarrow 2\ Fe_3O_4 + H_2O \qquad \Delta H = -16.3\ \frac{kJ}{mol} \qquad \text{Eq. 1.8}$$

$$3\ Fe_2O_3 + CO \rightarrow 2\ Fe_3O_4 + CO_2 \qquad \Delta H = +24.8\ \frac{kJ}{mol} \qquad \text{Eq. 1.9}$$

$$2\ CrO_3 + 3\ H_2 \rightarrow Cr_2O_3 + 3\ H_2O \qquad \Delta H = -684.7\ \frac{kJ}{mol} \qquad \text{Eq. 1.10}$$

$$2\ CrO_3 + 3\ CO \rightarrow Cr_2O_3 + 3\ CO_2 \qquad \Delta H = -808.2\ \frac{kJ}{mol} \qquad \text{Eq. 1.11}$$

CrO_3 reduces to Cr_2O_3 (Eq. 1.10 and Eq. 1.11) during the pretreatment, creating a solid crystalline solution. In the final reduced state of the catalyst, these are solid solutions of Fe_3O_4 – Cr_2O_3 of the spinel-type [13]. Because of the exothermic reaction (Eq. 1.8, Eq. 1.10 and Eq. 1.11) care must be taken during and after pretreatment (reduction process) to avoid catalyst sintering and loss in activity and surface area. It is also important to avoid "over-reduction" of the active magnetite material to more reduced iron oxides, carbides, or metallic iron species since they produce undesired by product which leads to extra hydrogen consumptions. In addition, "over-reduction" can lead to damage of the catalyst pellets in industrial applications. This leads to a significant pressure drop across the reactor bed [15]. The advantage of HT shift catalysts is their tolerance to small amounts of sulfur (<50 ppm) and chlorine, which are often promoted by Cu [16]. Assuredly, sulfur and chlorine compounds are potential sources of poisoning when their concentrations in the reaction medium are high [13].

1.1.2.2 Low Temperature Shift Catalysts

In the 1960´s the low temperature shift reaction was integrated into industrial WGS processes by using Cu-based catalysts in the temperature range $200 - 250\ °C$. In contrast to ferrochrome catalysts for the HT shift reaction the copper-based catalysts are easily poisoned by sulfur compounds. However, the main advantage of LT shift catalysts is their high activity at low temperature. The CO concentration at the exit of the LT shift reaction can be less than 0.3%. During the development and improvement of these catalysts, a decrease in catalytic activity was observed with increasing reaction temperature. The problem was the susceptibility of copper to sintering and the subsequent loss of copper surface area during the activation (reduction from copper oxide to metallic copper). [10, 12, 17]

$$\mathbf{CuO\ +\ H_2\ \rightarrow\ Cu\ +\ H_2O} \qquad\qquad \Delta H = -\ 80.8\ \frac{kJ}{mol} \qquad\qquad \text{Eq. 1.12}$$

The development was focused on the catalyst activity and stability as well as on resistance to poisoning and sintering. In particular the authors observed an enhancement that a mixture of $CuO\text{-}ZnO\text{-}Al_2O_3$ afforded high and stable copper surface areas. Furthermore, addition of ZnO and Al_2O_3 as structural promoters influenced the activity and decreased the poison resistance. [8, 10] Almost exclusively, $CuO\text{-}ZnO\text{-}Al_2O_3$ based catalysts are used for the industrial LT shift reaction. Gines et al. [18] reported a detailed study concerning the activity and structure-sensitivity of the WGS reaction over $CuO\text{-}ZnO\text{-}Al_2O_3$ based catalysts with different Cu/Zn and (Cu + Zn)/A1 atomic ratios. They prepared different catalysts by the co-precipitation method at $60\ °C$ and constant pH at 7. Subsequently, the catalysts were calcined at temperature between 400 and $700\ °C$. Catalysts with copper metallic surface area between 3 and 35 m^2/g for Cu loading of $30 - 50$ wt.%, Al/Zn atomic ratios of 0 and 2.5 and Cu dispersion between 0.5% and 5% were obtained. A remarkable outcome of the catalytic results was that the turnover frequency did not change due to variations in Cu loading, dispersion, and surface area. The WGS activity test results showed that the WGS reaction over $CuO\text{-}ZnO\text{-}Al_2O_3$ catalysts with copper as active metal is a structure insensitive reaction. Thus the specific WGS rate was proportional to the copper metal surface area, without regard to changing the Al/Zn ratio, the mean copper crystalline size and the copper loading [18]. They concluded that the $CuO\text{-}ZnO\text{-}Al_2O_3$ catalysts exhibited superior activity with CuO in a finely dispersed phase and that both the metallic copper

dispersion and catalytic activity were related to the amount of hydrotalcite contained in the precursor precipitate; the higher the content of the hydrotalcite in the precursor, the higher the catalytic activity of the resulting catalyst [18]

1.1.3 Water Gas Shift Catalysts Development

As discussed above, the WGS reaction is limited due to the thermodynamics at high temperatures and kinetics at low temperature. Therefore, industrial WGS processes consist of two fixed bed reactors (Figure 1.3) over Fr/Cr catalysts for the HT and Cu/Zn catalysts for the LT shift reaction. These catalysts are activated before operation by carefully controlled reduction process over several days. Furthermore, upon shutdown the catalysts must be purged with inert gas to avoid condensation and re-oxidation. Moreover, they are pyrophoric and might be deactivated during repeated startup/shutdown cycles due to condensation of water. [11] In general, industrial WGS catalysts are designed to operate at steady state conditions for months to years without interruption. In recent years, smaller scale hydrogen production for fuel cell applications has received growing attention. In this case, the HT and LT WGS catalysts cannot be used due to the above-mentioned restrictions. Hence, research activities have focused on the WGS catalysts development, aiming at preparation of catalysts for single step WGS reaction and small-scale hydrogen production for fuel processes which exhibit high activity and stability, are less pyrophoric and less sensitive to poisons.

Several publications have focused on noble metal catalysts on oxide supports. In general, it is accepted that the WGS reaction over oxide-supported noble metal catalysts occurs in a bi-functional way, where both the metal and support play essential roles in the mechanism [19]. Supported noble metal based catalysts are regarded as promising single step WGS catalysts since they are stable at high temperature where the kinetics are more favorable and catalysts are less sensitive to poisoning compared to Cu catalysts (LT shift catalysts) and also more active than iron based catalysts (HT shift catalysts) [20]. In the early 1990s it was already known that Pt group metals (e.g. Pt, Rh, Pd, Ru) are highly active catalysts for WGS reaction. Among the investigated catalysts are Pt, Pd, Rh, Au [21-31] particles on several different "reducible" and irreducible" support such CeO_2, ZrO_2, TiO_2, Al_2O_3, SiO_2, CeO_2-ZrO_2 [19, 23, 27, 32-39]. These catalysts are fairly active in the temperature range between 250 and 450 °C. The most

investigated noble metal catalysts are Pt based materials. Non-noble metal catalysts on partially reducible metal oxide supports (Cu/CeO_2, Fe/CeO_2, Cu/TiO_2) have also been studied [33, 40, 41].
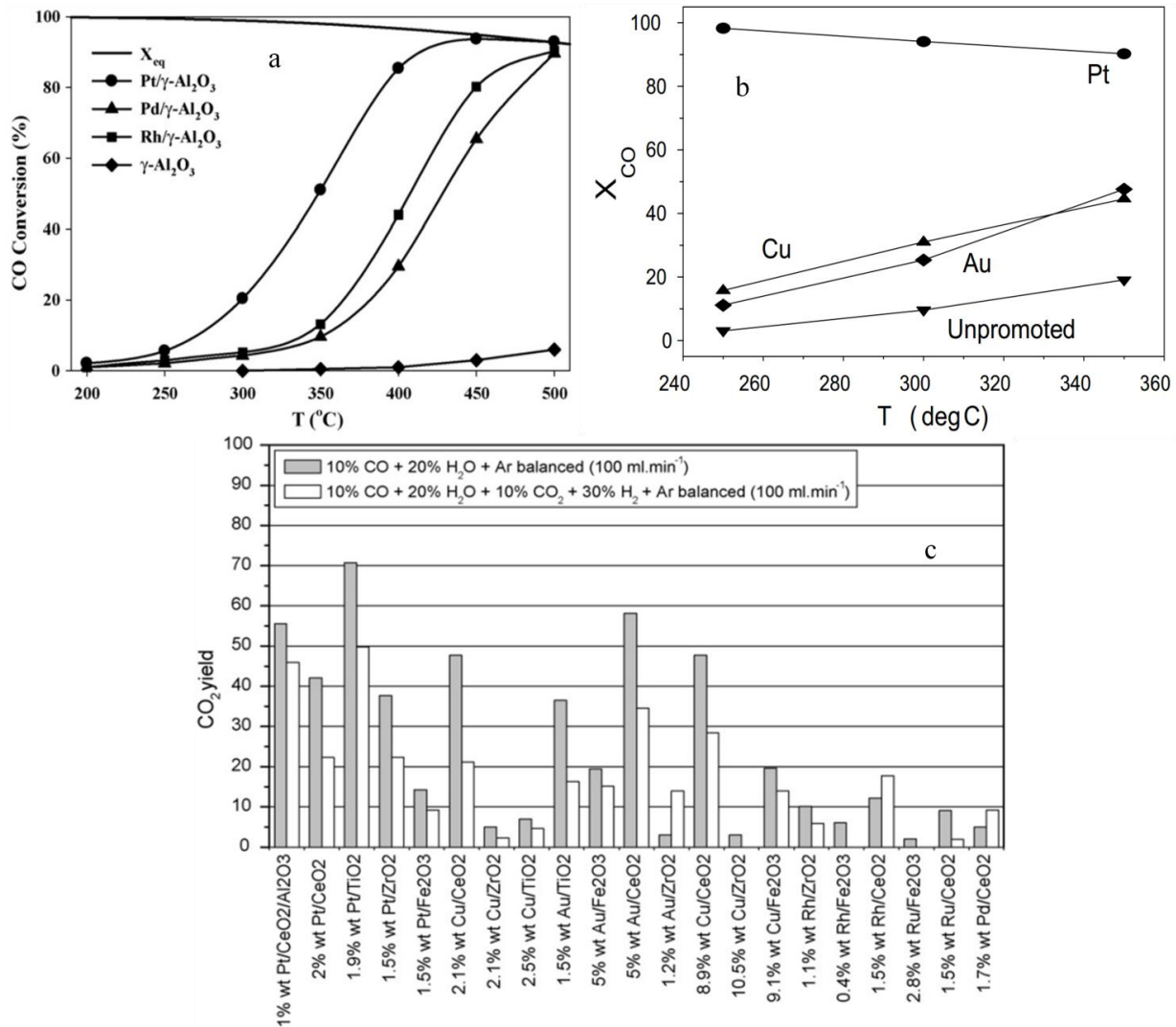
Figure 1.4: (a) Effect of WGS reaction temperature on CO conversion obtained over Pt, Pd and Rh (0.5 wt%) supported on Al_2O_3 with permission from [30], (b) catalyst testing over Pt, Cu and Au supported on CeO_2 with permission from [42] and (c) CO_2 yield at 300 °C with a reformate mixture (10% CO, 10% CO_2, 20% H_2O, 30% H_2, 30% Ar) and a pure reactant mixture (10% CO, 20% H_2O, 70% Ar) with permission from [29].

The catalytic activity of a wide variety of supported noble metal catalysts (Pt, Rh, Ru and Pd) for WGS reactions was investigated by Panagiotopoulou and Kondarides [43]. They found that the catalytic performance of these materials depended strongly on the nature of the metallic phase and the metal oxide support. Pt based catalysts were generally more active than Ru, Rh and Pd.

Additionally, Pt based catalysts showed significantly higher activity on reducible oxides (TiO_2, CeO_2) compared to irreducible oxides (Al_2O_3, SiO_2). Olympiou et al. [30] compared Pt, Pd and Rh on Al_2O_3 and observed a large difference, as shown in Figure 1.4a. The activity increased in the order Pd<Rh<Pt which is correlated to the surface coverage of CO formed on this noble metal under WGS conditions ($\theta_{CO}^{Pd} < \theta_{CO}^{Pt}$). Further investigations were performed on the comparison of Pt, Cu and Au on CeO_2 by Jacobs et al. [42]. They showed that supported Pt exhibited the highest activity (Figure 1.4b). Thinon et al. [29] screened 20 bifunctional WGS catalysts as depicted in Figure 1.4c. Bifunctional implies that both the reducible support and metal sites contribute to the activity. $Pt/CeO_2/Al_2O_3$ and Pt/TiO_2 were found to be the most active catalysts for the high temperature water gas shift reaction whereas gold and copper catalysts showed promising results for low temperature applications. In their study Rh and Ru based catalysts produced significant amounts of methane.

Ceria based catalysts are particular famous in the field of automotive exhaust gas catalysis for oxygen storage capacity (OSC); these materials release oxygen under reducing conditions and take up oxygen under oxidizing conditions [44, 45]. CeO_2 is also known to affect the dispersion of the supported metal particle, to promote WGS and steam reforming reactions, to increase the thermal stability of the support and to promote noble metal reduction and oxidation [45]. In 1993 Shido and Iwasawa [34] studied the mechanism of WGS on Rh/CeO_2 catalysts and suggested that the WGS reaction occurred on the Ce–O pair, not on the metallic Rh species, since under similar WGS reaction conditions the Rh/SiO_2 catalysts were inactive. Bunluesin et al. [21] investigated the kinetics of the WGS reaction. They found that compared to alumina-supported metals, WGS rates were significantly higher on ceria supported Pt, Pd and Rh [21]. Consequently, ceria plays an important role with respect to the WGS reaction.

Besides Pt based catalysts, Au based catalysts have also received considerable attention. Since at low temperature Pt, Rh and Pd based catalysts show low WGS activity, gold catalysts can offer some advantages in the range of 180–250 °C [10]. Oxide supported Au catalysts were observed as low temperature catalysts for CO oxidation by Haruta et al. [10, 46, 47]. Haruta and co-workers recognized that the catalytic activity was high for CO oxidation using catalysts containing Au particles smaller than 5 nm on different metal oxides (e.g. TiO_2, α-Fe_2O_3, Co_3O_4) [46, 47]. Bruch [24] pointed out that oxide-supported gold catalysts were very active at low temperature for the WGS reaction and were certainly more active than Pt based catalysts.

As a promising alternative to standard noble metal based catalysts the doping with alkali metals of these catalysts has been investigated more closely for low temperature WGS reactions in recent years, since the WGS rate can be enhanced by modifying the support through addition of promoters. The reports have shown significant improvement in the WGS rate when doping alkali metals (Na, Li, K) to Pt/CeO_2 [48, 49], Pt/TiO_2 [50-53], Pt/ZrO_2 [54, 55], and Pt/Al_2O_3 [53, 56]. Alkali metal promoted noble metal catalysts led to weakening of the C–H bond of formate [49, 54], which has been proposed as the rate-limiting step in the low temperature WGS mechanism [34, 57]. Further studies showed that by addition of Na or K ions to Pt/SiO_2 catalysts, the catalytic performance was promoted significantly for the low temperature WGS reaction, compared to Na- or K-free Pt/SiO_2 [56]. Panagiotopoulou and Kondarides [50] observed that alkalis interacted strongly with the TiO_2 surface and created new sites (oxygen defect vacancies) at the metal/support interface, which are proposed to be catalytically active sites for the WGS reaction.

1.1.4 Reaction Mechanisms

The reaction mechanism depends on the nature of the catalyst and process conditions. A number of different mechanisms for WGS reactions over metal oxides have been proposed. In most case the important active intermediate species involved are still under discussion.

1.1.4.1 Mechanisms over Industrial Catalysts

The WGS reaction mechanism for HT and LT shift catalysts has been studied thoroughly and various mechanisms were proposed. In the literature the WGS reaction mechanisms are classified as "*redox mechanisms*" and "*associate mechanisms*".

For the iron oxide based water-gas shift catalysts the debate on the mechanism is less controversial. The HT shift reaction is based on the "*redox mechanisms*". One of the first proposed mechanisms for HT shift catalysts was that the WGS reaction proceeds according to an Eley Rideal type mechanism, via alternating reduction and oxidation of the surface of iron oxide [13]:

$$CO + (O) \leftrightarrow CO_2 + (\quad) \qquad\qquad \text{Eq. 1.13}$$

$$H_2O + (\quad) \leftrightarrow H_2 + (O) \qquad\qquad \text{Eq. 1.14}$$

where (O) is an oxygen atom on the oxide surface and ( ) is a vacant site on the surface caused by removal of an oxygen atom through reduction by CO. Subsequently, the surface is reoxidized by H_2O. In 1973 Oki and co-workers proposed a multistep Langmuir Hinshelwood type mechanism, which was reported by Ratnasamy and Wagner [10]. They reported according to calculation by Oki and co-workers that while the evolution of gaseous H_2 from adsorbed H atoms was the rate determining step at low CO conversions, adsorption of CO controls the reaction rate at steady state conditions, near equilibrium conditions in industrial reactors [10]:

$$H_2O + 3* \leftrightarrow 2H* + O* \qquad\qquad \text{Eq. 1.15}$$

$$CO + * \leftrightarrow CO* \qquad\qquad \text{Eq. 1.16}$$

$$CO* + O* \leftrightarrow CO_2* + * \qquad\qquad \text{Eq. 1.17}$$

$$CO_2* \leftrightarrow CO_2 + * \qquad\qquad \text{Eq. 1.18}$$

$$2H* \leftrightarrow H_2 + 2* \qquad\qquad \text{Eq. 1.19}$$
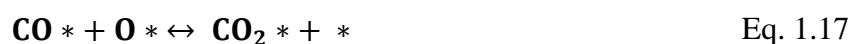
where * refers to an adsorption site. Ratnasamy and Wagner elucidated that the HT shift reaction over Fe_2O_3/Cr_2O_3 catalysts probably proceeds by an oxidation-reduction mechanisms [10]. Further experimental data also revealed the "*redox mechanisms*" to be valid. Rhodes et al. (1995) also discussed the mechanisms of WGS reaction for the shift catalysts, iron oxide. They found also that the redox couple (Fe^{2+}/Fe^{3+}) was labile and capable of dissociating water readily [15].

The LT shift reaction was explained by several authors using both types of mechanisms: *redox mechanisms*" and "*associate mechanisms*". Ovesen et al. [58] (1992) proposed an eight step model (Eq. 1.20 – Eq. 1.27), based on a surface redox mechanism from single crystal studies on copper [59]:

1	$H_2O + * \rightleftarrows H_2O*$	Eq. 1.20
2	$H_2O* + * \rightleftarrows OH* + H*$	Eq. 1.21
3	$2OH* \rightleftarrows H_2O* + O*$	Eq. 1.22
4	$OH* + * \rightleftarrows O* + H*$	Eq. 1.23
5	$2H* \rightleftarrows H_2 + 2*$	Eq. 1.24
6	$CO + * \rightleftarrows CO*$	Eq. 1.25

$$7 \qquad CO* + O* \rightleftarrows CO_2* + * \qquad \text{Eq. 1.26}$$

$$8 \qquad CO_2* \rightleftarrows CO_2 + * \qquad \text{Eq. 1.27}$$
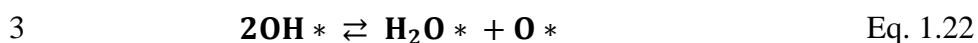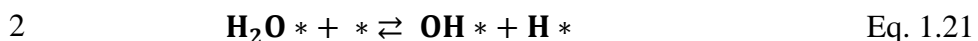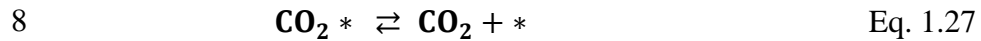
where * represents a free surface site and X* an absorbed species. The model was successfully tested against kinetic data for a working Cu-based catalyst [58]. Van Herwijnenm and de Jong [60] found a good agreement when this model was applied to measurements for an industrial ($Cu/ZnO/Fe_2O_3$) catalyst at 1 bar [59]. Ovesen et al. [59] (1996) further modified this model (8 steps based on redox mechanisms) to include $Cu/ZnO/Al_2O_3$, Cu/Al_2O_3 and Cu/SiO_2 by adding three further steps (to Eq. 1.20 – Eq. 1.27) to explain the formate mechanisms. They suggested that formate coverage was negligible at atmospheric conditions and was significant at higher pressure [59]:

$$9 \qquad CO_2* + H* \rightleftarrows HCOO* + * \qquad \text{Eq. 1.28}$$

$$10 \qquad HCOO* + H* \rightleftarrows H_2COO* + * \qquad \text{Eq. 1.29}$$

$$11 \qquad H_2COO* + 4H* \rightleftarrows CH_3OH + H_2 + 5* \qquad \text{Eq. 1.30}$$

The WGS reaction mechanism at high pressure follows the reaction sequence consisting of steps (Eq. 1.20 – Eq. 1.30) with reaction steps 2, 4, 7, and 10 as possible slow steps (water dissociation and carbon monoxide oxidation) [59]. In these mechanisms formate is present on the surface, but it does not participate in the catalytic cycle for CO_2 formation [59]. Rhodes et al. (1995) discussed also the WGS reaction mechanisms for the LT shift reaction and identified the associative mechanism as a Langmuir Hinshelwood process, which involves the dissociative adsorption of water to form reactive hydroxyl groups, that when combined with adsorbed CO produces a surface intermediate structure (formate and/or carbonate), which subsequently decomposes into CO_2 and H_2 following the reaction steps (Eq. 1.31 – Eq. 1.35) [15]:

$$CO + * \rightarrow CO* \qquad \text{Eq. 1.31}$$

$$H_2O + * \rightarrow H_2O* \qquad \text{Eq. 1.32}$$

$$H_2O* + CO* \rightarrow [\text{intermediate}] \rightarrow CO_2* + H_2* \qquad \text{Eq. 1.33}$$

$$CO_2* \leftrightarrow CO_2 + * \qquad \text{Eq. 1.34}$$

$$H_2* \leftrightarrow H_2 + * \qquad \text{Eq. 1.35}$$

1.1.4.2 Mechanisms over Noble Metal Catalysts

Various studies on the mechanism have also been reported for the WGS reaction over supported noble metal catalysts. Similarly, two main types of mechanisms were suggested: the "*redox mechanism*" and the "*associative mechanism*" with a certain probability that surface carbonates or carboxylates could be intermediates involved in the rate determining step. Although many mechanistic and kinetic studies via noble metal based catalysts (*e.g.* Pt/CeO_2) have been published in recent years, there is still disagreement on the nature of the reaction intermediates and the role of the support.

The "*redox mechanism*" has been reported for WGS reactions over Pt, Rh, and Pd (Pt group) supported on ceria. The key point is that the catalyst is oxidized by H_2O and reduced by CO. In other words, CO adsorbs on metallic sites to form a M–bond carbonyl species, which reduces the support and releases CO_2 (step a and b shown in Figure 1.5). The water adsorbs and dissociates on a partly reduced support, releasing H_2 and reoxidizing the support (step c shown in Figure 1.5).

Figure 1.5: Redox reaction mechanism scheme for WGS reaction on Pt/CeO_2 with permission from [61].

Bunluesin et al. [21] (1998) compared the WGS kinetics on ceria supported Pd, Pt and Rh with alumina supported catalysts. They showed that over ceria supported Pt, Rh and Pd the WGS rates were significantly higher compared to either ceria by itself or the alumina supported metals. They proposed that the reaction followed a mechanism in which metal-adsorbed CO is oxidized by ceria, which in turn is oxidized by water [21]. Pt, Rh and Pd were equally effective as catalysts. Depending on the support there are two types of "*redox mechanisms*" [62]:

monofunctional *redox mechanisms* on the noble metal:

$$M + H_2O \rightleftarrows M - O + H_2 \qquad \text{Eq. 1.36}$$

$$M + CO \rightleftarrows M - CO \qquad \text{Eq. 1.37}$$

$$M - O + M - CO \rightleftarrows 2M + CO_2 \qquad \text{Eq. 1.38}$$

bifunctional noble metal–support *redox mechanisms*::

$$S + H_2O \rightleftarrows S - O + H_2 \qquad \text{Eq. 1.39}$$

$$M + CO \rightleftarrows M - CO \qquad \text{Eq. 1.40}$$

$$S - O + M - CO \rightleftarrows M + CO_2 + S \qquad \text{Eq. 1.41}$$

where M and S are noble metal and support surface sites respectively. Vignatti et al. [62] studied the WGS reaction on Pt particles supported on reducible and non-reducible supports, namely Pt/SiO$_2$, Pt/CeO$_2$, and Pt/TiO$_2$ catalysts, by *in situ* diffuse reflection infrared Fourier transform spectroscopy (DRIFTS). They reported that on reducible support (CeO$_2$ and TiO$_2$) the WGS reaction was catalyzed via a bifunctional metal–support mechanism (Eq. 1.39 – Eq. 1.41), whereas non-reducible SiO$_2$ catalyzed the WGS reaction through a monofunctional *redox mechanism* (Eq. 1.36 – Eq. 1.38).

The "*associative mechanism*" is based on an adsorption/desorption model. In this model the adsorbed species interact to form an adsorbed intermediate "*formate*" which then decomposes to form CO$_2$ and adsorbed hydrogen. In other words, the terminal OH groups on partially reduced ceria react with CO forming bridge formates that are converted to bindentate formates by co-adsorbed water, subsequently formates decompose to form H$_2$ and CO$_2$ [62]. The *associative formate mechanism* was proposed by Shido and Iwasawa in 1992 [34]. They compared the reaction mechanism on Rh/CeO$_2$ and Rh/SiO$_2$ and observed that the catalytic WGS reaction proceeds not on Rh metallic particles, but on Ce–O pair sites of Rh/CeO$_2$, whereas Rh/SiO$_2$ was inactive under similar conditions. They argued that the addition of Rh increases the reaction rate by changing the local structure or surface morphology around the reaction site on CeO$_2$. Shido and Iwasawa [34] suggested that the terminal OH groups on Ce ions react with CO to form bidentate formates (surface formate); 65% of the surface formates decompose to ─OH+CO (backwards decomposition) and 35% of surface formates decompose to H$_2$+CO$_2$ (forward decomposition). In the literature it has been suggested that the transformation of these formates could be influenced further by the presence of water. The co-absorbed water also promotes the decomposition of the unidentate carbonate which can react to form CO$_2$ or surface carboxylates

and bindentate carbonate [10, 24, 34]. Likewise there are two types of "*associative mechanism*" depending on the surface intermediates: "formate" mechanism (Figure 1.6 top) and "carbonate/carboxylate" mechanism (Figure 1.6 bottom).
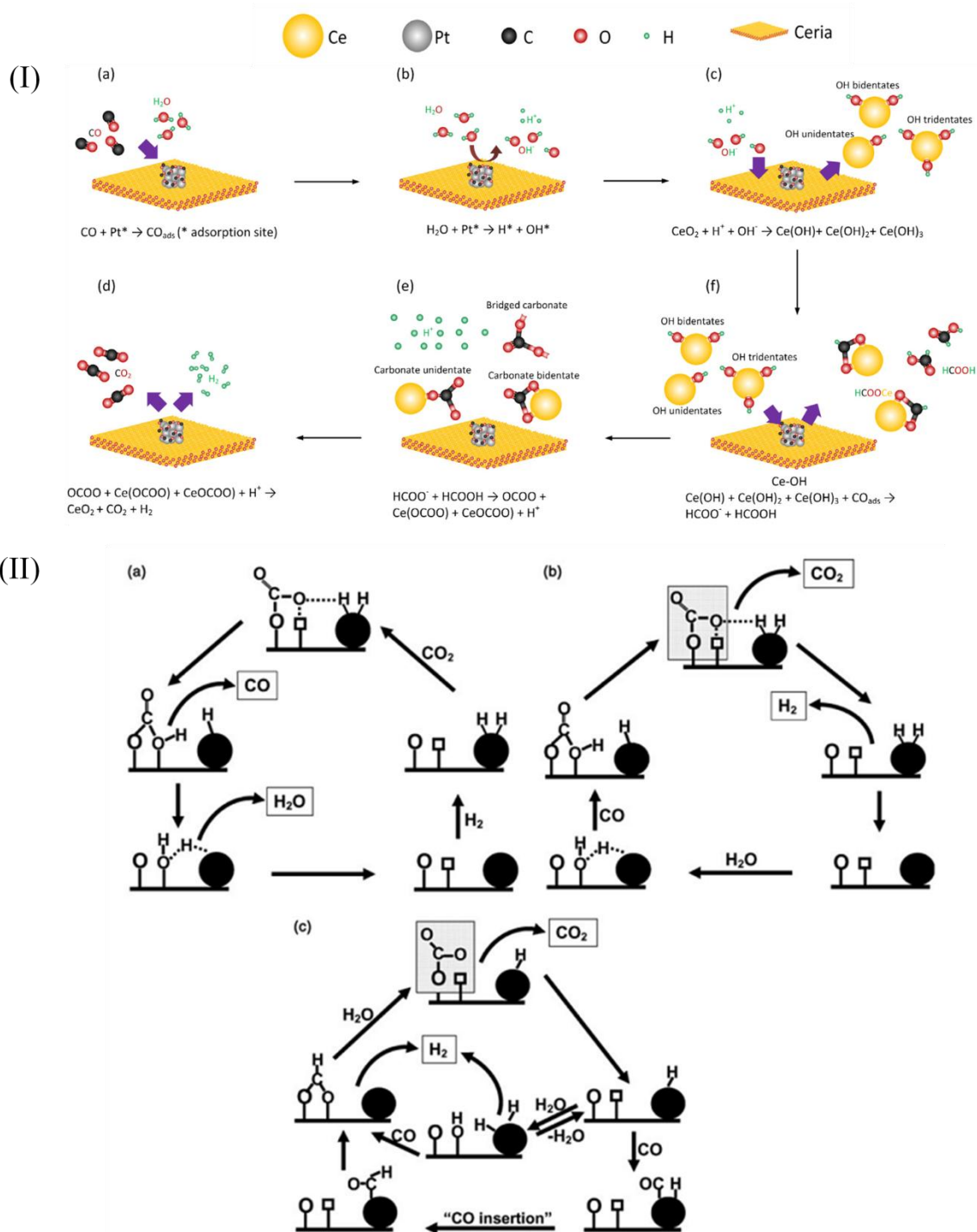
Figure 1.6: Formate mechanism on Pt/CeO_2 (I) with permission with [61] and proposed "carbonate/carboxylate" mechanism for the WGS reaction (II) with permission from [24].

Gokhale et al. [63] proposed the surface carboxylic species from theoretical calculation to investigate the WGS reaction on copper crystallite in Cu/ZnO industrial WGS catalysts. Their alternative model for the WGS reaction involves the oxidation of absorbed CO by absorbed OH, to form carboxyl (COOH) species which decompose to CO_2 [63]. Burch [24] published a discussion of the relative merits of the various mechanisms, showing the proposed "carbonate/carboxylate" mechanism for the reverse (image a in Figure 1.6 bottom) and forward (image b in Figure 1.6 bottom) WGS reaction. In both cases, the importance of the carbonates and/or carboxylates was emphasized. This publication also introduced the "universal mechanism" (image c in Figure 1.6 bottom) for WGS reaction to try to integrate formate and redox mechanisms into a single model [24]. The dominant mechanism depends on the reaction conditions, specifically temperature and S/C ratio. It can change from redox-type, to a process dominated by surface intermediate species, including formates, carbonates and carboxylates [10, 24]. At higher temperatures the redox process would be expected to be most important. At low temperatures, especially in the presence of a substantial amount of carbon dioxide, the final carbonate decomposition step in the mechanism should dominate [24].

1.2   Water Gas Shift Reaction in Membrane Reactor

As mentioned before, unlike fossil fuels, hydrogen as an energy source produces water as the only byproduct. Hence, due to an increasing demand for renewable energy sources and concerns about environmental issues the demand for hydrogen has grown continuously. This is a clear motivation for improving strategies for hydrogen production, separation and purification from pre-existing industrial process. One of the primary sources of hydrogen production is the hydrocarbon based sources. The flow coming out from a reformer or a coal gasification plant contains 50% hydrogen and 45% CO, which can later be converted via water gas shift reaction to produce further hydrogen [64]. Subsequently, hydrogen needs to be purified after being processed. Hydrogen can be purified using several techniques, such as pressure swing adsorption (PSA), cryogenic distillation (CD) or membrane separation [9, 65]. The pressure swing adsorption processes are commercial separation techniques for high purity hydrogen (99.999% H_2) in the chemical and petrochemical industries [66]. CD is a commercially available as well, yielding hydrogen purity below 95%. However, the capital cost and energy consumption for PSA and CD are high [9, 65]. Alternatively, membrane separation techniques are considered for high

purity and hydrogen production. In 2006 researchers started to work in an R&D (Research & Development) project for the development of a new schema for hydrogen production through stream reforming based on integration chemical reaction and membrane separation [67], in a so-called membrane reactor. According to the IUPAC definition, a membrane reactor (MR) is a system for simultaneously processing a reaction (e.g. WGS reaction) and a membrane based separation in the same physical device (Figure 1.7b) [68].
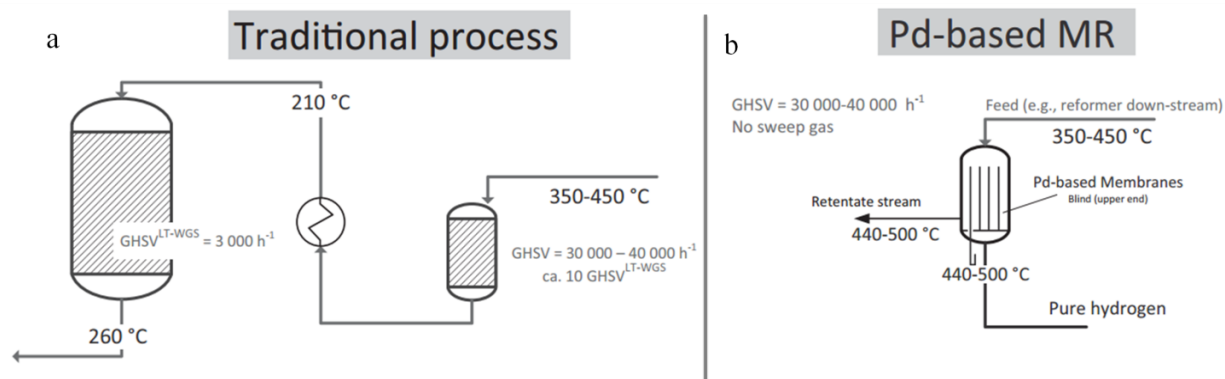
Figure 1.7: Schematic drawing of ''traditional reactor process (TR)'' (a) and ''Pd-based membrane reactor (MR)''(b) for WGS reactions (the values for temperature and GHSV indicate a typical operation parameter) with permission from [69].

As discussed in section 1.1 and 1.1.2, the traditional reactor process (TR, Figure 1.7a) is based on a multi stage CO shift reactor: in the first reactor a large amount of CO is converted into CO_2 and H_2 over Fe_2O_3/Cr_2O_3 catalysts at high temperature (Eq. 1.6). The second reactor is operated at low temperature using CuO/ZnO catalysts to further decrease the final CO concentration in the feed gas. The H_2 rich stream coming out from the TR process is directed to a pressure swing adsorption (PSA) unit for H_2 separation from the other gases, in particular CO [69]. The membrane reactor represents an attractive approach to integrate the WGS reaction and H_2 separation in a single unit. Pd-alloy membrane reactors (Figure 1.7b) are the most commonly used for selective hydrogen removal in applications because of their high H_2 selectivity [64]. The potential advantages of membrane reactors compared to traditional reactors are lower capital and downstream separation costs, as well as enhanced yield and selectivity [67]. Another important advantage of membrane reactors is that one of products is continuously removed from the reaction gas, thereby shifting the equilibrium of the reaction "to the product side" according to Le Chatelier´s principle. This implies, that using MRs for WGS reaction leads to: (i) higher CO conversion compared to TR under the same operation conditions or (ii) similar CO conversion as

in TR, but working under milder operation conditions [8]. In other words, removal of a product such as hydrogen from the reaction volume offers several advantages: (i) conversion enhancement of equilibrium-limited reactions, (ii) depletion of undesired secondary reactions, (iii) recovery of a concentration of rich stream, (iv) more favorable operating condition (e.g. temperature, GHSV) [70]. Membranes and membrane reactors for pure hydrogen production have been widely investigated, since the choice of the membrane integrated in the MRs depends on parameters such as separation selectivity, membrane life time, mechanical and chemical stability, operating conditions and the cost [71]. Generally hydrogen selection membranes can be categorized into: (i) polymeric membranes, (ii) porous membranes and (iii) dense metal membranes [65, 71]. Dense metal membranes are commonly used for high purity hydrogen production. They are made of Pd and Pd-alloys, mainly Pd–Ag, Pd–Cu, and Pd–X–Au and decrease the embrittlement and the poisoning of the membrane when in contact with contaminants such as CO and H_2S [71]. The mechanisms of hydrogen permeation through dense metal membranes have been thoroughly studied and reported. The well-known solution diffusion mechanism and the steps involved in hydrogen transport from high to low pressure gas regions are the following 7 steps listed in Figure 1.8: (1) diffusion through the boundary layer to the surface of the membrane, (2) reversible dissociative adsorption on the surface, (3) dissolution of atomic hydrogen into the bulk metal, (4) diffusion to the opposite face through the bulk metal, (5) associative of hydrogen atom on the surface, (6) desorption of molecular hydrogen and (7) diffusion of molecular hydrogen away from the surface [72, 73].
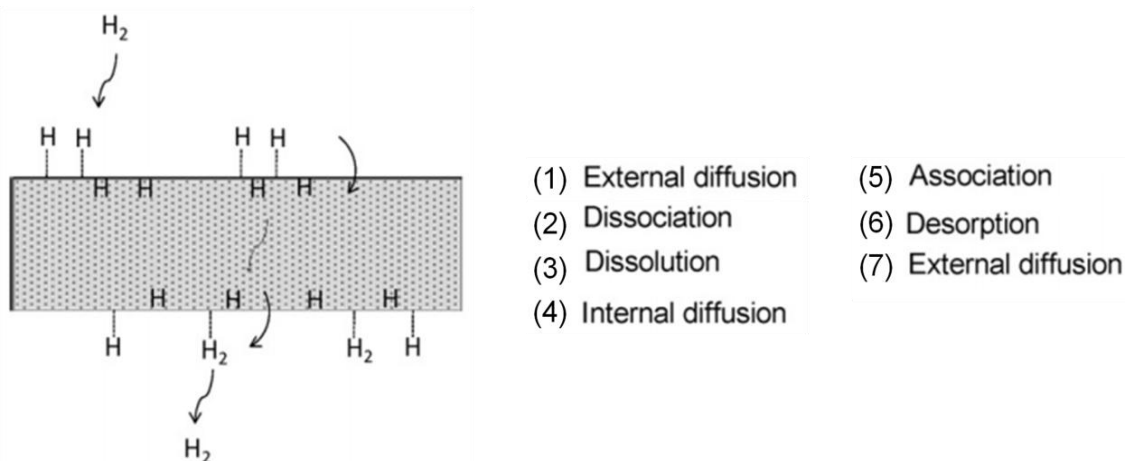
Figure 1.8: Solution diffusion mechanism of hydrogen permeation through a palladium membrane reprinted with permission from [72].
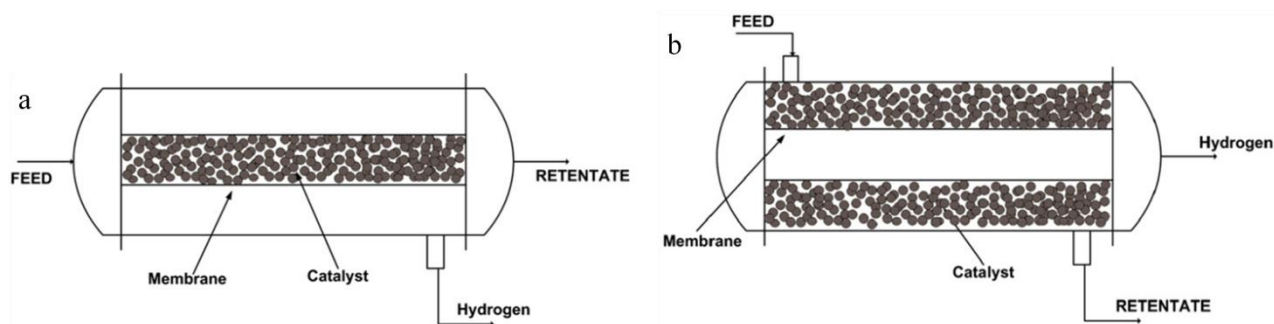
Figure 1.9: Typical packed bed membrane reactors: (a) catalysts in tube and (b) catalyst in shell, with permission from [71]. The retentate is the part of the feed that does not pass through the membrane whereas the permeate contains the species passing through the membrane.

The performance of membrane reactors has been studied for dehydrogenation and several reactor types have been proposed in the literature [68, 71], including packed bed membrane reactors (PBMR), fluidized bed membrane reactors (FBMR) and membrane micro reactors (MMR). The majority of studies have been performed in packed bed membrane reactors (PBMR), since the effect of the hydrogen permeation through membranes on the reaction system was the aim of the first studies on membrane reactors. In a PBMR the catalyst is located as a fixed bed and in contact with a H_2 selective membrane. A typical PMBR design for a lab scale application is shown in Figure 1.9. The most common PMBR is the tubular one where the catalyst may be packed either in the membrane tube (Figure 1.9a) or in the shell side (Figure 1.9b) [71]. Tokyo Gas works on an advanced membrane reformer system development for highly efficient hydrogen production from natural gas. In the membrane reformer, natural gas is reformed in the catalyst bed and hydrogen can be separated from a reformed gas mixture by a hydrogen separation membrane. The working principle of the membrane reformer is similar to Figure 1.9b [74]. Tokyo Gas has developed and operated the membrane reformer for the production of $40 \, Nm^3 H_2$/h from natural gas, and an efficiency of 81.4% was reported [74]. However, there is an increasing interest in membrane micro reactors. Micro reactors offer several advantages, including high surface area to volume ratio, high heat and/or mass transfer [75, 76]. In other words, only a low amount of catalyst is required for a micro structured plate per reactor volume, which allows a more efficient utilization of the catalyst due to the improved heat and mass transfer properties [77]. Germani et al. [78] tested $Pt/CeO_2/Al_2O_3$ WGS catalysts containing 1.7 wt.% Pt and 10.7 wt.% CeO_2 in a microreactor and as powder in a quartz tube reactor. In Figure 1.10a CO conversion are compared for the catalyst coating in the micro structured plate

and powder catalyst in the tube reactor [78]. The results show that the catalytic performance is much higher if the catalyst is used as a coating in micro channels.
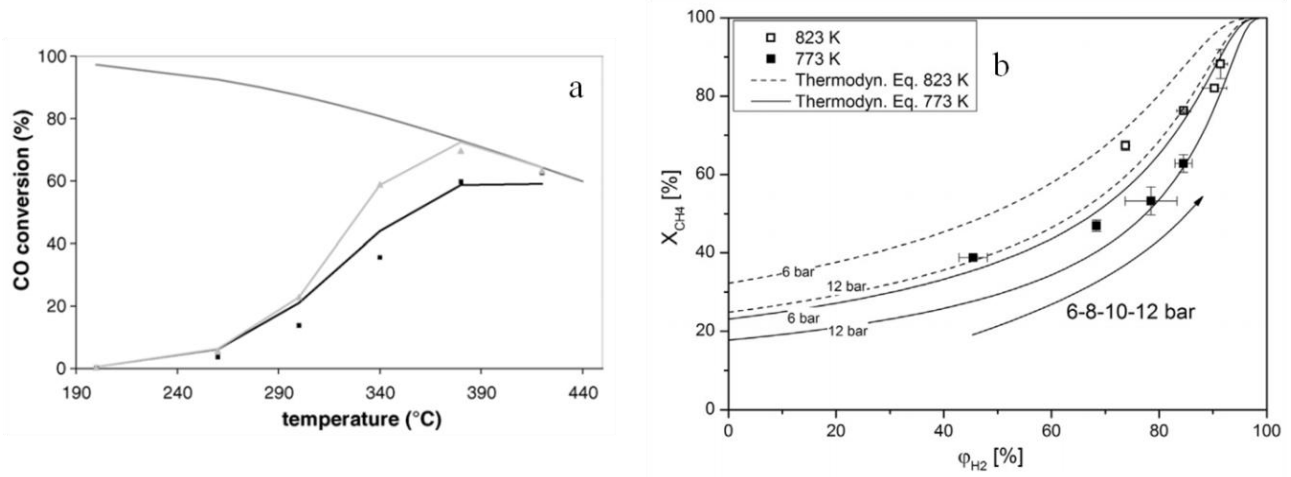
Figure 1.10: (a) Comparison between stainless steel microchannels (grey) coated with $Pt/CeO_2/Al_2O_3$ catalyst (containing 1.7 wt.% Pt, 10.7 wt.% CeO_2) and as powder samples (black); the symbols represent experimental data, the lines model calculations, with permission from [78]. (b) Methane conversion as a function of hydrogen recovery for an integrated steam methane membrane micro channel reformer, reprinted with permission from [76].

Goerke et al. [79] investigated Au/CeO_2 and Ru/ZrO_2 catalysts for the water-gas shift reaction in microchannels and found that at small average residence times of less than 30 ms, which are typical for micro structured reactors, the water gas shift reaction at $250 - 300$ °C over a Ru/ZrO_2 catalyst was able to reduce the CO content by more than 95% [79]. They furthermore observed that when coated onto Fe/Cr alloy foils rather than stainless steel, the ruthenium catalyst exhibited high activity while the gold catalyst showed little activity [79]. Boeltken at al. [76] successfully developed a modular micro structured membrane reactor for *in situ* extraction of hydrogen. They integrated a Pd membrane with a thickness of 12.5 µm with laser welding between microstructure plates. The system showed very promising results, (Figure 1.10b) e.g. at 12 bar feed pressure, 550 °C and GHSV of 29.000 h^{-1} the resulting methane conversion was 87%, hydrogen recovery reached 92%, and hydrogen purity was above 99.5%.

1.3 Flame Spray Pyrolysis

Catalysts play a key role in the chemical industry where chemical reactions are used to transform raw materials into high-value products. The development of catalysts is an interdisciplinary field of research. [80] Most commonly, catalysts are synthesized using multi-step wet chemical techniques. Incipient-wetness, impregnation, precipitation, sol-gel, just to name a few, are batch processes requiring several after-treatment steps, such as filtration, drying and calcination [80, 81]. More than 80% of all technical catalysts are currently produced using precipitation and impregnation/coating [80]. Figure 1.11 shows a schematic route of catalyst preparation. The first step starts with the precipitation of the support which is washed, filtered, dried and calcined, consecutively. This step is followed by the impregnation of active metal. Finally, after repeated steps, drying and calcination the catalysts are obtained. In contrast to this multi-step wet chemistry procedure, an alternative catalysts preparation method in a single step is flame aerosol technology that allows large scale production of nanoparticles [82].
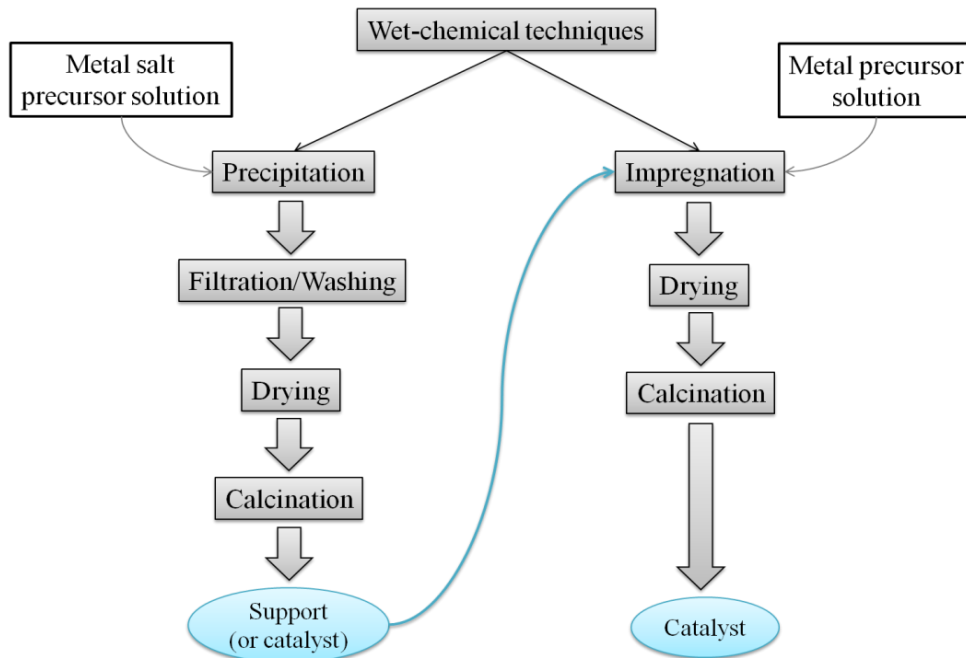
Figure 1.11: Preparation routes for technical catalysts (adapted from [80]).

The flame aerosol technology is the most widely used method for the production of commercial quantities of nanoparticles [83]. Since the 1970s this technology is employed widely for large-scale production of carbon blacks as reinforcing agents, fumed SiO_2 as the major flowing aid in

industry (pharmaceuticals, cosmetics etc.), TiO_2 for pigments and catalysis, Al_2O_3, ZnO as well as other ceramic nanoparticles made by industrial leaders such as Cabot, Cristal (formerly SCM and Millenium Chemicals), DuPont, Evonik (formerly Degussa) in millions of tons, valued at more than $15 billion/yr [82-84]. The success of this technology is based on the obvious advantages of a single step process.

Depending on the state of the supplied precursor (aqueous-based, solvent based, vapor) various flame aerosol reactors have been used. They can be classified into four general categories: (i) *vapor-fed aerosol flame synthesis* (VAFS), (ii) *liquid-fed aerosol flame synthesis* (LAFS), (iii) *flame-assistant spray pyrolysis* (FASP), and (iv) *flame spray pyrolysis* (FSP) [82, 85]. VAFS is most commonly used industrial method for production of fumed silica, alumina and pigmentary titania. In this process a metal precursor (chlorides, e.g. $SiCl_4$, $AlCl_3$ and $TiCl_4$) is evaporated and fed into a flame to manufacture most present ceramic commodities. A disadvantage of VAFS is the limited availability of volatile precursors at reasonable cost. LAFS, also called furnace process, is used to produce carbon black. This technique is more versatile since a liquid precursor solution, emulsion or slurry is utilized to obtain the desired particles. In contrast to VAFS and LAFS, the flame assisted spray pyrolysis (FASP) is more flexible because precursors are usually in an aqueous solvent and supplied in a state of low combustion enthalpy (<50% of total combustion energy). These non-combustible liquid precursors (inorganic precursor) are dispersed into fine droplets that are evaporated and ignited by an external hydrocarbon flame as a heat source. The FASP reactors allow the use of inexpensive precursors and solvents (e.g. metal salts; nitrates, ethanol). Depending on the process conditions the precursor reacts in droplets or gas phase to form hollow, micron or nano sized particles respectively. In a FSP set-up an organic solvent precursor with significantly higher combustion enthalpy (>50% of total energy of combustion) is sprayed and ignited, resulting in formation of nanoparticles. The organic precursor solution is dispersed either ultrasonically or with the aid of a gas (e.g. O_2) through a nozzle [82, 85-87].

Flame spray pyrolysis which is the focus of this work is a rather new technique compared to other flame aerosol reactors. The advantage of FSP is a self-sustaining flame, usage of liquid feed and less volatile precursors. Furthermore, it can be scaled up for high temperature flames and large temperature gradients. FSP was first introduced in the 1970s by Sokolowski et al. [88] for synthesis of Al_2O_3 nanoparticles by combusting an ultrasonically dispersed spray of aluminum

acatylacetonoate in benzene/ethanol. Two decades later the process was further developed by Bickmore et al. [89] in 1996 who used a single pilot-scale FSP to synthesize nanosized spinel $MgAl_2O_4$. Mädler et al. [90] introduced a FSP set up (Figure 1.12) using an air-assisted nozzle surrounded by six CH_4/O_2 flamelets for production of SiO_2 using hexamethyldisiloxane (HMDSO) as metal precursor and ethanol, iso-octane, or methanol as organic solvent. Figure 1.12 shows that in this case the precursor solution is injected with a syringe pump though the capillary tube while the dispersion gas passes through the annular gap. The sprayed precursor droplets are ignited by supporting CH_4/O_2 flamelets and the particles are collected on a filter above the flame using a vacuum pump. [90]
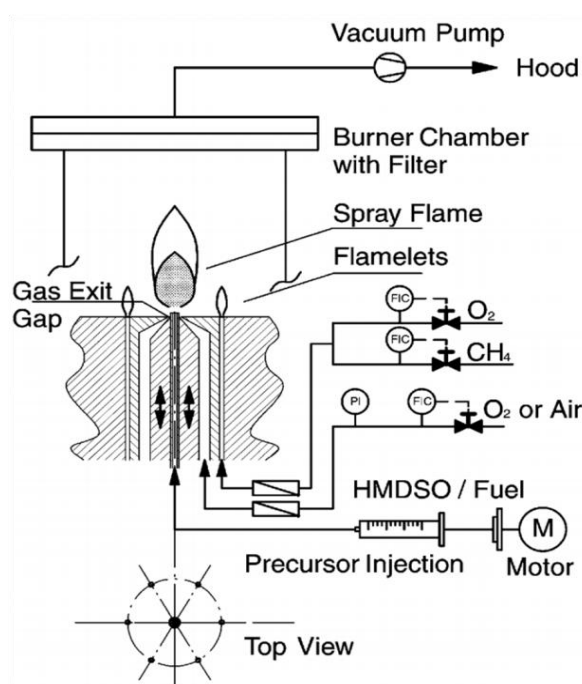
Figure 1.12: FSP set-up with an air-assisted nozzle and CH_4/O_2 supply for the supporting flames, nanoparticles on a filter are collected with the aid of a vacuum pump with permission from [90].

The flame temperature for FSP was found to be 2765 K [91] and 2600 K [90] due to the highly exothermic nature of the precursor solutions (high combustion enthalpy) with extremely short residence times (milliseconds) with high temperature gradients (170 K/cm) along the flame axis using Fourier transform infrared (FTIR) spectroscopy [82]. The flame temperature profile along the axis and the flame height above the nozzle can be controlled by adjusting the feed rate and dispersion/oxidant gas. Increasing feed rate, for instance 27.1 to 81.1 mL/min, increased the spray flame height from 13 to 37 cm [91]. Mueller et al. [91] observed that the temperature for

both feed rates closer to the nozzle was 2765 K and the temperature decreased by 45 K/cm and by 30 K/cm for the flame height 13 and 37 cm, respectively. In other words, increasing the feed rate results in a higher enthalpy content of the flame that leads to longer particle residence times at high temperatures. Schulz et al. [92] observed the flame temperature along the flame axis and found out that the temperature profile showed a maximum close to the nozzle and rapidly decreased towards tip due to entrainment of ambient air. Mädler et al. [90] investigated axial measurements for two dispersion/oxidant flow rates for air and oxygen, respectively. Their measurements clearly showed the higher average flame temperature for oxygen compared to air as dispersion/oxidant gas. They also adjusted the dispersion/oxidant flow rate and the results showed that the temperature dropped very rapidly with increasing dispersion/oxidant flow rate. For instance, in case of O_2 as dispersion/oxidant gas the temperature at a distance of 12 mm from the nozzle was 2340 K for 2.8 L/min and 1660 K for 4.6 L/min [90]. In all cases the temperature close the nozzle tip is quite high and similar because the visible spray ignition just starts at this location [90, 91]. Temperature and the temperature gradients are the most important feature of FSP. High temperature promotes the formation of homogeneous and highly crystalline materials, and also due to high temperature gradients and short residence time the particles form at the nanoscale, the particle sintering is slowed down, and the specific surface area increases [82].

Figure 1.13: Formation of nanoparticles in FSP flames according to [87, 93].

Figure 1.13 illustrates the principle of the formation of particle and growth in the flame. Their formation can proceed through the droplet-to-particle or a gas-to-particle route, thus leading

homogeneous morphology and size. The sprayed liquid precursor evaporates and/or decomposes into metal vapor. Due to supersaturation nucleation takes place. Afterwards, the particles grow by coalescence and sintering. Finally, the particles further aggregate (forming hard agglomerates by chemical bonds) and agglomerate (mainly physical bonds) and are subsequently collected on the filter. In the case of supported noble metals, the support is formed first and then noble metal particles nucleate at lower temperature heterogeneously on the support (Figure 1.13) [87]. Strobel et al. [94] and Teoh et al. [95] prepared Pt/Al_2O_3 (1–10 wt% Pt) and Pt/TiO_2 (0.1–4 wt% Pt) catalysts by FSP. They obtained well-dispersed Pt particles (below 5 nm) supported on Al_2O_3 or TiO_2. The platinum dispersion on both supports depended strongly on the Pt loading and support surface area, resulting in an almost linear increase in Pt particle size with the Pt loading (Al_2O_3 or TiO_2). They also reported that it is possible by substitution of Ti^{4+} (0.61 Å) by Pt^{4+} (0.63 Å) in single flame processes [95]. With regard to supported metal catalysts, it can be concluded that preparation of supported noble metals by FSP generally results in well-dispersed noble metal nano particles, nonporous supports, high crystallinity and often high thermal stability.

Generally, catalysts are multicomponent materials which can be also produced by FSP. In some multicomponent materials, segregation of particulate phases is necessary, only desired with little physical inter-particle mixing. Besides, in the synthesis of oxide-supported noble metal catalysts, it should be possible to tailor the size of the noble metal clusters independently of support particle size. To achieve the desired segregation of phases or to control particle formation separately, a novel two nozzle FSP (double flame spray pyrolysis) process was developed. In a DFSP set-up the precursors are prepared separately and ignited in individual flames that intersect at a defined distance, following which the nanoparticles are collected on a filter. The DFSP method was first reported by Strobel et al. [96] for the synthesis of a $Pt/Ba/Al_2O_3$ catalyst used for NO_x storage-reduction. They observed that spraying all three components together across the nozzle resulted in formation of $BaAl_2O_4$, which is not active for NO_x storage-reduction. However, the application of two separate nozzles, one as alumina and the other as a barium oxide/platinum source, resulted in $Pt/Ba/Al_2O_3$ consisting of individually crystalline $BaCO_3$ and Al_2O_3 nanoparticles well mixed at the nano level [96]. Likewise, Høj et al. [97] used a two nozzle system for synthesis of $CoMo/Al_2O_3$ to avoid the formation of an inactive $CoAl_2O_4$ mixed phase. To eliminate an inactive phase in MnO_x/Al_2O_3 and FeO_x/Al_2O_3 catalysts Tepluchin et al. [98] also applied the two nozzle FSP system.

1.4 *In situ* X-ray Absorption Spectroscopy

X-ray absorption spectroscopy (XAS) is a well-established technique for studying in an element specific manner the local structure around selected absorber atoms in a material. The application field of XAS is quite wide. It is possible to perform XAS analysis on almost any category of materials. Some examples of samples are crystals, amorphous systems, glasses, disordered films, membranes, gases, liquids, bulk solids, solution etc. Likewise, it is feasible to analyze these samples under desired reaction conditions. Some samples can be measured under special conditions, such as high and low temperature, high and low pressure, and alternative gas atmospheres (reactive or inert) or under reaction conditions relevant for catalytic studies.
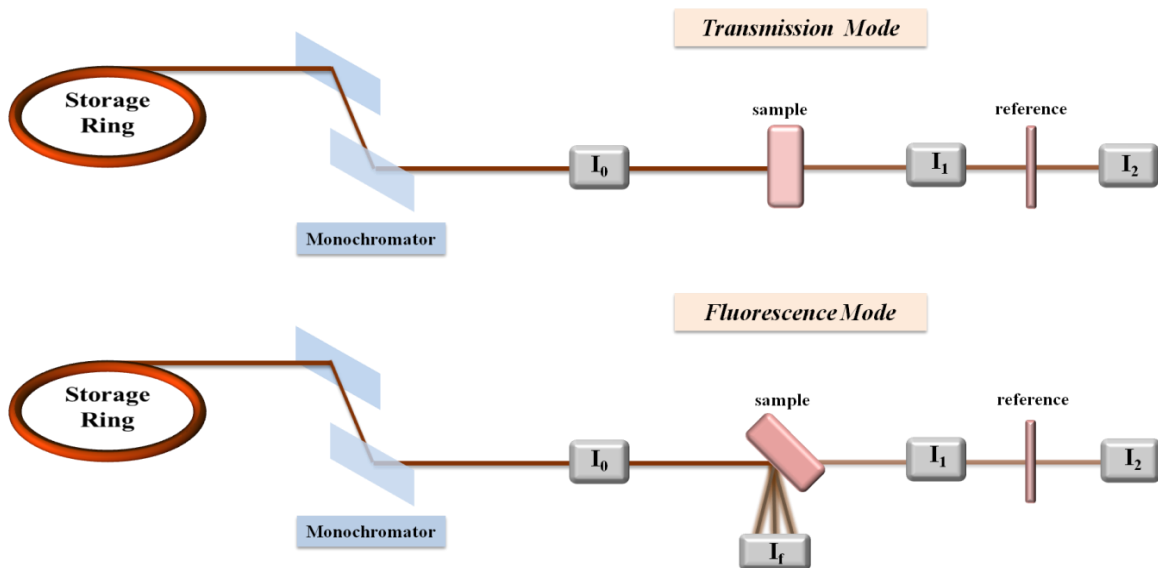
Figure 1.14: Experimental set-up for XAS measurements in transmission (top) and in fluorescence (bottom) mode (I_0: incoming intensity, I_1 and I_2: transmitted intensity, recorded from the first, second and third ionization chambers; I_f: intensity of fluorescence radiation, recorded from fluorescence detector).

XAS experiments require a high intensity tunable X-ray source, such as a synchrotron light source. A synchrotron consists of an evacuated storage ring in which high energy electrons circulate close to the speed of light. Electrons are kept in a closed orbit by bending magnets which cause them to emit electromagnetic radiation. In straight sections of the ring insertion devices (Undulator/wiggler) can be installed which provide higher intensities and a broader photon energy range. So-called beamlines are placed tangentially at intervals around the ring, guiding the synchrotron light to various end stations designed for specific experiments. Figure

1.14 shows a simple schematic of a typical XAS beamline. The radiation from the storage ring is a broad spectrum from infrared to hard X-rays. To obtain monochromatic light for XAS measurements in many cases double crystal monochromators are used (Figure 1.14). The monochromatic beam intensity is detected by ionization chambers. The incoming intensity and the intensity transmitted by the sample, as well as after a reference sample for energy calibration are measured, as shown in Figure 1.14. Additionally, fluorescence detector is placed perpendicular to the incident beam to measure the fluorescence radiation (Figure 1.14).

In a typically XAS experiment, monochromatic x-rays with defined energy pass through a homogenous sample of well-defined thickness *d*. The x-rays photons can be absorbed by the atoms in this sample thereby exciting electron from core levels to an empty state above the Fermi level. To excite an electron from a core level, the photon energy absorbed must be equal or higher than the energy of core level. The core level energy (absorption energy) is characteristic for each chemical element, due to the unique electronic structure. The linear absorption coefficient µ of the sample at a given energy can be calculated from the logarithmic ratio of the incoming and transmitted intensity using Lambert-Beer´s law: [99, 100]

$$I_1(E) = I_0(E)e^{(-\mu(E)\,d)}$$

$$
\begin{aligned}
I_0(E) &= \quad \text{incident intensity} \\
I_1(E) &= \quad \text{transmitted intensity} \\
d &= \quad \text{thickness of sample} \\
\mu(E) &= \quad \text{absorption coefficient}
\end{aligned}
$$

XAS experiments can be performed in transmission or in fluorescence mode (illustrated in Figure 1.14). Depending on the mode µ(E) can be calculated as follows [101]:

transmission mode:

$$\mu(E) \propto \ln\frac{I_0}{I_1}$$

fluorescence mode:

$$\mu(E) \propto \frac{I_f}{I_0}$$

$$I_f = \quad \text{intensity of fluorescence radiation}$$

The absorption coefficient μ(E) describes how strongly x-rays are absorbed as at a specific photon energy and depends on the sample density ρ, the atomic number Z, atomic mass A, and photon energy E [101]:

$$\mu \approx \frac{\rho Z^4}{AE^3}$$

In general, the absorption coefficient decreases with increasing photon energy, but at a specific photon energy above the so-called absorption edge the absorption coefficient suddenly increases [102]. For example, a photon energy of ca. 23220 eV is required to excite an electron from the 1s orbital of rhodium into the continuum, leading to a sharp increase in the absorption coefficient, known as the Rh K-edge. Excitations of electrons from n=1 states are referred to as K-edges, from n=2 as L-edges, etc. [100]. Above the absorption edge the absorption coefficient decreases further with increasing energy, until the next absorption edge is reached. A typical XAS spectrum is shown in Figure 1.15. In general, XAS spectra can be divided in two regions: the *x-ray absorption near edge structure* (XANES), typically up to 50 eV above the absorption edge, and the *extended x-ray absorption fine structure* (EXAFS), shown in Figure 1.15. In the 1970s, the EXAFS theory was developed by Stern, Sayers and Lytle who pointed out that the fine structure in x-ray absorption spectra is related to the details of the nearest atomic environment around the absorbing atom [103]. Soon, EXAFS and XANES spectroscopy evolved as broadly available characterization tools [103]. XANES is strongly sensitive to oxidation state and coordination chemistry of the absorbing atoms, while the EXAFS is used to determine bond distances, coordination numbers, and types of neighbors around the absorbing atom. [101]

An important and common application of XANES in catalysis research is to interpret shifts in the edge position or changes in whiteline intensity and the features close to the edge including pre-edge peaks (see Figure 1.15) to analyze changes in the oxidation state and/or coordination geometry of the absorbing atoms. With suitable reference spectra and theory the information can be obtained in a precise and reliable manner. This approach of directly comparing measured spectra with spectra of well-known data or calculated spectra is called fingerprinting. Additionally, fingerprinting is possible even in case of very low concentrations where the signal-to-noise ratio is extremely low. Measured XANES spectra can be fit to linear combinations of reference spectra. The coefficients in the linear combination directly provide the relative concentrations of different species in the sample (linear combination fitting). Linear combination

fitting results can therefore show the ratio of oxidized/reduced phases at a certain point. [100, 101]
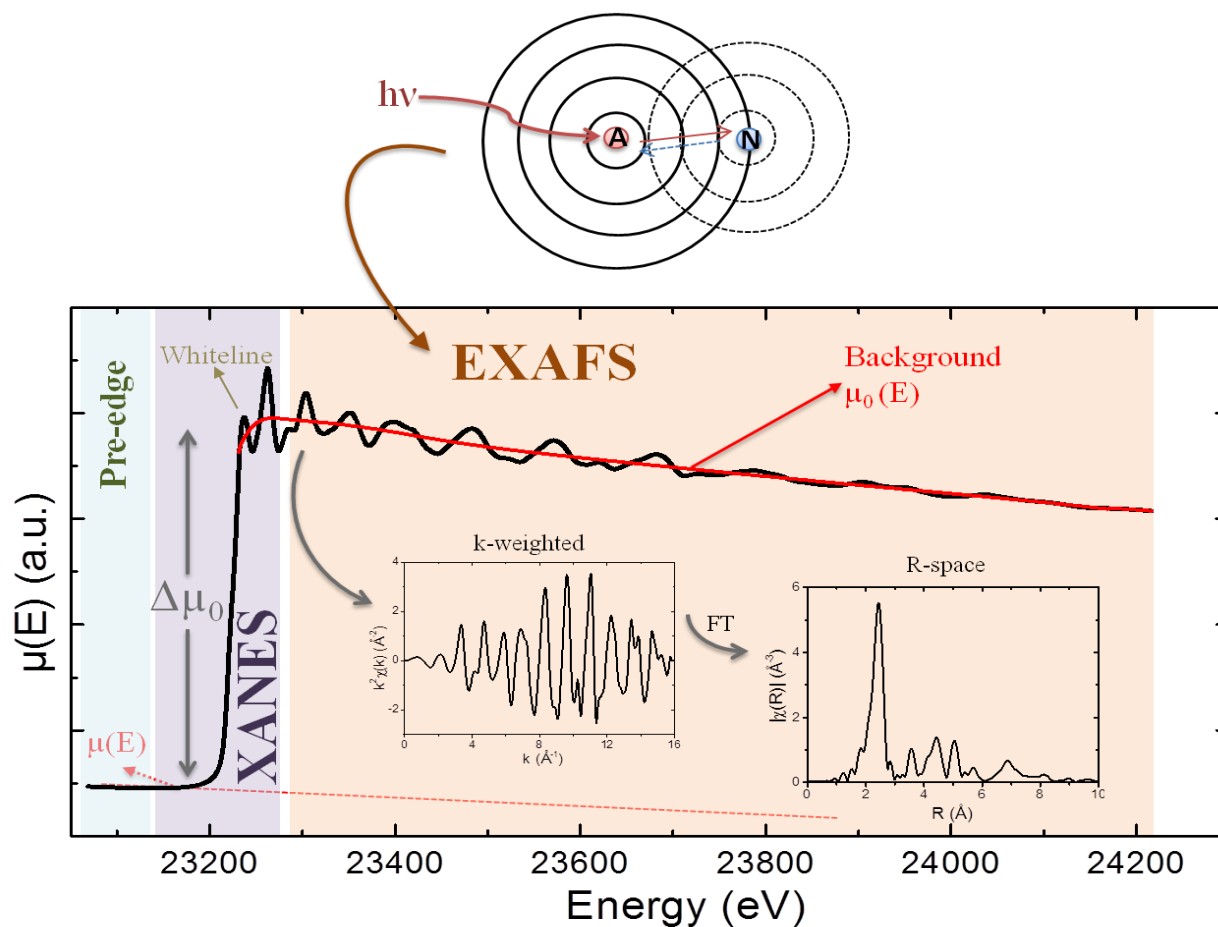
Figure 1.15: XAS spectra of a Rh foil (recorded at SNBL/ESRF). The measured XAS spectrum is shown with the XANES (light purple) and EXAFS (light orange) regions. (top: core-electron from absorbing atom (A) is ejected, and the corresponding electron wave is scattered by the neighbor atom (N)).

The so-called EXAFS oscillations at energies above the XANES region (see Figure 1.15) are due to interference of outgoing and backscattered photo-electron waves from neighboring atoms, as illustrated in Figure 1.15 (top) [104]. The EXAFS function $\chi(E)$ is obtained from the raw data by subtraction of the atomic background $\mu_0(E)$ from the measured absorption coefficient $\mu(E)$, and division by the measured edge jump $\Delta\mu_0$, as followed [101]:

$$\chi(E) = \frac{\mu(E) - \mu_0(E)}{\Delta\mu_0(E)}$$

After background subtraction and normalization, the absorption data is converted into k-space, in order to describe the oscillation as a function at the photo-electron wave number k. The EXAFS function $\chi(E)$ is converted into a k dependent function $\chi(k)$ [101]:

$$k = \sqrt{\frac{2m(E - E_0)}{\hbar^2}}$$

where E_0 is the absorption edge energy and m the electron mass. The EXAFS data thus extracted from a Rh K-edge of a Rh bulk foil is shown in Figure 1.15 (k-weighted). The experimental data $\chi(k)$ can be weighted by multiplication with different powers of k^n (typically n= 1, 2, or 3) to emphasize the oscillations at high k-values.[101, 105] Although the EXAFS data $\chi(k)$ can be analyzed in k-space using theoretical models, it is usually Fourier transformed into R-space (Figure 1.15) [105]. The desired structural information is extracted from experimental data by fitting to the theoretical formula [100, 105]:

$$\chi(k) = S_0^2 \sum_i N_i \frac{f_i(k)}{kr_i^2} e^{-\frac{2r_i}{\lambda(k)}} e^{-2k^2\sigma_i^2} \sin\left(2kr_i + \delta_i(k)\right)$$

S_0^2 = amplitude reduction factor

$\lambda(k)$ = mean free path of the photo-electron

N_i = number of backscattering atoms at distance r_i (coordination number) in coordination sphere i

σ_i^2 = Debye-Waller factor

δ_i = phase shift

$f_i(k)$ = backscattering amplitude

r_i = average distance from absorbing atom to backscattering atom (in i-th coordination shell)

A still increasing number of research groups are interested in the relationship between physicochemical properties of catalysts and their activity and selectivity. Characterization of catalysts after preparation and after reaction can provide useful information. However, the important point is to understand the catalysts behavior under reaction conditions since the catalyst structure may change during the reaction. Therefore, "*in situ" or "operando*" studies are

receiving increased attention. *In situ* characterization techniques are a powerful tool to find the relationship between structure and performance of catalysts. Among the most important applied spectroscopic *in situ* characterization techniques is X-ray absorption spectroscopy, mainly EXAFS and XANES. The appropriate design and construction of *in situ* spectroscopic reactors/cells requires suitable materials and geometries. The catalysts should be placed in this reactor, allowing measurement of spectroscopic data under realistic reaction conditions, such as high temperature, high pressure, in gas phase or liquid phase while simultaneously analyzing the outlet gas online to determine the catalytic activity and selectivity. A very important aspect of *in situ* reactor or cell design is the window material (spectroscopic window) in order to maximize the signal to noise ratio. [106, 107]

Grunwaldt et al. [108] tested Pt-Rh/Al$_2$O$_3$catalysts for partial oxidation of methane. The *ex situ* characterization of this catalyst showed that the noble metal particles were in an oxidized state after preparation and after catalytic partial oxidation of methane. However, the results of the *in situ* experiment showed that the noble metal particles were in a reduced state when the catalytic activity was higher. This indicated that metal-like particles are responsible for the partial oxidation of methane [108]. Further investigations by Grunwaldt et al. [109] of Rh/Al$_2$O$_3$ catalysts for partial oxidation of methane showed that the particle size increased significantly during treatment in hydrogen. Investigations of the catalyst in a CH$_4$/O$_2$ reaction mixture showed that the catalyst changed structure at that time when the CPO reaction ignited at about 330 °C [109]. *In situ* x-ray absorption spectroscopy can be combined with other characterization techniques such as x-ray diffraction (XRD), Raman, or infrared spectroscopy (IR). One example for the combination *in situ* XAS/XRD is the investigation of Pd/ZrO$_2$ catalysts for total oxidation of methane [110]. In this case, the question was also which oxidation state is responsible for activation or deactivation. Both the XAS data and the XRD patterns demonstrated that a strong deactivation occurred during thermal reduction of the catalyst accompanied by sintering of the Pd particles [110].

2 Motivation

Hydrogen is a feedstock used for various applications in both industrial and research including clean fuel for fuel cells. Furthermore, it is a key component for chemical storage of renewable energy. The water gas shift reaction is important for hydrogen production and purification and an important step in many industrial processes. For instance, in ammonia production CO deactivates the catalyst used for ammonia synthesis. The WGS reaction is used in this process as first step to reduce the amount of CO and at the same time to increase the concentration of hydrogen. In recent years the energy demand in Asia, especially in China has increased significantly due to the tremendous population and considerable economic growth. Clean, sustainable and renewable energy sources are therefore of vital importance for the further development of the Chinese and the world economy. In this context, hydrogen plays a key role for chemical storage and renewable energy. Accordingly, efficient hydrogen production and purification is a challenge for Chinese as well as German researchers.

The aim of this project was to study hydrogen selective membranes and the integrated catalysts "at work", using advanced x-ray based techniques at synchrotron light sources under real operating conditions in a micro-structured membrane reactor.

The main goal was to develop a new micro-structured membrane reactor specially designed for *in situ* x-ray absorption spectroscopy measurements. The geometry and material of this special micro-structured membrane reactor should be suitable for such *in situ* XAS measurements to achieve high signal-to-noise ratios. Moreover, it should be possible to integrate a catalyst and membrane into the micro-structured membrane reactor and to observe structural changes of both the catalyst and membrane simultaneously under real WGS reaction conditions and during *in situ* extraction of the produced hydrogen. Likewise it should be possible to analyze the retentate and permeate separately and to correlate physicochemical properties of catalysts and membranes and the catalytic activity. From the point of view of safety the reactor should be gas tight and mechanically stable even at elevated temperature and pressure. This micro-structured membrane reactor is one of the first designs which can be applied at synchrotron radiation sources with high energy flux for *in situ* XAS measurements on catalysts and membranes.

Another equally important objective of this thesis was to synthesize nanostructured high performance catalysts for WGS reactions using flame spray pyrolysis (FSP) as a preparation method. FSP is considered an appropriate method for preparation of catalysts with highly dispersed active centers and high stability in a single step. Moreover, catalysts prepared by FSP exhibit a high specific surface area and a high degree of nanocrystallinity. FSP derived catalysts for WGS reactions have not yet been investigated deeply. For this work, reducible oxides (CeO_2, ZrO_2, mixed-oxide CeO_2/ZrO_2 and TiO_2) as support for noble metal (Rh and Pt) particles were prepared for high temperature WGS reactions and characterized using different characterization methods with a strong focus on *in situ* X-ray absorption spectroscopy (XAS). The catalytic performance was studied under different WGS reaction conditions. Additionally, some of the catalysts were tested in a plug flow reactor (quartz capillary micro reactor) which can also be used for *in situ* studies at synchrotron light sources under WGS reaction conditions. One important and challenging aspects of these synchrotron based studies for the WGS reaction was the using high amounts of water vapor. The reaction conditions applied during these experiments were as close as possible to real WGS reaction conditions.

PART II: EXPERIMENTAL

3 Materials and Methods

3.1 Catalysts Preparation

The FSP set up at the Institute for Chemical Technology and Polymer Chemistry, KIT is based on previous designs by Mädler, Pratsinis and especially Stark [83, 90, 111] (Figure 3.1a). A conventional single flame (SF) [112], as well as a double flame (DF) spray pyrolysis set up were used for the synthesis of metal oxide supported Rh and Pt nanoparticles. The DF set up consists of two separate nozzles, each able to disperse and ignite a precursor solution. Cerium (III) 2-ethylhexanoate 49% in 2-ethylhexanoic acid (12%Ce, Alfa Aesar), Zirconium(IV) oxide 2-ethylhexanoate in mineral spirits ($\approx$6% Zr, Alfa Aesar), Titanium(IV) isopropoxide (Tetraisopropyl orthotitanate, Merck) were diluted with xylene (VWR) to 0.5 M metal concentration. For single flame (SF) experiments (Figure 3.1b), platinum acetylacetonate (Pt(acac)$_2$, Pt-%: 49.6, Strem chemicals and chempur) and rhodium acetylacetonate (25% Rh, abcr GmbH&Co.KG and Chempur) were added to the support precursor solutions, respectively. These combined liquid precursors were dosed at 5 mL/min using a syringe pump (World Precision Instruments) and dispersed with 5 L/min O$_2$ gas at a 3 bar annular nozzle pressure. The spray flame was ignited with a premixed flame of CH$_4$ (1.6 L/min) and O$_2$ (0.75 L/min). For double flame (DF) experiments (Figure 3.1c), the noble metal precursor and the support precursor were dissolved in xylene separately. Both precursor solutions were fed into the flame at the same flow rate (5 mL/min). The angle φ between the nozzles was kept at 120° and the inter nozzle distance d set at 6 cm (Figure 3.1d) [96]. A cylindrical steel vessel with a glass fiber filter (75 cm diameter, Whatman GF6) was placed above the flame. The produced particles were collected on this filter with the aid of a vacuum pump (R5, Busch).
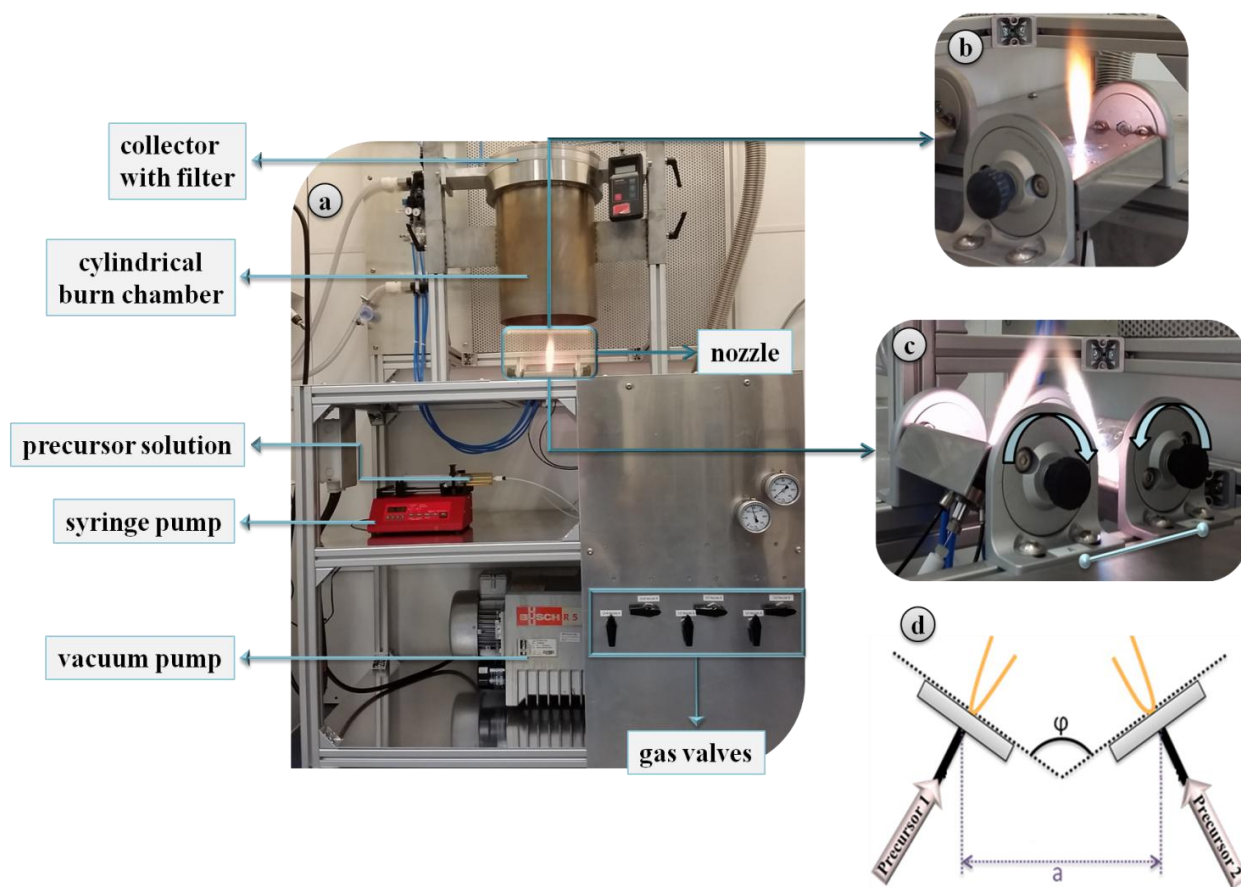
Figure 3.1: (a) Photograph of the FSP set-up at Karlsruhe Institute of Technology (KIT) with description of the different components. (b) Photograph of single flame spray pyrolysis and (c) double flame spray pyrolysis geometry. (d) Schematic drawing of the DFSP set up showing the angle φ between the two nozzles and the inter-nozzle distance a between each nozzle center.

3.2 Characterization

3.2.1 X-ray Diffraction

Structural information and properties of crystals can be best accessed by x-ray diffraction based on the well-known Bragg law (Figure 3.2). The Bragg law describes the main principle of X-ray diffraction in terms of a scattering of X-rays by sets of lattice planes. The lattice planes can be described by a set of indices, the so-called Miller indices (hkl) and the distance d between parallel planes, the so-called interplanar spacing. The X-rays penetrate deep inside a crystal lattice where additional scattering occurs. All the X-rays are scattered in the same direction and the scattered waves interfere. In case of constructive interference that the waves reflected from the different

parallel planes are in phase, i.e. the path length difference of an integer *n* multiple of the wavelength λ. The incidence angle and the reflection angle are equal. [113, 114] The Bragg equation (Figure 3.2) describes for which angles constructive interference occurs:

$$n\,\lambda = 2\ d_{(hkl)}\ \sin\theta$$

n = integer
λ = wavelength
d = interplanar distance of parallel lattice planes
θ = incidence angle
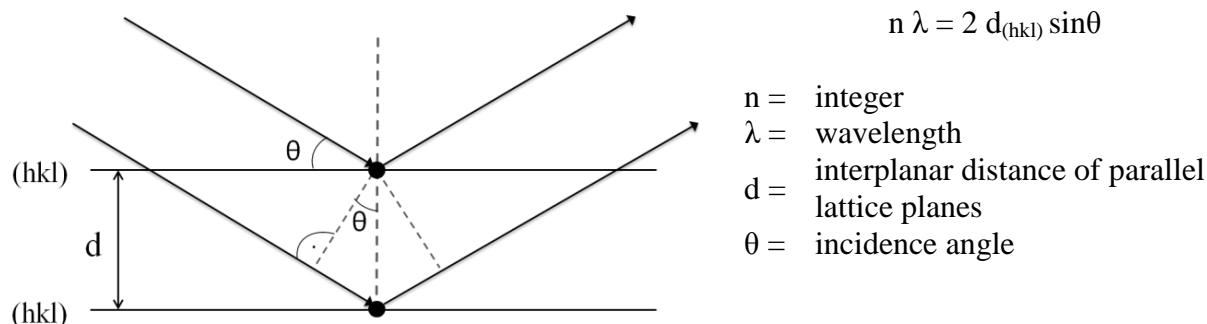
Figure 3.2: Illustration of the geometry used for the simplified derivation of Bragg's law (left) and the Bragg equation (right).

XRD is used to identify crystalline phases of catalysts by means of lattice structural parameters, and to estimate crystallite sizes. In 1918, Scherrer established an equation to estimate a mean crystallite size from X-ray profile width [115]. The size of the crystallites or crystalline domains can be determined applying the Scherrer equation [113]:

$$L_{hkl} = \frac{k\lambda}{\beta cos\theta}$$

L_{hkl} = average crystallite size
k = Scherrer constant (fixed 0.9)
λ = wavelength
β = full-width-at-half-maximum (FWHM) of the reflection
θ = Angular peak position

To determine the FWHM, a Voigt function (OriginPro 9.1), a convolution of Gauss and Lorentz functions, were used in this study [113].

In this work, the structure of different samples was determined on rotating sample holders by powder x-ray diffraction using a Bruker D9 Advance diffractometer in the range 10-80° (2 s/step, step size 0.016°) using Cu K_α radiation (λ= 0.15406 nm), a nickel filter and a graphite monochromator.

3.2.2 Transmission Electron Microscopy

Transmission electron microscopy (TEM) is the most common tool to determine the size and shape of particles and the distribution of supported particles on a catalyst carrier. In a TEM, a primary electron beam of high energy and high intensity passes through a condenser to produce parallel beams that hit the sample[116]. The attenuation of the beams depends on the density and the thickness of sample. The operating conditions of a TEM tool are 100–400 kV, typically 100–200 kV [116, 117]. As in XRD, TEM allows also the identification of crystallographic phases. Furthermore, fluorescence X-rays emitted from a sample are characteristic for a specific chemical element and allow to analyze the chemical composition of a selected area of the sample. This technique is called Energy-Dispersive X-ray Analysis (EDX) [116].

For the TEM measurements in this work, a suspension of the catalyst sample in ethanol was deposited onto a holey carbon supported grid. The ethanol was used for suspension and was evaporated before the measurements. Transmission Electron Microscopy (TEM) images were acquired using a JEOL HEM-2100 system with an acceleration voltage of 200 kV (measured at DICP in Dalian/China).

3.2.3 Physisorption

Physisorption is also physical adsorption, occurs when a gas (*the adsorptive*) is brought into contact with the surface of a solid (*the adsorbent*). In general physisorption is used to determine the specific surface area of the adsorbent. The principle of surface area measurements is that determine how many molecules an inert gas such as nitrogen or argon are needed to form a complete monolayer on the surface of a sample. Typically, in practice the molecules may absorb beyond the monolayer to form multilayers. [116, 118]

The Brunauer-Emmett-Teller (BET) method is widely used for measuring the specific surface area of a material. The BET method considers multilayer adsorption and the surface area is calculated from the linear part of the adsorption/desorption isotherm with well-known BET-equation [118]:

$$\frac{\left(\frac{p}{p_0}\right)}{\left[n\left(\frac{1-p}{p_0}\right)\right]} = \left(\frac{1}{n_m C}\right) + \left[\frac{(C-1)}{n_m C}\right]\left(\frac{p}{p_0}\right)$$

p = equilibrium pressure of adsorbate

p_0 = saturation pressure of adsorbate

n = amount of gas absorbed

n_m = amount of a monolayer of adsorbed gas

C = BET constant

According to the BET equation, n_m and C can be calculated from the slope and intercept of a linear BET plot of $p/n\left(\frac{1-p}{p_0}\right)$ versus p/p_0 in the range of $0.05 - 0.3$ [118]. Subsequently, the specific surface area S_{BET} can be obtained from n_m, L (Avogadro constant) and σ (occupied by adsorbate) molecule [118]:

$$S_{BET} = n_m \, L \, \sigma$$

In this work, the specific surface area of the as prepared catalysts was determined by nitrogen adsorption/desorption at 77 K using the BET method (Belsorp mini II by Bell Inc., Japan). All samples were degassed at 300 °C in vacuum for 2h.

3.2.4 Chemisorption

Chemisorption is the most widely used technique for the determination of the dispersion of a catalyst, i.e. the number of active center on the catalyst surface. If the stoichiometry of adsorbate/surface atom ratio is known the measurement of the quantity of a gas adsorbed selectively (formation of an irreversible adsorbed monolayer) on the metal gives the metal dispersion [117]. The dispersion is defined as the ratio of the number of the metal atoms on the surface N_s to the total number of the metal atoms N_T [117]:

$$D = \frac{N_s}{N_T}$$

CO-Chemisorption is a common method for studying supported noble metal catalysts. H_2, O_2 and NO are commonly used gases for chemisorption [119]. All surface noble metal atoms must be

free from other surface adsorbates. Therefore, sample pretreatment such as oxidation and/or reduction is a necessary step. The relationship between metal dispersion (D) and average particle size (d) is [117]:

$$D = 6 \, \frac{(v_m/a_m)}{d}$$

where, v_m is the volume occupied by an atom in the bulk metal, a_m the area occupied by a surface atom. The values of v_m and a_m for Pt are $15.10 \, \text{Å}^3$ and $8.07 \, \text{Å}^2$ and for Rh they are $13.78 \, \text{Å}^3$ and $7.58 \, \text{Å}^2$, respectively [117].

The CO:metal stoichiometry is presented in various forms on metals such as iron, nickel, palladium, rhodium, and platinum. CO can be adsorbed dissociatively (CO:metal $\geq$ 2) or adsorbed associatively in a form as linear (n=1), bridged (n=2), and capped (n=3) form [117]. As in the present study, a CO:metal stoichiometry of 1:1 is commonly used for Pt and Rh. The support material also affects the CO absorption. For instance, the presence of cerium based oxide makes it difficult to determine Pt metal particle sizes [120]. Tanabe et al. [121] showed that in case of cerium oxide based noble metal catalysts, CO adsorption measurements give extremely large values of the amount of CO adsorption on the catalyst surface. Realistic dispersion values for ceria supported noble metal particles can be obtained at lower adsorption temperature (-77 °C), which indicates a CO spillover from Pt to the support at higher temperatures [121].

In this work two different methods were used for the determination of Rh and Pt dispersion. Regardless of the method, the catalysts were subjected to the following pretreatment: a certain amount of sample was filled in a reactor, oxidized in O_2/CO for 20 min, and then kept only in O_2 for 40 min at 500 °C. Afterwards, the sample was cooled down in N_2 to 400 °C, reduced in H_2/N_2 for 1h at 400 °C and finally, flushed with N_2. After the pretreatment, the reactor was cooled down to room temperature. Depending on the support, the following procedure was applied:

(i) *TiO_2 supported catalysts*: CO in N_2 was flown through the sample at room temperature until saturation occurred. This step was followed by the temperature programmed desorption of CO by increasing the temperature to 500 °C.

(ii) *CeO_2, $Ce_xZr_{1-x}O_2$ supported catalysts*: The sample was cooled down in a continuous N_2 gas flow to -78 °C in an isopropanol/dry ice bath. The measurement started with a concentration of 100 ppm CO in nitrogen.

3.2.5 Temperature Programmed Reduction

Temperature programmed reduction (TPR) is a simple and useful method for obtaining information about the temperature required for the complete reduction of a catalyst. Usually a metal oxide is reduced, typically in a flow of H_2, to its metallic state. Metal oxide particles supported on carriers may exhibit different reduction behaviors compared to unsupported metal oxides [122]. It is assumed that the reduction may be hindered or promoted, which depends on the nature of the oxide/support interaction [122].

In the present work, the reduction temperatures of various catalysts were obtained *in situ* by recording X-ray Absorption Near Edge Structure (XANES) spectra in rapid continuously scanning mode (Quick-EXAFS mode [123]) during TPR. XANES-TPR allows the tracking of the exact temperature to reduce a catalyst. In contrast to a standard TPR, not only the H_2 consumption is monitored, XANES-TPR also shows the degree of reduction of a catalyst under certain conditions. In addition, isosbestic points in XANES can indicate a direct transformation between the metal oxide phases and reduced metal species. In other words, XANES-TPR shows whether direct reduction occurs or the reduction process involves intermediate species. For these experiments a catalyst powder (100-200 μm sieve fraction) was fixed in a quartz capillary between two quartz wool plugs. The XANES spectra were recorded while heating under reducing conditions (5% H_2/He; total flow 50 mL/min) from room temperature to 450 °C at 5 °C/min with a gas blower (FMB Oxford) [110]. Under steady state conditions before and after reduction long EXAFS spectra were acquired in step scanning mode. The spectra were energy calibrated, normalized and background-subtracted using the Athena interface of the IFEFFIT software package (version 0.8.056) [124]. Athena was also used for the linear combination (LC) fitting. LC analysis of XANES spectra was performed in the energy range from 30 eV below to 50 eV or 70 eV above the Pt L_3-/Rh K-edge using the first and final spectra of the TPR series as reference spectra. XANES measurements were performed at the SNBL and BM25 beamline at the European Synchrotron Radiation Facility (ESRF) synchrotron radiation source (Grenoble/France) and at the XAS beamline at the ANKA synchrotron radiation source (Karlsruhe/Germany).

3.2.6 Elemental Analysis

The determination of the chemical composition is important for evaluating the stability and other properties of the catalysts during the development for optimization of synthesis methods in laboratory or in large-scale technical applications [125]. This analysis includes the precise detection and determination of specified chemical elements in the fresh and in the used catalysts. It may also include the determination of the concentration of contaminants and catalyst poisons.

The chemical composition of the catalysts prepared in this work was determined by ICP-OES (Inductively Coupled Plasma Optical Emission Spectroscopy, using an Agilent 725 equipment). Argon was used as carrier gas and to create the plasma. Chemical digestion was performed by a microwave digestion system (Anton Parr). 30 mg of sample was decomposed in 6 mL HCl and 2 mL HNO_3 in a Microwave oven (600 Watt) for 45 min at 240 °C and 60 bar.

3.3   Experimental Equipment

3.3.1 Micro-structured Membrane Reactor

One main objective of this work was the development of a micro-structured membrane reactor for *in situ* synchrotron based characterization of catalysts and membranes under WGS reaction conditions. This new reactor was designed in collaboration between IKFT/ITCP and IMVT. More specifically, IMVT contributed with its expertise in optimization of micro reactor design and fabrication while ITCP/IKFT contributed with experience and know-how in the design of spectroscopic cells for *in situ* X-ray adsorption spectroscopic measurements. For this particular application it must be considered that the membrane and the X-ray windows should be sufficiently thin to achieve a high signal-to-noise-ratio in the XAS data and furthermore for maximum H_2 permeability in order to efficiently separate the hydrogen from the gas mixtures [65, 68]. The reactor (Figure 3.3) consists of two plates with nine micro channels, one for feed gas and powder catalyst and one for removing hydrogen from the reaction products. These channels are separated by a hydrogen selective membrane foil welded onto a metal support. As shown in Figure 3.3, sub-assembly 1 and sub-assembly 3 are analogous. They consist of 2 mm thick metal plates with two long centered slits for the X-ray beam (a-1), an X-ray window foil

(b-1) and a micro structured plate with nine channels for integration of catalyst and feed gas (retentate part, c-1) and for perfusion and swap gas (permeate part, c-3). The micro-structured channels are 1 mm deep, 0.1 cm wide and 20 cm long. Sub-assembly 2 consists of a micro structured plate with 9 slits for connecting membrane and channels (d), membrane foil (e), and metal fame for welding the membrane into plate (e).
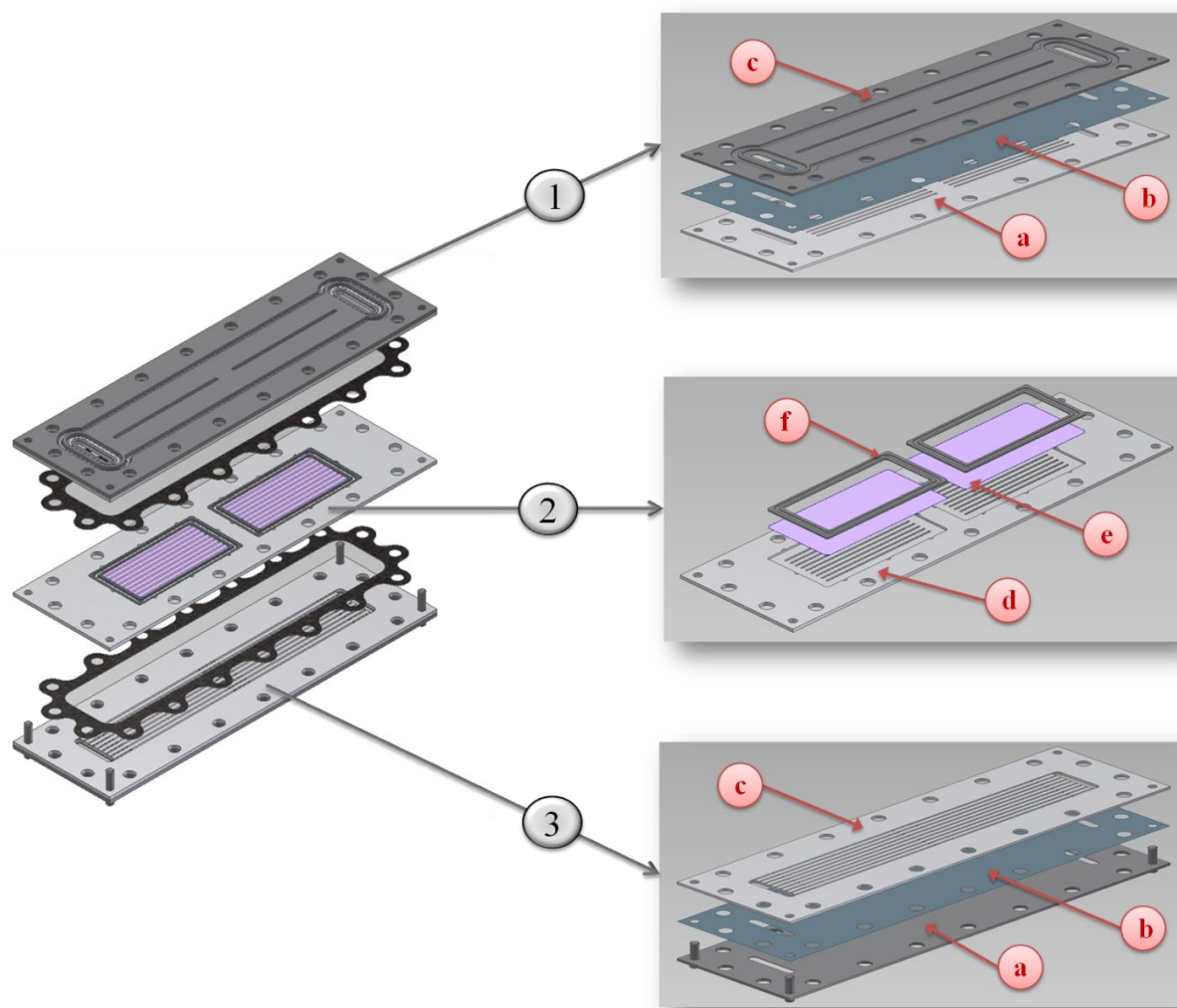
Figure 3.3: Micro-structured membrane reactor for *in situ* XAS studies under WGS reaction conditions. Sub-assembly 1 (retentate): channels for catalysts and feed gas, X-ray window. Sub-assembly 2: membrane for hydrogen separation. Sub-assembly 3 (permeate): channels for swap gas for hydrogen, X-ray window.

The X-ray window material should be sufficiently transparent for X-rays beams in required photon energy range for the XAS measurements and mechanically, thermally and chemically stable under the WGS reaction conditions. For this reactor two different X-ray window materials

were applied an amorphous Fe-B-Si foil with a thickness of 25 μm and a 38 μm in thickness Ni-B-Si foil. More detailed information about these window materials will be discussed by Gietzelt et al. [126]. As membrane foil, two commercially available membranes were used; a Pd foil with a thickness of 16 μm and an 8.5 μm thick PdAg foil. Possible combinations of X-ray window materials and membrane foils with the corresponding thickness are listed in Table 2.1.

Table 2.1: Possible combinations for X-ray windows and membranes for the micro-structured membrane reactor

Combination			Total Thickness [μm]
x-ray window	Membrane	x-ray window	
Fe	Pd	Fe	66
Fe	PdAg	Fe	58.5
Ni	Pd	Ni	96
Ni	PdAg	Ni	84.5
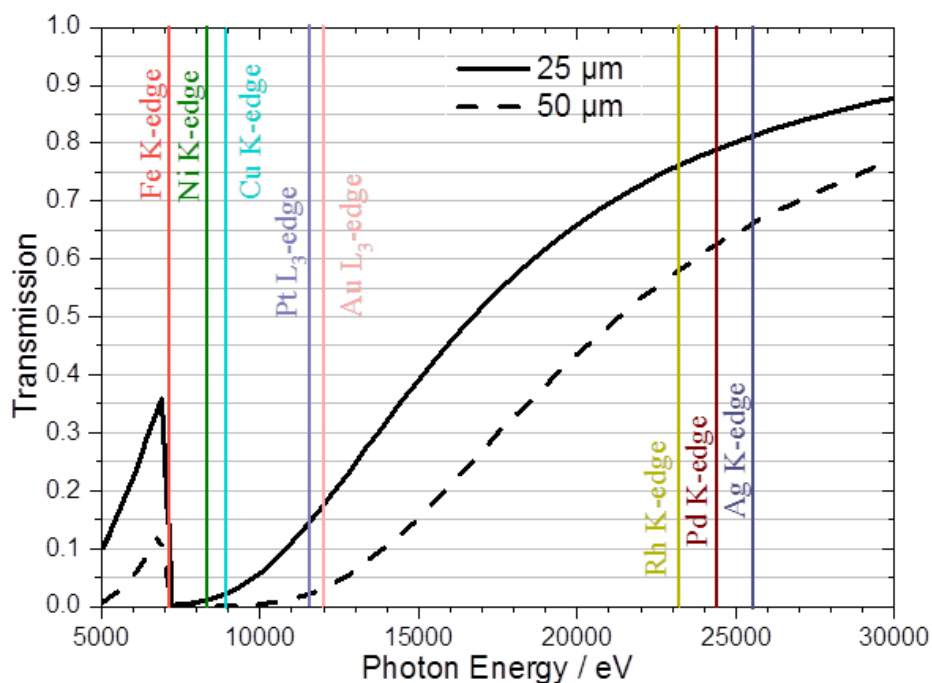
Figure 3.4: Calculated X-ray transmission through Fe based window materials (thickness of one window → 25 μm and two windows → 50 μm) as a function of photon energy. The adsorption edges of different elements illustrated in relation to the transmission of X-rays.

XAS spectra represented the probability of photon absorption as a function of photon energy. The intensity of initial beam is attenuated in this case through the window material. Figure 3.4 shows

the calculated X-ray transmission through the window material as a function of the photon energy using a program package that clearly contains all necessary physic-chemical information (the center for X-ray optics CXRO) [127]. The attenuation of the transmission decreases with increasing thickness of the Fe based window material (analogous to Ni based foil), for instance the transmitted beam for Rh reduces from 75% to 58%. In Table 2.1 the possible combinations of membrane and window materials of different thickness are listed, which implies that the transmitted beam is further attenuated cause of increasing of the material thickness. The edge energies of some chemical elements relevant for the WGS experiments are included on Figure 3.4. For high data quality (signal-to-noise) the metals with absorption edges at high photon energies, such Rh, Pd or Ag are favored for the *in situ* experiment in this reactor. Note that the transmitted photon intensity is further reduced e.g. by the catalysts support, in this case CeO_2. XAS measurement at the Rh or Pd adsorption edges require high photon energies which are available e.g. at the European Synchrotron Radiation Facility (ESRF) and only recently at the established CAT-ACT beamline at ANKA [128].
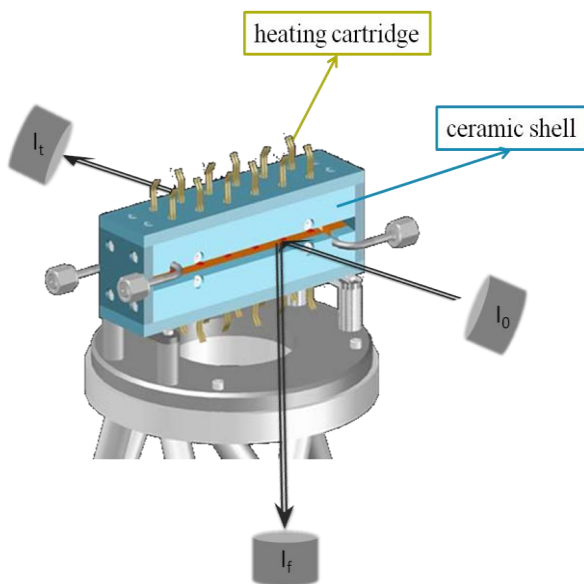
Figure 3.5: Schematic drawing of the XAS set-up using the WGS microreactor. The intensities of the incoming (I_0) and transmitted (I_1) monochromatic beam are measured in transmission mode. The intensity of a specific x-ray fluorescence line (I_F) is detected in fluorescence mode.

The micro-structured membrane reactor is thermally isolated by a ceramic shell (Figure 3.5). A total of 24 holes for heating cartridges (Figure 3.5) are distributed on the top and on the bottom of the ceramic shell which allow temperatures up to 400 °C. The schematic drawing of the micro-structured membrane reactor in Figure 3.5 further indicates how it is placed between the ionization chambers at a beamline. Several tests of the set-up at beamlines revealed that this

membrane reactor is well suitable for *in situ* XAS measurements both in the transmission and in fluorescence modes.

3.3.2 Gas Dosing Unit for *in situ* XAS Experiments at Synchrotron Light Sources

One of the challenges for *in situ* WGS experiments is to provide water at different concentration levels. For this purpose a new and movable *in situ* set-up equipped with a gas dosing system including a water evaporator was built (Figure 3.6). This mobile unit allows to study catalysts and membranes under WGS conditions either in quartz capillaries (heated by a gas blower, section 3.4.2) or in a microreactor (section 3.3.1). The first version of this movable set up consisted of two main components:

1. Gas dosing unit for reaction gas mixture including four mass flow controllers (Bronkhorst, flow range $20 - 50$ mL/min) for carbon monoxide, carbon dioxide, hydrogen and helium (balance gas) and a liquid delivery system with a vapor control. At room temperature the liquid (in this case water) is dragged from a steel vessel by applying 5 bar N_2. The water flow is regulated by a liquid mass flow controller (μ-Flow, Bronkhorst).The required water flow rate is controlled by a control valve and carrier gas mixing valve (controlled evaporator mixer CEM, Figure 3.6). Finally, all the gases and vapor are mixed at a mixing point (Figure 3.6a).
2. The other channel plate is connected to one mass flow controller for helium, in order to swap the hydrogen after separation by the membrane.

With this set-up (Figure 3.6a) it was possible to analyze either the reactant gas after the water gas shift reaction or the produced hydrogen (with swap gas). During the first set of experiments dedicated to this work several problems occurred with this *in situ* setup:

I.   The liquid flow controller could not be properly calibrated. Water vapor could not be dosed accurately.

II.   The outlet gas after the reaction could not be analyzed in order to observe the conversion of CO.
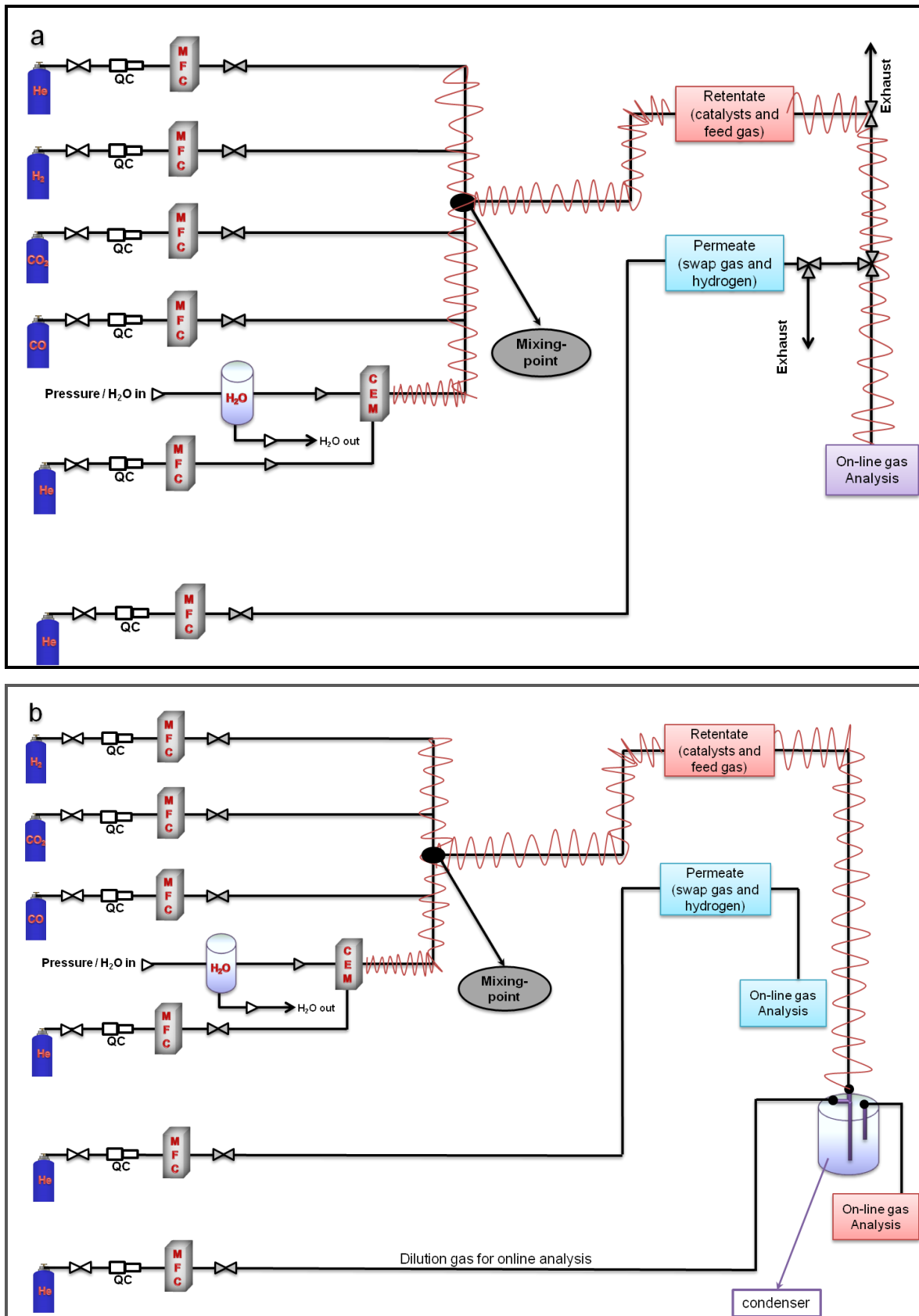
Figure 3.6: Gas dosing and water evaporation control system: (a) first version, (b) upgraded version

III.   It was not possible to monitor the outlet gas for both channels parts.

IV.   During switching from reactant to product side, for online analysis of the outlet gas, a pressure surge occurred in the membrane microreactor, which lead to a crack in the membrane foil.

V.   The outlet gas could not be analyzed by mass spectrometry (MS) due to condensation of water in the thin capillary inside the mass spectrometer. Accordingly, it was not possible to analyze the conversion of CO by mass spectrometry.

In order to solve these problems the movable *in situ* set-up was upgraded. The outlet lines were separated, in order to be able to analyze the outlet. The produced H_2 was analyzed by mass spectrometry (Pfeiffer Vacuum Thermostr GSD 320 T) whereas CO and CO_2 were detected by an Infrared spectrometer (Hartmann & Braun Uras 10 E) (Figure 3.6b). After the WGS reaction, the reactant mixture was flown through a condenser installed upstream of the IR-spectrometer, in order to minimize the amount of water vapor entering the IR. Since the reaction flow was 50 mL/min, the outlet gas had to be diluted to achieve a flow of 300 mL/min before entering IR-spectrometer (range of detection is $0 - 3$ vol.% for CO and that is $0 - 2$ vol.% for CO_2).

3.4   Catalytic Activity Experiments

The catalysts were tested in two different reactors. In this section both reactors are described in general. A detailed description of the experimental procedures is given in the corresponding chapter (section $4.1 - 4.3$).

3.4.1 Catalytic Tests in Fixed Bed Reactor

The flame made catalysts were tested under WGS reaction conditions in continuous flow in a fixed bed quartz reactor at atmospheric pressure at Dalian Institute of Chemical Physics (DICP), as shown in Figure 3.7 (top). The test unit consists of mass flow controllers for CO, H_2, CO_2 and He or N_2, temperature controller, a furnace, a water pump, a condenser and a gas chromatograph (Figure 3.7 bottom). The dry feed gases were premixed and water was injected into a pre-heater with a calibrated double-plunger pump (Elite P230), where they were vaporized and mixed with

the dry feed gas components. As shown in Figure 3.7 (top), the quartz reactor (diameter 8 mm) is placed in the furnace with an individual temperature controller. A thermocouple in contact with the catalyst bed was placed inside reactor to measure the reaction temperature. After the reaction the gas passes through a condenser for water vapor removal. Subsequent gas analysis was performed using a gas chromatograph (Shimadzu GC-8A) with a TCD detector for CO, CO_2, and CH_4 analysis.
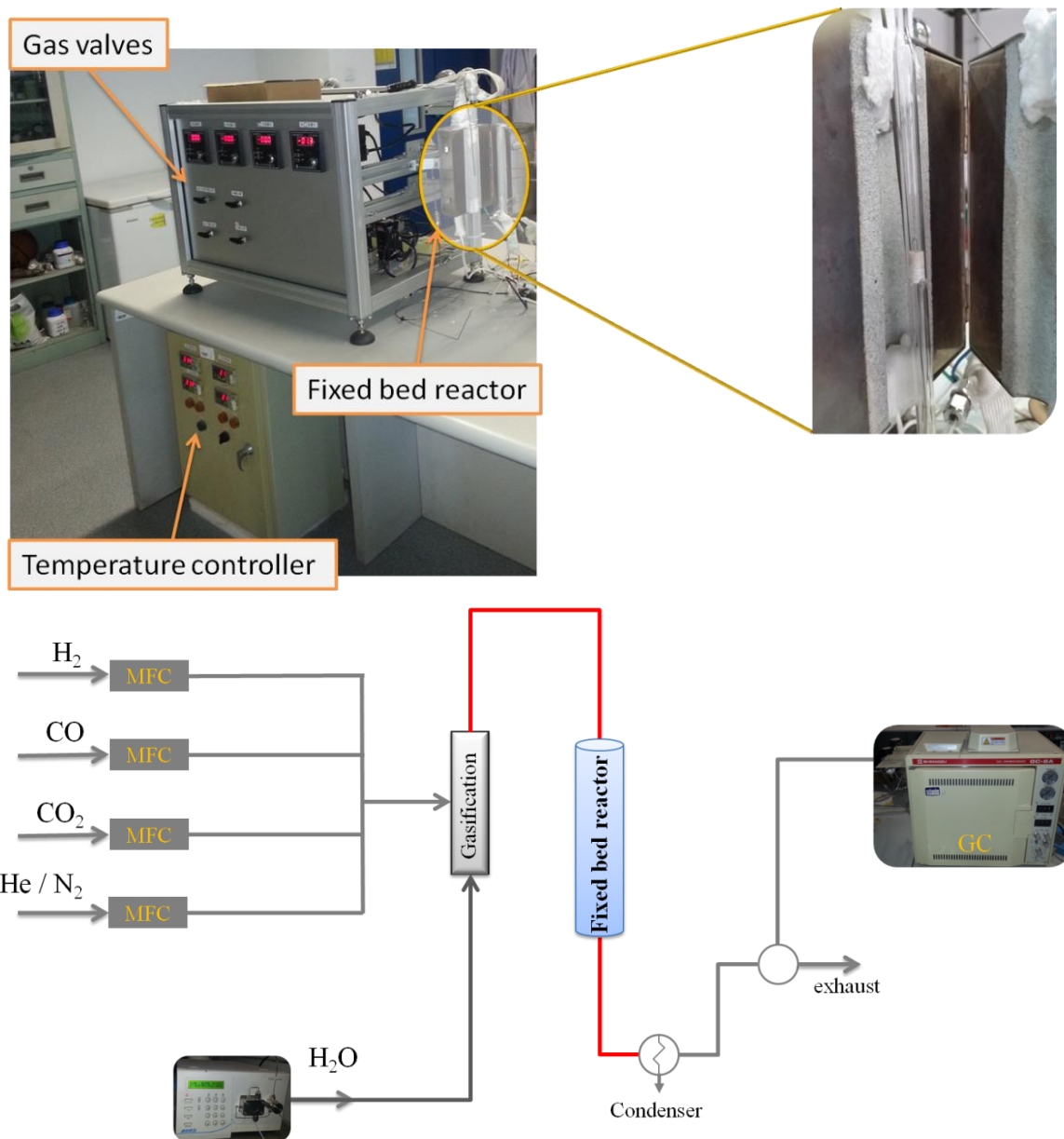
Figure 3.7: Photograph (top) and a schematic drawing (bottom) of activity test set-up for water gas shift reactions at Dalian Institute of Chemical Physics (DICP, China).

CO conversion (X_{WGS}) due to WGS was calculated from the CO, CO_2 and CH_4 concentrations at the reactor inlet and outlet using Eq. 3.1 :

$$X_{WGS} = \frac{[CO]_{in} - [CO]_{out}}{[CO]_{in}} = \frac{[CO_2]_{out} - [CO_2]_{in}}{[CO]_{in}} \qquad \text{Eq. 3.1}$$

if methanation did not occur or remained negligible. If this was not the case, the following equation (Eq. 3.2) was used to determine WGS CO conversion:

$$X_{WGS} = \frac{[CO_2]_{out} - 3[CH_4]_{out} - [CO_2]_{in}}{[CO]_{in} - 4[CH_4]_{out}} \qquad \text{Eq. 3.2}$$

This equation takes into account that 4 mole CO are consumed and 3 mole CO_2 per mole CH_4 are formed according to the following net reaction:

$$\textbf{4 CO} + \textbf{2 H}_2\textbf{O} \rightleftarrows \textbf{3 CO}_2 + \textbf{CH}_4$$
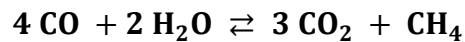
CH_4 selectivity (S_{CH4}) was calculated as follows:

$$S_{CH_4} = \frac{[CH_4]_{out}}{[CO_2]_{out} + [CH_4]_{out} + [CO]_{out}} \qquad \text{Eq. 3.3}$$

3.4.2 Catalytic Tests in quartz Capillary Microreactor

A hot air furnace was used for heating the sample in a quartz capillary micro reactor (Gas Blower, FMB Oxford) [110]. Such capillary micro reactor set-ups have been successfully applied to synchrotron based *in situ* experiments and can also provide kinetic data [129-131]. This type of reactor allows XAS experiments while simultaneously analyzing on-line the outlet gas acquired under working conditions. In this work, this capillary set-up was also used "off-line" (without synchrotron light) at ITCP for catalytic tests (Figure 3.8 top). The capillary micro reactor set-up consists of a quartz capillary with a diameter of 3 mm loaded with catalyst powder between two quartz wool plugs and connected to a gas inlet and outlet, like a plug flow reactor. For gas dosing and online gas analysis the set-up described more precisely in section 3.3.2 was used (Figure 3.8 bottom). For catalytic data in the laboratory a 3 mm diameter quartz capillary (50 μm thickness) was used.
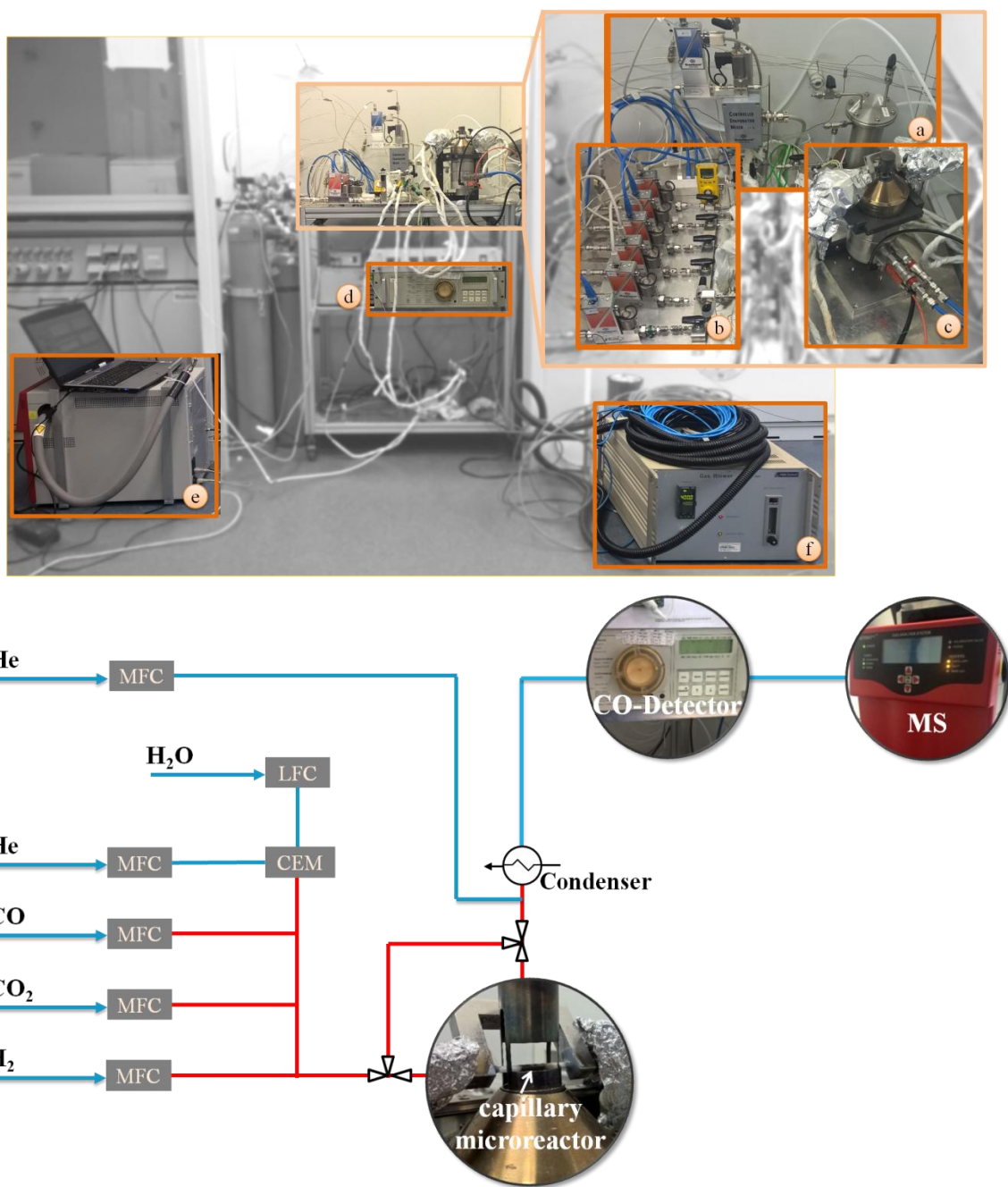
Figure 3.8: Photograph (top) and a schematic drawing (bottom) of the set-up for WGS activity test. Liquid Delivery System and controlled evaporation and mixing (a), mass flow controllers (b),gas blower (c), CO detector (d), mass spectrometer (e) and temperature controller for the gas blower (f).

In this case, CO conversion (X_{WGS}) of WGS was calculated from the CO and CO_2 concentrations CO and CO_2 were detected by an Infrared spectrometer (Hartmann & Braun Uras 10 E, Figure 3.8 bottom):

$$X_{CO} = \frac{[CO]_{in} - [CO]_{out}}{[CO]_{in}} \qquad \text{Eq. 3.4}$$

$$X_{CO} = 1 - \frac{CO_{out}}{CO_{in}} \qquad \text{Eq. 3.5}$$

The selectivity of the catalysts was determined with the approximate intensity of the H_2 signal detected by the mass spectrometer. The produced H_2 takes into account that 1 mole CO is consumed and 1 mole H_2 is formed by WGS reaction and for the methanation 3 mole H_2 are consumed per mole CH_4. It is assumed that CH_4 formation occurs at high temperatures up to 350 °C. In Figure 3.9 the intensity of the H_2 signal is shown as a function of CO conversion for a double flame made Rh/CeO_2 catalyst. The fitted linear regression was used to identify the relationship between co conversion and the intensity of H_2. The divergence encountered after 350 °C is related to the CH_4 selectivity (S_{CH4}).
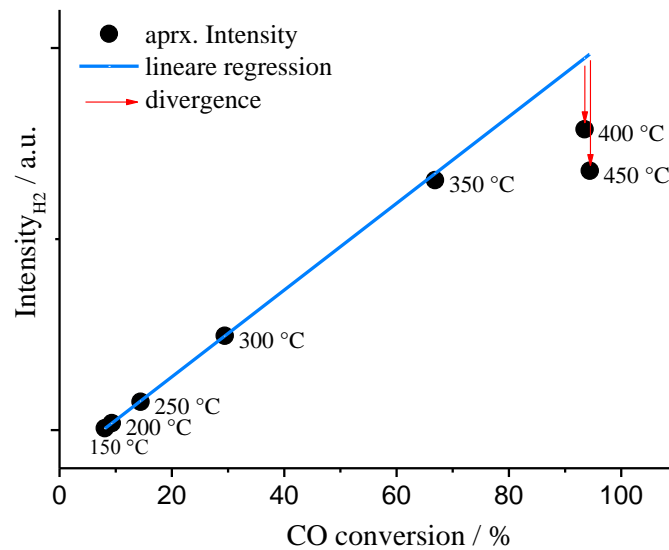
Figure 3.9: Estimation of the extent of methanation during the test of a double flame made Rh/CeO_2 catalyst.

PART III: CATALYTIC STUDIES

4 Single and Double Flame Made Noble Metal Catalysts for WGS Reactions

Supported metal catalysts consist of small metal nanoparticles dispersed on the surface of support with a high surface area. The support oxide does not only provide a large metal surface but it also has a strong influence on the stability, activity and selectivity of the catalysts and likewise on the surface area and the interaction of the support with the active phase, which is controlled by catalytic reactions [132]. The nature of oxide supports significantly affects the performance of noble metal catalysts for the water gas shift reaction. In this work the effect of the support oxide on Pt and Rh based catalysts prepared by flame spray pyrolysis was investigated using different characterization methods such as XRD, BET, chemisorption and TPR-XANES, and the catalytic performance for the WGS reaction was tested. These results are summarized in this chapter.

The first section of this chapter (4.1) describes first studies of ceria supported Rh and Pt catalysts prepared by single flame spray pyrolysis for the WGS reactions. The results were used as a basis for further investigation of flame made catalysts for high temperature WGS reactions.

In the second section (4.2) characterization and catalytic test results of titania supported noble metal catalysts for WGS reactions. The catalysts were prepared by single and double FSP and studied under different WGS reaction conditions were studies.

In the last section (4.3) structural and physicochemical properties and the catalytic performance of Pt and Rh on different supports were systematically compared. The results of the measurements described in this chapter can be highly valuable to establish structure-activity relationships.

4.1 Investigation of Structure and Activity of Ceria Supported Catalysts

4.1.1 Introduction

Ceria (CeO_2) is of great interest for three way catalysts in automotive emission control [133], for water gas shift reactions [11, 21, 33, 38, 42], and for hydrocarbon oxidation catalysts in diesel exhaust after treatment [134, 135]. Ceria is widely used as support, because of its high oxygen storage capacity and its ability to facilitate reduction between Ce^{3+} and Ce^{4+} [44]. As well-known in the literature ceria can strongly affect catalyst performance, influence on the dispersion of the supported metal, improve catalyst stability, and catalytic performance for WGS and steam reforming reactions, store and release oxygen, and promote noble metal oxidation and reduction [136].

CeO_2 has a fluorite-type (calcium fluoride, CaF_2) structure in which oxygen is coordinated by 4 Ce atoms (CN=4) in tetrahedral structure, and the Ce atoms are surrounded by 8 oxygen atoms (CN=8) in cubic structure [137]. CeO_2 contains cerium in oxidation state 3+ and 4+, and can easily change between both oxidation states. In a reducing atmosphere at increasing temperature CeO_2 forms oxygen-deficient permanently, non-stoichiometric CeO_{2-x} oxides [136]. The reduction behavior has been analyzed by temperature programmed reduction and the profiles showed primarily two peaks at ca. 500 and 750 °C [138]. It was assumed that the peak at low temperature indicates the most easily reducible surface capping oxygen and the peak at high temperature is caused by removal of bulk oxygen [136, 138]. The presence of a noble metal deposited on ceria changes the redox behavior by shifting the first TPR peak to lower temperature, while the peak at high temperature is not affected [138, 139]. It is assumed that the metal interacts not with bulk oxygen but with surface oxygen [139]. Besides the ability to facilitate reduction, the oxygen storage capability of CeO_2 is a key factor for catalytic applications, as mentioned above. The CO conversion via the water gas shift reaction was estimated to account for 33% from the CO+O (surface oxygen of CeO_2) thus mainly resulting from the oxygen storage capacity of ceria [140]. The WGS activity increased in presence of noble metal atom. The enhancement of WGS reactivity via the presence of noble metal (Rh/CeO_2) compared to pure ceria and was established by addition of a small amount of Rh the rate of WGS

reaction increased [34, 141]. Ceria-supported precious metals exhibit very interesting properties for use as water-gas-shift (WGS) catalysts.

4.1.2 Experimental Part

Rh/CeO_2 and Pt/CeO_2 catalysts were prepared by single flame spray pyrolysis using solutions of the corresponding initial precursor in xylene. The concentration of the noble metal precursor was 1 mol/L. Details of the preparation by FSP were already described in section 3.1. Catalytic activity measurements were performed at temperatures between 200 and 450°C and atmospheric pressure. 150 mg catalyst powder as 100–200 μm sieve fraction were filled into a quartz glass tube (see section 3.4.1). The reaction gas mixture was 5 vol% CO, 20 vol% H_2O and 75 vol% He balance (GHSV of 50,000 ml/g_{cat} h).

4.1.3 Results and Discussion

4.1.3.1 Structural Characterization

Pure ceria and several ceria-supported rhodium and platinum catalysts were synthesized by flame spray pyrolysis. ICP-OES was used to determine the amount of noble metal in these samples. The structural properties of these samples are summarized in Table 4.1. As expected [142] the flame made pure ceria sample shows high specific surface area ($137 \ m^2 \ g^{-1}$) compared to CeO_2 prepared by calcination of nitrate ($83 \ m^2 g^{-1}$) [112]. Increasing metal content leads to a decrease in surface area from $125 \ m^2 g^{-1}$ to $105 \ m^2 g^{-1}$ and from $130 \ m^2 g^{-1}$ to $93 \ m^2 g^{-1}$ for Rh/CeO_2 and Pt/CeO_2, respectively (Table 4.1). In general, the specific surface area of these flame made catalysts is higher compared to conventionally prepared catalysts [43, 143-146].

Table 4.1: Structural properties of FSP made samples: specific surface area (S_{BET}), CeO_2 mean crystallite size of the supports (d_{CeO2}), the results for dispersion and noble metal particle size were obtained from TEM and dispersion [112].

Sample	S_{BET} [m^2g^{-1}]	d_{CeO2} [nm] [a]	TEM particle size [nm]	Dispersion [%]	Particle size [nm] [b]
3.1 wt.% Rh/CeO$_2$	105	17	~2.1	37	2.9
1.9 wt.% Rh/CeO$_2$	125	11	—	37	2.9
3.7 wt.% Pt/CeO$_2$	93	14	~2.7	24	4.7
1.7 wt.% Pt/CeO$_2$	130	11	—	33	3.4
CeO$_2$	137	16	—	—	—

[a] $2\theta = 28.6$ peak used to determine d_{CeO2};

[b] calculated using metallic dispersion corresponding to particle size (section 3.2.4)
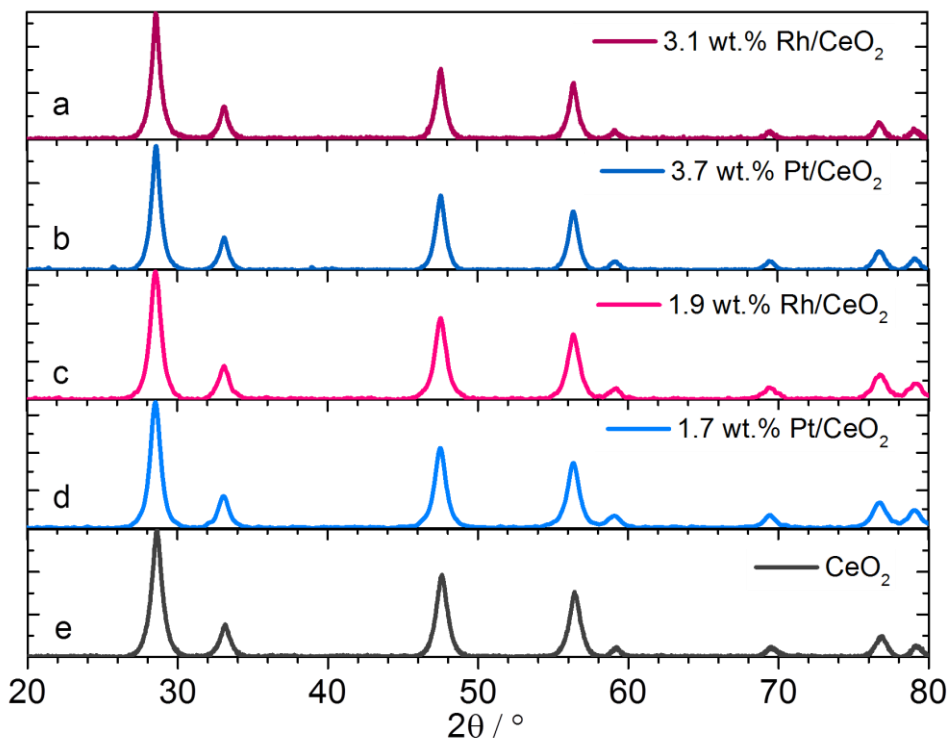
Figure 4. 1: XRD patterns of 3.1 wt.% Rh/CeO$_2$ (a), 3.7 wt.% Pt/CeO$_2$ (b), 1.9 wt.% Rh/CeO$_2$ (c) and 1.7 wt.% Pt/CeO$_2$ (d) catalysts compared to on XRD pattern of pure ceria (e).

Flame spray synthesis resulted in highly nanocrystalline ceria (Figure 4. 1). Ceria crystallite size for pure CeO$_2$ as well as for the Rh/CeO$_2$ and the Pt/CeO$_2$ catalysts were estimated using the XRD data and the Scherrer equation. The CeO$_2$ crystallite sizes calculated from the width of the

ceria reflection at $2\theta = 28.6°$ and are shown in Table 4.1. The values range between 11 and 17 nm. The results reveal that the presence of noble metals has some influence on the crystallite sizes. With increasing noble metal content the crystallite size slightly increases, which is in agreement with the decreasing surface area observed for each metal respectively. The samples only show reflections corresponding to the fluorite type structure of ceria. None of the XRD patterns in Figure 4. 1 show any evidence of Pt, PtO_2, Rh or Rh_2O_3 phases, probably due to high dispersion and small noble metal crystallite sizes (< 5 nm), which cannot be distinguished from the background [113]. TEM images of 3.7 wt.% Pt/CeO_2 and 3.1 wt.% Rh/CeO_2 after the WGS reaction are shown in Figure 4.2 (images of all fresh catalysts can be found in Appendix Figure A.1). The images show stepped crystal support surfaces. Furthermore, according to these images WGS reaction conditions do not have a signification influence on the particle size. After the reaction the Pt and Rh particles are still highly dispersed, they did not aggregate and the nano crystalline structure of the support is preserved. The TEM images show that the noble metal nanoparticles are spherical with average diameters of 2.7 and 2.1 nm for 3.7 wt.% Pt/CeO_2 and 3.1 wt.% Rh/CeO_2, respectively. These values were obtained from noble metal particle size distributions extracted from different TEM images. In the images of 1.9 wt.% Pt/CeO_2, 1.7 wt.% Rh/CeO_2, and 3.1 wt.% Rh/CeO_2 in Figure A.1 noble metal particles cannot be seen clearly, especially in case of Rh. This might be due to well-dispersed noble metal particles on the support, but it is also possible that the ceria hindered the determination of such nanoparticles. Hence, the contrast between support and noble metals is too low to identify the nanoparticles [147].
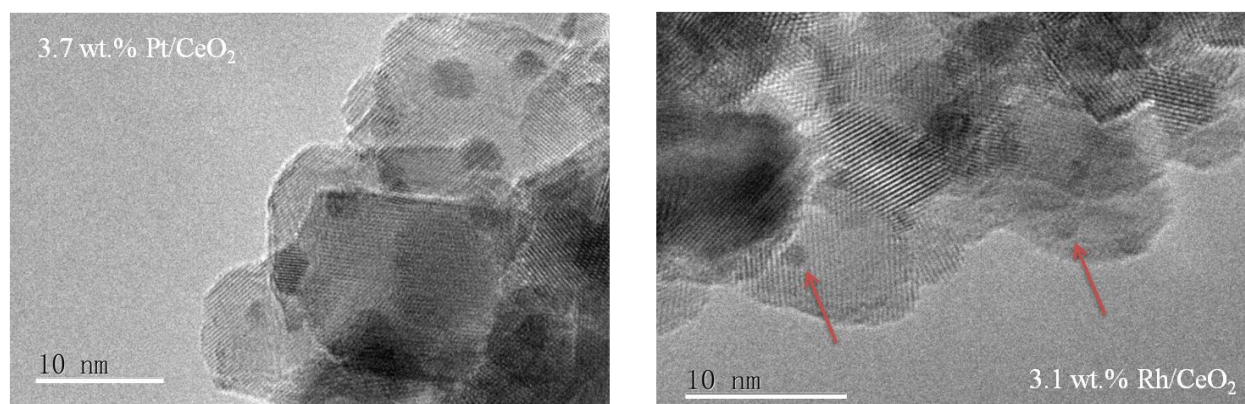
Figure 4.2: TEM images of ceria supported noble metal catalysts after WGS reaction: 3.7 wt.% Pt/CeO_2 (left) and 3.1 wt.% Rh/CeO_2 (right), recorded at Dalian Institute of Chemical Physic (DICP), Chinese Academy of Sciences (CAS) in Dalian/China.

The TEM images show that the noble metal particles are highly dispersed. The dispersion was further investigated by low temperature CO chemisorption (section 3.2.4). This method is hindered the misleading since that the metal particles are supported on a redox material (CeO_2). This can be due to strong metal-support interaction (SMSI) [148] and reactive adsorption of CO at hydroxyl groups on the reduced ceria surface [149]. Values for metallic dispersion determined by this method are included in Table 4.1. They are higher for Rh based catalysts compared to Pt based catalysts and the dispersion of Pt decreases with increasing metal loading. Metal particle sizes were estimated from the dispersion and are summarized in Table 4.1. In case of Rh these particle sizes are in good agreement with the TEM results whereas for the Pt particles they strongly differ from those obtained with TEM.

4.1.3.2 Reduction Behavior

In situ x-ray absorption spectroscopy was used to obtain further information about the structure of the catalysts and to study the reduction behavior of the noble metal particles. The reduction behavior of metal particles depends on the dispersion and incorporation into the sample matrices [110, 150].

Figure 4.3 shows Rh K-edge and Pt L_3-edge XANES spectra recorded *in situ* during reduction of the flame made 3.1 wt.% Rh/CeO_2 and 3.7 wt.% Pt/CeO_2 catalysts (temperature programmed reduction in 5% H_2/He, total flow 50 mL/min), respectively. The decrease in white line intensity at approx. 50°C in the Rh K- and at approx. 150°C in the Pt L_3-edge spectra indicates that the noble metal oxides are reduced in that temperature range. The relative concentrations of oxidized and reduced species were determined by linear combination fitting of the XANES data using the first and last spectrum of the TPR series as reference spectra. The fitting results for 3.1 wt.% Rh/CeO_2 and 3.7 wt.% Pt/CeO_2 catalysts are shown in Figure 4.4. The concentration of oxidized Rh species abruptly changes within less than 50 °C, as depicted in Figure 4.4 and the change shows a step increasing in the reduction. The Rh species seem to be completely reduced at 75 °C (Figure 4.3a and Figure 4.4). On the other hand, the reduction of Pt proceeds continuously (Figure 4.4) and full reduction could be observed at 250 °C (Figure 4.3b). The TPR results show that the rhodium oxide is reduced to metallic Rh at lower temperature (50% of Rh atoms in a metallic state at 70 °C) compared to platinum (50% metallic Pt at 145 °C). Compared to catalysts

prepared by conventional methods the reduction temperatures of these flame made Rh/CeO$_2$ and Pt/CeO$_2$ catalysts are lower [112, 139, 146, 151].
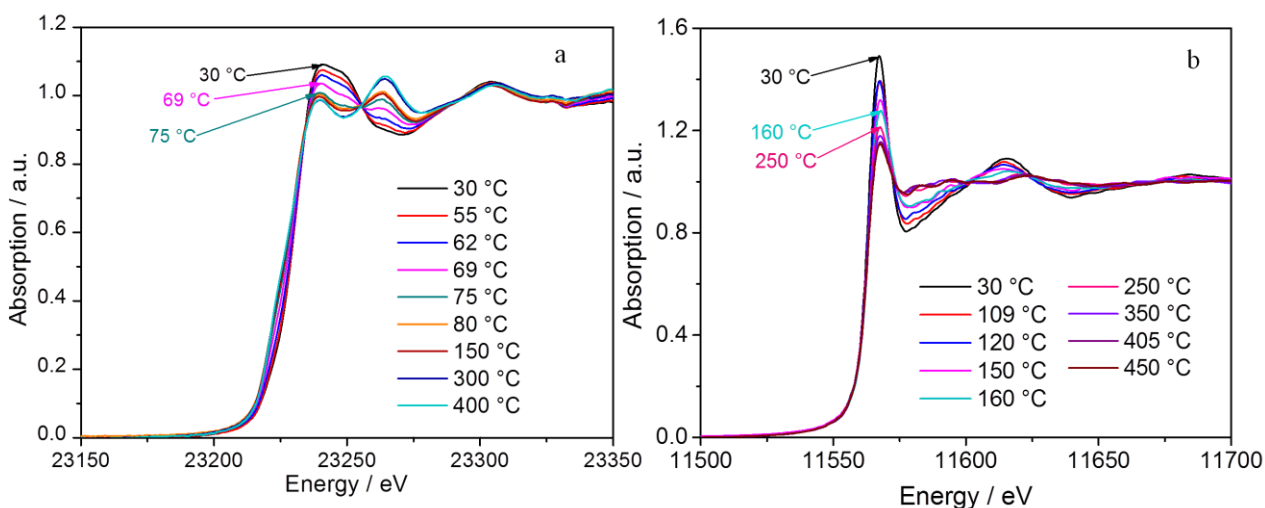
Figure 4.3: (a) Rh K-edge and (b) Pt L^3-edge XANES spectra of 3.1 wt.% Rh/CeO$_2$ and 3.7 wt.% Pt/CeO$_2$ catalysts recorded during temperature programmed reduction (5% H$_2$/He, total flow 50 mL/min).
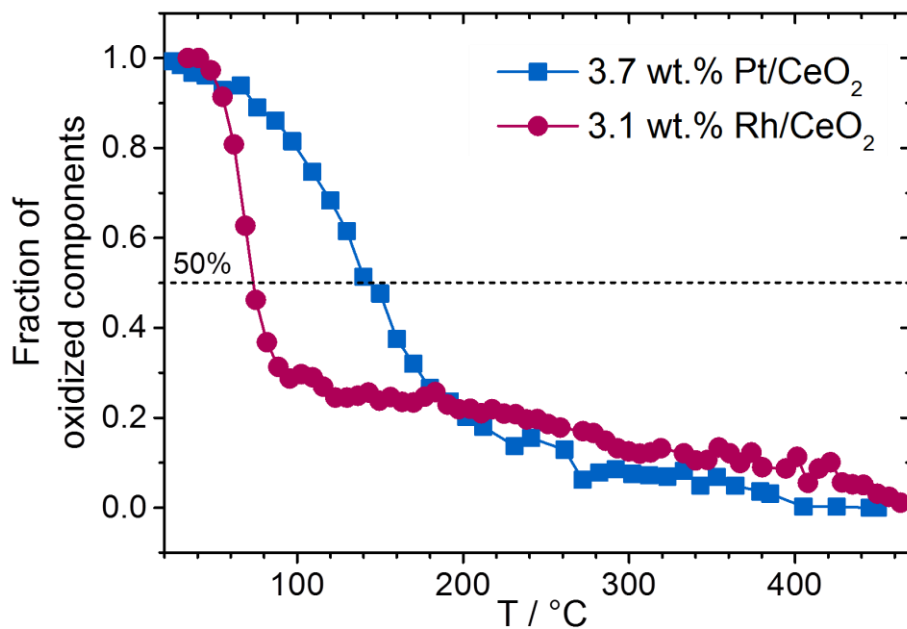
Figure 4.4: Changes in relative concentrations of oxidized Rh and Pt species during temperature programmed reduction.

Before (as prepared) and after *in situ* reduction EXAFS spectra of the 3.1 wt.% Rh/CeO$_2$ and 3.7 wt.% Pt/CeO$_2$ catalysts were recorded at room temperature in step scanning mode. Additionally, 3.1 wt.% Rh/CeO$_2$ was reduced for 2h in a flow of 10% H$_2$/N$_2$ at 450°C, afterwards

diluted with cellulose and pressed into pellets (*ex situ* reduced). Fourier transformed k^2- and k^3- weighted EXAFS data of the as prepared as well as *ex situ* and *in situ* reduced 3.1 wt.% Rh/CeO_2 and 3.7 wt.% Pt/CeO_2 catalysts are shown in Figure 4.5 and Figure 4.6. They provide a qualitative impression of the atomic environment around the Rh and Pt absorber atoms, respectively. These curves are related to the radial distribution of neighbor atoms around the absorber atoms, i.e. the peaks in Figure 4.5 and Figure 4.6 represent different atomic coordination shells. Quantitative information obtained from fitting the Fourier transformed EXAFS data are presented in Table 4.2 and in Table 4.3 for Rh and Pt based catalysts, respectively.

Fourier transformed EXAFS data of Rhodium (III) oxide (Rh_2O_3), the Rh precursor (Rhodium (III) acetylacetonate), Rh foil and as prepared 3.1 wt.% Rh/CeO_2 (after FSP, without treatment), are included in Figure 4.5 for comparison. In both Rh_2O_3 and the precursor Rh is coordinated by six oxygen atoms in the first coordination shell. However, for the precursor a significantly lower value for the Debye-Waller-Factor σ^2, which is related to the atomic disorder (mean square deviation of atomic distance), was obtained from EXAFS fitting. This could be due to the rigid bidentate chelate structure of the precursor. In Rhodium (III) oxide the Rh absorbers are coordinated by one Rh atom in the second shell at a distance of 2.69 Å and in the Rh foil by 12 Rh atoms in the first (2.68 Å), and 6 in the second shell (3.79 Å). The first shell (between 1 and 2 Å in Figure 4.5) in the Fourier transformed absorption data of the as prepared 3.1 wt.% Rh/CeO_2 can be attributed to oxygen atoms. According to Table 4.2, the values for the Rh–O bond length (and Debye-Waller-Factor) obtained from the as prepared Rh/CeO_2 catalyst are higher than those for the precursor. This suggests a shift towards oxide-like Rh-O bonds and thus indicates that during preparation the precursor was at least partly incorporated into CeO_2, resulting in a rhodium oxide-like structure. The bond length obtained for the second shell in the as prepared sample (2.72 Å) could in principle correspond to either metallic or oxide backscattering (cf. bond lengths in Table 4.2). The white line intensity and edge energy in the spectra of the as prepared Rh/CeO_2 catalyst suggest that in this sample oxidized rhodium is the dominating Rh species. On the other hand, the oscillations obtained from a backward Fourier transform of the second shell for the as prepared Rh/CeO_2 sample and the metallic Rh foil (Figure A.2) are out of phase, which may be due to a significant shift in bond lengths (cf. bond lengths in Table 4.2). Therefore, the structure of Rh in the as prepared Rh/CeO_2 sample can be described as a mixture of oxide-like and metallic clusters, which are smaller and more disordered than those

found after reduction of the catalyst. Furthermore, the low reduction temperature suggests that the Rh species are probably located on the surface of the CeO_2 particles. This indicates that the above mentioned second shell can be attributed to Rh in a metallic cluster.

The Fourier transformed EXAFS data in Figure 4.5 show further that the *ex situ* Rh/CeO$_2$ catalyst was reoxidized in air, thus confirming the previous conclusion that the Rh oxide-like clusters are located on the surface of CeO_2 and rather small. However, this sample was only partly reoxidized as shown by the lowe0r number of oxygen neighbors in the first shell and higher number of Rh neighbors in the second shell compared to the as prepared sample. The distance between the absorbing and the neighboring atoms (1st shell) in both samples is comparable. On the other hand, *in situ* reduction produced metallic clusters with 8.7±0.7 Rh atoms in the first coordination shell. The cluster size estimated from this coordination number using a method developed by Jentys [152] is 1.7 nm, which shows that flame spray pyrolysis is well-suited for the production of small Rh particles as catalytically active centers.
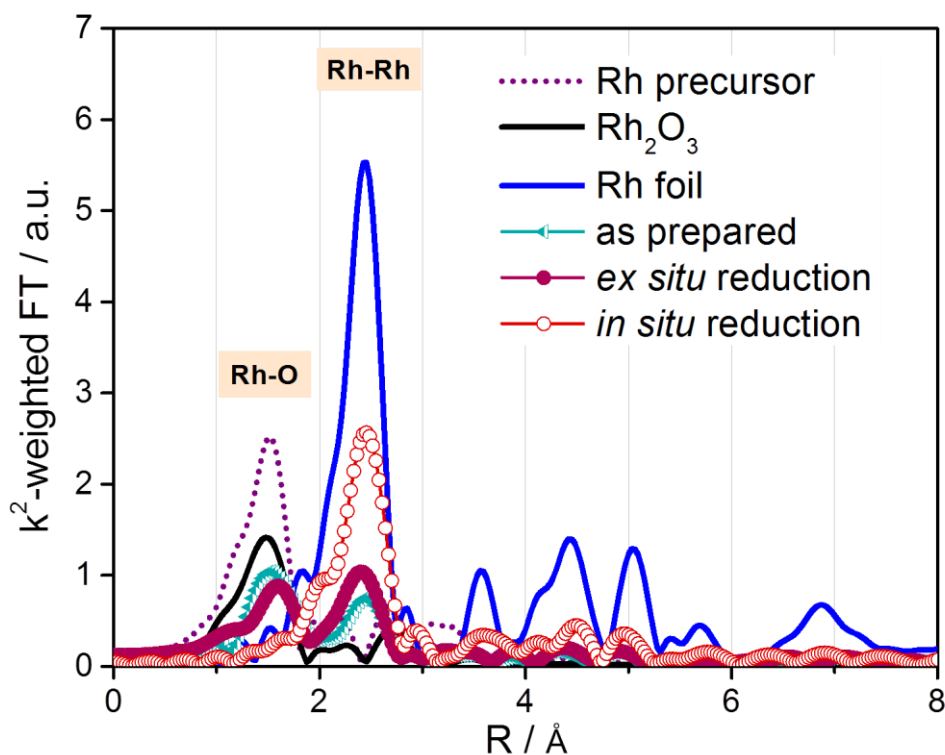
Figure 4.5: k^2–weighted Fourier transformed EXAFS data of 3.1 wt.% Rh/CeO$_2$ catalysts after preparation and after reduction with (*ex situ* reduction) and without (*in situ* reduction) exposureto air as well as rhodium oxide and metallic Rh foil.

Table 4.2: Structural parameters for the atomic environment around the Rh absorber atoms obtained from refined EXAFS data fitted in R-space. (Fit results; N: number of neighboring atoms at distance r (± 0.01), σ^2: mean-square disorder in the atomic distance (Debye-Waller factor). Set parameter; amplitude reduction factor S_0^2).

Sample	Rh—O			Rh—Rh		
	N	r [Å]	$\sigma^2 \cdot 10^{-3}$ [Å^2]	N	r [Å]	$\sigma^2 \cdot 10^{-3}$ [Å^2]
as prepared	6 [a]	2.03 [b]	3.8±1.0 [b]	2.7±1.0 [b]	2.72 [b]	5.5±2.4 [b]
ex situ reduced	4.2±0.3 [b]	2.03 [b]	3.8±1.0 [b]	3.9±0.7 [b]	2.68 [b]	4.7±1.1 [b]
in situ reduced	—	—	—	8.7±0.7 [b]	2.67 [b]	5.5±0.4 [b]
Rh foil	—	—	—	12 [a]	2.68 [b]	3.7±2.6 [b]
				6 [a]	3.79 [b]	6.0±1.1 [b]
Rh$_2$O$_3$	6 [a]	2.01 [b]	4.9±0.7 [b]	1 [a]	2.69 [b]	12.3±4.2 [b]
Rh precursor	6 [a]	1.99 [b]	2.5±0.1 [b]	—	—	—

[a] fixed parameter, [b] varied parameter

The low reduction temperature of the flame made 3.7 wt.% Pt/CeO$_2$ catalyst points out that the Pt species can easily be reached by H$_2$. In order to gain a deeper insight into the structure of the metal particles on the support, variations in the Pt–Pt bond length and the Debye-Waller-Factor (mean square deviation in the inter-atomic distances determined by EXAFS) were analyzed as a function of temperature (Figure A.3). The results show that the Pt-Pt bond length decreases with increasing temperature, whereas the Debye-Waller-Factor increases due to increasing thermal disorder. Although one may expect expansion with increasing temperature, a contraction (or negative expansion) of Pt clusters probed by EXAFS has been previously reported for ~ 1nm particles along with calculations showing that in addition to the high surface to bulk atoms ratio, the adsorbed H$_2$ plays a major role with respect to this anomalous behavior [153]. Fourier transformed EXAFS data of the Pt foil, the Pt precursor (Pt(C$_5$H$_7$O$_2$)$_2$), platinum (IV) oxide (PtO$_2$), the as prepared 3.7 wt.% Pt/CeO$_2$ catalyst (after FSP, without treatment), and the *in situ* reduced Pt/CeO$_2$ sample are shown in Figure 4.6. The contributions of the Pt–O peak (1st coordination shell at approx. 1.5 Å in Figure 4.6a) to the EXAFS data of the precursor and as prepared are almost equal, but significantly lower compared to the Pt–O peak in the PtO$_2$ data,

which indicates a lower number of oxygen atoms in this shell, as shown in Table 4.3. The coordination numbers for Pt foil and PtO_2 (1st shell) in Table 4.3 were set (fixed values from database, all other parameters were fitted), and the structural parameters obtained from EXAFS fitting correspond well to literature data [154, 155].
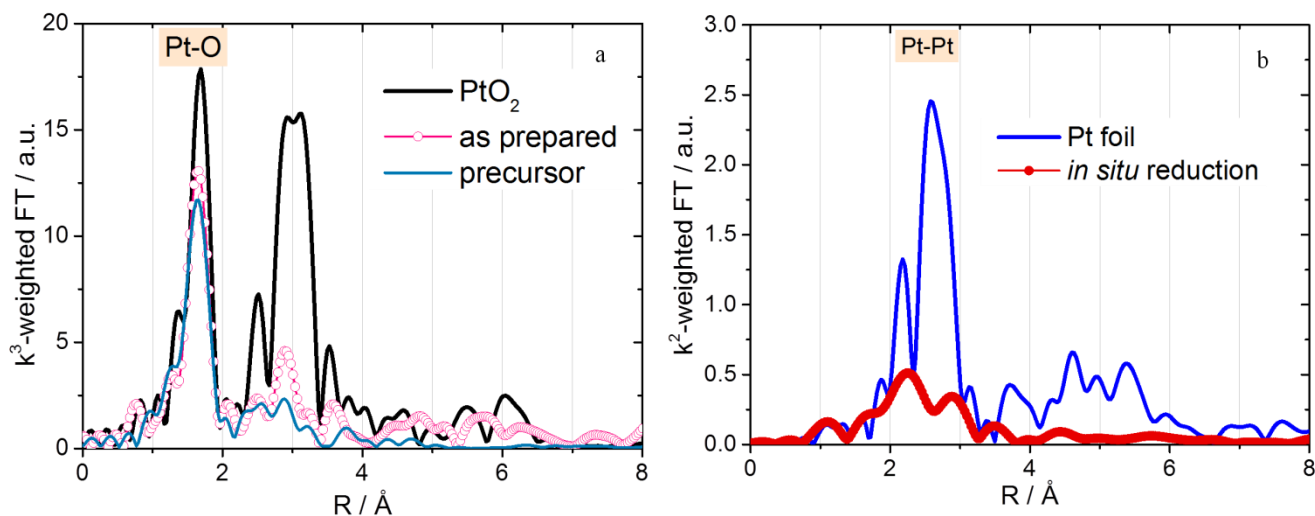
Figure 4.6: k^2 and k^3–weighted Fourier transformed EXAFS data of (a) platinum oxide (PtO_2), Pt precursor ($Pt(C_5H_7O_2)_2$) and 3.7 wt.% Pt/CeO_2 catalyst after preparation and (b) metallic Pt foil and 3.7 wt.% Pt/CeO_2 catalyst after reduction.

Table 4.3: Structural parameters for the atomic environment around the Pt absorber atom obtained from refined EXAFS data (N: number of neighboring atoms at distance r (±0.01) from absorbing atom, σ^2: mean-square disorder in the atomic distance (Debye-Waller factor). k^2– and k^3–weighted EXAFS data and fitting curves in Figure A.4.

Sample	Pt−O			Pt−Pt		
	N	r [Å]	$\sigma^2 \cdot 10^{-3}$ [Å^2]	N	r [Å]	$\sigma^2 \cdot 10^{-3}$ [Å^2]
Pt precursor	4 [a]	1.99 [b]	1.4±0.2 [b]	—	—	—
as prepared	4.7±0.5 [b]	1.99 [b]	1.4±1.0 [b]	—	—	—
in situ reduced	—	—	—	6.9±0.7 [b]	2.70 [b]	8.9±0.8 [b]
Pt foil	—	—	—	12 [a]	2.76 [b]	4.7±0.1 [b]
PtO_2	6 [a]	2.02 [b]	1.9±0.5 [b]	9.9±1.7 [b]	3.11 [b]	4.1±0.7 [b]

[a] fixed parameter, [b] varied parameter

In PtO_2 each absorber atom is surrounded by 6 oxygen atoms in the first shell, whereas in as prepared Pt/CeO_2 catalysts platinum has about 4.7 oxygen neighbors. In the Fourier transformed data of PtO_2 further features can be attributed to a second coordination shell with 9.9±1.7 Pt neighbors by EXAFS fitting. However, for the as prepared sample the backscattering signal in this R range was too weak to be analyzed. The backscattering amplitude depends on the atomic number of the scattering atoms (as rule of thumb heavier atoms scatter more strongly), the number of scatters, bond distance and on the Debye-Waller factor σ^2. In the present samples, the low intensities of futures features corresponding to the second coordination shell may be due to of low coordination numbers and a high degree of structural disorder. This assumption is supported by the small size of the metallic Pt particles in the in situ reduced catalyst, as discussed below. The refined structural parameters in Table 4.3 show that the chemical environment of Pt in the as prepared Pt/CeO_2 catalyst is similar to the chemical environment of Pt in the precursor. The first coordination shell (between 1 and 2 Å Figure 4.6a) in the as prepared Pt/CeO_2 sample is attributed to oxygen atoms, since the bond distance (1.99 Å) is the same as for Pt–O bonds in the precursor. These results show that during preparation the Pt precursor was not converted into PtO_2 or metallic platinum. EXAFS refinement shows that after reduction the Pt absorbers are surrounded by 6.9±0.7 Pt atoms in the first coordination shell. Moreover, the Pt–Pt bond length is shorter (2.70 Å) compared to bulk Pt (2.76 Å). The size of the resulting Pt clusters was estimated to be ca. 1.2 nm using the approach mentioned above [152].

4.1.3.3 Water Gas Shift Activity Tests

Figure 4.7 shows CO conversion in 5 vol.% CO and 20 vol.% H_2O as a function of temperature for the flame made Pt and Rh based catalysts. Before the catalytic test the flame made catalysts were reduced *ex situ* at 400 °C for 2 h. At low temperature (200 °C) the flame made catalyst with high Pt loading (3.7 wt.%) shows the highest activity, followed by the catalyst with lower Pt loading (1.7 wt.%) and the Rh based catalysts. At 350 °C all catalysts reach the equilibrium curve. Figure 4.7 shows that the conversion of CO at 200 °C is 34% for 3.7 wt.% Pt/CeO_2 and 20% for 1.7 wt.% Pt/CeO_2 and increases abruptly to 97% and 81% at 250 °C, respectively. Compared to 0.74 wt.% Pt/CeO_2 catalysts prepared by IWI (52% at 250 °C) the catalytic performance of these FSP made catalysts is higher [112]. In case of the Rh based catalysts CO conversion for both catalysts is similar in the entire temperature range. At 200 °C the conversion

of CO is below 10% and at 250 °C about 30%. However, at 300 °C CO conversion increases suddenly to 90% over both Rh based catalysts. The 3.1 wt.% Rh/CeO_2 catalyst was also studied under WGS conditions during cooling down (from 450 °C to 200 °C). The results in Figure 4.7 show that this catalyst exhibits similar activity during heating up and cooling down. This implies that the catalyst is very stable, in agreement with the TEM image in Figure 4.2, which still shows a high degree of dispersion and proves that the Rh particles did not aggregate. A disadvantage of Rh/CeO_2 is the formation of methane (CH_4) starting at 300°C, which has been previously reported [156]. Above 350°C the formation of methane decreases with increasing temperature.

The turnover frequency (TOF) describes the catalytic level of activity; the larger the TOF, the more active are accessible catalytic sites on the catalyst. TOF is defined as the ratio of the moles transformed into the desired product per unit time to mole of active site:

$$TOF = \frac{\dot{n}_{X_{CO}}}{n_{cat}} = \frac{\dot{V}_{CO} \cdot X_{CO} \cdot \rho_{CO} \cdot \frac{1}{M_{CO}}}{m_{cat} \cdot p_{metal} \cdot D \cdot \frac{1}{M_{metal}}} \qquad \text{Eq. 4.1}$$

($\dot{n}_{X_{CO}}$: rate of product formed per unit time, n_{cat}: mole of active sites, $\dot{V}_{CO}$: CO flow, X_{CO}: CO conversion, ρ_{CO}: density, M_{CO}: molar mass of CO, m_{cat}: amount of catalyst, p_{metal}: particle loading, D: dispersion, and M_{metal}: molar mass of metal in this case Pt and Rh). The TOF calculated for the flame made catalysts at 200 °C are shown in Table 4.4. The TOF of CO conversion strongly depends on the nature of the metallic phase. The TOF values corroborates that the flame made Pt based catalysts show much higher catalytic activity active than the Rh based catalysts; intrinsic activity for CO conversion ($TOF_{200 \, °C}$ $^{s-1}$) increased from 0.02 s^{-1} for 3.1 wt.% Rh/CeO_2 to 0.22 s^{-1} for 3.7 wt.% Pt/CeO_2. At 200 °C the TOF decrease in order to 3.7 wt.% Pt/CeO_2 > 1.7 wt.% Pt/CeO_2 > 1.9 wt.% Rh/CeO_2 > 3.1 wt.% Rh/CeO_2. Panagiotopoulou et al. [43] also reported rates in terms of TOF for different catalytically active metals on CeO_2. They observed that the CO conversion decreased in the order to Pt > Rh ≈ Ru > Pd. In this study Pt based catalysts also showed higher activity compared to the Rh based catalysts.
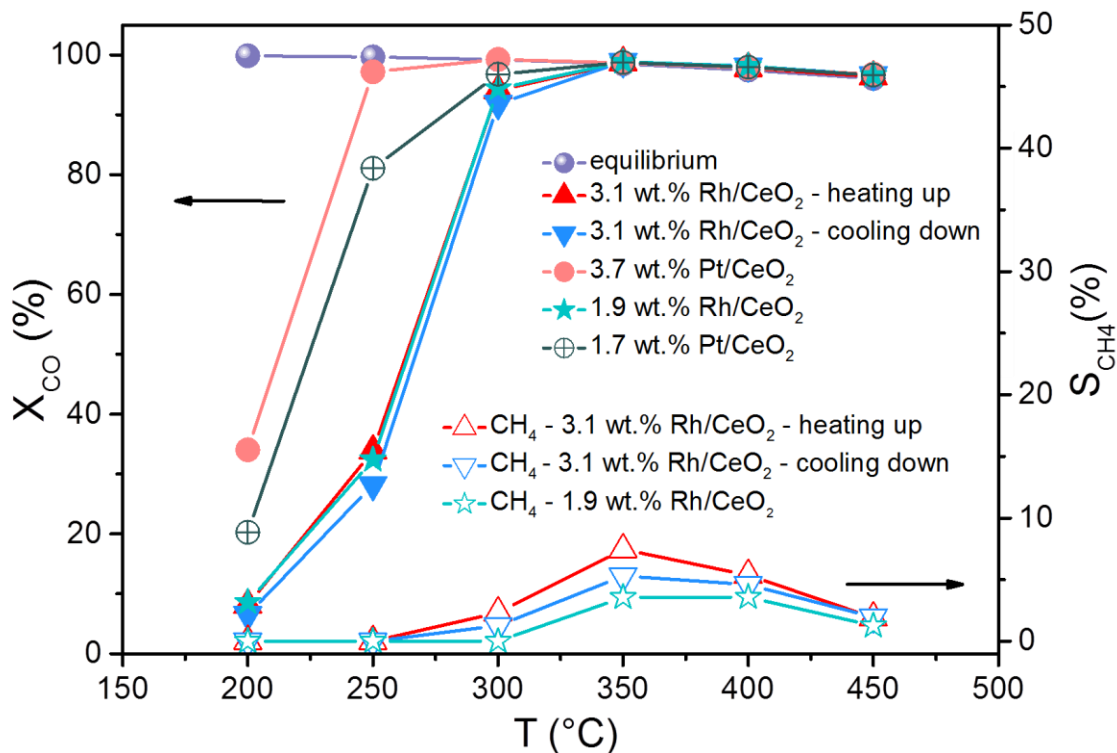
Figure 4.7: Influence of temperature on CO conversion over flame made Pt/CeO_2 and Rh/CeO_2 catalysts (150 mg catalysts, sieve fraction diameter 100–200 µm, feed composition 5 vol.% CO, 20 vol.% H_2O in balance He, total flow 125 mL/min, GHSV = 50,000 mL/g_{cat} h).

Table 4.4: Turnover frequencies (TOF) at 200°C.

Sample	TOF [1/s]
3.7 wt.% Pt/CeO_2	0.22
1.7 wt.% Pt/CeO_2	0.19
3.1 wt.% Rh/CeO_2	0.02
1.9 wt.% Rh/CeO_2	0.04

The catalytic activity of the flame made materials with low loading (1.9 wt.% Rh/CeO_2, 1.7 wt.% Pt/CeO_2) was also measured under typical WGS operating conditions, i.e. in a 32 vol.% CO, 11 vol.% CO_2, 11 vol.% N_2, 18 vol.% H_2, 28 vol.% H_2O feed gas, as in ref. [157]. Figure 4.8 shows CO conversion and formation of methane over these two catalysts as a function of temperature under these reaction conditions. In general, the Pt catalyst remains more active. Over Rh/CeO_2 methane formation occurs at temperatures above 350°C, whereas in the presence of the Pt based catalysts methane levels are insignificant in the whole temperature range.
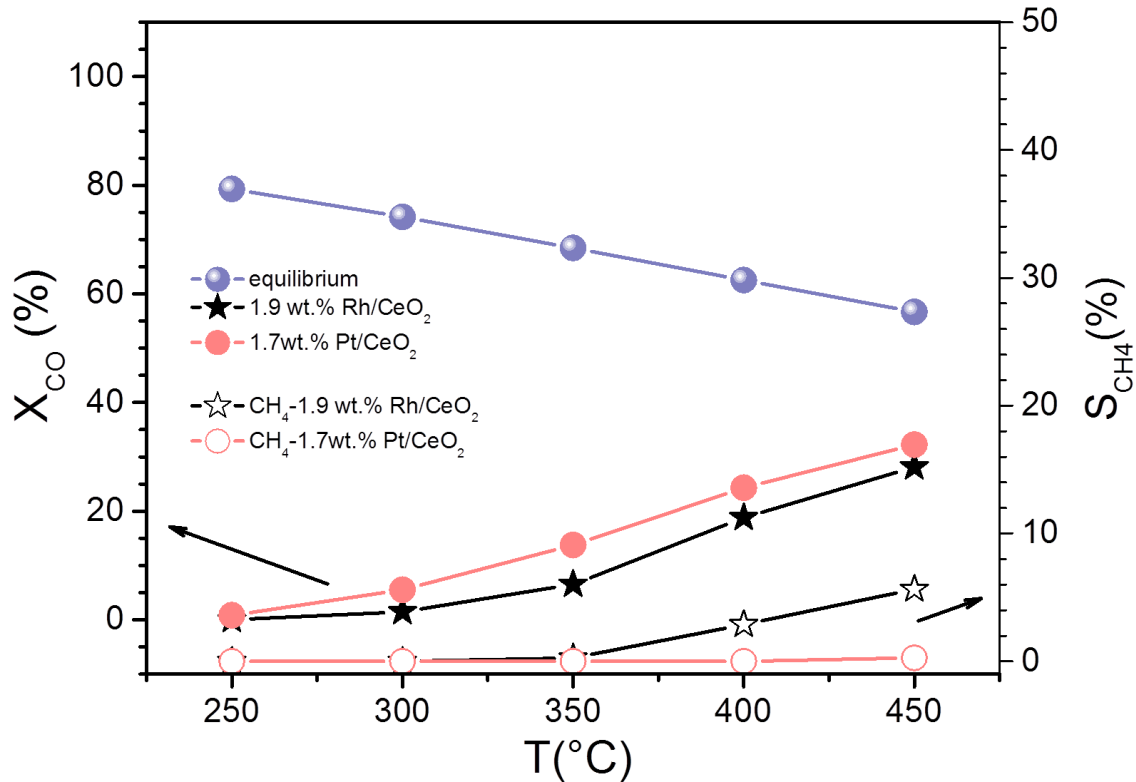
Figure 4.8: Influence of temperature on CO conversion over FSP made Pt/CeO_2 and Rh/CeO_2 catalysts with low loading (amount of catalysts 25 mg diluted with 100 mg quartz sand, sieve fraction 250-400 μm, feed composition 32 vol.% CO, 11 vol.% CO_2, 11 vol.% N_2, 18 vol.% H_2, 28 vol.% H_2O, GHSV = 150,000 mL/g_{cat} h based on total gas flow except N_2).

Piermartini et al. [157] achieved ca. 15% CO conversion at 400°C using 5 wt.% Pt/CeO_2 catalyst prepared by sol-gel methods. At this temperature the flame made 1.7 wt.% Pt/CeO_2 reaches a level of CO conversion around 23%, and the 1.9 wt.% Rh/CeO_2 catalyst 19% as shown Figure 4.8. Although the noble metal loading of the sol-gel made catalyst is much higher compared to these FSP made catalysts, CO conversion over these FSP made catalysts exceeds the performance of the sol-gel made catalysts. However, in case of FSP made catalysts the dispersion of noble metal particles on the support is high (Pt dispersion is 33% for FSP made catalyst and 16% for sol-gel made catalysts). Hence, the most active catalysts for the water-gas shift reaction investigated in this work are the Pt based catalysts. This is in agreement with a recent, comprehensive study of several metals on ceria by Jacobs et al. [42]. They studied the role of different metals (Fe, Co, Ni, Pt) on ceria with respect to WGS reactions and found that the WGS rate was about 20 times higher with Pt. In summary, flame spray pyrolysis is a promising method for producing high active and stable catalysts for WGS reactions. This is in accordance with

Meland et al. [158], who came to similar conclusions when comparing the catalytic performance of flame made, mainly copper-based, materials and catalysts prepared by conventional methods.

4.1.4 Conclusions

For this study several highly active ceria supported Pt and Rh catalysts were prepared in one step by flame spray pyrolysis. These catalysts exhibited a high specific surface area (93–130 m^2g^{-1}) and a high degree of nanocrystallinity. According to the TEM results, the metallic phase consists of highly dispersed spherical nanoparticles with relatively small diameters (2.1–2.7 nm). The reaction conditions hardly influence the particle size, i.e. the particles do not aggregate (Figure 4.2), indicating that the catalysts are stable under WGS conditions. Structural changes during reduction were analyzed by X-ray absorption spectroscopy. XANES spectra, recorded *in situ*, indicate that the material prepared by flame spray pyrolysis was reduced at lower temperature compared to catalysts prepared by conventional methods. EXAFS uncovered rather small Rh (1.7 nm) and Pt (1.2 nm) particles after reduction (CN_{Rh} = 8.7±0.7, CN_{Pt} = 6.9±0.7).

The catalytic results support the conclusion that the Pt based catalysts are more active than Rh based materials and promising catalysts for water gas shift reactions at high temperature. Rh based catalysts also have the disadvantage that above 250°C methane is formed as by-product which was not detected over Pt-based catalysts. Hence, flame spray pyrolysis seems to be a promising method for the synthesis of high temperature water gas shift catalysts for membrane and micro reactors, since this technique allows to synthesize the corresponding catalysts in one single step and obtained catalysts are stable due to their microcrystalline structure (higher temperature during synthesis).

4.2   Investigation of Titania Supported Noble Metal Catalysts

4.2.1 Introduction

It has been shown that titanium dioxide (TiO_2) as a support is generally effective for activity and selectivity enhancement, and also a promising promoter and as a catalytic material for photocatalytic reactions [159-161]. Furthermore, titanium dioxide is used in many applications as

white pigments in painting and coating of metals [162]. Additionally, it has become important in the field of sensor technology to detection of combustible or toxic gases [163]. TiO_2 crystallizes in three different phases: rutile, anatase and brookite [3]. Rutile and anatase are usually used as a support for catalytic materials [164]. The catalytic activity is significantly by the phase of the supports [165]. In the rutile and anatase phase the Ti atoms are coordinated by six oxygen in an octahedral configuration [3]. The difference between both crystal phases is the occupancy of octahedral site by Ti cations [164]. In the rutile phase the oxygen atoms are surrounded by three Ti atoms in a trigonal-planar configuration [3]. Rutile is the most stable TiO_2 crystal phase and the change from anatase to rutile occurs below 600 °C for pure anatase which can be shifted to lower temperature in the presence of foreign atoms [164, 166, 167].

TiO_2 as a reducible support for WGS catalysts is an attractive alternative to CeO_2. Noble metals such as Au on TiO_2 are known to be effective for low temperature WGS reactions [168]. Furthermore, the advantage of TiO_2 supported materials is that no formation of methane was observed. A large number of studies on Pt/TiO_2 catalysts mostly prepared by impregnation of commercially available TiO_2, has been published [19, 35, 36, 52, 169-171]. The preparation method ultimately affects the surface composition, size and morphology of the supported nanoparticles as well as the metal–support interface. As a consequence, by applying specific preparation techniques a high degree of metal–support interaction can be achieved [132, 164]. In case of easily reducible metals and a strong metal–support interaction (SMSI) the metal nanoparticles are formed at the surface of the support [132]. In case of strong MSI noble metals supported on reducible metal oxides are reduced at higher temperature compared to materials with week MSI which results in differences in catalytic activity [172, 173]. This phenomenon occurs for reduction temperatures above 300 °C [174]. Oxidation treatment usually reverses the SMSI state [164]. With regard to SMSI behavior Pt/TiO_2 and Rh/TiO_2 catalysts are among the most widely investigated systems [164].

4.2.2 Experimental Part

Catalytic activity measurements for water gas shift reaction were performed at atmospheric pressure and temperatures between 250 and 450°C. 75 mg catalyst powder as 100–250 μm sieve fraction were filled into a quartz glass tube (8 mm diameter, Figure 3.7 in section 3.4.1). The

composition of the reaction gas mixture was 5 vol% CO, 20 vol% H_2O and 75 vol% He balance (total flow 187.5 mL/min), resulting in a GHSV of 150,000 mL/g_{cat} h.

Further catalytic tests were performed in a quartz capillary micro reactor (Figure 3.8 in section 3.4.2). 60 mg of catalyst powder was filled into the capillary between quartz wool plugs. The test was carried out at atmospheric pressure between 200 – 500 °C and GSHV = 50,000 mL/g_{cat} h at a gas hourly space velocity. For the catalytic experiments three different test procedures were applied:

(i) The catalysts were used as prepared and the composition of the reaction gas mixture was 5 vol% CO, 20 vol% H_2O and 75 vol% He balance.

(ii) The fresh catalysts were reduced at 500 °C for 2 h and then cooled down to 200 C° in H_2. Afterwards, the catalysts were investigated under the same WGS reaction conditions as in (i).

(iii) For long term stability tests, a feed gas consisting of 10 vol.% CO, 10 vol.% CO_2, 40 vol.% H_2, 20 vol.% H_2O, 20 vol.% He (a typical reformate mixture) was dosed. First, the catalysts were heated from 200 °C to 400 °C in this gas mixture and the gas composition was analyzed in 50 °C intervals. Subsequently, at 400 °C the catalysts were tested under steady state conditions to analyze their deactivation.

4.2.3 Results and Discussion

4.2.3.1 Catalysts Characterization

Specific surface areas and results of elemental analysis by ICP/OES of the as prepared catalysts are presented in Table 4.5. Pt based catalysts prepared by SF and DF spray pyrolysis exhibit specific surface areas of 80 m^2g^{-1} and 70 m^2g^{-1}, respectively. These values are similar to the specific surface area of commercial titanium dioxide (80 m^2g^{-1}) and comparable to impregnated material with 1.9 wt.% Pt loading (78 m^2g^{-1}) [29]. Commercial TiO_2 of type P25 from Degussa has been frequently used as support for WGS catalysts and exhibit specific surface areas of 41 m^2g^{-1} [19, 169]. The BET surface area of 0.5 wt.% Pt/TiO_2(P25) prepared by wet-impregnation is received 39 m^2g^{-1} [169]. Pure rutile and anatase phase of TiO_2 impregnated with

3 wt.% Pt were reported to have specific surface areas of 44 m^2g^{-1} and 74 m^2g^{-1} respectively [36]. As shown in Table 4.5, the specific surface area of Rh catalysts prepared by SF for this study is slightly higher (79 m^2g^{-1}) for compared to the double flame made material (67 m^2g^{-1}). The reason for this can be traced back to higher temperature in the double flame.

Table 4.5: Chemical composition, BET specific surface areas (S_{BET}), dispersion and metallic particle size of catalysts prepared by double flame (DF) and single flame (SF) pyrolysis

	Loading wt.%	S_{BET} $[m^2g^{-1}]$	Dispersion [%]	d $[nm]^a$	Loading wt.%	S_{BET} $[m^2g^{-1}]$	Dispersion [%]	d $[nm]^a$
		Pt				Rh		
SF	0.3	81	64	1.8	0.2	79	54	2.0
	0.4	80	45	2.5	0.6	79	33	3.3
DF	0.3	70	63	1.8	0.2	67	55	2.0
	0.4	70	55	2.1	0.5	67	42	2.6

[a] calculated using metallic dispersion (section 3.2.4)

Grossmann et al. [175] investigated the temperature profile of xylene-based flames used for the synthesis of TiO$_2$-supported Pt nanoparticles and observed a significant gradient in the SF temperature profile along the flame axis (1800 K at 10 cm and 1000 K at 20 cm distances above the nozzle levels) due to entrainment of ambient air. They also found out that the flame temperature of two nozzles along the flame axis between 10 and 20 cm exceeds the temperature of a single flame by up to 300 K. This enhancement is attributed to a decrease in cold ambient air between two flames of two nozzles [175]. The flame temperature strongly influences coagulation and sintering of the particles and thus resulted in larger particle size and a decrease in the specific surface area [176].

Pt and Rh cluster size distributions for the SF and DF made materials were obtained from TEM images (Figure 4.9a-d). The smallest mean particle size was observed for the SF 0.4 wt% Pt/TiO$_2$ catalyst (d_{Pt-TEM}=1.8 nm), the particles prepared by DF had larger diameters (d_{Pt-TEM}=2 nm for 0.4 wt.% Pt/TiO$_2$; d_{Rh-TEM}=3 nm for 0.5 wt.% Rh/TiO$_2$). Although the contrast between titania and Rh is significantly high to allow clear identification of small noble metal particles (Figure 4.9d), the Rh particles on the SF made Rh/TiO$_2$ catalyst cannot be seen clearly (Figure 4.9c). Nevertheless, in all cases Rh and Pt clusters are well-dispersed on TiO$_2$. However, some regions

in double flame made samples are noble metal-lean (0.6 wt% Pt, 0.7 wt.% Rh) and some surface regions of the samples are noble metal-rich (0.8 wt.% Pt, 1.0 wt.% Rh), which was confirmed by EDX (Energy-dispersive X-ray spectroscopy, Figure A.5). A qualitative comparison of the TEM images suggests that the Pt cluster size distribution is high in case of the SF made samples. In contrast, the Pt particle dispersion is broader in case of the double flame made samples. A similarly result in non-uniform dispersion is obtained for Rh particles prepared by DFSP. These results are in agreement with Grossmann et al. [175] who compared catalysts prepared by SF with catalysts prepared by DF with different intersections distances, and found that increasing the intersection distance of the DF at a constant intersection angle leads to a decrease in Pt dispersion. This indicates that shorter intersection distances leads to similar results as SF with a high dispersion of Pt on TiO_2 and therefore smaller particle sizes [175], which is also in agreement with Minnermann et al. [177]. For SF set-ups, Schulz et al. [92] assumed that Pt and TiO_2 were formed successively, i.e. TiO_2 particle formed first and provided sites for nucleation of Pt, which leads to high dispersion of Pt clusters. In the double flame geometry, the formation and growth of Pt particles proceeds via homogeneous nucleation and subsequent growth to larger particles without support contact by noble metal coagulation–coalescence, which indicates larger noble metal particle sizes and slightly smaller dispersion [175]. The noble metals particles were regularly distributed and no larger agglomerates could be detected by energy dispersive X-ray spectroscopy. Potentially, the DF technique prevents encapsulation of the particles as reported earlier [96, 98].

Additionally the noble metal dispersion *D* was determined by CO-Chemisorption (cf. Table 4.5). *D* is defined as the ratio of surface accessible precious metal atoms to the total content of precious metal in the sample (section 3.2.4). For spherical particles, a relationship between metal dispersion and particle size can be established. Particle sizes thus calculated are included in Table 4.5. The dispersion of Pt and Rh on TiO_2 increases with decreasing noble metal loading in the precursor solution, respectively. In addition, the dispersion of Pt on TiO_2 is distinctly higher compared to Rh on TiO_2. However, for both noble metals with high loadings double flame made samples exhibit higher dispersion than single flame made samples. Teoh et al. [95] showed the dispersion of Pt on TiO_2 as a function of metal loading and observed increasing dispersion with decreasing Pt loading. Likewise, Strobel et al. [94] determined the dispersion of Pt on Al_2O_3 from H_2 chemisorption measurements and came to similar conclusion. Compared to impregnated Pt

catalysts supported on TiO_2 (rutile; 38.6%, anatase; 28.1%) the flame made catalysts in this work show higher noble metal dispersion [36]. Diameters of Rh and Pt particles on TiO_2 estimated from the dispersion and diameters obtained from TEM images, for instance d_D=2.1 nm and d_{Pt-TEM}=2 nm for 0.4 wt.% Pt/TiO_2; d_D=2.6 nm and d_{Rh-TEM}=3 nm for 0.5 wt.% Rh/TiO_2.
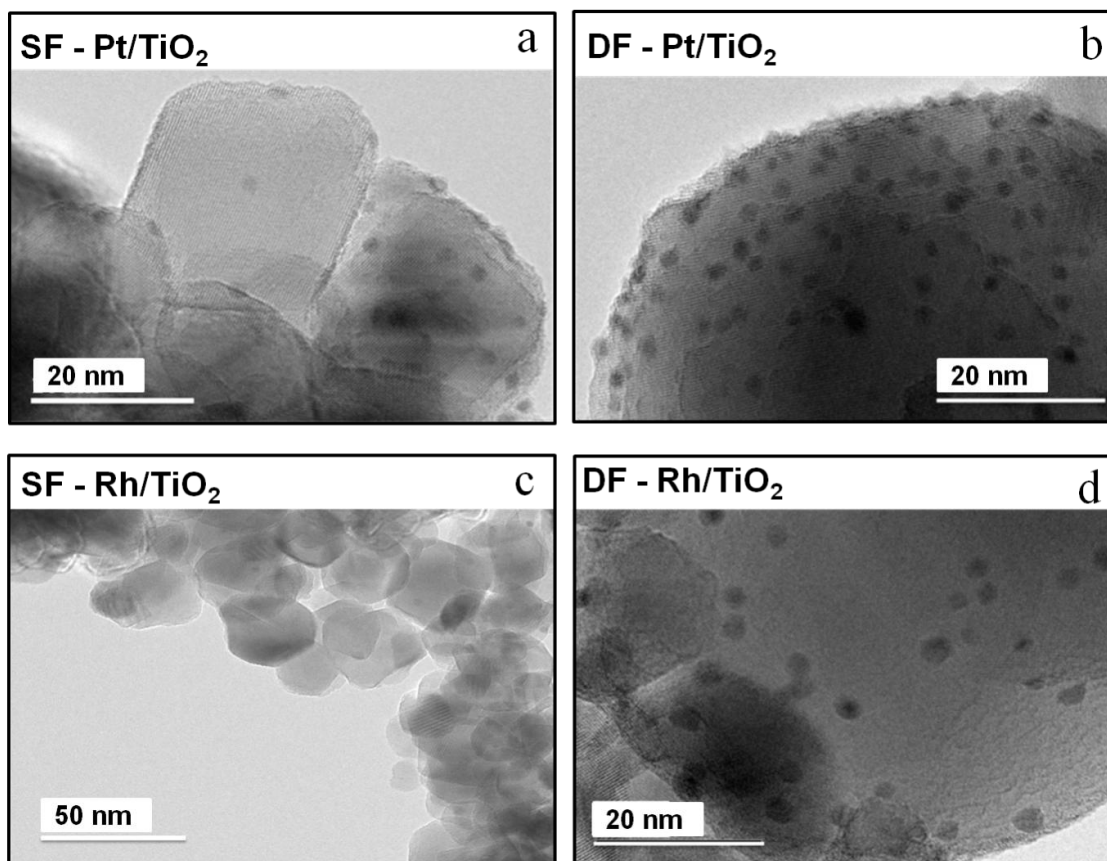
Figure 4.9: TEM images of TiO_2 supported Pt nanoparticles made by single flame (SF), and double flame (DF) spray pyrolysis and Rh nanoparticles made by double flame spray pyrolysis (DF) after the WGS reaction, recorded at Dalian Institute of Chemical Physic (DICP), Chinese Academy of Sciences (CAS) in Dalian/China.

XRD patterns of the Pt- and Rh-containing samples prepared by DF and SF are shown in Figure 4.10 and Figure A.6 (in Appendix). For both the Rh/TiO_2 and the Pt/TiO_2 catalysts the TiO_2 crystallite sizes were calculated from XRD reflection widths using the Scherrer equation (section 3.2.1). TiO_2 crystallite sizes (d_{TiO2}) calculated from anatase and rutile reflection, are summarized in Table 4.6 and Table A.1 (Appendix).
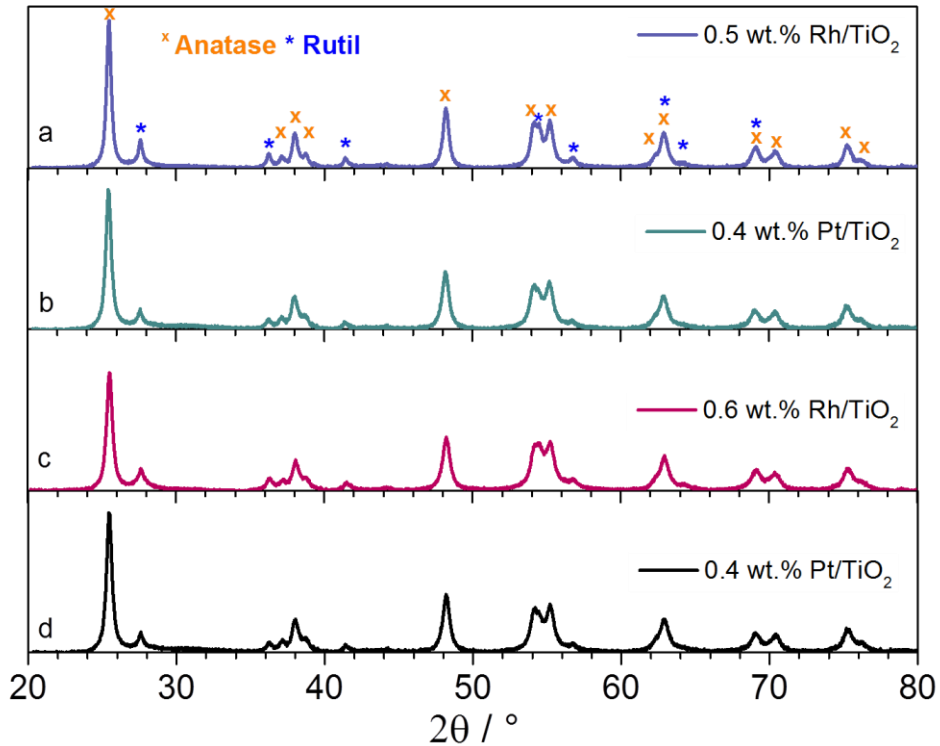
Figure 4.10: XRD diffraction patterns of double flame spray made Rh (a) and Pt (b) as well as single flame spray made Rh (c) and Pt (d) particles supported on TiO$_2$.

Table 4.6: TiO$_2$ crystallite sizes calculated from the reflection at $2\theta = 25.5°$ (anatase) and $2\theta = 27.5°$ (rutile) in the XRD patterns of Pt/TiO$_2$ and Rh/TiO$_2$.

		d$_{Anatase}$ [nm]	d$_{Rutile}$ [nm]
Single flame	0.4 wt.% Pt/TiO$_2$	18	<7
	0.6 wt.% Rh/TiO$_2$	17	<7
Double flame	0.4 wt.% Pt/TiO$_2$	20	8
	0.5 wt.% Rh/ TiO$_2$	21	8

The FSP made TiO$_2$ particles are completely crystalline since there is no amorphous background in the XRD pattern. As shown in Figure 4.10 and Figure A.6, catalysts with different Rh and Pt loading prepared by SF and DF show anatase/rutile reflections with the same anatase/rutile ratio. It has been reported that the transformation of anatase into rutile takes place at 600 °C and this temperature can be shifted to lower temperature by addition of foreign atoms [164, 166, 167]. Probably under these conditions anatase is the dominant phase with a small fraction of rutile. Similar observation were made by Teoh et al. [95]. They synthesized TiO$_2$ and Pt/TiO$_2$ catalysts

by single flame spray pyrolysis and found that the TiO_2 crystallites were predominant anatase with the remainder being rutile, and the rutile content was found to increase with increasing Pt loading [95]. In case of the catalysts prepared for this work the anatase and rutile crystallite sizes are slightly larger in the DF catalysts compared to the SF material, which is well reflected in results for the specific surface area. For instance, the specific surface area and the anatase crystallite size ($d_{Anatase}$) of 0.4 wt.% Pt/TiO_2 are 80 m^2/g and 18 nm for the SF and 70 m^2/g and 20 nm for the DF made catalysts, respectively. The rutile crystallites are smaller than anatase crystallites, which is in good agreement with the literature [95]. The larger anatase and rutile crystallite sizes in double flame made samples can again be attributed to longer residence time in the flame at high temperature. None of the XRD patterns in Figure 4.10 gives any evidence of metallic or metal oxide Rh and Pt phases. Since crystallite sizes below 5 nm cannot be distinguished from the background [113], these results are in good agreement with the particle sizes estimated from CO chemisorption data and TEM images, which show metallic particles with diameters between 2 and 3 nm.

Figure 4.11 shows Rh K-edge XANES spectra of the single flame made 0.6 wt.% Rh/TiO_2 and the double flame made 0.5 wt.% Rh/TiO_2 catalyst recorded during heating from room temperature to 400 °C (resp. 500 °C) in 5% H_2/He (50 mL/min). After reduction in H_2/He (1. run), the gas feed was switched to 5% O_2/He and the samples were cooled down to room temperature in this gas mixture. Afterwards, the samples were reduced again while recording Rh K-edge XANES spectra recorded (2. run). In Figure 4.11a and b the reduction behavior of the as prepared sample (first run) is compared with the reduction behavior of the reduced sample after reoxidation (second run). Correspondingly, the relative concentrations of oxidized species, determined by linear combination fitting using the initial and final spectra of the TPR series as reference spectra, are shown in Figure 4.12. In Figure 4.11a, no abrupt decrease in whiteline intensity could be observed in the spectra of the single flame made Rh/TiO_2 catalyst in the first run. The fitting results in Figure 4.12 show that the reduction of Rh proceeds continuously over a broad temperature range in this sample and at 280 °C ca. 50% of the Rh atoms have been converted into a metallic state. Before the second reduction cycle the sample was reoxidized in 5% O_2/He during cooling down. In the second TPR run, a significant change in reduction behavior was observed. Compared to the first run the temperature at which 50% of the Rh species are in a metallic state is shifted by 160 °C (to 120 °C), as shown in Figure 4.12.
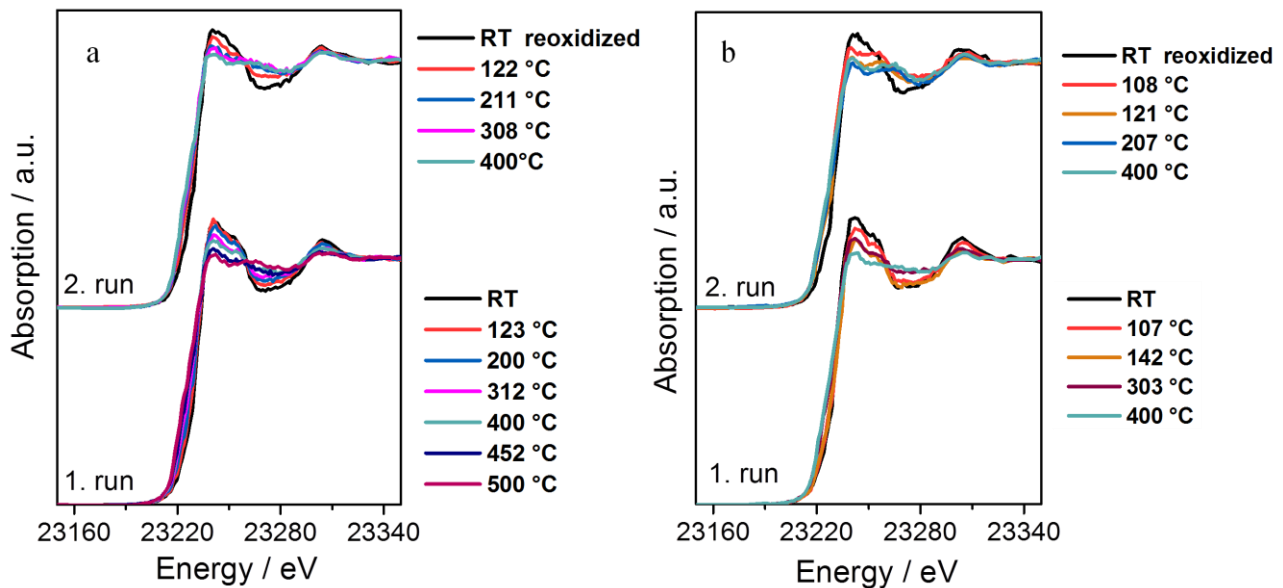
Figure 4.11: Comparison of the reduction behavior of TiO$_2$ supported Rh catalyst. XANES spectra of single flame made 0.6 wt% Rh/TiO$_2$ (a) and double flame made 0.5 wt% Rh/TiO$_2$ (b) during temperature programmed reduction in 5% H$_2$/He (total flow 50 mL/min).

The reduction temperature of the double flame made Rh/TiO$_2$ catalyst is lower compared to the single flame made catalyst. During the first TPR run a decrease in whiteline intensity in the spectra of the DF made catalyst can be observed at 140 °C (Figure 4.11b). The linear combination fitting results show that ca. 50% of the Rh species at 160 °C are in a metallic state. This sample was also reoxidized in oxygen during cooling down resulting in an increase in whiteline intensity (Figure 4.11b), and the reduction temperature for the second TPR run is shifted to lower temperature by ca. 80 °C (to 80 °C) compared to the first run. However, compared to single flame made Rh/CeO$_2$ catalysts (reduction temperature ca. 75 °C for 3.1 wt.% Rh/CeO$_2$ in section 4.1.3.2 and 114 °C for 4.3 wt.% Rh/CeO$_2$ in section 5.3.2) these single flame and double flame made Rh/TiO$_2$ catalysts exhibit a higher reduction temperature [112, 178]. Obviously, the support (CeO$_2$ or TiO$_2$) plays an important role in the reduction of Rh. A stronger interaction between Rh and TiO$_2$ support and likewise the concentration of Rh probably affects the reduction of the noble metal. The difference in reduction temperature between SF (at 280 °C, 50% of the Rh species are in a metallic state) and DF (at 160 °C 50% of the Rh species are in a metallic phase) made catalyst is ca. 100 °C for the first TPR run, probably due to higher noble metal dispersion in the single flame made materials. Stark et al. [179] compared the reduction behavior of flame made Pt (0 – 2 wt %) on Ce$_{0.5}$Zr$_{0.5}$O$_2$ and found also that platinum in small

concentrations with high dispersion on $Ce_{0.5}Zr_{0.5}O_2$ was much more difficult to reduce. They also observed that Pt during a second reduction could be much easier reduced as the particles had migrated to the surface. Activation of the flame made samples during the second run and the decrease in low temperature activity might be related to the change in the nature of the Rh constituent.
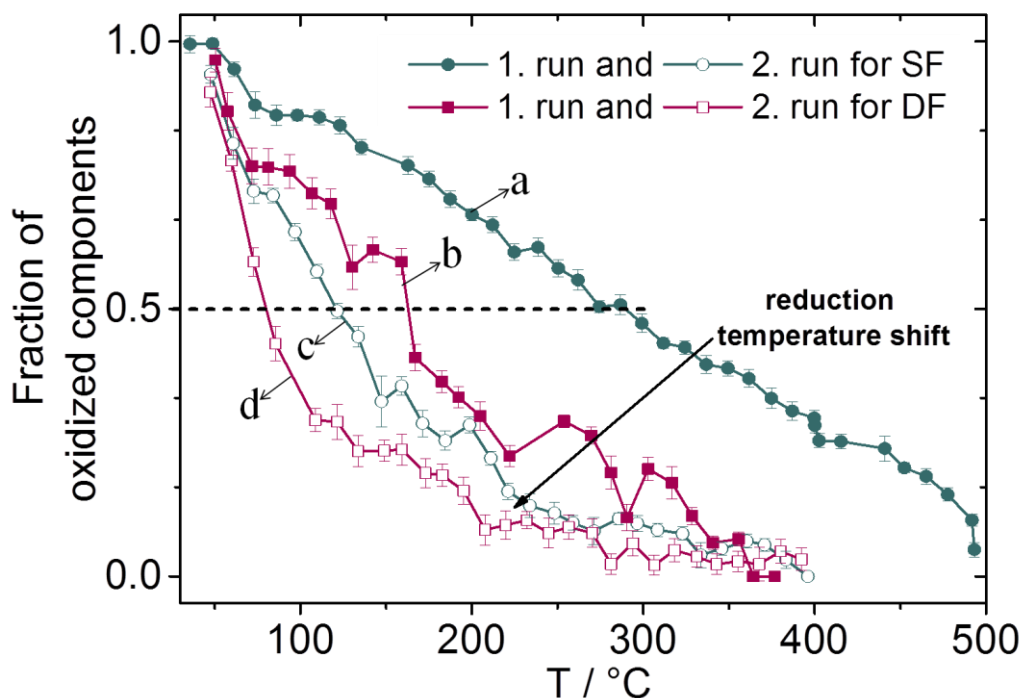
Figure 4.12: Changes in relative concentrations of oxidized Rh species during TPR obtained from linear combination fitting of XANES spectra. (a) First reduction of the SF made sample, (b) first reduction of the DF made sample, (c) second reduction of the SF made sample, and (d) second reduction of the DF made sample.

4.2.3.2 Catalytic Performance Tests

Figure 4.13 shows CO conversion over single and double flame made Pt/TiO_2 and Rh/TiO_2 catalysts as a function of temperature. These catalysts were tested in fixed bed reactor (section 3.4.1) without pretreatment in a product-free reaction gas mixture (5 vol.% CO, 20 vol.% H_2O, 75 vol.% He, GSVH = 150,000 mL/g_{cat} h). Similar reaction parameters were also used in previous studies (section 4.1.3.3) [112, 178, 180]. Figure 4.13a show that at 250 °C CO conversion over the Rh based materials is 0% for catalysts with low Rh loading and 5% for catalysts with higher Rh loading. First CO conversion increases slowly with increasing

temperature. At 350 °C the conversion rises significantly, especially for catalysts with higher Rh loading. Below 350 °C CO conversion is below 10% for the SF catalysts and the double flame catalyst with low loading. However, for the SF made 0.6 wt.% Rh/TiO_2 CO conversion increases from 12% (at 350 °C) to 64% (at 450 °C) and for the DF made 0.5 wt.% Rh/TiO_2 from 17% to 77%, respectively. The TPR results showed that the SF made 0.6 wt.% Rh/TiO_2 catalyst is reduced at higher temperature compared to the DF made 0.5 wt.% Rh/TiO_2 catalyst. The effect of easily reducible metal could also be observed in the catalytic performance data.
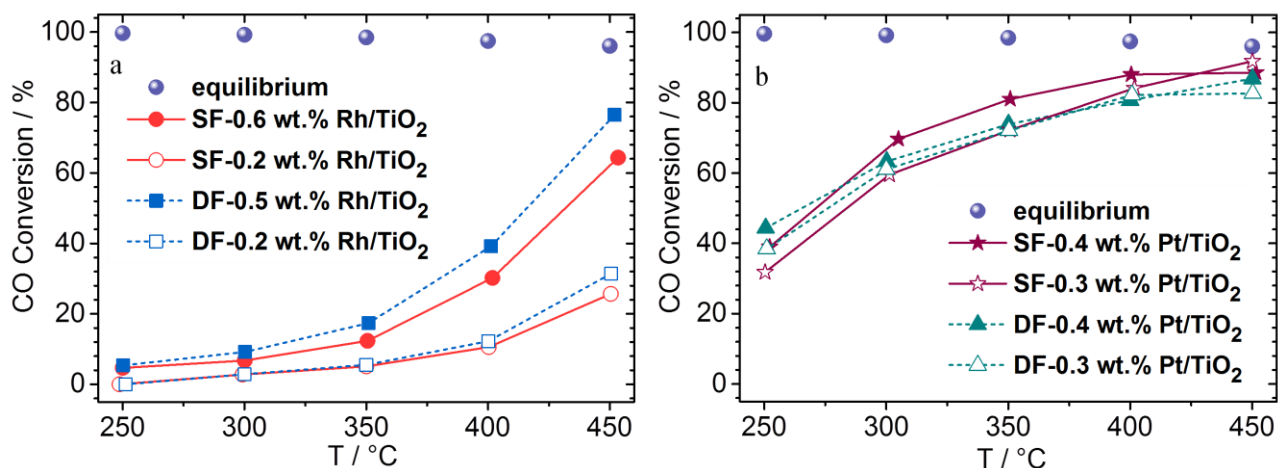
Figure 4.13: Effect of reaction temperature on the conversion of CO over single flame (SF) and double flame (DF) made Rh (a) and Pt (b) particles supported on TiO_2 (5 vol.% CO, 20 vol.% H_2O, 75 vol.% He total flow = 187.5 mL/min, m = 75 mg, GHSV = 150,000 mL/g_{cat} h).

According to Figure 4.13 for a specific loading the easily reducible DF made Rh based catalysts show higher activity compared to SF made catalyst, since the Rh particles might be located more on the surface (Figure 4.9c-d). The higher CO conversion at high temperature for DF made Rh based catalyst might be also caused by small Rh particle sizes (d_D = 3.3 nm for SF and d_D = 2.6 nm for DF). The effects of metal loading and preparation method on the activity of the Pt based counterparts are shown in Figure 4.13b. At 250 °C the double flame made 0.4 wt.% Pt/TiO_2 catalyst shows higher activity compared to the double flame made 0.3 wt.% and both single flame made Pt/TiO_2 catalysts. Above 300 °C CO conversion over the double flame made Pt based catalysts is similar. Interestingly, at high temperature the activity of the SF made 0.3 wt.% Pt/TiO_2 catalyst reaches the same level as the double flame made Rh based catalysts. This might be due to the effect of metal dispersion (64%) and high surface area (81 m^2g^{-1}) on

catalytic activity. In the whole temperature range the Pt based catalysts show higher activity compared to the Rh based catalysts. Panagiotopoulou et al. [169] prepared different catalysts by impregnation of commercially obtained titanium dioxide powder and used Pt, Rh, Ru and Pd as noble metals. They also observed that a 0.5 wt.% Pt/TiO_2 catalyst showed higher activity compared to a 0.5 wt.% Rh/TiO_2 catalyst. However, these Pt based catalysts showed lower activity at 250°C compared to flame made catalysts prepared in this work and both catalysts show higher activity at high temperature than flame made catalysts prepared for this study. Note that the gas hourly space velocity (GSVH = 150,000 mL/g h) for this study is higher than in the case of Panagiotopoulou et al. (GSVH = 120,000 mL/g h) [169]. The effect of contact time on the degree of CO conversion was investigated in previous studies [31, 178]. A noticeable change in CO conversion at different temperatures was observed. It was found that increasing GHSV leads to in a decrease in catalyst performance. In previous study (in section 4.1.3.3) single flame made 1.9 wt.% Rh/CeO_2 and 1.7 wt.% Pt/CeO_2 were tested under similar reaction conditions. These catalysts showed higher activity at low temperature compared to single flame TiO_2 supported noble metal catalysts. For instance CO conversion at 250 °C was ca. 30% for 1.9 wt.% Rh/CeO_2 and ca. 80% for 1.7 wt.% Pt/CeO_2. It should be considered that the time (GSVH = 50,000 mL/g h) was much shorter and the noble metal loading was rather higher. Miao et al. investigated Pt (0.73 − 0.82 wt.%) based catalyst with different supports, such as hydroxyapatite ($Ca_{10}(PO_4)_6(OH)_2$, HAP), fluoroapatite (FAP) and CeO_2 under the same reaction parameters as in this study [180]. At 250 °C the CO conversion was ca. 20% over Pt/CeO_2, almost 0% over Pt/HAP (pH value 9) and less than 10% over Pt/FAP. In this work, the conversion of CO at 250 °C is 39% and 32% for single flame and 38% and 44% for double flame made Pt/TiO_2 catalysts, respectively. Indeed, according to ref. [180] the Pt/HAP catalysts show higher activity at high temperature and reach the equilibrium point, except Pt/HAP with pH value 9 and 9.5. Note that in this study the Pt loading is lower, indicating that the TiO_2 supported flame made catalysts exhibit promising catalytic performance for the WGS reaction.

For further investigations the Rh/TiO_2 and the Pt/TiO_2 catalysts were reduced in 5% H_2/He at 500 °C prior to catalytic tests. These tests were performed using the quartz capillary micro reactor set-up (section 3.4.2). The experimental procedures are described in section 4.2.2. These experiments show the effects of the pre-treatment on the catalytic activity, since the TPR experiment suggested that the Rh particles had migrated to the surface during second reduction.
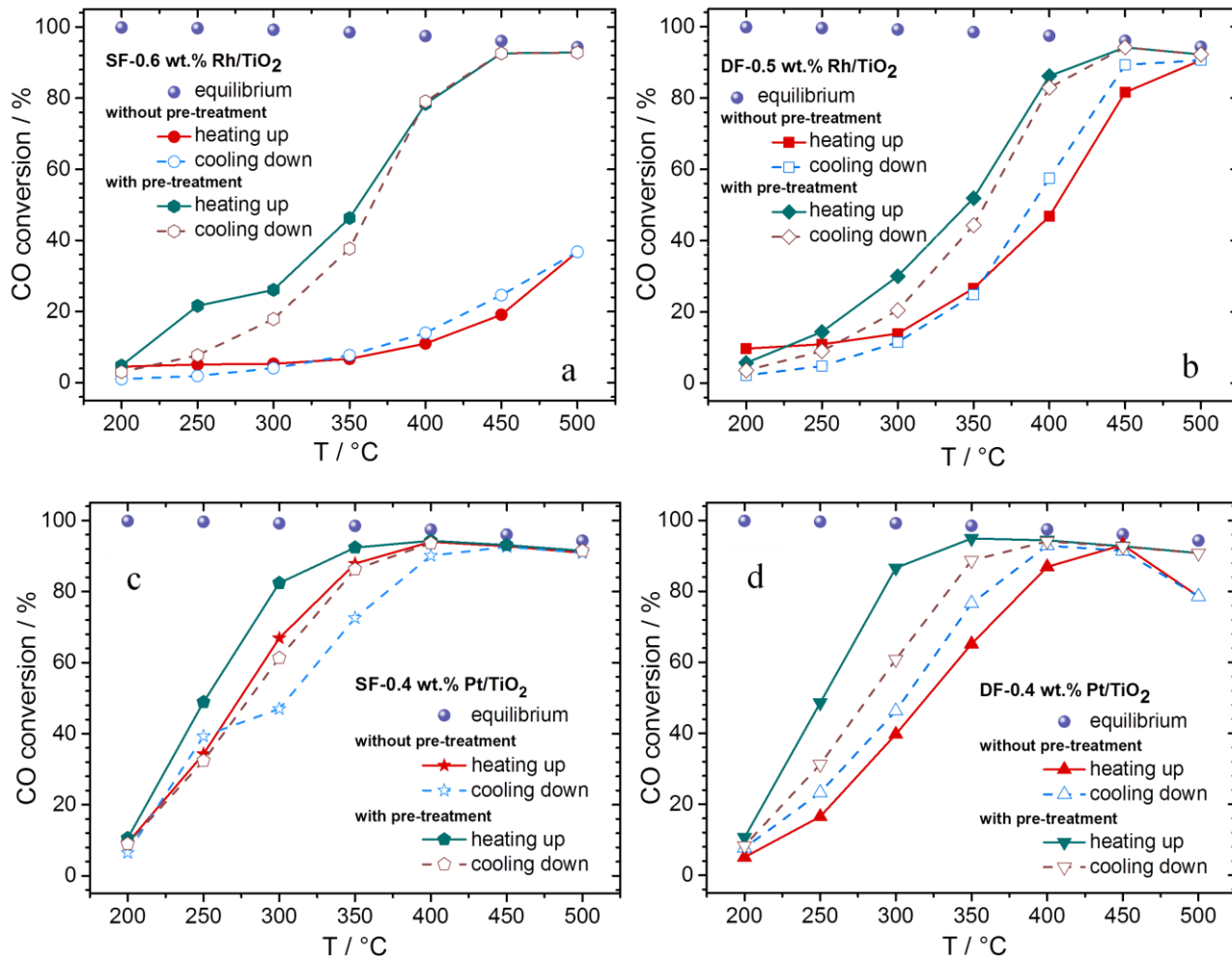
Figure 4.14: CO conversion over reduced and as prepared Rh/TiO$_2$ (a, b) and Pt/TiO$_2$ (c, d) catalysts as a function of temperature. Reaction parameters: S/C = 4, total feed flow = 50 mL/min, m = 60 mg, GHSV = 50,000 mL/g$_{cat}$ h (reaction gas mixture: 5 vol.% CO, 20 vol.% H$_2$O, and 75 vol.% He).

Figure 4.14 shows CO conversion over reduced and as prepared Rh/TiO$_2$ and Pt/TiO$_2$ catalysts under WGS conditions (S/C = 4, GHSV = 50,000 mL/g h). For the SF made 0.6 wt.% Rh/TiO$_2$ without reduction (Figure 4.14a) CO conversion is 5.5% at 300 °C and 37% at 500 °C, however after pre-treatment CO conversion for this catalyst increases abruptly to 26% at 300 °C and to 93% at 500 °C (ca. at the equilibrium point, Figure 4.14a). This might be caused by migration of Rh particles to the surface where they are easily accessible for WGS. In case of the DF-0.5 wt.% Rh/TiO$_2$ the reduction of the catalyst was facilitated compared to the single flame made material (Figure 4.12). This might be caused by preferential deposition of Rh particles on the surface during preparation. Therefore, the active Rh particles were easily accessible for WGS reaction.

This implies that during preparation by single flame spray pyrolysis Rh^{3+} ions are substituted into the TiO_2 lattice (Rh^{3+} = 66 pm and Ti^{4+} = 60 pm [181]). Teoh et al. [95] reported that in single flame process it is possible by substitution of Ti^{4+} by Pt^{4+}, due to similarity in ionic radius (Pt^{4+}=62 pm, and Ti^{4+} = 60 pm [181]). In case of double flame spray pyrolysis the substitution is diminished, since the noble metal and support particles formed separately. Still, in case of DF made 0.5 wt.% Rh/TiO_2 catalyst pre-reduced at 500 °C leads to further improvement of the WGS activity (Figure 4.14b). For instance at 350 °C CO conversion over the pre-treated sample is 52% compared to 27% over as-prepared sample and in both cases (with and without pre-treatment) CO conversion reaches the equilibrium curve at 500 °C. This could be caused by an increased susceptibility to reduction due to the presence of CO, since the DF method avoids encapsulation of the particles. In our previous studies [178] Rh/CeO_2 was investigated *in situ* under WGS reaction conditions using XAS. The results showed that at 200 °C the Rh species are in a reduced state under WGS reaction conditions. The Rh/TiO_2 catalysts exhibit similar activity during heating up and cooling down cycles which indicates for their stability. Besides the substitution of Rh ions in the TiO_2 lattice, the phenomenon of strong metal support interaction (SMSI) can also be critical relevance. As discussed in section 4.2.1, this phenomenon occurs when the catalyst is reduced at higher temperature (> 300 °C) and thus affects the catalytic activity [182]. Since the conversion of CO over SF made 0.6 wt.% Rh/TiO_2 (Figure 4.14a) is extremely low, it is possible that a strong SMSI could be induced during WGS. It is also conceivable that a strong SMSI exists before reduction and is attenuated after reduction. In case of DF made 0.5 wt.% Rh/TiO_2 the SMSI could be weak (if it exists) and can be reversed under WGS reaction conditions at high temperature. CO conversion measurements over the SF made 0.4 wt.% Pt/TiO_2 catalyst provide similar results with and without pre-treatment and up to 400 °C CO conversion almost reaches the equilibrium curves in both cases (before and after reduction, Figure 4.14c). Azzam et al. [182] investigated the deactivation of Pt/TiO_2 catalysts and excluded any influence of SMSI on these materials. As a conclusion, for SF-0.4 wt.% Pt/TiO_2 SMSI does not occur. In case of the double flame made 0.4 wt.% Pt/TiO_2 (Figure 4.14d) significant differences in CO conversion with and without pre-treatment is observed (e.g. at 350°C ca. 48% and 87% over this catalyst respectively). A similar trend is also observed for DF made 0.5 wt.% Rh/TiO_2. The catalytic performance of Pt/TiO_2 catalysts shows similar performance to Pt/CeO_2 and $Pt/Ce_xZr_{1-x}O_2$ catalysts independent of the preparation methods (discuss later in section 4.3.3.2). For instance, at 350 °C CO conversion was 81% for SF-Pt/TiO_2, 77% for Pt/CeO_2 catalyst and 94%

$Pt/Ce_xZr_{1-x}O_2$ catalyst. Note that the Pt loading on TiO_2 (0.4 wt.%) is lower than Pt on CeO_2 (0.94 wt.%) and $Ce_xZr_{1-x}O_2$ (0.76 wt.%).
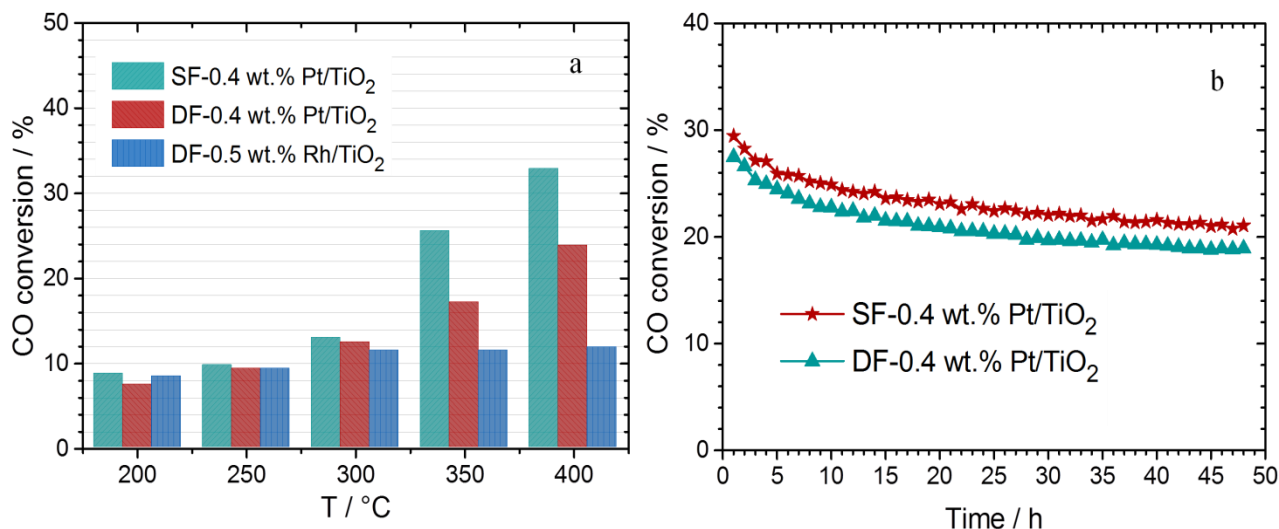
Figure 4.15: (a) CO conversion as a function of temperature over Pt (SF and DF) and Rh (DF) particles supported on TiO_2 and (b) CO conversion at 400 °C as a function of time for SF and DF made Pt based catalysts (60 mg of sample, 10 vol.% CO, 10 vol.% CO_2, 20 vol.% H_2O, 40 vol.% H_2, 20 vol.% He, total flow 50 mL/min, GHSV = 50,000 mL/g_{cat} h).

DF made 0.5 wt.% Rh/TiO_2, DF made 0.4 wt.% Pt/TiO_2 and SF made 0.4 wt.% Pt/TiO_2 were investigated further under WGS operating conditions, i.e. in a 10 vol.% CO, 10 vol.% CO_2, 20 vol.% H_2O, 40 vol.% H_2, 20 vol.% He feed gas (S/C = 2) and the results are shown in Figure 4.15a. In general, Pt based catalysts were more active. At 350 °C CO conversion is 25.5% for SF made 0.4 wt.% Pt/TiO_2, 17% for DF made 0.4 wt.% Pt/TiO_2 and 11.4% for DF made 0.5 wt.% Rh/TiO_2. The SF made Pt based catalyst is more active than the DF made Pt catalyst. A similar behavior is also observed in product-free gas mixture (Figure 4.13b, Figure 4.14c-d). The reason can be traced back to the phenomenon of strong metal support interaction, as discussed above: For the SF 0.4 wt.% Pt/TiO_2 catalysts the SMSI can be excluded and in case of DF made 0.4 wt.% Pt/TiO_2 it is possible that a weak SMSI occurs. Thinon et al. [29] investigated 1.9 wt.% Pt/TiO_2 under similar reaction conditions (10% CO, 10% CO_2, 20% H_2O, 30% H_2, 30% Ar; S/C = 2; GHSV = 60,000 mL/g h) and measured CO conversion at around 58% at 350 °C which is much higher compared to the flame made Pt based catalysts prepared for this work. Note that compared to Thinon´s work (1.9 wt.% Pt/TiO_2) the noble metal loading of flame made catalysts (0.4 wt.% Pt/TiO_2) in this work is much lower [29]. This reveals that the flame made Pt based

catalysts show higher activity. SF-0.4 wt.% Pt/TiO_2 has excellent activity in WGS (67% at 300 °C).The stability time on the stream of the catalysts needs to be taken into account for catalysts application. Under WGS reaction conditions at 400 °C the flame made Pt based catalysts were studied for 48 h. The results are shown in Figure 4.15b. The Pt based catalysts were subjected to stability tests since they show higher performance compared to Rh based catalysts (Figure 4.14). A slight deactivation (≈30% for both catalysts) was observed under these steady state conditions. For SF and DF made Pt/TiO_2 catalysts CO conversion decreased continuously from 29.5% and 27.5% to 21% and 19% at the end of a 48 h run, respectively. Azzam et al. [171] studied the catalytic activity of Pt/TiO_2 catalysts (prepared by wet impregnation of commercially available TiO_2) as a function of time and observed after 20 h of testing that the catalysts lost about 40% of their initial activity. Zhu et al. [52] studied the activity and stability of Na promoted Pt/TiO_2 and reported that at 300 °C CO conversion decreased continuously from 75.2% to 52.3% after 20 h (feed gas $= CO + H_2O$; GHSV $= 15000$ mL/g h), i.e. hence ≈ 30% deactivation. The results for the flame made catalysts prepared for this study show a slowly progressing decrease in CO conversion over time. The catalysts are obviously much remarkably since compared to other studies the time for the tests is longer, the temperature higher and the test is performed in a typically reformer feed gas. The decrease in activity with time might be caused by deactivation of Pt or the oxide (support), or both since oxide supported noble metal catalysts are bifunctional in the WGS reaction [21, 62, 170, 183]. However, Azzam et al. [171] reported that the deactivation of Pt/CeO_2 catalysts was caused by formation of stable carbonate species on the ceria surface leading to self-poisoning. In case of Pt/TiO_2 catalysts carbonates were not stable on the titania surface under WGS reaction conditions. Azzam et al. [171] observed that the Pt particles had an average size of 1.2 nm before the 20 h activity test, which increased to 2.7 nm after the test. They considered that this might be due to Pt sintering and a decrease in metal surface area. The TEM images (Figure 4.9) of flame made catalysts were recorded after the WGS reaction (Figure 4.13) and the results show no sintering of the noble metal particles (Pt and Rh). Accordingly these catalysts are stable. Based on stability test results in this study, the Pt particles might sinter in the reformer gas mixtures, since a slight decrease in CO conversion were observed.

4.2.4 Conclusion

In this work catalysts with different loadings of Pt and Rh on titania were synthesized and the catalysts with low loading showed higher dispersion. Flame made TiO_2 supported Pt and Rh catalysts exhibit high surface areas, high dispersion and fairly small nanoparticle sizes (1.8–3.3 nm) as evidenced by complementary TEM and CO-chemisorption. Compared to DF made materials (70 and 67 m^2g^{-1}) SF made catalysts show slightly higher surface areas (80 and 79 m^2g^{-1}), which is well reflected by the larger crystallite size of DF made samples. All flame made TiO_2 supports are highly nanocrystalline Moreover, generally the catalysts prepared by double flame spray pyrolysis exhibited a slightly higher dispersion of noble metals on the support after reduction. The XANES features in the spectrum of the reduced Rh species and the corresponding linear combination fitting results show that for single flame made Rh based catalysts the reduction temperature (at 280 °C about 50% Rh species in metallic phase) is significantly much higher compared to double flame made catalysts (at 160 °C about 50% Rh species in metallic phase). After an oxidation treatment these temperatures were shifted in both cases by ca.100 °C to lower temperature. However, the reduction temperature for the SF catalyst is still high (120 °C) and for the DF made Rh/TiO_2 close to the reduction temperature of Rh/CeO_2. Potentially, the Rh particles are encapsulated in the lattice, and might be migrated to the surface after treatment.

The titania supported Rh and Pt catalysts were tested in a fixed bed reactor and in a quartz capillary micro reactor. In general, independent of preparation methods the Pt based catalysts showed higher activity compared to the Rh based catalysts, especially at low temperature. DF made Rh based catalysts showed slightly higher CO conversion compared to SF made catalysts in the fixed bad reactor, whereas Pt based catalysts showed similar behavior. The low CO conversion over SF made Rh/TiO_2 catalysts could be caused of either by the substitution of Rh ions in the TiO_2 lattice or by SMSI. Furthermore, all catalysts were reduced prior to the WGS reaction and then tested in the quartz capillary micro reactor. The comparison of CO conversion between reduced and non-reduced catalysts showed huge differences for Rh/TiO_2 catalysts, implying that the Rh particles immigrated to the surface which is good agreement with TPR results. The DF made Rh based and all Pt based catalysts show similar catalytic activities before and after H_2 pretreatment. Furthermore, it seems that all catalysts after H_2 treatment reach the

equilibrium points at high temperature. In general the activity of Rh and Pt based catalysts for WGS reactions was related to the preparation methods and pre-treatment conditions, especially for Rh/TiO$_2$ catalysts the preparation method plays a major role.

4.3 Screening of Ceria, Zirconia and Ceria-Zirconia Supported Noble Metal Catalysts

4.3.1 Introduction

It is well-known that ceria can easily switch between the oxidation states Ce^{3+} and Ce^{4+}. Due to storage and release of oxygen in CeO$_2$ it found its primary application in catalysis as an oxygen carrier as already discussed in section 4.1.1. The redox properties can be enhanced by replacing some cerium cations with foreign cations, such as zirconium [38, 184]. Furthermore, modification of the ceria lattice with Zr cations (Ce$_x$Zr$_{1-x}$O$_2$) leads to higher thermal stability and to enhanced catalytic performance in exhaust gas after treatment compared to pure ceria and zirconia [185, 186]. Zirconium has a small ionic radius (0.72 Å for Zr^{4+} compared to 0.92 Å for Ce^{4+}) and introduces lattice strain which promotes the formation of oxygen vacancies and the reduction of Ce^{4+} to Ce^{3+} [38, 181, 187].

Zirconium dioxide is applied as white pigment, mainly for porcelain and also for ceramics since ZrO$_2$ is thermally, chemically and mechanically resistant [3]. The crystal structure of CeO$_2$ was briefly discussed in section 4.1.1. Zirconium dioxide has a distorted fluorite type-structure and the coordination number is smaller (CN = 7) compared to the fluorite type-structure (CN = 8) [3]. The small coordination number can be attributed to the small ionic radius (0.84 Å) [137]. The crystal system of Ce$_x$Zr$_{1-x}$O$_2$ depends on the compositional region of x ($0 \leq x \leq 1$). The best composition for oxygen storage capacity is attributed to Ce$_x$Zr$_{1-x}$O$_2$ with x > 0.5 [186]. The surface area of Ce$_x$Zr$_{1-x}$O$_2$ synthesized by conventional methods, such as co-preparation or sol-gel, is in the range between 60 and 90 m^{2}g^{-1} after calcination at temperatures between 700 and 800 K [188, 189]. On the other side, FSP synthesis of Ce$_x$Zr$_{1-x}$O$_2$ results in high surface area with high temperature stability, e.g. the surface area of Ce$_x$Zr$_{1-x}$O$_2$ (x = 0.1 − 0.9) is 130 − 170 m^{2}g^{-1} for as prepared samples and 82 − 68 m^{2}g^{-1} (x = 0.3, 0.5 and 0.7) for calcined sample at ~1170 K [190].

4.3.2 Experimental Part

Ceria, zirconia and ceria-zirconia supported Rh and Pt catalysts were prepared as described in section 3.1. Catalytic screening was performed in a tubular reactor (Figure 3.7 in section 3.4.1) as well as in the quartz capillary micro reactor (Figure 3.8, in section 3.4.2).

In case of the tubular reactor the catalytic activity was tested at atmospheric pressure and temperatures between 250 and 450 °C. 75 mg catalyst powder as 100–250 µm sieved fraction were filled into the quartz glass tube. A feed stream of 187.5 mL/min consisting of 5 vol.% CO, 20 vol.% H_2O and 75 vol.% He balance (GHSV of 150,000 mL/g_{cat} h) was used. Furthermore the same 100–250 µm sieved catalysts were diluted with 400 mg quartz sand in the same grain size range and used for the measuring the reaction rates. The samples were pretreated in a product-free feed (5% CO, 20% H_2O, 75% He) mixture at 400 °C for 12 h. The amount of catalyst was varied to limit CO conversion to 20% at maximum and a feed stream of 15 vol.% CO, 5 vol.%CO_2, 30 vol.% H_2O, 40 vol.% H_2 and 10 vol.%N_2 in order to determine the reaction rates r_{cat} based on the total catalyst weight between 300 and 400 °C, similar as in [191].

For the catalytic screening test in the quartz capillary micro reactor (3 mm diameter) the reactant gases had steam to CO ratios S/C = 2 and S/C = 4. 60 mg catalyst powder as 100–250 µm sieved fraction were used and exposed to a feed gas (total flow 50 mL/min) of 5% CO, 10% H_2O and 85% He for S/C = 2 and 5 vol.% CO, 20 vol.% H_2O and 75 vol.% He for S/C = 4 (GHSV = 50,000 mL/g_{cat} h). The catalytic performance of the catalysts was investigated in a temperature range between 150 and 450 °C and the outlet gas composition was analyzed in 50 °C intervals during heating up and cooling dawn. These performance tests were repeated after reaching 150 °C (light off temperature measurements). Catalyst stability was investigated by treating the fresh catalysts (60 mg) in the reformate gas stream at 400 °C for 48 h. The formate gas stream consisted of 10 vol.% CO, 10 vol.%CO_2, 20 vol.% H_2O, 40% H_2 and 20% He, resulting in a GHSV of 50,000 mL/g_{cat} h.

4.3.3 Results and Discussion

4.3.3.1 Structural Properties

Table 4.7 summarizes structural properties of the catalysts prepared by single and double flame spray pyrolysis based on different characterization methods. The calculated Rh and Pt loading was 1 wt.% for all catalysts. However, according to elemental analysis measured by ICP-OES (section 3.2.6) the noble metal loading varied between 0.70 and 0.95 wt.%. A discrepancy between calculated and measured metal loading after preparation was also observed in the literature [179]. The Rh based and Pt based catalysts show similar surface areas ranging from 91 to 136 m^2g^{-1}. Among these catalysts the mixed oxide ($Ce_xZr_{1-x}O_2$) supported catalysts prepared by SF have the highest surface area (136 m^2g^{-1}). Strobe et al. [192] prepared Pt/Ba/$Ce_xZr_{1-x}O_2$ by double flame spray and observed specific surface area around 90 m^2g^{-1} which increased slightly with increasing ceria content. The surface area of Rh/$Ce_xZr_{1-x}O_2$ prepared by single flame spray pyrolysis was 106 m^2g^{-1} [193]. In general the results in the Table 4.7 for the specific surface area are in good agreement with the literature. The BET results show that the SF made catalysts exhibit higher surface areas compared to the corresponding DF made materials, in accordance with the literature [98, 177]. For instance the specific surface area of Rh/$Ce_xZr_{1-x}O_2$ is 136 m^2g^{-1} for the SF made catalyst and 105 m^2g^{-1} for the material prepared by DF. A difference in surface area of SF and DF made catalysts was also observed in case of TiO_2 supported noble metal catalysts as already discussed in section 4.2.3.1. The reason for these differences can be attributed to different temperature distributions in SF and DF set-ups. Noble metal particle dispersion was determined using low temperature CO chemisorption for all prepared catalysts, apart from the ZrO_2 supported materials. These dispersion results provide an indicator for the noble metal cluster size. The obtained values for dispersion and particle size are included in Table 4.7. Ceria and ceria/zirconia supported noble metals exhibit dispersion between 36 and 49%. The particle diameters estimated from the dispersion are 3.0 nm for SF and DF made Pt/CeO_2, and 2.2 and 2.6 nm for SF and DF made Rh/CeO_2, respectively. For SF and DF prepared mixed oxide supported Pt and Rh samples similar results are obtained (2.5 − 3.0 nm). The particle diameters estimated from the dispersion for SF and DF made Pt/$Ce_xZr_{1-x}O_2$ are in accordance with TEM results ($d_D = 2.8$ nm and $d_{TEM} = 2.1$ nm for SF made Pt/$Ce_xZr_{1-x}O_2$ and $d_D = 2.5$ nm and $d_{TEM} = 2.0$ nm for DF made Pt/$Ce_xZr_{1-x}O_2$). The TEM images of SF and DF made Pt/$Ce_xZr_{1-x}O_2$ are shown in Figure A.7 in the Appendix.

Table 4.7: Chemical composition of the produced catalysts, BET specific surface areas (S_{BET}), dispersion and metal particle diameters (obtained from TEM and dispersion) of the samples prepared by double flame (DF) and single flame (SF) spray pyrolysis.

Noble metal	Support	Method	Loading [wt.%]	S_{BET} [m^{2}g^{-1}]	Dispersion [%]	d [nm]
Pt	CeO$_2$	SF	0.94	105	37	3.0[a]
		DF	0.90	91	36	3.0[a]
	ZrO$_2$	SF	0.84	119	-	1.5[b]
		DF	0.95	97	-	< 2[b]
	Ce$_x$Zr$_{1-x}$O$_2$	SF	0.81	136	40	2.8[a] (2.1[b])
		DF	0.76	117	44	2.5[a] (2.0[b])
Rh	CeO$_2$	SF	0.70	106	49	2.2[a]
		DF	0.70	94	42	2.6[a]
	ZrO$_2$	SF	0.94	110	-	3.8[b]
		DF	0.89	100	-	2.3[b]
	Ce$_x$Zr$_{1-x}$O$_2$	SF	0.89	136	41	2.7[a]
		DF	0.70	105	37	3.0[a]

[a] calculated using metallic dispersion; [b] obtained from TEM images
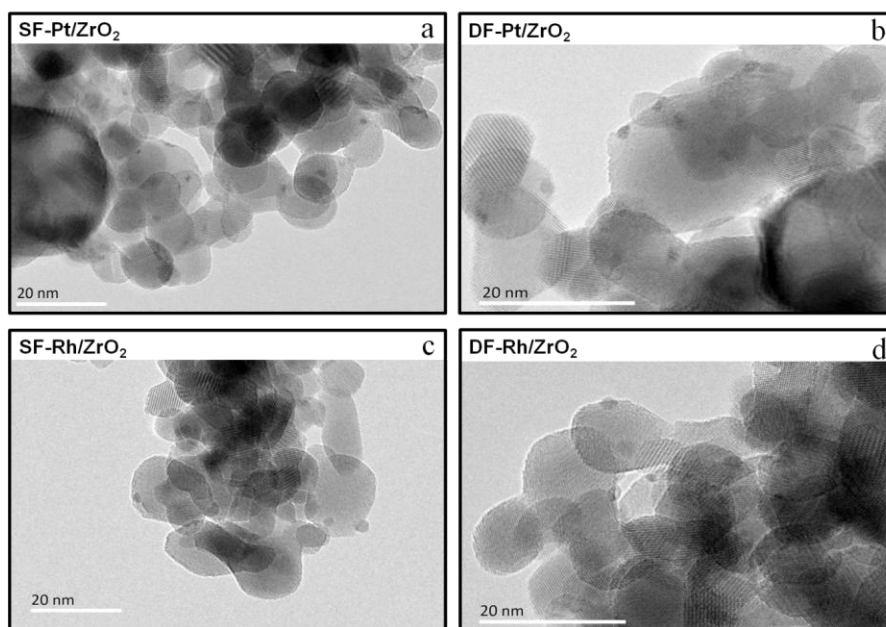
Figure 4.16: TEM images of ZrO$_2$ supported Pt (a-b) and Rh (c-d) nanoparticles made by single flame (SF), and double flame (DF) spray pyrolysis after WGS reaction, recorded at Dalian Institute of Chemical Physic (DICP), Chinese Academy of Sciences (CAS) in Dalian/China.

The dispersion of Rh and Pt on ZrO_2 could neither be determined by low temperature CO chemisorption nor by adsorption–desorption of CO chemisorption which resulted in unexpectedly large amounts of CO. This is probably due to carbonate species on the zirconia surface being responsible for an unrealistically large CO adsorption as a result of CO spillover onto the support. Perrichon et al. [120] investigated dispersion of Pt particles on CeO_2, ZrO_2 and $Ce_xZr_{1-x}O_2$ by chemisorption of H_2 and CO. They used IR spectroscopy to detect CO chemisorption in order to quantitatively analyze the adsorbed/desorbed gas molecules and found evidence for coordination of CO molecules on the metal particles [120]. The H_2 chemisorption was based on the use of a double isotherm at 195 K where hydrogen spillover on the support is suppressed [120]. Both methods allow to discriminate the adsorption on the Pt surface from the adsorption on the CeO_2, ZrO_2 and $Ce_xZr_{1-x}O_2$ supports. Menegazzo et al. [194] determined the dispersion of Au particles on ZrO_2 by CO chemisorption using a pulse flow system at 157 K on pre-hydrated samples where gold particles could not be detected by TEM. In contrast to this work, Pt and Rh particle sizes could be determined by TEM. TEM images of SF and DF made ZrO_2 supported Rh and Pt samples are shown in Figure 4.16. The particle sizes estimated from these measurements are 1.5 nm for the SF made and ca. 2.0 nm for the DF made Pt/ZrO_2 catalysts whereas Rh particles on ZrO_2 had diameters of 3.8 and 2.3 nm for SF and DF, respectively. According to the particle sizes determined by TEM, the Pt dispersion on ZrO_2 is 65% for SF and 50% for DF materials which is higher compared to Rh dispersion (SF = 30%, DF = 45%). The flame made Pt/ZrO_2 catalyst exhibits higher Pt dispersion compared to literature [195].

The phase composition of Pt and Rh based catalysts was further analyzed by XRD, and the results are shown in Figure 4.17 and Figure A.9 (Appendix). The crystallite sizes of the support were estimated using the Scherrer equation (section 3.2.1) and summarized in Table 4.8. The crystal phases of SF and DF made CeO_2 and ZrO_2 supported catalysts is similar. However, differences in crystallite size between catalysts prepared by SF and DF were observed as expected from BET surface area analysis. Compared to SF catalysts (e.g. 11 nm for Pt/CeO_2), DF made catalysts (e.g. 13 nm for Pt/CeO_2) exhibit higher crystallite sizes (Table 4.8). These results are in line with the previous studies (section 4.1 and 4.2).
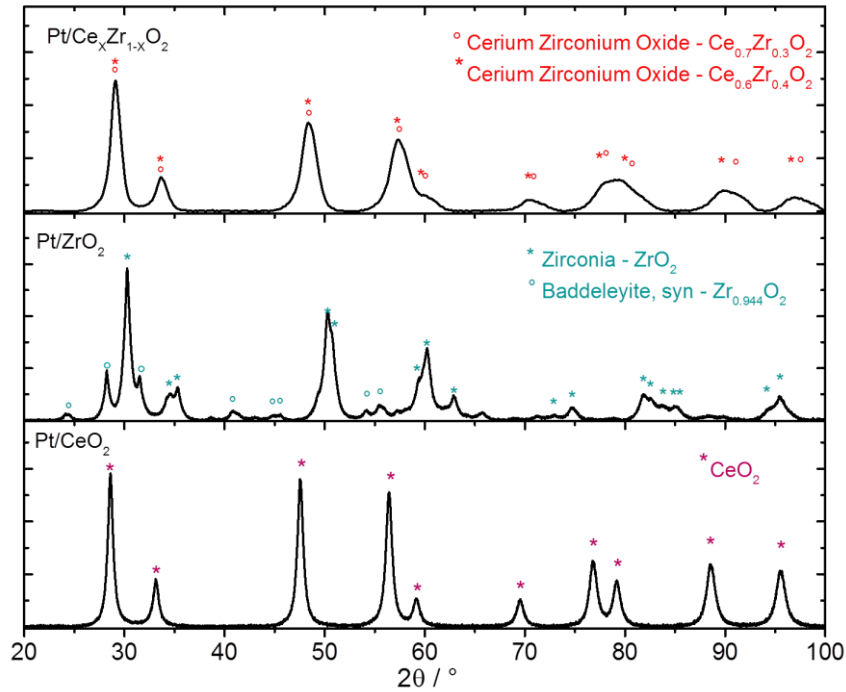
Figure 4.17: XRD diffraction patterns of double flame spray made CeO_2 (bottom), ZrO_2 (middle) and $Ce_xZr_{1-x}O_2$ (top) supported Pt catalysts (obtained from ICDD (The International Centre for Diffraction Data) Database).

Table 4.8: Crystallite sizes estimated from the XRD reflection at $2\Theta=29.2°$ for cerium-zirconium oxide, from the reflex at 28.6° for CeO_2 and from the reflex at 30.3° for ZrO_2 in the XRD patterns Pt and Rh based samples.

Support	Method	Crystallite size (support) [nm]	
		Pt	Rh
CeO₂	SF	11	11
	DF	13	12
ZrO₂	SF	10	10
	DF	11	11
Ce$_x$Zr$_{1-x}$O₂	SF	<7	<7
	DF	<7	<7

The XRD pattern of SF and DF CeO_2 show reflection to the fluorite type of ceria, which is also observed previous studies (section 4.1.3.1 and 5.3.2). In case of ZrO_2, Mueller et al. [196] synthesis of zirconia nanoparticles by flame spray pyrolysis and reported that the crystal structure consisted of tetragonal phase and monoclinic phase. The appeared reflection in their XRD pattern is in agreement with our work, this implies that the SF and DF made ZrO_2 supported catalysts

consists of tetragonal (denoted Zirconia in Figure 4.17) and the monoclinic (denoted Baddeleyite in Figure 4.17) phase compositions. Normally, ZrO_2 has a monoclinic structure at room temperature and atmospheric pressure, which transforms to a tetragonal structure at about 1100°C and then to a fluorite-type cubic structure at 2370°C [197, 198]. In contrast, in case of mixed oxide the assignment of phase composition was more demanding. The phase of the mixed oxide could not be clearly identified since different Ce:Zr ratios show similar reflections. The XRD patterns of these samples indicate varying Ce:Zr rations. According to database the obtained phases correspond to Ce:Zr = 0.81:0.19 and Ce:Zr = 0.6:0.4 for SF and Ce:Zr = 0.7:0.3 and Ce:Zr = 0.6:0.4 for DF. Stark et al. [199] reported the XRD pattern of flame spray made $Ce_xZr_{1-x}O_2$ starting from pure ceria (x = 1) to pure zirconia (x = 0). They observed that the broad signals the stable mixed ceria/zirconia phase slowly shifted to higher diffraction angle. This slowly shift affirmed the mixing of the ceria/zirconia [199]. The presence of Rh and Pt did not influence the phase composition and the crystallite sizes of the supports. As expected from the particle sizes no evidence of Pt, PtO_2, Rh or Rh_2O_3 phases was found (section 4.1 and 4.2).
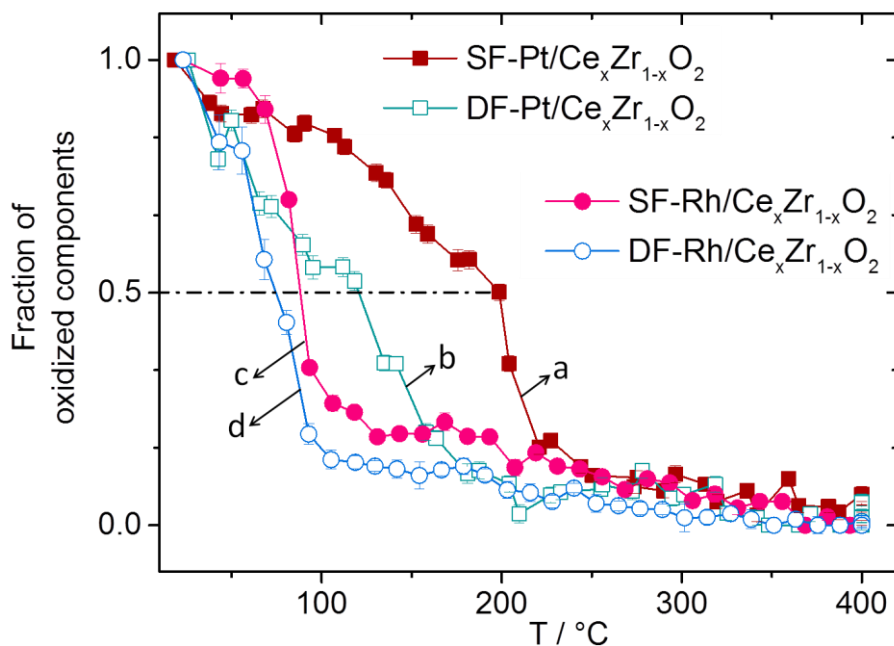
Figure 4.18: Comparison of changes in relative concentrations of oxidized Pt (a-b) and Rh (c-d) species on $Ce_xZr_{1-x}O_2$ prepared by single and double flame spray pyrolysis during TPR obtained from linear combination fitting of XANES spectra. On average Pt-K edge scans at ANKA (Karlsruhe, Germany) were recorded in temperature interval of 12 °C and Rh K-edge at BM25 at ESRF (Grenoble, France) in interval of 13 °C.

The reduction behavior of the supported Rh and Pt particles were again investigated by TPR-XANES in 5% H_2/He (total flow 50 mL/min, described in section 3.2.5). Rh K-edge and Pt L_3-edge XANES spectra were recorded *in situ* during reduction of the flame made CeO_2, ZrO_2 and $Ce_xZr_{1-x}O_2$ supported Rh and Pt catalysts like in section 4.1 and 4.2. The relative concentrations of oxidized and reduced species were determined by linear combination fitting of the XANES data using the first and last spectrum of the TPR series as reference spectra. The fitting results are shown in Figure 4.18 and Figure A.8. A striking influence of the supports and preparation methods on the reduction temperature was found. For single flame made $Pt/Ce_xZr_{1-x}O_2$ ca. 50% of the Pt atoms are in a metallic phase at 200 °C, for double flame catalyst at 120 °C (Figure 4.18a and b). Compared to literature these temperatures are lower [112, 179]. On other hand, the difference in reduction temperature for $Rh/Ce_xZr_{1-x}O_2$ is much less pronounced; at 89 °C for SF and at 75 °C for DF about 50% of the Rh species are in a metallic phase (Figure 4.18c and d). Similar results were obtained for Rh/CeO_2 and Rh/ZrO_2 (Figure A.8). The difference in reduction behavior between SF and DF made catalysts might be due to incorporation of noble metal into the bulk which can lead to high temperature reduction [179, 200]. In case of the double flame material, the noble metal and support are formed separately and mixed at a defined intersection point. This implies that the noble metals are stored on the surface of support. In section 4.2.3.1 the reduction temperature for SF and DF made Rh/TiO_2 catalysts was already discussed. The results showed that the Rh particles were encapsulated in the lattice in case of SF. The influence of the support on reduction temperature could also be investigated for Rh based catalysts. The temperature at which 50% of Rh species are reduced is 115 °C for Rh/ZrO_2, 90 °C for Rh/CeO_2 and 88 °C for $Rh/Ce_xZr_{1-x}O_2$, respectively. In general the reduction temperature is lower for Rh based catalysts compared to Pt based catalysts, e.g for SF at 115 °C 50% of Rh species and at 161 °C 50% of Pt species are in a metallic phase on ZrO_2.

4.3.3.2 Catalytic Activity and Kinetic Rate Measurements

The effects of different supports and the preparation methods on the catalytic performance in terms of CO conversion via the WGS reaction are shown in Figure 4.19. These experiments were performed in the fixed bed reactor at DICP in Dalian (section 3.4.1) according to the experimental procedures described in the experimental section (4.3.2). The equilibrium curve of CO conversion as function of temperature is also shown in Figure 4.19.
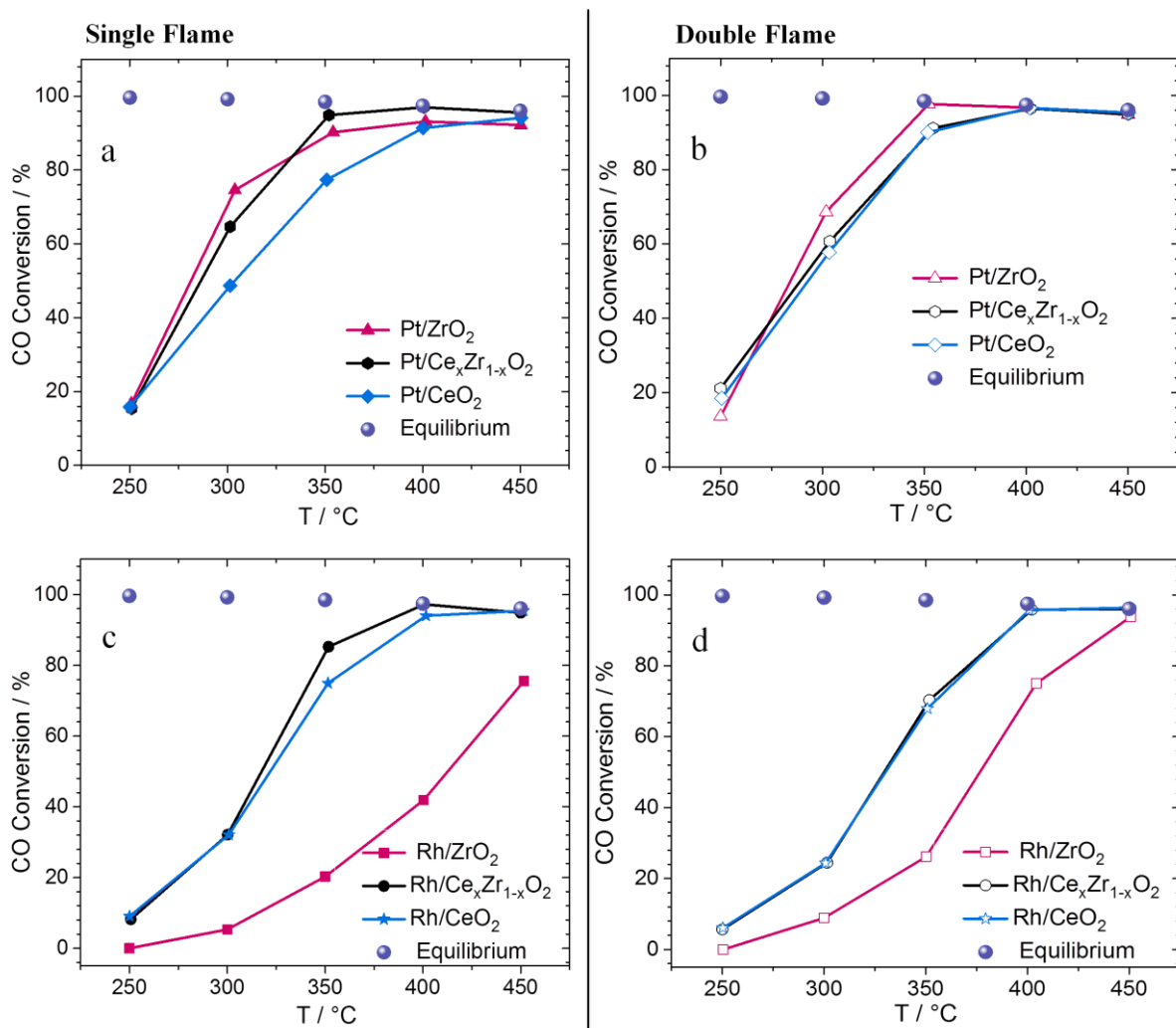
Figure 4.19: Effect of preparation method and support on the conversion of CO over Pt (a-b) and Rh (c-d) catalysts supported on CeO_2, ZrO_2 and $Ce_xZr_{1-x}O_2$ prepared by single flame (SF, left) and double flame (DF, right) spray pyrolysis (5 vol.% CO, 20 vol.% H_2O, 75 vol.% He, total flow = 187.5 mL/min, GHSV = 150,000 mL/g_{cat} h).

In case of the Pt based catalysts (Figure 4.19a and b) the activities at 350 °C decrease in the following order: $Pt/Ce_xZr_{1-x}O_2$ > Pt/ZrO_2 > Pt/CeO_2 for the SF and Pt/ZrO_2 > $Pt/Ce_xZr_{1-x}O_2$ ≈ Pt/CeO_2 for the DF made materials. CO conversion over the SF made CeO_2 supported Pt catalyst increases only slightly with temperature. Addition of Zr into CeO_2 support induced the increase in catalytic activity. This can be due to higher specific surface area and higher Pt dispersion on the support. The specific surface areas of $Ce_xZr_{1-x}O_2$ and Pt dispersion on $Ce_xZr_{1-x}O_2$ are higher compared to CeO_2 (see Table 4.7). In case of Rh based catalysts (Figure 4.19c and d) the ZrO_2 supported catalysts show much lower activity compared to ceria and mixed oxide supported catalysts. The Rh/CeO_2 and $Rh/Ce_xZr_{1-x}O_2$ catalysts reach conversions up to 80% at 350 °C,

whereas the Rh/ZrO$_2$ catalysts only achieve a conversion of 26 %. All samples reach the equilibrium point at 400 °C (except SF flame made Rh/ZrO$_2$). Compared DF made Rh/ZrO$_2$ catalyst to SF made Rh/ZrO$_2$ catalyst, the DF made Rh/ZrO$_2$ catalyst shows higher activity and reaches the equilibrium curve at 450 °C. As shown in Figure 4.19d, first CO conversion for DF made Rh/ZrO$_2$ catalyst increases slowly with increasing temperature and rises significantly at 350 °C. As the TPR results indicated, the noble metal particles are formed on the surface of the supports if they are prepared by double flame spray pyrolysis since the reduction temperature is much lower (Figure A.8 in Appendix). The effect of easily reducible metal could also be observed in the catalytic performance data. As previous studies have shown, Pt based catalysts are highly active compared to Rh based catalysts for both preparation methods. A disadvantage of the Rh based catalysts is that they promote methanation [156, 201, 202]. In a previous study a significant methane yield was observed over 3.1 wt.% and 1.9 wt.% Rh/CeO$_2$ catalysts (section 4.1, Figure 4.7) from 300 °C onwards. However, in case of these catalysts discussed in this section, methane formation was not observed over Rh based catalysts. The difference between both studies is the lower loading of Rh on the support (0.70 – 0.94 wt.%) and higher GHSV (150,000 in this study, 50,000 in the previous work).

The apparent activation energies were investigated between 300 and 400 °C for Pt based catalysts and between 320 and 400 °C for Rh based catalysts, as shown in Figure A.10. The apparent activation energies were determined using the Arrhenius equation [116]:

$$r = Ae^{-\frac{E_A}{RT}}$$

$$\ln(r) = \ln(A) - \frac{E_A}{R}\frac{1}{T}$$

where A is the preexponential factor, R the gas constant, T temperature, r the reaction rate and E$_A$ the activation energy (in kJ/mol). In principle the activation energy is derived from an Arrhenius plot of ln(r) versus 1/T and the slope of the Arrhenius plot yields the activation energy [116]. The obtained WGS kinetic parameters (r$_{cat}$, r$_{metal}$ and E$_A$) are compared to published data [29, 180, 191, 195] in Table 4.9, obtained in a reformer gas mixture. In order to better compare the catalysts with different noble metal contents, reaction rates normalized to the noble metal content (r$_{metal}$) are presented as well.

Table 4.9: WGS reaction rates and activation energies of Rh based catalysts at 320 °C and Pt based catalysts at 300 °C (15 vol.% CO, 5 vol.%CO_2, 30 vol.% H_2O, 40 vol.% H_2 and 10 vol.%N_2) compared to literature values.

Catalyst		Method	Loading [wt.%]	r_{cat} [$\mu mol_{CO}g_{cat}^{-1}s^{-1}$]	r_{metal} [$mol_{CO}mol_{metal}^{-1}s^{-1}$]	E_A [kJ/mol]
Pt	CeO$_2$	SF	0.94	6.94	0.14	54
		DF	0.90	6.19	0.13	60
	ZrO$_2$	SF	0.84	3.64	0.09	61
		DF	0.95	7.44	0.15	51
	Ce$_x$Zr$_{1-x}$O$_2$	SF	0.81	8.42	0.20	58
		DF	0.76	7.33	0.19	63
Rh	CeO$_2$	SF	0.70	5.30	0.15	77
		DF	0.70	2.57	0.07	88
	ZrO$_2$	SF	0.94	1.76	0.04	69
		DF	0.89	1.46	0.03	69
	Ce$_x$Zr$_{1-x}$O$_2$	SF	0.89	7.15	0.16	68
		DF	0.70	4.58	0.13	75
[a] Pt/CeO$_2$		IWI	0.74	16.0	0.42	82[180]
[b] Pt/CeO$_2$		IWI	2.0	15.0	0.15	65[29]
[b] Pt/ZrO$_2$		IWI	1.5	20.0	0.26	58[29]
[c] Pt/CeO$_2$		Precipitation	1.0	—	—	54[195]
[c] Pt/ZrO$_2$		Precipitation	1.0	—	—	83[195]
[c] Pt/Ce$_{0.6}$Zr$_{0.4}$O$_2$		Precipitation	1.0	—	—	58[195]
[a] Pt/HAP-10.5		IWI	0.77	21.6	0.55	83[180]
[a] Pt/SrHAP-11		IWI	0.81	29.3	0.70	70[191]

[a] similiar reaction composition in this work: 15 vol.% CO, 5 vol.% CO_2, 30 vol.% H_2O, 40 vol.% H_2, 10 vol.% N_2 (S/C = 2)

[b] reaction composition: 10 vol.% CO, 20 vol.% H_2O, 10 vol.% CO_2, 30 vol.% H_2 (S/C = 2)

[c] reaction composition: 6.4 vol% CO, 7.1 vol% CO_2, 0.7 vol% CH_4, 43.0 vol% H_2, 28.4 vol% H_2O, and 14.4 vol% N_2 (S/C = 4.4)

Independently from the FSP method the reaction rates of the Pt based catalysts are rather similar, whereas Rh based catalysts show stronger variations in the reaction rates. These differences in reaction rates can be confirmed by a strong correlation of WGS activity as shown in Figure 4.19c

and d. The apparent activation energies are between 51 and 63 kJ/mol for Pt based catalysts, and 68 and 88 kJ/mol for Rh based catalysts. A comparison of SF made with DF made catalysts, the apparent activation energies are slightly different (e.g. 54 kJ/mol for SF-Pt/CeO$_2$, 60 kJ/mol for DF-Pt/CeO$_2$, 77 kJ/mol for SF-Rh/CeO$_2$ and 88 kJ/mol for DF-Rh/CeO$_2$). Moreover, compared to literature the WGS activation energies of the flame made Pt based catalysts are lower (Table 4.9). Jeong et al. [195] reported values (54 kJ/mol for Pt/CeO$_2$, 58 kJ/mol for Pt/Ce$_x$Zr$_{1-x}$O$_2$) which are comparable to the SF made catalysts but lower than values obtained the DF made catalysts. Moreover, the activation energy of flame made Pt/ZrO$_2$ catalysts is lower (61 and 51 kJ/mol for SF and DF respectively), compared to Pt/ZrO$_2$ catalyst (83 kJ/mol) reported by Jeong and coworkers [195]. E$_A$ of Rh based catalysts in a similar range reported for Pt based catalysts in the literature catalysts (Table 4.9). Clearly, the activation energy of the catalysts depends strongly on the preparation method and also on the supports.

The light off curves of CO conversion for two different steam/CO (S/C) ratios for all samples run in micro reactor set-up (section 3.4.2) are shown in Figure 4.20 – Figure 4.25. Each experiment was performed twice (labeled 1.run and 2.run). Since these experiments were performed in the quartz capillary micro reactor, they can be carried out at synchrotron light sources for *in situ* XAS experiments in the future. In Table A.2 the performance of catalysts in a product free reaction mixture is shown. In addition an overview of the average light-off temperatures of the catalysts is given. Each temperature was averaged for 50% CO conversion for all activity measurements respectively. These results show that Pt based catalysts reach 50% CO conversion in the temperature range between 261 and 290 °C, Rh based catalysts at slightly higher temperature (307 – 330 °C), which is not the case for ZrO$_2$ supported Rh catalysts. In general, double flame made catalysts shows higher activity for WGS reaction compared to single flame made catalysts.
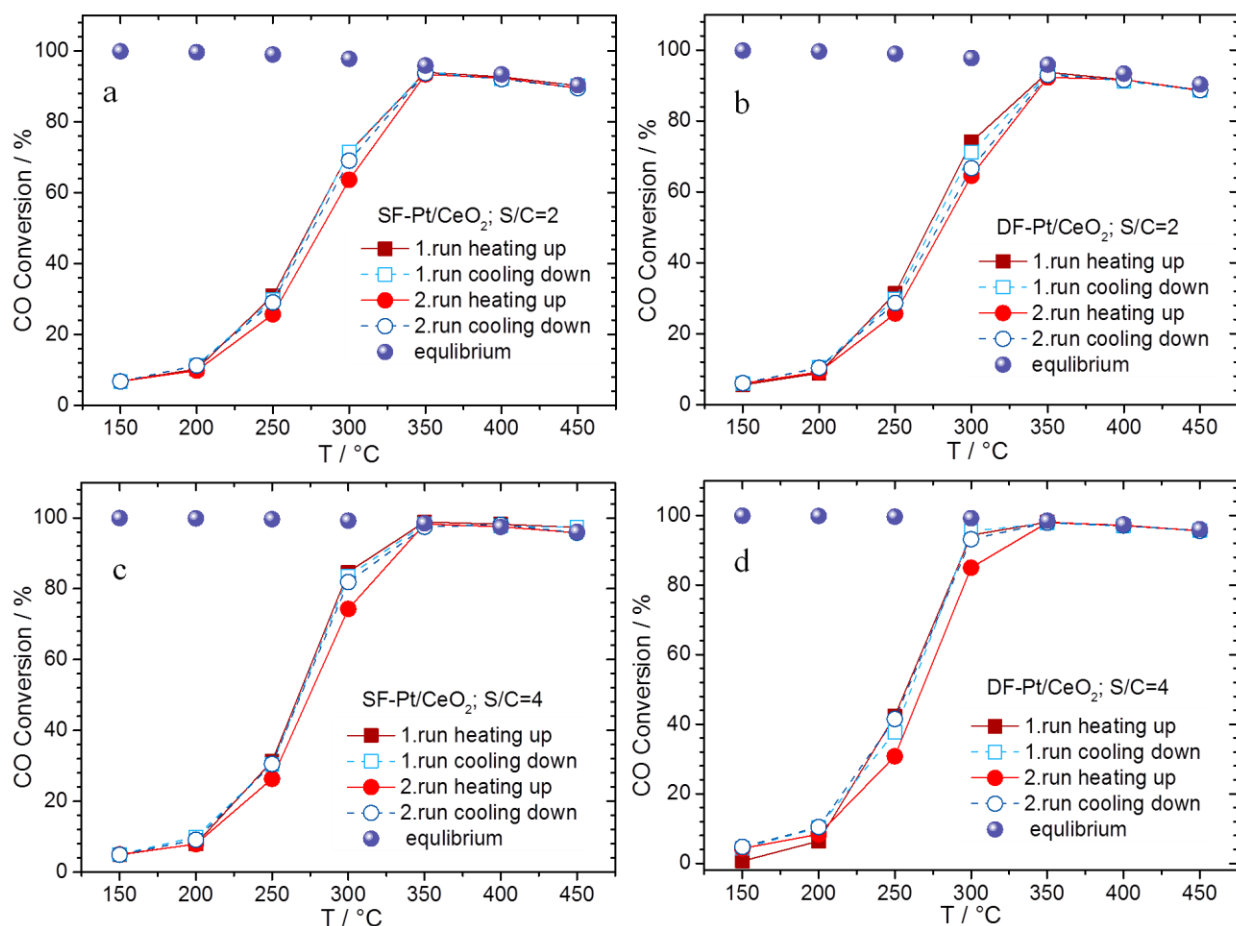
Figure 4.20: Water gas shift light off curves for SF (a and c) and DF (b and d) made Pt/CeO$_2$ catalysts in 5% CO, 10% H$_2$O, 85% He (S/C = 2) and 5 vol.% CO, 20 vol.% H$_2$O, 75 vol.% He (S/C = 4) GHSV=50,000 mL/g$_{cat}$ h (solid symbols and lines: heating up and open symbols and dashed lines: cooling down).

Ceria supported Pt particles show the best performance compared to the other used catalysts analyzed in these test series (Table A.2 and Figure 4.20). The average LO-temperature is ca. 261 °C for DF and 270 °C for SF (S/C = 4), and 276 °C for DF and SF (S/C = 2). All Pt/CeO$_2$ catalysts reach the equilibrium point at 350 °C independent of S/C ratios and synthesis method. Further variance in these catalytic performance tests was observed for the DF made Pt/CeO$_2$ catalyst at a S/C ratio of 4. At 300 °C CO conversion reaches almost the equilibrium curve. Figure 4.20c and d shows that a higher amount of water affects the maximum achievable conversion at the thermodynamic limit and leads to an increase in the conversion of CO at lower temperatures, as well. Similar catalytic activity was expected with respect to the small differences in the results of characterization (loading, BET surface area and dispersion). During heating up and cooling down cycles the general trends in the light off curves for Pt/CeO$_2$ catalysts are

similar, as shown in Figure 4.20. Close resemblance in CO conversion during cycles indicates that the catalysts are very stable. However, over all ceria supported Pt catalysts CO conversion during heating in the second cycle (2.run, Figure 4.20) is lower compared to first cycle. Nevertheless, CO conversion during heating in the second cycle reaches the equilibrium point at 350 °C and the behavior during cooling down in the second cycle is comparable to the first cycle. The reason for achieving equilibrium points at high temperature might be the formation of carbonaceous species on the surface. At high temperature the apparent activation energy could be overcome to decompose eventual carbonaceous species. It is assumed that at high temperature the redox bifunctional mechanisms are preferred [203]. According to ref. [170, 203] *in situ* IR spectroscopy of a series of Pt/CeO_2 catalysts recorded while switching between oxidizing and reducing atmosphere indicated the formation of formate and carbonate compounds on the surface of those catalysts. The rate limiting step of the WGS reaction is strongly suggested to be associated with C-H bond breaking in the formate intermediate [149, 204].

Compared to the literature [29, 195, 203], the flame made Pt/CeO_2 catalysts prepared in this work exhibit higher activity. Thinon and co-workers [29] studied 2 wt.% Pt/CeO_2 catalyst prepared by incipient wetness impregnation (IWI) under analogous reaction conditions (10% CO and 20% H_2O; S/C = 2; GHSV = 60,000 mL/g_{cat} h). CO conversion at 300 °C was ca. 40% for the IWI prepared Pt/CeO_2 compared to ca. 70% made Pt/CeO_2 made by SF and DF spray pyrolysis. Note that the Pt loading in case of flame made catalysts is much lower compared to IWI prepared Pt/CeO_2. The reason for the difference in activity can be traced back to the difference in catalysis surface area (IWI: 54 m^2/g, FSP: 91-105 m^2/g). Kalamaras et al. [203] prepared 0.6 and 2 wt.% Pt/CeO_2 catalysts by sol gel method and tested them in 3% CO and 10% H_2O (S/C = 3.33). The results showed that the activity was significantly lower compared to the FSP catalysts prepared for this work (36% for 0.6 wt.%, 40% for 2 wt.% Pt/CeO_2) [203]. The particle sizes and dispersion of 0.6 wt.%, and 2 wt.% Pt/CeO_2 prepared by sol gel method are 3 and 8 nm and 37% and 13.7% respectively, whereas the particle size and dispersion for SF and DF made catalysts are 3.0 nm and 37%.
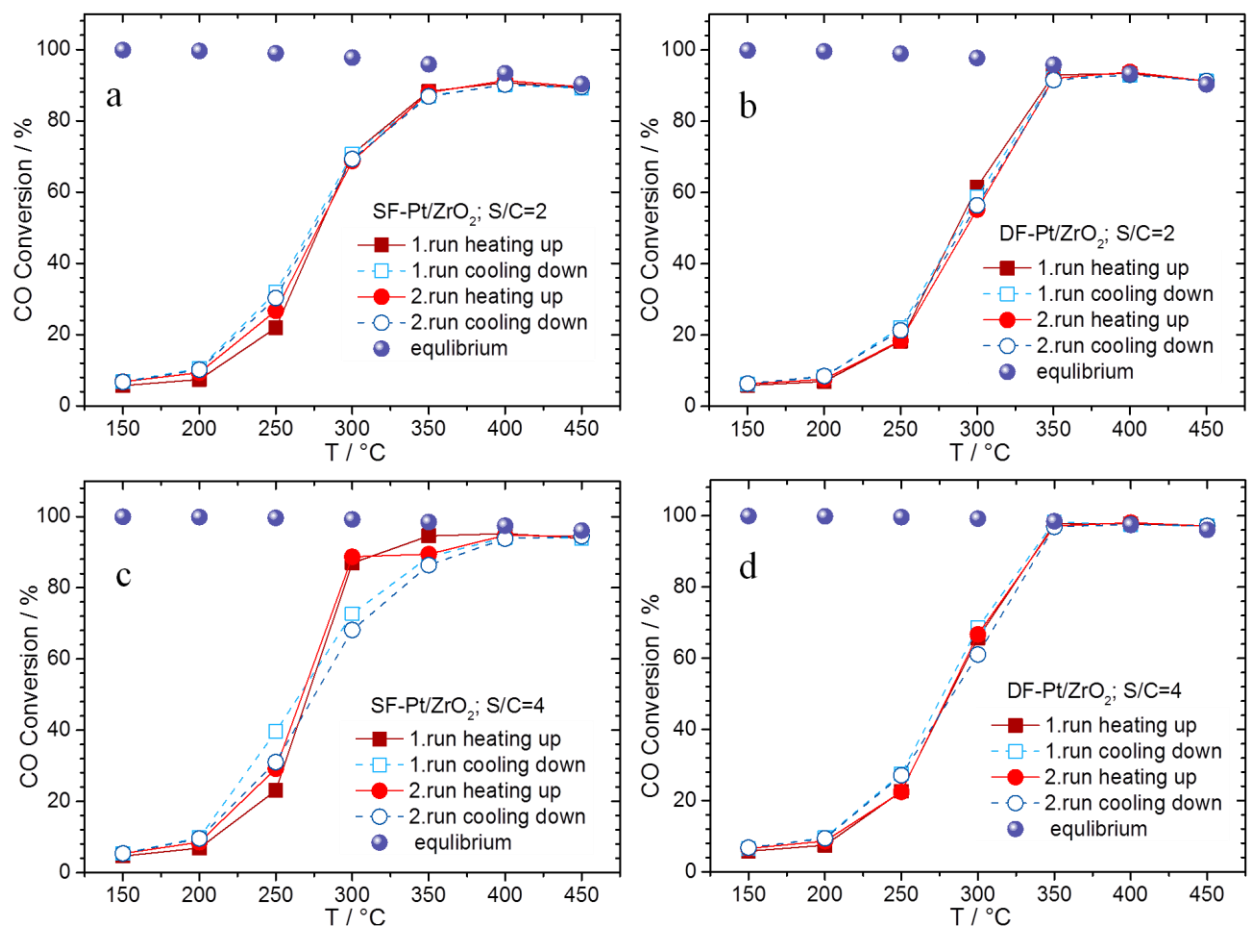
Figure 4.21: Water gas shift light off curves for SF (a and c) and DF (b and d) made Pt/ZrO$_2$ catalysts in 5 vol.% CO, 10 vol.% H$_2$O, 85 vol.% He (S/C = 2) and 5 vol.% CO, 20 vol.% H$_2$O, 75 vol.% He (S/C = 4) GHSV=50,000 mL/g$_{cat}$ h (solid symbols and lines: heating up and open symbols and dashed lines: cooling down).

Figure 4.21 clearly demonstrates that the Pt/ZrO$_2$ catalysts show similar WGS activity under the same conditions which were applied to the Pt/CeO$_2$ catalysts. With regard to the average LO-temperature, the SF made Pt/ZrO$_2$ catalysts exhibit analogous performance and the DF made Pt/ZrO$_2$ catalysts show lower performance compared to the Pt/CeO$_2$ catalysts. In case of zirconia supported Pt catalysts differences between the synthesis methods (SF and DF) appear. Independent of S/C ratios, DF made Pt/ZrO$_2$ catalysts reach equilibrium conversion at 350 °C whereas SF made catalysts CO conversion is close to equilibrium conversion only above 400 °C. Since the specific surface area is higher and the Pt particle sizes are smaller for SF-Pt/ZrO$_2$ compared to DF- Pt/ZrO$_2$ (Table 4.7), the difference in activity between SF and DF made catalysts could be explained by substitution of noble metal in the ZrO$_2$ lattice. It assumed that in the DF set-up support and nanoparticles are formed in individual flames before intersecting at a

defined distance, which allow well-dispersed noble metal particles on the support [96]. The general trends of the light off curves for Pt/ZrO_2 catalysts, except for SF made Pt/ZrO_2 (S/C = 4), hardly varied during the test cycles. Moreover compared to Pt/CeO_2, these catalysts exhibit superior stability during heating in the second cycle. In case of the Pt/ZrO_2, formation of formate and carbonate compounds on the surface of the catalysts was not observed which was confirmed by *in situ* FTIR, but Pt–CO bands appeared [170]. The WGS reaction pathway is suggested to follow the associative route with a redox regeneration, implying that the surface hydroxyl (OH) groups react with CO leaving oxygen vacancies, followed by surface regeneration with H_2O [170]. The catalytic performance of these Pt/ZrO_2 catalysts compared to literature is considerably high. Thinon et al. [29] investigated Pt/ZrO_2 catalyst in a product free gas mixture (10 vol.% CO, 20 vol.% H_2O, 70 vol.% Ar; GHSV = 60,000 mL/g h) close to the reaction condition applied in this work. At 300 °C they reached 38% CO conversion over a IWI prepared 1.5 wt.% Pt/ZrO_2 catalyst whereas the light of curves in Figure 4.21a and b shows 70% for the SF made, 60% for the DF made Pt/ZrO_2 catalysts despite the low Pt loading (SF: 0.84 wt%, DF: 0.9 wt.%). Jeong et al. [195] tested 1 wt.% Pt/ZrO_2 prepared by co-precipitation for WGS reactions reached 10% CO conversion at 280 °C and 30% at 320 °C, whereas at 300 °C CO conversion is ca. 65% for the DF and 85% for the SF made Pt/ ZrO_2 catalyst. The difference in CO conversion is extremely high and FSP made catalysts exhibit attractive performance.

Figure 4.22 shows WGS catalytic performance results of $Pt/Ce_xZr_{1-x}O_2$ in terms of CO conversion as a function of temperature (light off curves). CO conversion increases with increasing temperature independent of S/C ratio and synthesizes methods. Over all these catalysts full CO conversion is reached at 400 °C. The results of CO conversion during test cycles (light off curves), except the results for SF made $Pt/Ce_xZr_{1-x}O_2$ catalyst (S/C = 2) are reproducible, implying that theses catalysts are stable. In case of the SF made $Pt/Ce_xZr_{1-x}O_2$ catalyst at S/C = 2, values for CO conversion during heating up and cooling down are similar during the first cycle (Figure 4.22, 1.run), whereas during the second cycle CO conversion is lower. However, during cooling down in the second cycle CO conversion is on a higher level again (Figure 4.22, 2.run cooling down). Compared to Pt based catalysts prepared by FSP for this work the $Pt/Ce_xZr_{1-x}O_2$ catalysts show higher LO-temperatures in the temperature range between 280 °C and 287 °C (Table A.2).
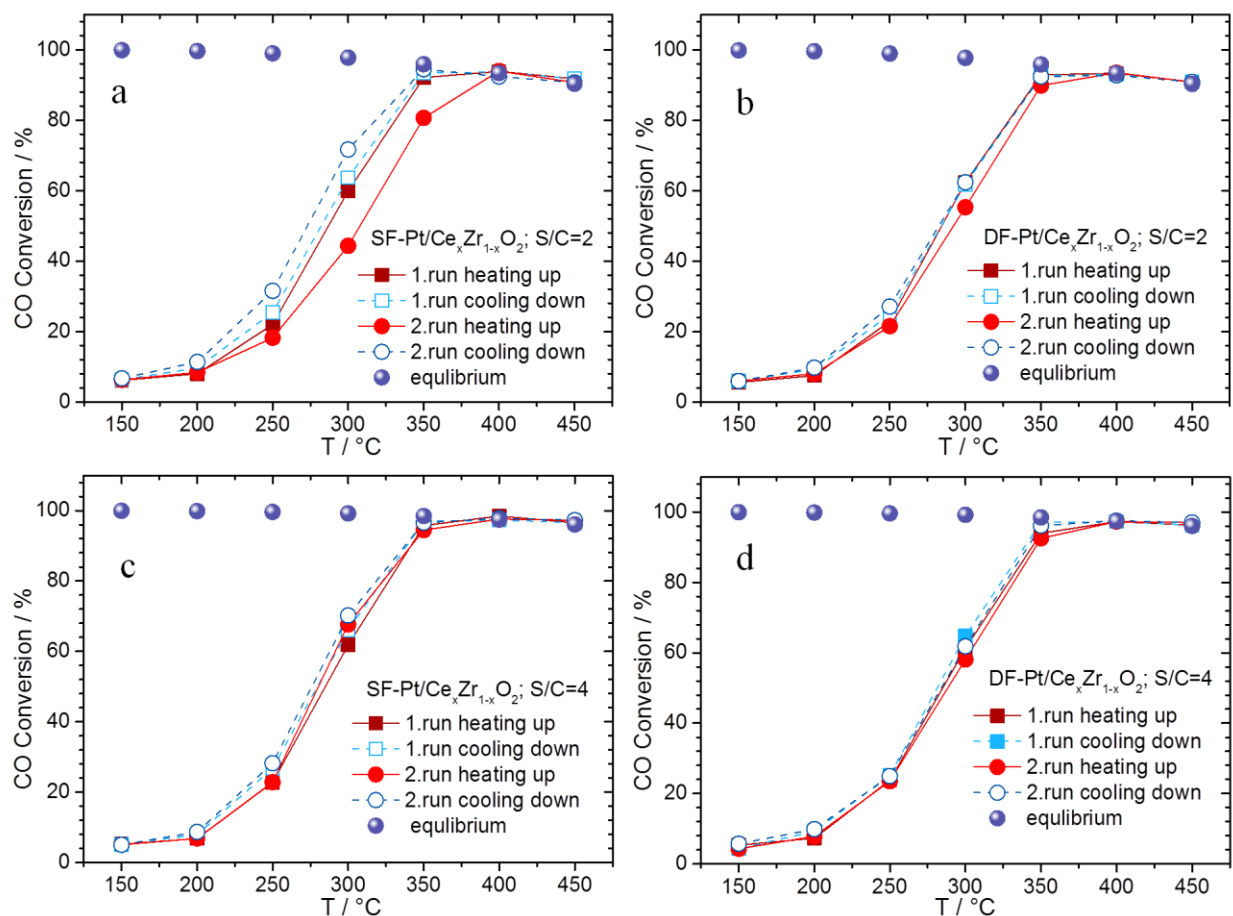
Figure 4.22: Water gas shift light off curves for SF (a and c) and DF (b and d) made $Pt/Ce_xZr_{1-x}O_2$ catalysts in 5 vol.% CO, 10 vol.% H_2O, 85 vol.% He (S/C = 2) and 5 vol.% CO, 20 vol.% H_2O, 75 vol.% He (S/C = 4) GHSV = 50,000 mL/g_{cat} h (solid symbols and lines: heating up and open symbols and dashed lines: cooling down).

According to literature, the WGS activity of $Pt/Ce_xZr_{1-x}O_2$ catalysts depends on the chemical composition of the support and catalysts with higher Ce:Zr ratio show higher activity, especially for $x \geq 5$, i.e. Zr-rich $Pt/Ce_xZr_{1-x}O_2$ catalysts are less active [195, 205-207]. Jeong et al. [195] varied CeO_2/ZrO_2 ratio in a range between x = 0.8 and x = 0.2 using co-precipitation methods. They found out that CO conversion decreased in the order $Pt/Ce_{0.8}Zr_{0.2}O_2 > Pt/Ce_{0.6}Zr_{0.4}O_2 > Pt/Ce_{0.4}Zr_{0.6}O_2 > Pt/Ce_{0.2}Zr_{0.8}O_2$ [195]. For the $Pt/Ce_{0.8}Zr_{0.2}O_2$ catalyst CO conversion was ca 70% at 280 °C and 83% at 320 °C, and for the $Pt/Ce_{0.6}Zr_{0.4}O_2$ catalyst ca 40% at 280 °C and 70% at 320 °C. Kalamaras et al. [207] investigated $Pt/Ce_xZr_{1-x}O_2$ catalysts with x=0.5 and 0.7 prepared by a sol-gel method, and observed similar trends. For 1 wt.% $Pt/Ce_{0.5}Zr_{0.5}O_2$ at 300 °C CO conversion was less than 90% and ca. 90% for 1 wt.% $Pt/Ce_{0.8}Zr_{0.2}O_2$. In case of this study, according to the XRD results the cerium to zirconium ratio was in a range between 1.5/1 (x=0.6)

to 4/1 (x=0.8) for the mixed oxide $Pt/Ce_xZr_{1-x}O_2$. However, DF made $Pt/Ce_xZr_{1-x}O_2$ catalysts show higher stability compared to SF made $Pt/Ce_xZr_{1-x}O_2$ catalysts under both reaction conditions (Figure 4.22). Compared to these flame made catalysts, the above mentioned sol-gel prepared catalysts are more active and the co-precipitation prepared catalysts seem less active. Note that the space velocity (GHSV), in other words residence time, is high in case of flame made catalysts, implying that WGS conversion decreases with increasing space velocity.

Independent of the support, Pt based catalysts are more active with respect to WGS than Rh based catalysts. The LO-temperature for WGS over Rh/CeO_2 catalysts (Table A.2) is ca. 50 °C higher compared to Pt/CeO_2 catalysts. Figure 4.23 shows a comparison of SF and DF made Rh/CeO_2 catalysts with S/C ratios of 2 and 4. The trends in the light off curves of Rh/CeO_2 and Pt/CeO_2 are similar. In case of Rh/CeO_2 catalysts full CO conversion is reached at 400 °C whereas for Pt/CeO_2 catalysts this temperature is 350 °C. During second cycles CO conversion is lower (Figure 4.23, 2. run heating up) but on a high level again during cooling down (Figure 4.23, 2. run cooling down). This phenomenon was observed for Pt/CeO_2 catalysts as well. However, in general the Rh/CeO_2 catalysts show high stability under WGS reaction conditions. Comparison of data recorded at different S/C ratios indicates that CO conversion increases with increasing S/C ratio (4). A similar trend was observed for Pt/CeO_2 catalysts. The reason for that can be traced back to the proposed reaction mechanism. Shido et al. [34] assumed that the decomposition of intermediates (formate) on the surface area and product formation (CO_2 and H_2) were accelerated by further addition of H_2O molecules. In general Rh based catalysts have been studied less extensively compared to Pt based catalysts. Thinon et al. [29] investigated a 1.5 wt.% Rh/CeO_2 catalyst prepared by IWI in a 10 vol.% CO and 20 vol.% H_2O gas mixture (S/C = 2; GHSV = 60,000 mL/g h) and observed CO conversion at 300 °C below 15%, whereas the 0.7 wt.% Rh/CeO_2 catalysts prepared by SF and DF for this work are considerably more active (ca. 30%).
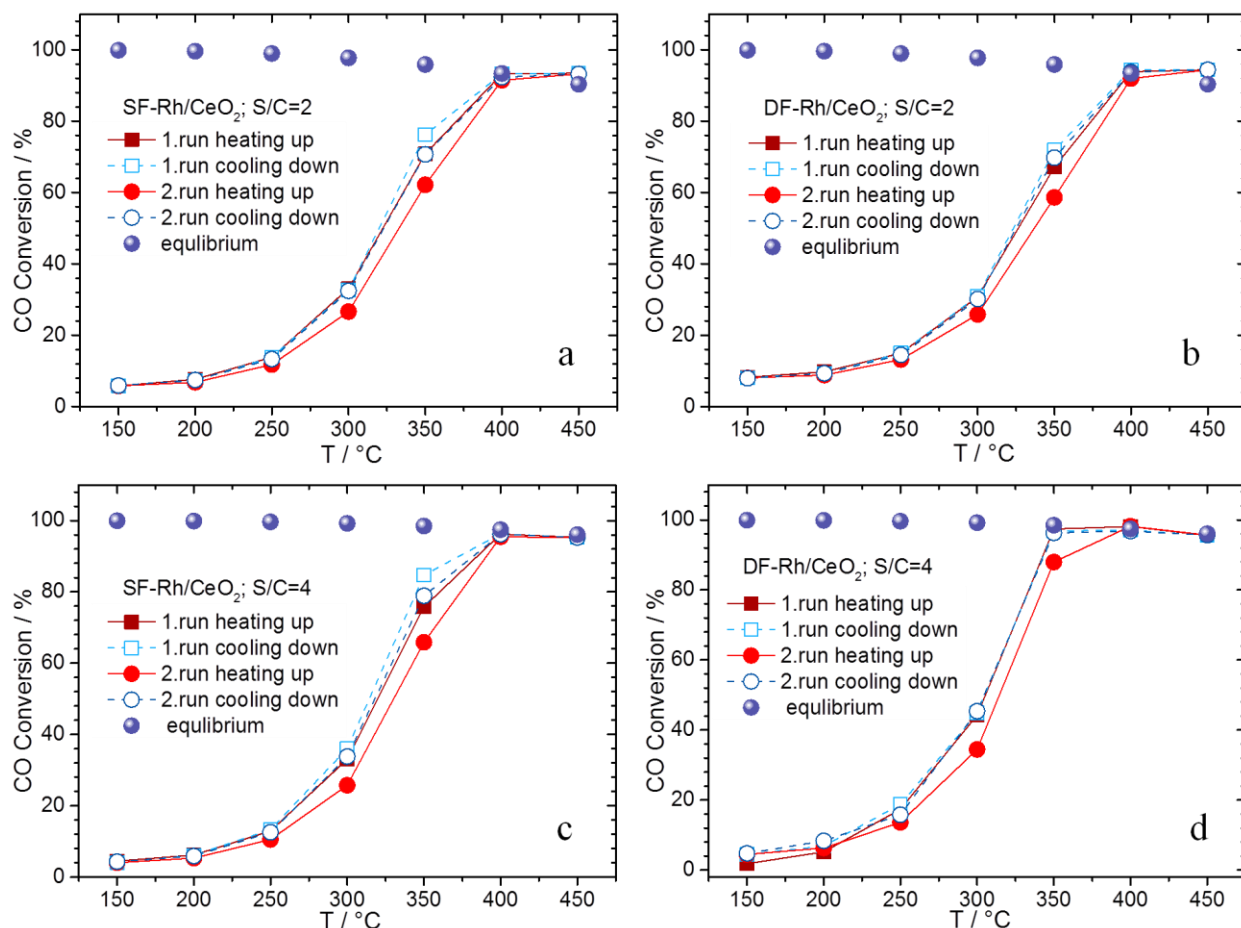
Figure 4.23: Water gas shift light off curves for SF (a and c) and DF (b and d) made Rh/CeO_2 catalysts in 5 vol.% CO, 10 vol.% H_2O, 85 vol.% He (S/C = 2) and 5 vol.% CO, 20 vol.% H_2O, 75 vol.% He (S/C = 4) GHSV = 50,000 mL/g_{cat} h (solid symbols and lines: heating up and open symbols and dashed lines: cooling down).

In Figure 4.24 a huge difference in CO conversion between SF and DF made Rh/ZrO_2 catalysts can be seen. In case of the SF made catalysts CO conversion increases only slightly with temperature for S/C ratios of 2 and 4. The catalytic performance of these Rh/ZrO_2 catalysts is much higher when prepared by double flame spray pyrolysis. At 450 °C in a 5 vol.% CO and 10 vol.% H_2O gas mixture CO conversion is 28% over the SF and 94% over the DF made Rh/ZrO_2 catalyst. This huge difference in conversion might be caused by substitution of noble metal in the ZrO_2 lattice. This is also observed for SF made Pt/ZrO_2. and Rh/TiO_2 catalyst (section 4.2.3.2). The ionic radius of Rh^{3+} is 66 pm which is close to ionic size of Zr^{4+} (72 pm) [181]. Hence, a zirconium ion could be replaced by a similarly large rhodium ion in the lattice. In case of highly active Pt/CeO_2 and Rh/CeO_2 catalysts the incorporation of noble metal into CeO_2

lattice is hampered, since the difference in ionic sizes is fairly large (Pt^{4+} =62 pm, Rh^{3+} = 66 pm and Ce^{4+} =94 [181]).
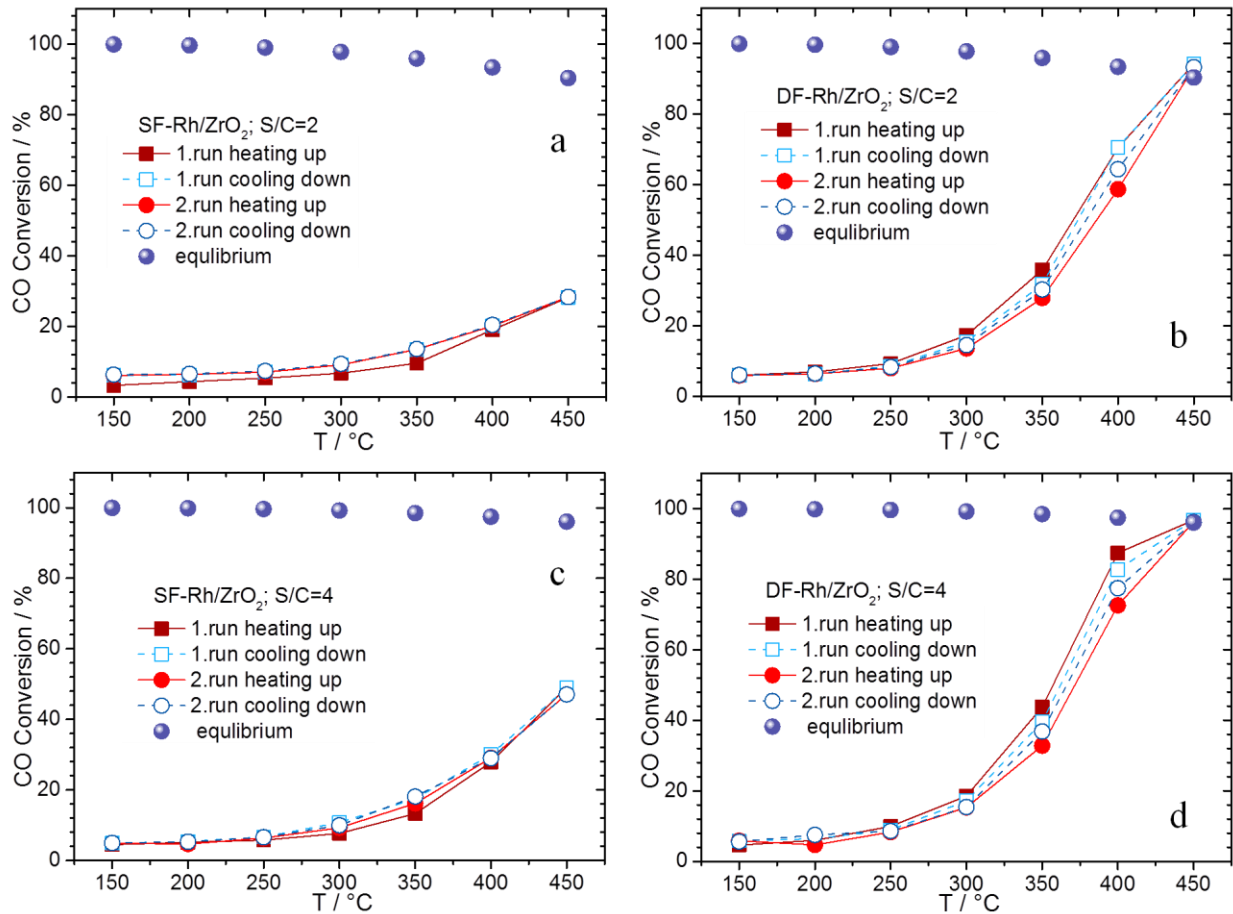
Figure 4.24: Water gas shift light off curves for SF (a and c) and DF (b and d) made Rh/ZrO_2 catalysts in 5 vol.% CO, 10 vol.% H_2O, 85 vol.% He (S/C = 2) and 5 vol.% CO, 20 vol.% H_2O, 75 vol.% He (S/C = 4) GHSV = 50,000 mL/g_{cat} h (solid symbols and lines: heating up and open symbols and dashed lines: cooling down).

The catalytic performance of $Rh/Ce_xZr_{1-x}O_2$ closely resembles Rh/CeO_2 catalysts. As shown in Figure 4.25, full CO conversion is reached at 400 °C. Moreover, during heating in the second cycle CO conversion is lower. During cooling down over $Rh/Ce_xZr_{1-x}O_2$ CO conversion is on a higher level again. Compared to $Pt/Ce_xZr_{1-x}O_2$ the WGS activity of $Rh/Ce_xZr_{1-x}O_2$ is lower, e. g. at 300 °C CO conversion at a steam to carbon ratio of 4 is 60% for SF made $Pt/Ce_xZr_{1-x}O_2$ catalysts and 37% for the SF made $Rh/Ce_xZr_{1-x}O_2$ catalyst.
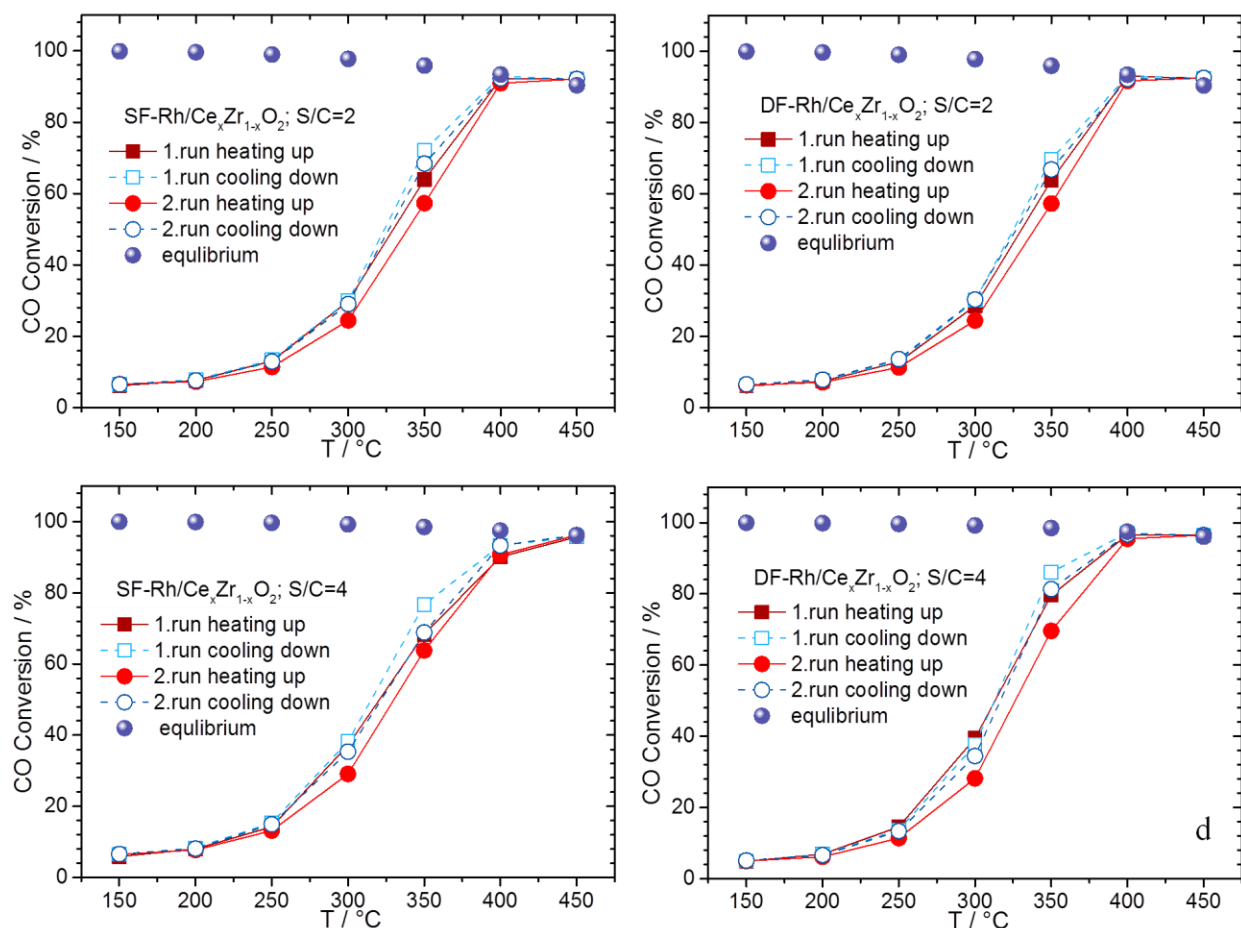
Figure 4.25: Water gas shift light off curves for SF (a and c) and DF (b and d) made $Rh/Ce_xZr_{1-x}O_2$ catalysts in 5 vol.% CO, 10 vol.% H_2O, 85 vol.% He (S/C = 2) and 5 vol.% CO, 20 vol.% H_2O, 75 vol.% He (S/C = 4) GHSV = 50,000 mL/g_{cat} h (solid symbols and lines: heating up and open symbols and dashed lines: cooling down).

Previous studies [112, 156] show that over Rh based catalysts methane was formed under WGS conditions as a byproduct $(CO + 3\,H_2 \rightleftarrows CH_4 + H_2O)$. However, the results of tube reactor experiments (GHSV = 150,000 mL/g_{cat} h and S/C = 4) in this work showed that methane was formed neither over Pt nor over Rh based catalysts (Figure 4.19). Interestingly, during experiments in the capillary micro reactor full CO conversion over equilibrium curve at high temperature was observed, especially for SF and DF made $Rh/Ce_xZr_{1-x}O_2$, DF made Rh/ZrO_2, SF and DF made Rh/CeO_2 at an S/C ratio of 2, which could be caused the formation of methane. Figure A.11 and Figure A.12 in the Appendix show the fraction of CO that is converted to methane (S_{CH4}) for each catalyst and each S/C ratio. Below 350 °C methane formation is below than 1% independent of catalysts and S/C ratios. However, S_{CH4} increases with increasing temperature. Pt based catalysts show less propensity to produce S_{CH4}, whereas the formation of

methane over Rh based catalysts is ca. 10% at high temperatures. In case of Rh based catalysts a strong influence of the support on S_{CH4} formation is observed in the order $Rh/CeO_2 > Rh/Ce_xZr_{1-x}O_2 > Rh/ZrO_2$. As discussed above, increasing steam to CO ratios (S/C = 4) lead to higher CO conversion, while methane formation decreases. Wheeler et al. [156] investigated the activation and selectivity of different metals on Al_2O_3 and CeO_2 under WGS reaction conditions. They observed the metals promote methanation in the order $Ru > Rh > Ni > Pt > Pd$. Methanation over Pt/Al_2O_3 and Pd/Al_2O_3 is below 1%, while on the other metals it is large and exceeds 10% on Ru/Al_2O_3 [156]. If ceria were used as support methane formation increased at higher temperature. The advantage of Pt/CeO_2 catalysts was that methane formation is negligible at temperatures where the CO conversion was at the maximum [156].

The turnover frequency (TOF) describes the catalytic level of activity; the larger the TOF, the more active the catalyst. TOF is calculated according to Eq. 4.1 as shown in section 4.1.3.3. Figure 4.26a and b show turnover frequencies of flame made Pt based catalysts in a temperature range between 150 and 300 °C. For X_{CO} the average of the LO curves (Table A.2) was used and CO conversion above 350 °C was not considered, since it reached equilibrium curve. CeO_2 and $Ce_xZr_{1-x}O_2$ supported Pt catalysts exhibit higher TOF values compared to ZrO_2 supported Pt catalysts. At the temperature above 250 °C in case of S/C = 2 (Figure 4.26a), the order of TOFs is $DF-Pt/CeO_2 > SF-Pt/CeO_2 \approx SF-Pt/Ce_xZr_{1-x}O_2 \approx DF-Pt/Ce_xZr_{1-x}O_2 > SF-Pt/ZrO_2 > DF-Pt/ZrO_2$. At S/C = 4 the TOF values decrease in the order $Pt/CeO_2 > Pt/Ce_xZr_{1-x}O_2 > Pt/ZrO_2$ independent of the synthesis method (Figure 4.26b). Turnover frequencies for Rh based catalysts are shown in Figure 4.26c and d. Independent of the S/C ratios and supports, for each support DF made catalysts exhibit higher TOFs compared to SF made catalysts. With respect to the synthesis method double flame spray pyrolysis clearly affects the catalytic performance of Rh based catalysts. For both steam to CO ratios, Rh/ZrO_2 catalysts exhibit rather low TOFs. The difference between SF and DF made Rh/CeO_2 and $Rh/Ce_xZr_{1-x}O_2$ are more obvious at S/C = 4 (Figure 4.26d), compared to S/C = 2 (Figure 4.26c).
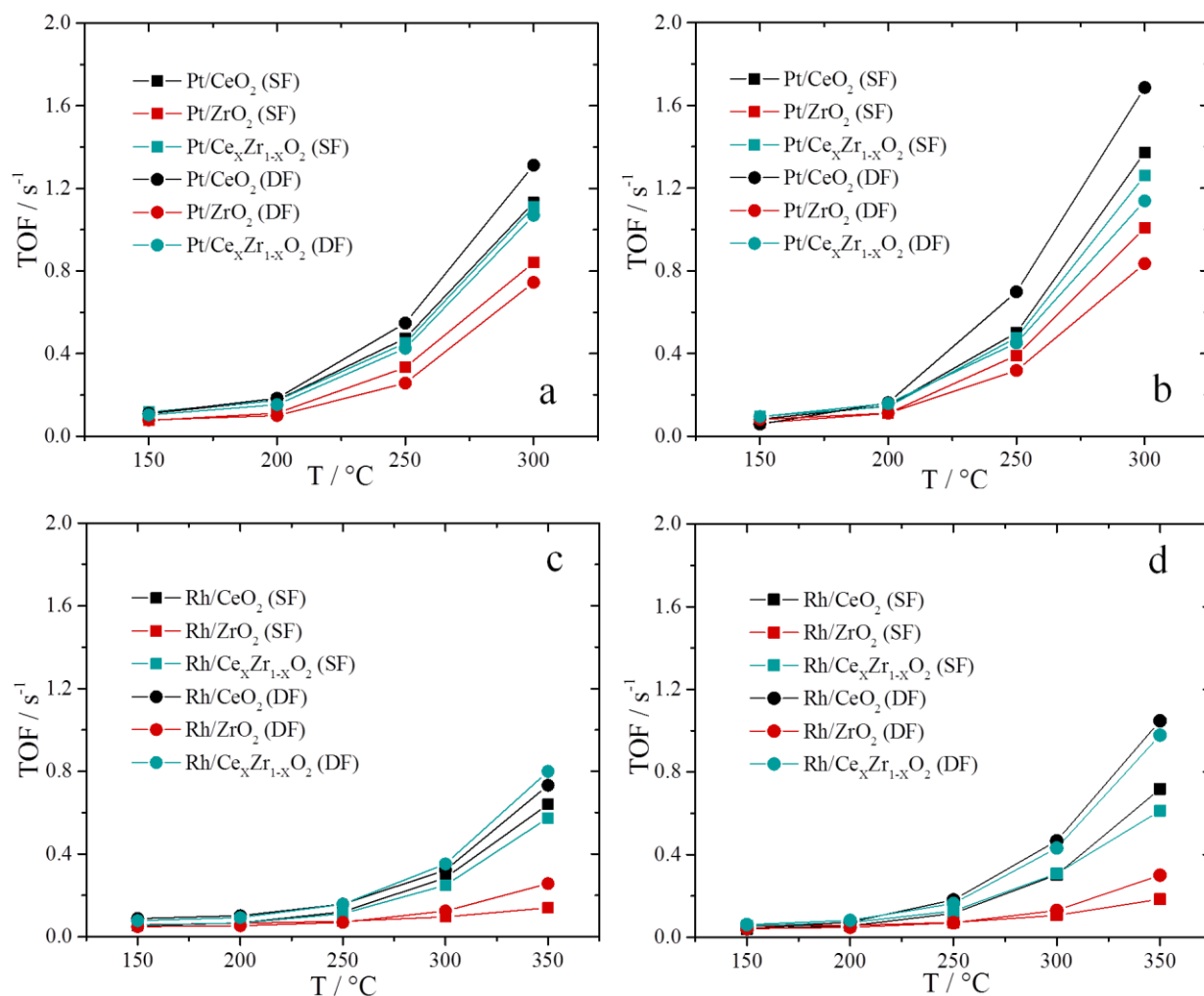
Figure 4.26: Turnover frequencies (TOF) of Pt based catalysts at S/C ratios of 2 (a) and 4 (b) and Rh based catalysts at S/C ratios of 2 (c) and 4 (d) prepared by SF (solid square) and DF (solid circle).

In Table 4.10 turnover frequencies for Pt based catalysts at 300 °C are listed. Since rhodium as catalytically active component in WGS reactions is not in the focus of current research due to the lower reaction rate and selectivity, only TOF values of Pt based catalysts could be compared with literature values [180, 195, 208]. Compared to Pt based catalysts prepared by conventional methods like incipient wetness impregnation and co-precipitation, the FSP made Pt based catalysts are highly active. For instance, the FSP made $Pt/Ce_xZr_{1-x}O_2$ catalysts show a TOF which is twice as high as the literature value for a catalyst prepared by precipitation (Table 4.10) [195]. It seems that ZrO_2 as a support leads to lower activity for the WGS reaction. However, its catalytic performance can be enhanced when using FSP as preparation method.

Table 4.10: Turnover frequencies (TOF) for Pt based catalysts at 300 °C

Catalysts	Method	TOF [1/s]	
Pt/CeO$_2$	SF	1.1 [a]	1.4 [b]
	DF	1.3 [a]	1.7 [b]
Pt/ZrO$_2$	SF	0.8 [a]	1.0 [b]
	DF	0.8 [a]	0.8 [b]
Pt/Ce$_x$Zr$_{1-x}$O$_2$	SF	1.1 [a]	1.3 [b]
	DF	1.1 [a]	1.1 [b]
Pt/CeO$_2$	IWI	0.73 [a,[180]]	
Pt/CeO$_2$	Precipitation	1.3 [c, [195]]	
Pt/ZrO$_2$	IWI	0.76 [d, [208]]	
Pt/ZrO$_2$	IWI	0.14 [c, [195]]	
Pt/Ce$_{0.6}$Zr$_{0.4}$O$_2$	Precipitation	0.49 [c, [195]]	
Pt/Ti/ZrO$_2$ (10 wt.% Ti)	IWI	1.01 [d, [208]]	
Pt/Ti/ZrO$_2$ (20 wt.% Ti)	IWI	0.66 [d, [208]]	
Pt/HAP-10	IWI	0.58 [a, [180]]	

[a] S/C = 2, [b] S/C = 4, [c] S/C = 4.44, [d] S/C = 3

According to the results shown in Figure 4.20 – Figure 4.25 and the calculated turnover frequencies (TOF) the catalytic performance of Pt based catalysts is promising and much higher compared to Rh based catalysts. Therefore, these catalysts were further investigated with respect to catalyst stability, which is important for future commercial applications of the catalysts. These measurements were carried out at 400 °C for 48 h under realistic reaction conditions close to reformate type feed gas. Figure 4.27 shows the stability test results for SF and DF made Pt/CeO$_2$, Pt/ZrO$_2$ and Pt/Ce$_x$Zr$_{1-x}$O$_2$ catalysts. Independent of the support CO conversion decreases with time on stream. Comparing the supports, the results show that SF and DF made catalysts with the same support have similar CO conversion over time. At the beginning of the experiment Pt/Ce$_x$Zr$_{1-x}$O$_2$ and Pt/ZrO$_2$ catalysts exhibit higher CO conversion compared to Pt/CeO$_2$ catalysts. Moreover, over time Pt/Ce$_x$Zr$_{1-x}$O$_2$ catalysts exhibit higher CO conversion compared to Pt/CeO$_2$ and Pt/ZrO$_2$ catalysts. Although Pt/ZrO$_2$ catalysts show high catalytic activity at beginning of the

experiment, they significantly deactivate during the long term stability test over time. These catalysts lose ca. 33% of their activity in 48 h which is the highest value compared to $Pt/Ce_xZr_{1-x}O_2$ (ca. 22%) and Pt/CeO_2 (ca. 21%) for both synthesis methods (SF and DF spray pyrolysis).
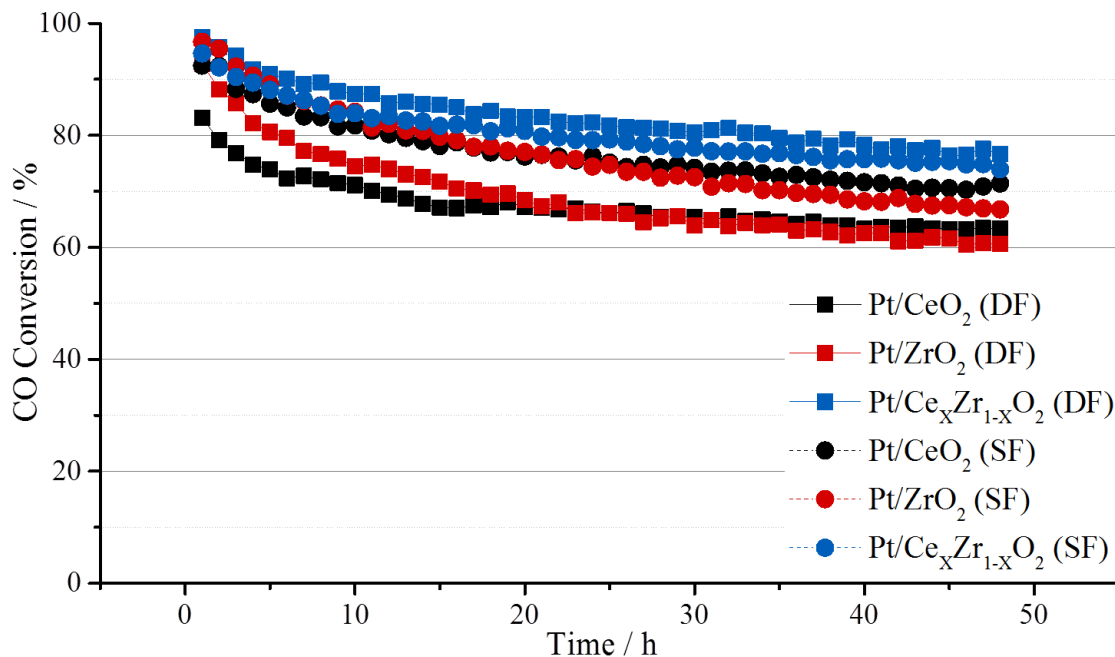
Figure 4.27: Stability of SF and DF made Pt/CeO_2 (black), Pt/ZrO_2 (red) and $Pt/Ce_xZr_{1-x}O_2$ (blue) catalysts in reformate type feed gas at 400 °C (10 vol.% CO, 10 vol.% CO_2, 20 vol.% H_2O, 40 vol.% H_2 and 20 vol.% He, GHSV = 50,000 mL/g_{cat} h).

Interestingly, CO conversion over SF made Pt based catalysts starts out similar whereas DF made catalysts show from the beginning differences in CO conversion. At the start of the experiment CO conversion for SF made catalysts is at 92–97% and decreases to 67–74% after 48 h. In case of DF made catalysts the Pt particles on the mixed oxide support exhibit high activity and after 48 h CO conversion is 77%, whereas CO conversion after 48 h is 63% and 61% for ceria and zirconia supported Pt catalysts respectively. In summary, SF and DF derived $Pt/Ce_xZr_{1-x}O_2$ catalysts show the highest stability. Jeong et al. [195] tested Pt/CeO_2 catalyst at 320 °C for 20 h at a steam to CO ratio of 2 (6.4% CO, 7.1% CO_2, 0.7% CH_4, 43.0% H_2, 28.4% H_2O, and 14.4% N_2, GHSV = 45,515 mL/g_{cat}h). At the initial time of the experiment CO conversion was ca. 90% and decreased to 85% after 20 h. It seems that Pt/CeO_2 catalysts prepared by co-precipitation are much more stable compared to the SF and DF made Pt/CeO_2 catalysts. The difference in reaction conditions is the addition of CH_4 in Jeong´s work which might avoid coke formation and

increases CO formation ($CH_4 + H_2O \rightleftarrows CO + 3\,H_2$) [195]. In general, catalyst deactivation can be caused by active metal sintering, decreasing dispersion or formation of carbonate species. In addition, high temperature and a reducing atmosphere promote sintering of particles. Azzam and co-workers [182] found that sintering was accelerated under WGS reaction conditions compared to experiments in H_2 or H_2/CO. Likewise the deactivation of WGS catalysts is due to formation of carbonate species on the catalysts surface area, which can block the active centers [209].

4.3.4 Conclusion

The present study shows that the WGS reaction activity of Pt and Rh based catalysts is highly influenced by the nature of the supports. CeO_2, ZrO_2 and $Ce_xZr_{1-x}O_2$ supported Pt and Rh catalysts exhibit high dispersion, small nano particle size (1.5 – 3.0 nm for Pt, 2.2 – 3.8 nm for Rh) and nanocrystallinity and high surface area of supports. The main difference between SF and DF made catalysts is that SF made catalysts have a higher specific surface area, whereas DF made catalysts have lower reduction temperature. These characteristics can be traced back to the synthesis methods since in case of DFSP noble metal clusters form independently of the support formation (see Figure 1.13).

The results of catalytic performance tests results in a tubular reactor as well as in a capillary micro reactor are in agreement, implying that the results are reproducible. The results show that noble metal particles on CeO_2, ZrO_2 and $Ce_xZr_{1-x}O_2$ can have very high WGS activity at a high steam to CO ratio (S/C = 4) which can be traced back to decomposing formate on the surface according to the proposed reaction mechanism. Furthermore, the results indicate that both SF and DF made catalysts show an excellent performance compared to literature. A comparison of Pt based catalysts with Rh based catalysts shows that Pt based catalysts can be considered as promising catalysts for WGS reactions. These catalysts reach full CO conversion (thermodynamic equilibrium point) at low temperature (350 °C). Additionally these catalysts exhibit higher selectivity compared to Rh based catalysts (methane formation starting at 350 °C). Regarding the supports, nano crystalline CeO_2 and $Ce_xZr_{1-x}O_2$ supported noble metal catalysts exhibit the highest activity and turnover frequency (TOF) as well as low activation energy in the WGS reaction. The difference between SF and DF made CeO_2 supported noble metal catalysts is low, but DF made catalysts reach the thermodynamic equilibrium point at lower temperature. In

case of Pt/ZrO_2 and Rh/ZrO_2 catalysts a huge difference between synthesis methods appears in CO conversion. The catalytic performance of Pt/ZrO_2 and Rh/ZrO_2 catalysts can be enhanced if double flame spray pyrolysis is used as synthesis method. The stability of Pt based catalysts was tested in a reformer gas mixture at 400 °C for 48 h. The results clearly show a decrease in CO conversion over time. However, the deactivation of Pt/CeO_2 and $Pt/Ce_xZr_{1-x}O_2$ catalysts was lower compared to for Pt/ZrO_2 catalysts. Nevertheless, the catalysts show high CO conversion at the beginning of the experiment. In the future, the SF and DF made catalysts can be improved by varying of parameters, such as solvents, concentration, angle and distance between the two nozzles, or/and residence time. Moreover, the sieve fraction of the catalysts can be optimized.

PART IV: ADVANCED SPECTROSCOPIC STUDIES

5 *In situ* XAS Characterization of Rh Catalysts and a Membrane Foil under WGS Reaction Conditions in a new Micro-Structured Membrane Reactor

5.1 Introduction

Micro reactors offer several advantages due to high surface area to volume rations, and high heat and/or mass transfer properties [75, 76]. Only a low amount of catalyst is required for a micro structured plate per reactor volume, which allows more efficient utilization of the catalyst due to the improved heat and mass transfer [77]. Membrane reactors can shift the equilibrium limitation of chemical reactions by continuously removing one of the reaction products from the reaction area. Therefore, integration of H_2 selective membranes into micro reactors can be highly beneficial for hydrogen production processes [68]. In order to gain a deeper understanding of such systems, both the catalysts and the membranes need to be characterized, preferentially under operating conditions [129] and in a spatially resolved manner [210, 211]. For this purpose, a special micro reactor was designed, which allows to characterize catalysts and membranes under WGS conditions using X-ray absorption spectroscopy (XAS). The results of this study can serve a basis for further development of both catalysts and membranes in the future.

5.2 Testing a Specially Designed Micro-Structured Membrane Reactor at the Synchrotron

5.2.1 Experimental part

In the micro-structured membrane reactor (described in section 3.3.1, Figure 5.1) specially designed for this study two channel plates, one for the catalytic bed and reactant gas flow and the other one for the produced H_2, are separated by a thin H_2 selective 8.5 µm thick PdAg or a 16 µm thick Pd alloyed membrane (Figure 5.1b). Two 38 µm thick Ni based foils as windows for monochromatic X-rays, heating cartridges in the reactor shell and gas connections allow XAS measurements at the Rh and Pd K-edge under reaction conditions.

X-ray absorption near edge structure (XANES) and extended X-ray absorption fine structure (EXAFS) measurements at the Rh K-edge (23220 eV) were performed at the Swiss Norwegian Beamline (SNBL) and at the Spanish CRG Beamline (BM25 SPline) at the European Synchrotron Radiation Facility (ESRF) in transmission and fluorescence mode. The micro-structured membrane reactor was first tested at SNBL and later used for two beamtimes at BM25A. For each beamtime a different experimental pathway was used:

Test study at Swiss Norwegian Beamline (SNBL, Experiment I):

720 mg (total amount) of a 10.5 wt% Rh/CeO_2 catalysts was dissolved in 1 mol/L NaOH. Each of the nine channels of the catalyst channel palette was coated with this solution and dried overnight. The first series of XAS spectra were recorded at room temperature under He at three points along the central channel. The aim of these measurements was to obtain structural information about the catalyst and the membrane close to the inlet, in the middle and at the outlet of the reactor while removing the produced hydrogen (Figure 5.1b). Afterwards the reactor was heated from room temperature to 150 °C with a heating rate of 5 °C/min under He. At this temperature the gas feed was switched from Helium to the WGS reaction gas mixture (8% CO, ca. 32% H_2O, 60% He, total flow 25 mL/min, *the exact amount of vapor (H_2O) is unknown*). Finally the reactor was heated from 150 °C to 310 °C at a heating rate of 5 °C/min under WGS reaction conditions. During heating EXAFS spectra were recorded at 20 °C intervals.
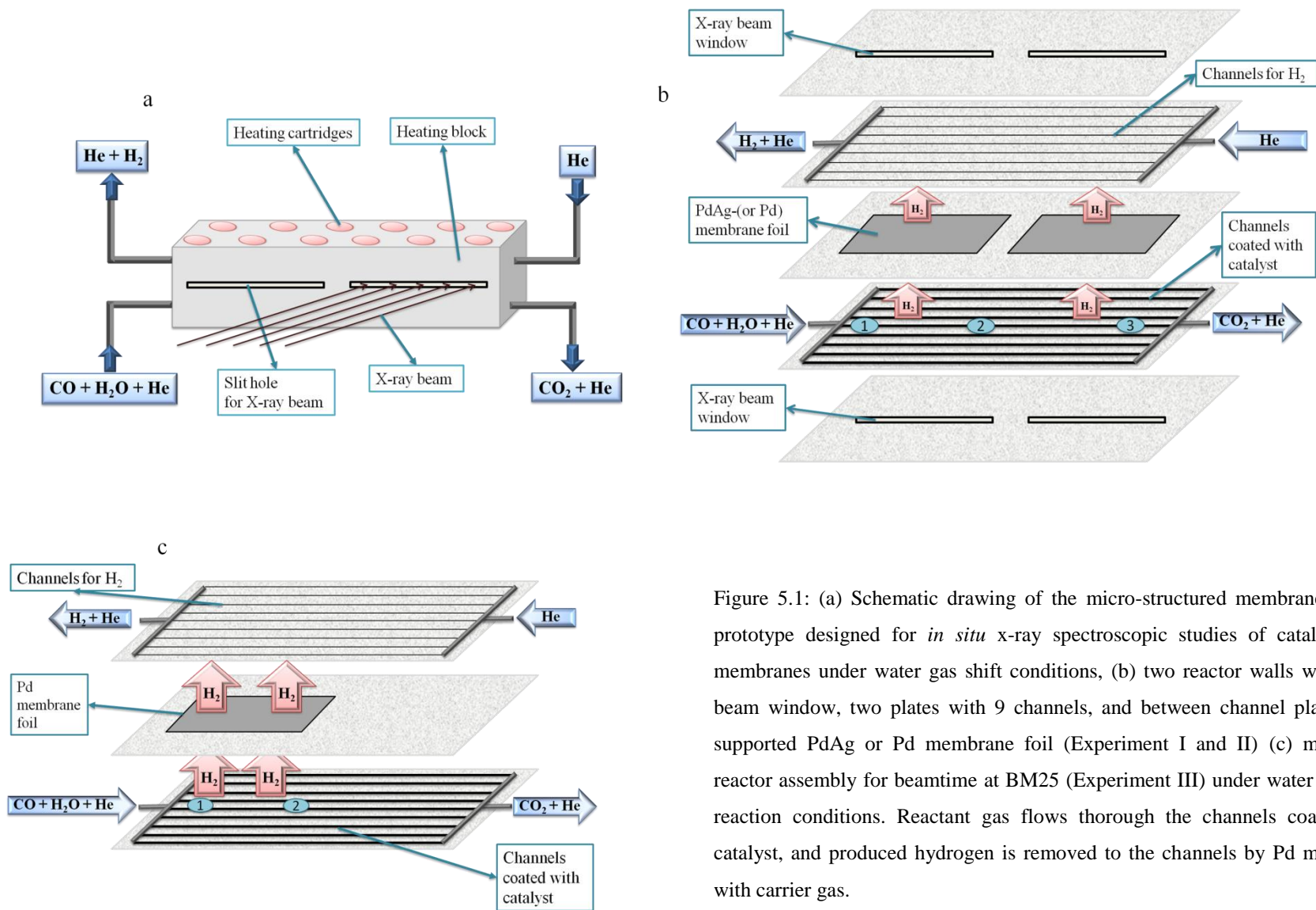
Figure 5.1: (a) Schematic drawing of the micro-structured membrane reactor prototype designed for *in situ* x-ray spectroscopic studies of catalysts and membranes under water gas shift conditions, (b) two reactor walls with x-ray beam window, two plates with 9 channels, and between channel plate metal supported PdAg or Pd membrane foil (Experiment I and II) (c) membrane reactor assembly for beamtime at BM25 (Experiment III) under water gas shift reaction conditions. Reactant gas flows thorough the channels coated with catalyst, and produced hydrogen is removed to the channels by Pd membrane with carrier gas.

Extended study at BM25A (Experiment II):

A further study with the same catalyst in the micro-structured membrane reactor was performed at the Spanish CRG Beamline (BM25 SPline) at ESRF using the same coating described previously at SNBL. The first series of EXAFS spectra were recorded at room temperature under He at three points along the central channel. Afterwards the reactor was heated to 400 °C under He. At this temperature, EXAFS spectra were recorded at three points along the central channel. During this beamtime the 10.5 wt.% Rh/CeO_2 catalyst was studied under three different WGS reaction conditions at 400 °C in the micro-structured membrane reactor (summarized in Table 5.1).

Table 5.1: Water gas shift reaction conditions for XAS experiments using the micro-structured membrane reactor at the BM25 beamline (Experiment II).

WGS reaction condition	S/C ratio	$\dot{V}_{total}$ [mL/min]	$\dot{V}_{CO}$ [mL/min]	$\dot{V}_{H2O}$ [mL/min]	$\dot{V}_{He}$ [mL/min]
1	1.5	50	4	6	40
2	1.5	50	2	3	45
3	2	50	12	24	14

Measurement with upgraded *in situ* set-up at BM25A (Experiment III):

For the first test series during this beamtime 50 mg of 10.5 wt.% Rh/CeO_2 catalyst was mixed with 0.2 ml NaOH (1 mol/L) and the central channel and two further channels of the membrane reactor were coated step by step with this mixture. The XAS spectra were recorded close to the inlet (position 1, Figure 5.1c). During this test the edge jump in the XAS spectra was too small, the absorption signal was poor and only at one position it was possible to acquire XAS spectra of sufficient quality could be acquired. Therefore, the central channel in the micro-structure membrane reactor was coated a second time using further 50 mg of 10.5 wt.% Rh/CeO_2 catalyst mixed with 0.1 ml NaOH (1 mol/L) in order to increase the thickness of the catalyst layer to improve data quality. Afterwards, it was possible to record spectra at a position close to the inlet (position 1, Figure 5.1c) and close to the middle of the window/membrane as labeled "close to the outlet" (position 2, Figure 5.1c). For both studies, the first series of XAS spectra was recorded

at room temperature under He. Afterwards the membrane reactor was heated up to 350 °C, and several spectra were recorded at this temperature under He. Afterwards the gas feed was switched from Helium to the WGS reaction gas mixture. As a gas mixture three different gas components were used. 10% CO was kept constant in the gas mixture and S/C ratios of 1.5/1, 1/1.5 and 1/1 were dosed (total flow 50 mL/min, He as balance gas).

5.2.2 Results and Discussion

5.2.2.1 *In situ* XAS Study on PdAg Membrane and Rh/CeO$_2$ Catalyst in a Micro-Structured Membrane Reactor Prototype

For these experiments commercial ultrathin hydrogen selective PdAg membrane with a thickness of 8.5 μm was installed in the micro-structured membrane reactor. At selected temperatures Pd K-edge EXAFS spectra of the membrane and Rh K-edge spectra of the catalyst were acquired at three positions along the central reactor channel. Figure 5.2 shows Pd K-edge absorption spectra of the PdAg foil in the micro-structured membrane reactor before and after coating with 10.5 wt.% Rh/CeO$_2$ catalyst at room temperature and after applying WGS reaction conditions at room temperature. In all cases XAS spectra of sufficient quality could be acquired. Clearly, neither heating nor the WGS reaction conditions have an influence on the chemical environment of the Pd atoms in the membrane. The Fourier transformed EXAFS data (Figure 5.2b) give a first impression of the atomic environment around the absorber atoms. Detailed information about the chemical environment was obtained by fitting these Pd EXAFS data (R-space; R = 1 − 3 Å, Figure A.13 in Appendix). The results are summarized in Table 5.2. The distance between absorber atom and neighbor atoms in the first shell is 2.76 Å, in the second shell 3.87 Å, and coordination numbers are 12 in the first shell, 6 in the second shell, respectively. All the resulting parameters show that there is no change in coordination numbers, disorder and bond-lengths around Pd atom during WGS. These results reconfirm that neither heating nor the WGS reaction conditions have an influence on the chemical environment of the Pd atoms in the membrane, indicating that the Pd membrane was stable and did not undergo any structural changes during reaction.
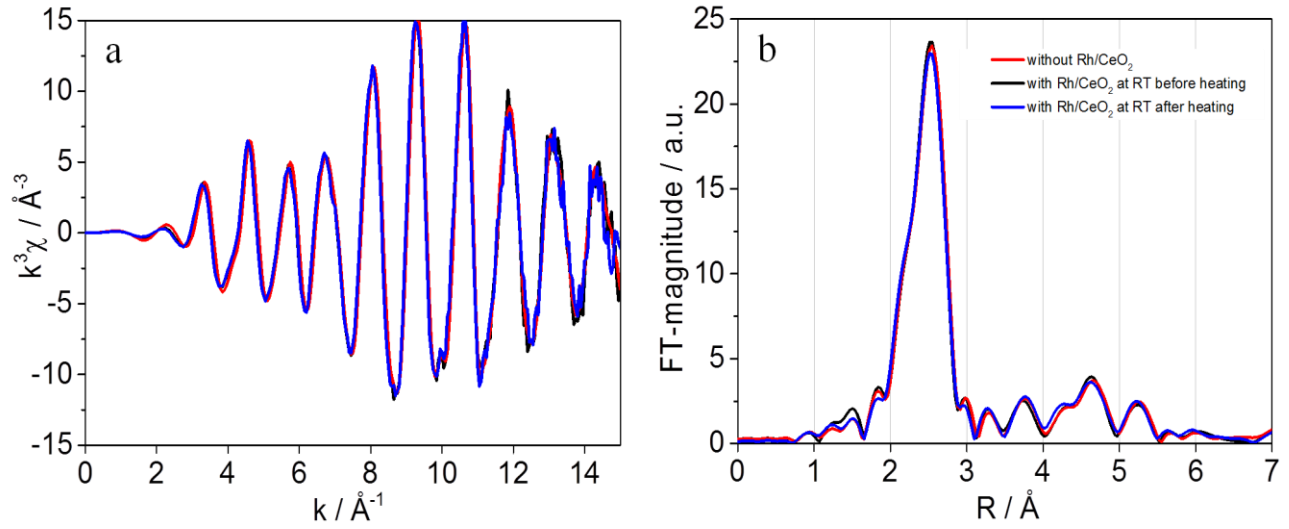
Figure 5.2: (a) k^3–weighted Pd K-edge EXAFS data and (b) corresponding Fourier transformed EXAFS data of the PdAg foil in micro-structured membrane reactor without catalyst, and with catalyst at room temperature and after the WGS reaction.

Table 5.2: Structural parameters obtained from fitting of Pd EXAFS data (Figure A.13). S_0^2: amplitude reduction factor (0.81 ±0.05), N: coordination number, r: interatomic distance; σ^2: Debye-Waller factor, χ_v^2: goodness of fit.

Bond	Shell	N	r [Å]	σ^2 10^{-3} [Å^2]	χ_v^2
without catalyst					
Pd – Pd	1st	12 [a]	2.76 (±0.002) [b]	6.8 (±0.3) [b]	22
	2nd	6 [a]	3.87 (±0.017) [b]	12.3 (±1.9) [b]	
with catalyst at RT before heating under He					
Pd – Pd	1st	12 [a]	2.76 (±0.002) [b]	6.8 (±0.3) [b]	295
	2nd	6 [a]	3.87 (±0.017) [b]	12.5 (±1.6) [b]	
with catalyst at RT after heating under He					
Pd – Pd	1st	12 [a]	2.76 (±0.002) [b]	7.2 (±0.4) [b]	30
	2nd	6 [a]	3.87 (±0.017) [b]	13.2 (±2.7) [b]	

[a] set parameter; [b] adjusted parameter

Figure 5.3 shows Rh K-edge XANES spectra of the catalyst layer in the central channel recorded *in situ* at the inlet side (Figure 5.1b, position 1) of the micro-structured membrane reactor under

WGS reaction conditions. The decrease in white line intensity at 170 °C indicates reduction of Rh oxide to a metallic phase under WGS reaction conditions. However, the reduction temperature of 10.5 wt.% Rh/CeO_2 was shifted to higher temperature under WGS reaction conditions compared to the temperature of reduction in H_2 (114 °C) reported later in this chapter (section 5.3.2, Figure 5.18a).
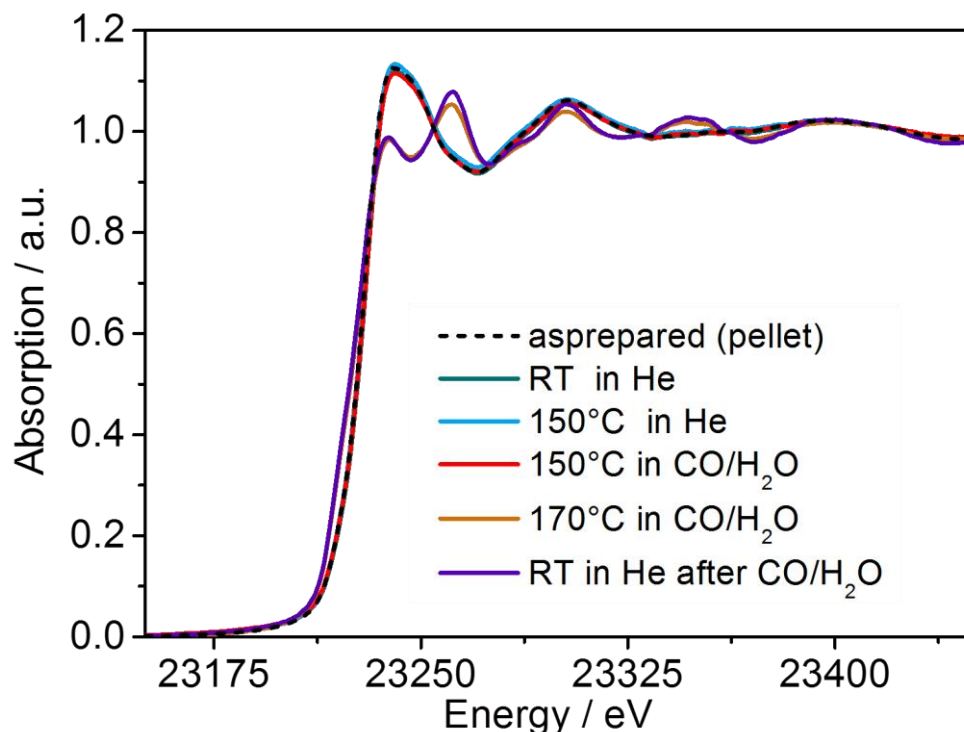
Figure 5.3: (a) Rh K near edge (XANES) spectra of 10.5 wt.% Rh/CeO_2 in the micro-structured membrane reactor under WGS reaction conditions and *ex situ* absorption data of the 10.5 wt% Rh/CeO_2 as prepared catalyst.

EXAFS spectra of the 10.5 wt.% Rh/CeO_2 were recorded at three different positions (Figure 5.1b). The Fourier transformed k^2–weighted EXAFS data provide qualitative information about the atomic environment around the Rh absorber atoms. EXAFS data recorded at position 1 and position 2 are compared in Figure 5.4 in order to gain information about the relationship between oxidation state of rhodium particles and the removal of the produced hydrogen during the reaction. Since the EXAFS data recorded at position 3 showed a high noise level at higher k values, this position was excluded from the analysis. The results in the EXAFS region show that at 170 °C under WGS reaction conditions the rhodium particles are in a reduced state at both positions (1 and 2). The EXAFS data recorded at these 2 points indicate that the structure of catalyst does not change along the central channel. The objective of these experiments was to

monitor changes in oxidation state of Rh along the channel. However, the results do not show any changes in this case. Since the results are similar for both positions, further EXAFS data are only shown for position 1 in the following.
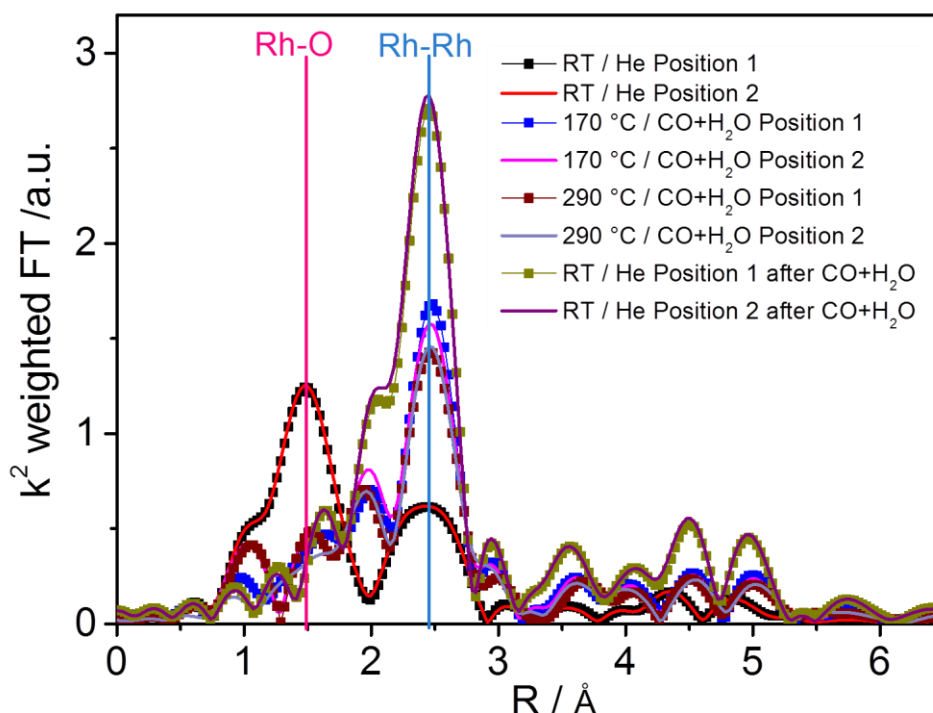
Figure 5.4: k^2–weighted Fourier transformed data of 10.5 wt.% Rh/CeO_2 catalyst at RT, at 150 °C under He, at 170, and 290 °C under 8% CO, 32% H_2O, 60% He and at RT after heating under He in the micro-structured membrane reactor at position 1 and position 2. Note that during in this first feasibility study the water vapor dosage could only be estimated.

Fourier transformed Rh K-edge EXAFS data of the 10.5 wt.% Rh/CeO_2 catalyst at room temperature, at 150 °C under He, and at 150 °C under WGS reaction conditions are presented in Figure 5.5a. The k^3–weighted EXAFS data and the corresponding fitting curves are shown in Figure 5.5b. The structural fitting parameters for data analysis are summarized in Table 5.3. The model used to fit the experimental data included two main shells: a Rh − O shell and a Rh − Rh shell (Figure 5.5b). This model was used in a previous study that indicated a rhodium (III) oxide (Rh_2O_3) structure with bonding distances 2.01 Å (Rh − O) and 2.69 Å (Rh − Rh) [112]. The radius of the first coordination sphere (2.03 Å) is very similar to the Rh − O bond length in Rh_2O_3. The corresponding coordination numbers (oxygen) are 4.5 (±0.6) and 4.7 (±0.5) for this catalyst, whereas in Rh_2O_3 Rh coordinates with 6 oxygen atoms.
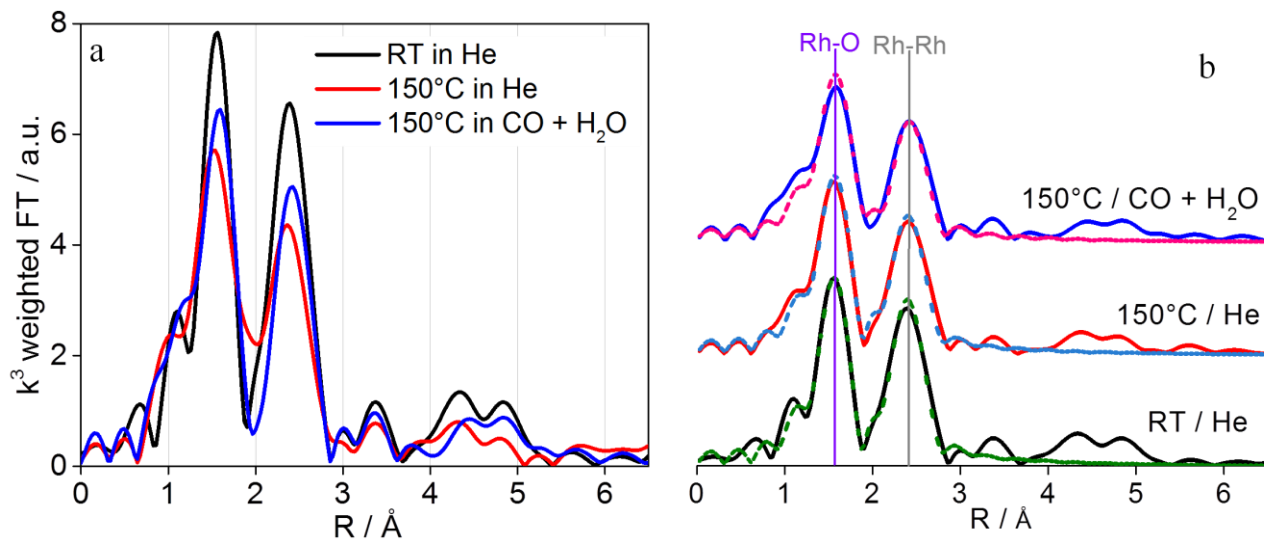
Figure 5.5: (a) k^3–weighted Fourier transformed EXAFS data of 10.5 wt.% Rh/CeO$_2$ catalyst at room temperature, at 150 °C under He and at 150 °C in CO + H$_2$O (b) fitted data obtained from analysis using Artemis program (experimental data: solid lines, fitting data: dash lines).

Table 5.3: Structural parameters obtained from fitting of Rh K-edge EXAFS data (Figure 5.5) (set parameter: amplitude reduction factor (S_0^2) = 0.75 ±0.05. varied parameter: N: coordination number, r: interatomic distance; σ^2: Debye-Waller factor, χ_v^2: goodness of fit).

Reaction conditions	Rh – O			Rh – Rh			χ_v^2
	N	r [Å]	σ^2 10^{-3} [Å^2]	N	r [Å]	σ^2 10^{-3} [Å^2]	
RT/He	4.5 (±0.6) [a]	2.03 (±0.01) [a]	3.6 (±1.0) [a]	4.0 (±0.9) [a]	2.70 (±0.02) [a]	7.1 (±1.2) [a]	60
150 °C/He	4.7 (±0.5) [a]	2.03 (±0.01) [a]	4.2 (±0.7) [a]	3.2 (±0.6) [a]	2.70 (±0.01) [a]	6.7 (±1.0) [a]	32
150°C/CO+H$_2$O	4.7 (±0.5) [a]	2.04 (±0.01) [a]	4.8 (±0.8) [a]	3.3 (±1.9) [a]	2.70 (±0.01) [a]	7.9 (±1.6) [a]	80

[a] varied parameter

Gayen et al.[212] reported that if Rh ions are substituted for Ce^{4+}, the first coordination shell around Rh ion will consist of oxygen ions. In pure bulk CeO$_2$ Ce^{4+} is coordinated with six O^{2-}

ions, but the surface Ce^{4+} ions have only four O^{2-} ions, thus the Rh ions substituting for Ce^{4+} sites are largely located in the surface layer of CeO_2 crystallites. In such a model Rh ions should have four O^{2-} ions as neighbors in the first shell which is observed in the present case [212]. The second peak at ca. 2.70 Å is attributed to Rh − Rh scattering at the second nearest neighbor distance in Rh_2O_3 [112]. Figure 5.5a shows a decrease in the amplitude of peaks due to increasing temperature and switching to the WGS gas mixture (8% CO, 32% H_2O, 60% He) indicating an increase in structural disorder. The Rh particle size in oxide state which was obtained from the coordination number is 1.5 nm in He at RT, in He and in CO/H_2O at 150 °C.
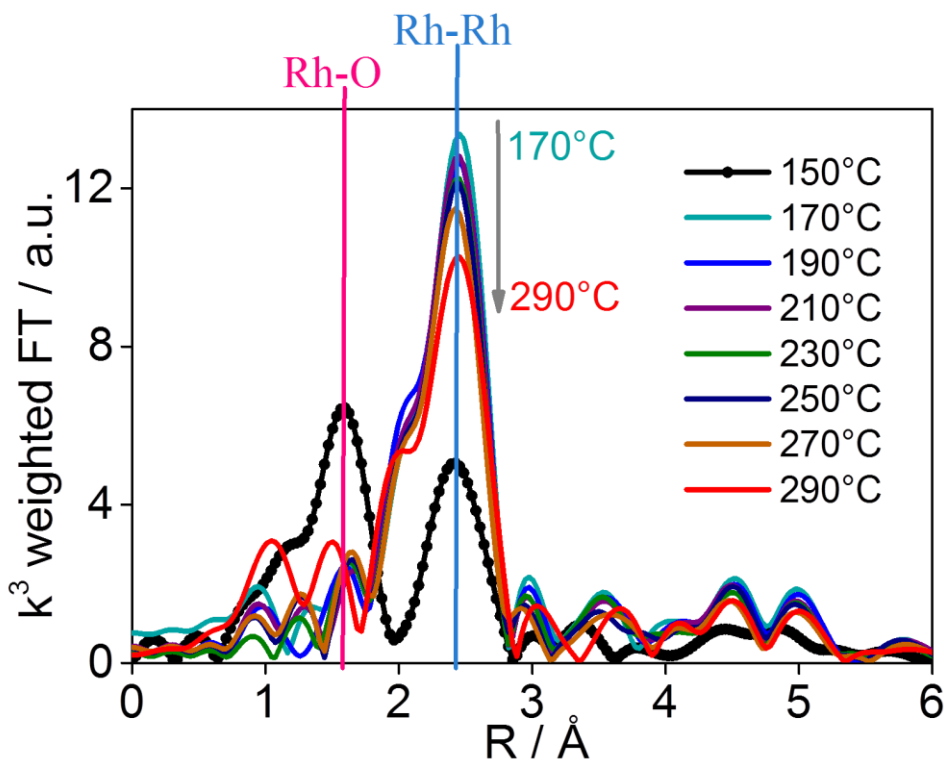
Figure 5.6: k^3–weighted Fourier transformed EXAFS data of 10.5 wt.% Rh/CeO_2 catalyst at different temperatures under WGS reaction conditions at position 1 (close the reactor inlet).

As mentioned above, the reactor was heated from 150 °C to 310 °C under WGS reaction conditions. During heating EXAFS spectra were recorded in 20 °C intervals. The magnitudes of the Fourier transformed Rh K-edge EXAFS data acquired at different temperatures are shown in Figure 5.6. Structural parameters were derived from data fitting of the k^3–weighted EXAFS data in R-space (R = 1 − 3 Å). The results of the EXAFS data analysis for different temperatures under WGS reaction conditions are presented in Table 5.4. The coordination numbers, Rh − Rh

bond lengths of the first coordination shell and Debye-Waller-factors were analyzed as a function of temperature (Figure A.14). After *in situ* WGS reaction, the first shell Rh − Rh coordination number increased and no oxygen backscattering was observed, indicating the formation of metallic Rh particles. In the reduced phase of the catalyst Rh had an average coordination number of 9, which corresponds to a particle size of 2.2 nm. The results also show that the Rh − Rh bond lengths do not change with increasing temperature, whereas the Debye-Waller-Factor increased due to increasing thermal disorder. However, the Rh − Rh distance in the 10.5 wt.% Rh/CeO_2 catalyst is shorter than compared to bulk rhodium (2.71 Å).

Table 5.4: Structural parameters obtained from Rh K-edge EXAFS data fitting (Figure 5.6) (set parameter: amplitude reduction factor $(S_0^2) = 0.75 \pm 0.05$. varied parameter: N: coordination number, r: interatomic distance; σ^2: Debye-Waller factor. χ_ν^2: goodness of fit).

Temperature [°C]	Bond	Shell	N	r [Å]	σ^2 10^{-3} [Å^2]	χ_ν^2
170	Rh – Rh	1st	8.7 (±1.2) [a]	2.69 (±0.02) [a]	7.5 (±0.7) [a]	448
190	Rh – Rh	1st	9.2 (±1.2) [a]	2.68 (±0.03) [a]	7.9 (±0.7) [a]	270
210	Rh – Rh	1st	9.4 (±0.8) [a]	2.68 (±0.03) [a]	8.0 (±0.5) [a]	125
230	Rh – Rh	1st	9.1 (±0.7) [a]	2.68 (±0.03) [a]	8.1 (±0.5) [a]	112
250	Rh – Rh	1st	8.9 (±0.8) [a]	2.68 (±0.03) [a]	8.1 (±0.6) [a]	82
270	Rh – Rh	1st	9.0 (±1.2) [a]	2.68 (±0.03) [a]	8.4 (±0.7) [a]	178

[a] adjusted parameters

5.2.2.2 Extended *in situ* XAS Study on a Rh/CeO_2 Catalyst in the Micro-Structured Membrane Reactor Prototype

A further study with the same catalyst was performed at the BM25 SPline beamline (the Spanish CRG Beamline, Experiment II) at ESRF. During this beamtime the 10.5 wt.% Rh/CeO_2 catalyst was studied under three different WGS reaction conditions in the micro-structured membrane reactor. The reaction conditions are summarized in Table 5.1. Prior to these measurements under WGS reaction conditions the catalyst was heated up under He to 400 °C.
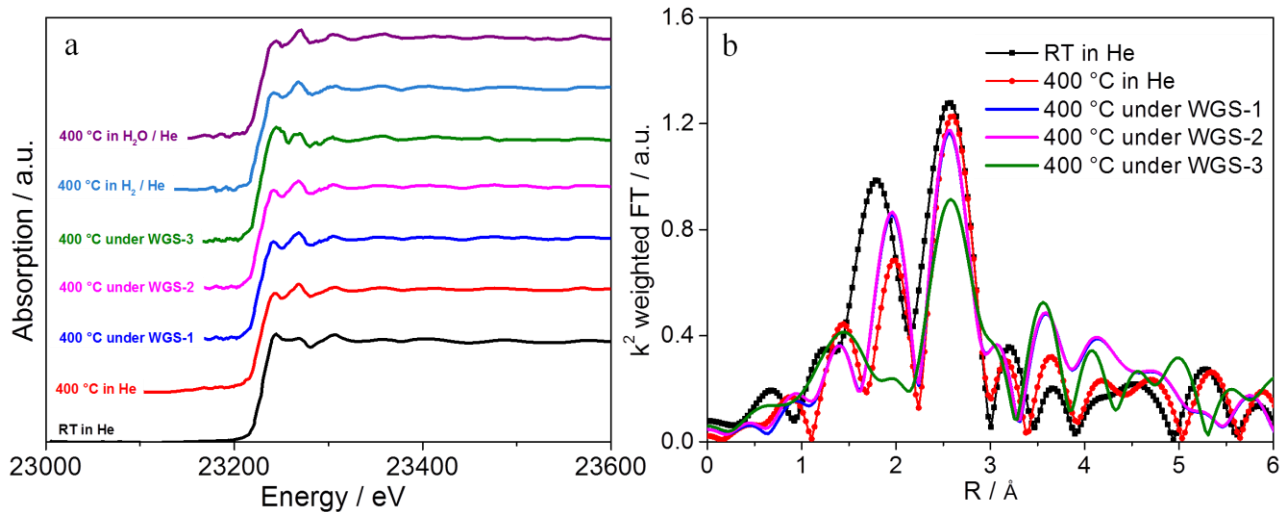
Figure 5.7: (a) XANES spectra at the Rh K-edge and k^2–weighted Fourier transformed EXAFS data of 10.5 wt.% Rh/CeO$_2$ at RT and at 400°C in He, and under different WGS reaction conditions (Table 5.1) in the micro-structured membrane reactor.

Figure 5.7a shows normalized XANES spectra of the 10.5 wt.% Rh/CeO$_2$ catalyst at Rh K-edge measured close to the reactor inlet (position 1; Figure 5.1b). The XANES spectra recorded at RT (black line, Figure 5.7a) show that the Rh/CeO$_2$ catalyst was reoxidized, since it was exposed to air for a long time, showing similar peak trends as reported in section 4.1.3.2, Figure 4.5. The whiteline intensity decreased with increasing temperature in He, indicating formation of metallic Rh particles. However, the k^2–weighted Fourier transformed spectra in Figure 5.7b show that a contribution from a Rh – O shell was still present. At 400 °C the gas feed was switched to WGS-1, WGS-2 and to WGS-3 reaction conditions subsequently (parameters in Table 5.1). The whiteline intensity in the spectra recorded under WGS-1 and WGS-2 reaction conditions shows that the catalyst was in a reduced state. On the contrary, the whiteline intensity increased under WGS-3 reaction conditions, indicating that the catalyst might be slightly reoxidized (Figure 5.7a). Under WGS-3 reaction conditions the water concentration was 4 times higher under WGS-1 and WGS-2 reaction conditions, indicating that after removal of hydrogen produced in the WGS reaction, the gas mixture may have an oxidizing effect on the catalyst. To understand better whether the H$_2$O vapor can reoxidize the catalyst, as a next step the catalyst was reduced in 5% H$_2$/He and then exposed to 12% H$_2$O/He. As shown in Figure 5.7a the whiteline intensity decreased during reduction in H$_2$. However, the catalyst was not changed into an oxidized state during the treatment with H$_2$O vapor as assumed. In conclusion, the high amount of H$_2$O vapor

leads to a corruption in the whiteline intensity. Since the catalyst in the micro-structured membrane reactor was previously used at the SNBL beamline (see above) the catalyst bed shows inhomogeneities, leading to a high noise level in the data. Therefore, structural parameters could not be extracted from the EXAFS data analysis for all conditions.

5.2.2.3 EXAFS Investigation of a Rh/CeO$_2$ Catalyst and a Pd Membrane in the Micro-Structured Membrane Reactor Prototype using an upgraded *in situ* Set-up

Since several problems (section 3.3.2) occurred with the mobile *in situ* setup upgraded for gas dosing and online gas analysis during the first two beamtimes, this set-up was upgraded. This upgraded set-up allows to accurately adjust the WGS gas mixture and to remove the produced hydrogen with a sweep gas during XAS measurements while simultaneously analyzing the catalysts activity by detecting the produced hydrogen and the consumed CO. 50 mg of 10.5 wt.% Rh/CeO$_2$ catalyst was used to coat the central channel and further two channels of the micro-structured membrane reactor. This catalyst was studied under three different WGS reaction conditions in the reactor. The reaction conditions are summarized in Table 5.5. First the catalyst was heated up to 350°C under He. Afterwards WGS reaction conditions 1, 2 and 3 were applied.

Figure 5.8 shows a comparison of Rh K-edge XAS spectra of the catalyst in different reaction atmospheres. The spectra were recorded in fluorescence mode close to the inlet (only one position was selected, where the catalyst bed was sufficiently homogeneous). First spectra were recorded at room temperature in He, afterwards the reactor was heated up to 350 °C in He. At that temperature the Rh species underwent a transition from an oxidized state to a reduced state. A decrease in white line intensity indicates that the oxygen rich environment around the Rh absorbers in the sample no longer exists. Decomposition of Rh species at high temperature was also observed during previous studies (Figure 5.7).

Table 5.5: Water gas shift reaction conditions for the micro-structured membrane reactor experiments at the BM25 beamline (Experiment III).

WGS reaction conditions	S/C ratio	H_2O [%]	CO [%]	He [%]
1	1.5/1	15	10	75
2	1/1.5	6.6	10	83.4
3	1/1	10	10	80
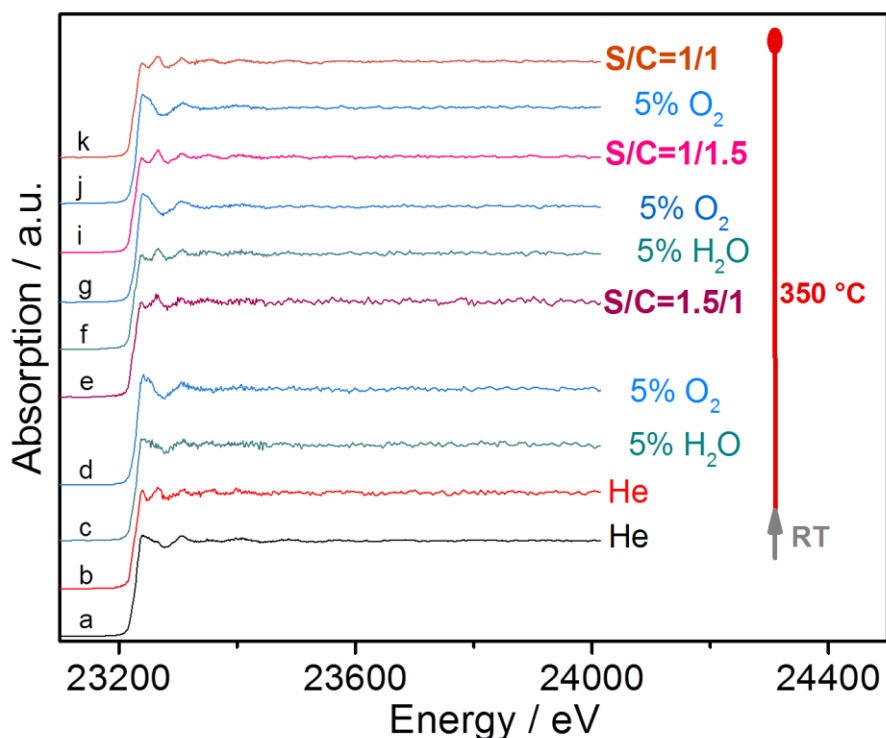
Figure 5.8: Rh K-edge XANES/EXAFS spectra of 10.5 wt.% Rh/CeO_2 in the micro-structured membrane reactor in different atmospheres; (a) He at room temperature, (b) He at 350 °C, (c and f) 5% H_2O/He, (d, g and j) 5% O_2/He, (e, i and k) CO/H_2O at 350 °C (recorded in fluorescence mode).

To reoxidize the catalyst, two different oxidizing atmospheres were used; H_2O vapor and O_2. When the sample was exposed to 5% H_2O vapor in He at 350 °C the XANES features indicate that the catalyst was slightly oxidized (Figure 5.8-c). Afterwards, 5% O_2 in He was used as an oxidant. The whiteline intensity significantly increased, indicating that the oxidation was almost complete (Figure 5.8-d). After these reoxidation steps at 350 °C, the gas mixture was switched to the first water gas shift reaction condition (S/C=1.5/1). An immediate decrease in whiteline

intensity was observed and the edge shifted slightly to lower energy as observed during previous studies indicating reduction. To investigate reoxidation after the WGS reaction the sample was first exposed to 5% H_2O/He and then to 5% O_2/He. H_2O as an oxidant did not lead to significant changes in whiteline intensity, as shown in Figure 5.8-f. Obviously rhodium cannot be reoxidized in water vapor after exposure to the WGS reaction conditions. However, exposure to O_2 after the WGS reaction led to a significant reoxidation as clearly seen in the XANES data (Figure 5.8-g). Using linear combinations of Rh_2O_3 (as a "fully oxidized" reference) and Rh foil (as a "fully reduced" reference) spectra, it was estimated that about 10% of the Rh atoms could be reoxidized with water vapor and more than 95% with O_2 after the WGS reaction. Since it was impossible to reoxidize the catalyst with water vapor after WGS, O_2/He was chosen as oxidant for the following measurements and after each WGS reaction cycle the catalyst was reoxidized with 5% O_2/He. After each reoxidation cycle similar results were obtained. Further WGS reactions were also performed and the results are shown in Figure 5.8. The oxidation state of Rh was not influenced by different S/C ratios. Linear combination fitting using the same reference spectra (Rh_2O_3 as a "fully oxidized" reference and Rh foil as a "fully reduced" reference), showed that at S/C ratios of 1.5/1, 1/1.5 and 1/1 approx. 95% of the Rh species are in a reduced state, whereas catalytic activity measurements and the MS product analysis clearly show differences for S/C ratios. The challenges of this work were to simultaneously analyze the gas composition on the retentate side (Figure 5.9 top) and permeate side (Figure 5.9 bottom) while at the same time performing XAS measurements. Figure 5.9 shows CO/CO_2 signals (retentate side; Uras) and concentration of the produced H_2 (permeate side; MS) measured *in situ* in the micro-structured membrane reactor coated with 50 mg of 10.5 wt% Rh/CeO_2 at 350 °C, ($\approx$ GHSV = 60,000 mL/g_{cat} h) and the corresponding WGS CO conversion is calculated as shown in section 3.4.2. Average values for CO conversion were calculated over 20 min (scan duration). The number for X_{CO} in the Figure 5.9 shows the range of the average values.
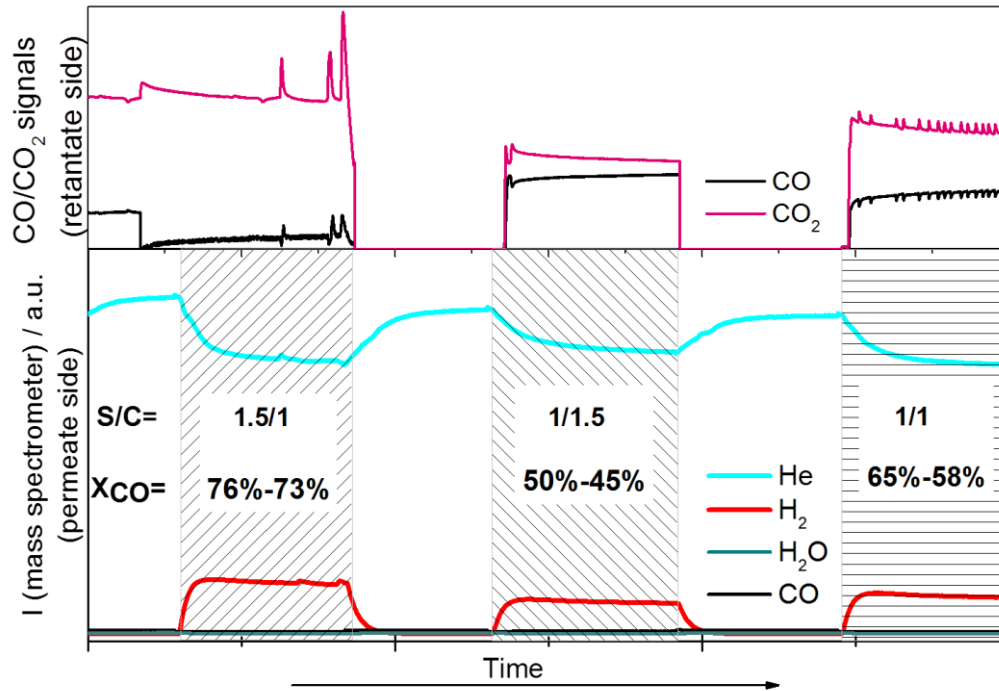
Figure 5.9: Traces of different MS signal of the gas outlet of the micro-structured membrane reactor at different S/C ratios with signals for the swap gas He (m/e = 4), the produced H_2 (m/e = 2) and the educts CO (m/e = 28) and H_2O (m/e = 18) (permeate side; bottom) and Uras signal for CO and CO_2 (retantate side; top). CO conversion was calculated $\left(\frac{[CO_2]}{[CO]+[CO_2]}\right)$ at the outlet of the retentate side (top).

The results show that CO conversion slightly increases with increasing S/C ratios. The conversion of CO is 76% for the highest S/C ratio, followed by 65% for 1/1 and 50% for 1/1.5, respectively (1.5/1 > 1/1 > 1/1.5). This can be traced back to the equilibrium of the water gas shift reaction, as the increase of H_2O as reactant would lead to higher CO consumption [13], as discussed in section 1.1.1. According to thermodynamics, elevated reaction temperature favors the reverse WGS reaction, but in the membrane reactor CO conversion can be improved by H_2 extraction from the reaction zone at higher temperature. In this micro-structured membrane reactor H_2 extraction can be monitored *in situ* (Figure 5.9). As soon as the reactant gas flow (CO and H_2O) through the catalytic bed is switched off the MS signal for H_2 also disappears. Moreover, Figure 5.9 shows that the increase in the signal for H_2 is well synchronized with the CO conversion. In addition, no MS signals of CO, CO_2, H_2O or other gases were detected on the permeate side, indicating that the H_2 selective Pd membrane foil is stable during *in situ* H_2 extraction (no crack in the membrane foil).

However, due to the poor signal-to-noise ratio only XANES data could be analyzed at this experimental stage, since the edge jump in the spectra was small. Therefore, the central channel of the microreactor was coated a second time using additional 50 mg of 10.5 wt.% Rh/CeO_2 catalyst, in order to increase the thickness of the catalyst layer and improve the data quality. As a result of this additional coating, the quality of EXAFS data was higher and EXAFS spectra could be recorded at two different positions (close to the inlet and in the middle of central channel, called outlet) and compared.

This thicker catalyst layer was heated up to 350°C in He. Figure 5.10a shows XANES spectra recorded at both positions (inlet and outlet of central channel). The low whiteline intensity in the spectra recorded in He at 350 °C shows that the catalyst is in a reduced state. Decomposition of oxidized Rh species at high temperature was also observed during previous studies (Figure 5.7 and Figure 5.8). Afterwards, spectra were recorded in 5% O_2/He and under WGS reaction conditions (S/C ratios of 1.5/1 and 1/1.5). Note that since previous measurements (Figure 5.7 and Figure 5.8) showed that water vapor is not a strong oxidant for this catalyst, the dynamic structural behavior in oxidizing atmosphere was additionally probed in study using 5% O_2/He. The increased whiteline intensity in Figure 5.10a indicates that an O-rich environment exists around the Rh atoms after the treatment with O_2, as expected from previous studies. The XANES spectra recorded at the inlet and outlet indicate that under both WGS reaction conditions (S/C ratios of 1.5/1 and 1/1.5) the catalyst is reduced to the same extent. More detailed information about the atomic environment of the absorbing Rh atoms under different reaction conditions was obtained from fitting the corresponding EXAFS data in R-space. The k^2–weighted EXAFS data of the catalyst layer at both positions and under both WGS reaction conditions are shown in Figure 5.10b. The signal-to-noise ratio in these spectra is higher compared to the first experiment during this beamtime (Figure 5.8) due to increased thickness of the catalyst layer. Comparison of the k^2–weighted EXAFS data at both positions did not indicate changes in the catalyst structure/oxidation state along the channel. Structural parameters were derived from fitting k^2–weighted EXAFS data in R-space. The resulting fit values for the coordination numbers CN, shell distances R, and Debye-Waller factors σ^2 (mean squared relative deviation) for Rh – Rh and Rh – O bonds are listed in Table 5.6.
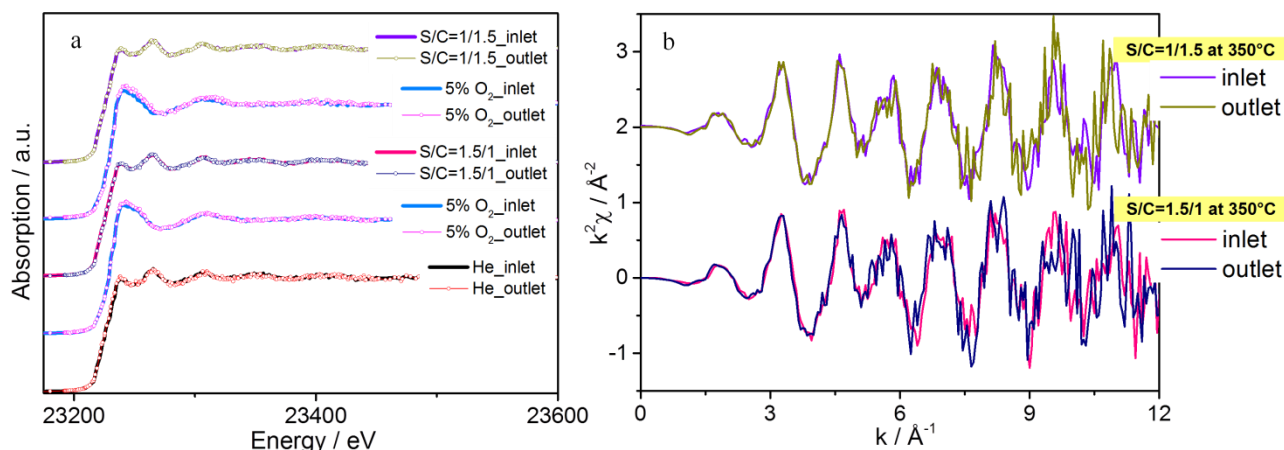
Figure 5.10: (a) Comparison of Rh K-edge XANES spectra of the 10.5 wt.% Rh/CeO_2 catalyst at 350°C under He, O_2 and WGS reaction conditions at positions close to the inlet and the outlet and (b) average of k^2–weighted Fourier transformed EXAFS data in the micro-structured membrane reactor (recorded in fluorescence mode).

After heating up in He, Rh – Rh scattering is dominant for both positions as shown in the Fourier transformed data in Figure 5.11a. The EXAFS fitting results show that at 350 °C in He the coordination number of the first Rh – Rh shell is 5.9 (± 1.27) (distance 2.66 Å) close to the inlet and 6.7 (± 0.99) (distance 2.64 Å) close to the outlet. An accurate determination of Rh – O coordination number close to the inlet was not possible due to its small contribution. Rh – O backscattering only weakly contributes also for the sample close to the inlet (high DW factor). After reoxidation in 5% O_2 the Rh – O contributions increased for both positions. In this case, results of linear combination fitting of XANES spectra using Rh_2O_3 and Rh foil as a reference spectra indicate that at the inlet 95% and at the outlet 98% of the Rh species are reoxidized. The coordination number of the Rh – O shell at the inlet (3.5 (± 0.84)) was slightly lower than at the outlet (4.3 (± 1.2)) with the same Rh – O bond length (2.01 Å). Weak Rh – Rh contributions still exist in the second shell, however due to the high the noise level at R values above 2 Å as shown in Figure 5.11a, an accurate determination of coordination number was not possible. Note that the previous study (in section 4.1.3.2) showed that this Rh – Rh contribution in the reoxidized sample (in the second shell) cannot be attributed to metallic Rh – Rh and it may also be due to the disordered nature of the Rh metallic-like phase.

Table 5.6: Structural parameters obtained from fitting of Rh K-edge EXAFS data (set parameter: amplitude reduction (S_0^2) factor = 1.06 ($\pm$0.17). varied parameters: N: coordination number, r: interatomic distance; σ^2: Debye-Waller factor. χ_ν^2: goodness of fit).

Atmospheres	Position	Rh – O			Rh – Rh			χ_ν^2
		N	r [Å]	$\sigma^2\ 10^{-3}$ [Å^2]	N	r [Å]	$\sigma^2\ 10^{-3}$ [Å^2]	
He	Inlet	1 [a, b]	1.77 ($\pm$0.26)	28.1 ($\pm$18.8)	5.9 ($\pm$1.27)	2.66 ($\pm$0.02)	8.2 ($\pm$1.9)	1.6
	outlet	—	—	—	6.7 ($\pm$0.99)	2.64 ($\pm$0.05)	10.1 ($\pm$1.4)	2.7
O$_2$	Inlet	3.5 ($\pm$0.84)	2.01 ($\pm$0.004)	6.3 ($\pm$3.2)	1 [a, b]	2.72 ($\pm$0.02)	7.9 ($\pm$3.7)	2.7
	outlet	4.3 ($\pm$1.2)	2.01 ($\pm$0.01)	2.3 ($\pm$2.3)	1 [a, b]	2.70 ($\pm$0.02)	10.3 ($\pm$4.7)	2.6
S/C = 1.5/1	Inlet	1 [a, b]	1.82 ($\pm$0.22)	13.3 ($\pm$4.9)	5.8 ($\pm$0.75)	2.68 ($\pm$0.006)	8.4 ($\pm$1.1)	3.1
	outlet	1 [a, b]	1.80 ($\pm$0.23)	23.5 ($\pm$14.1)	6.3 ($\pm$1.2)	2.68 ($\pm$0.008)	8.9 ($\pm$1.8)	3.4
S/C = 1/1.5	Inlet	1 [a, b]	1.80 ($\pm$0.02)	20.7 ($\pm$6.6)	6.03 ($\pm$0.63)	2.68 ($\pm$0.007)	8.4 ($\pm$0.9)	3.1
	outlet	1 [a, b]	1.84 ($\pm$0.20)	24.8 ($\pm$11.9)	6.07 ($\pm$0.95)	2.69 ($\pm$0.004)	8.9 ($\pm$1.4)	1.4

[a] Poor fit, as also indicated by fitting accuracy due to low contribution. [b] fixed parameter.
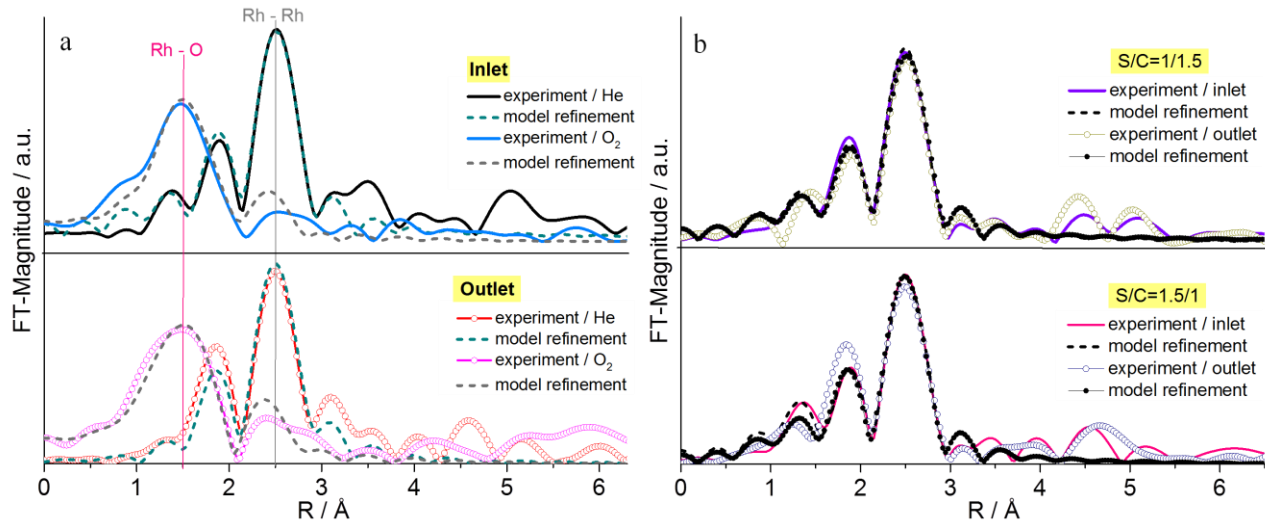
Figure 5.11: k^2–weighted Fourier transformed Rh K-edge EXAFS data and results derived from data analysis using the Artemis software (a) in He and O_2, (b) under WGS reaction conditions.

Under consecutive WGS reaction conditions the Fourier transformed data show a dominant Rh – Rh peak (Figure 5.11b). The absorbing Rh atoms were surrounded by ca.6 neighboring Rh atoms at a distance of 2.68 Å for both reaction conditions and the results at the inlet and the outlet are similar (Table 5.6). The low coordination number of Rh can either be a consequence of the small particle size (ca. 1 nm) or due to formation of $Rh^I(CO)_2$ species [109]. Still a detectable Rh – O contribution exists which indicates that rhodium is not completely in the Rh^0 state. However, the corresponding Rh – O coordination number could not be extracted from the data. Thus, Rh – O only weakly contributes as seen from the high DW factor. *In situ* measurements under WGS reaction conditions in the quartz capillary micro reactor (Figure 5.15 and Figure A.16, Table 5.9) show that the same catalyst (10.5 wt.% Rh/CeO_2) under WGS reaction conditions was in a reduced state and there was no detectable Rh – O backscattering which could indicate that rhodium was present in Rh^0 state. The difference between both experiments is that in the case of the micro-structured membrane reactor the hydrogen was extracted *in situ*. The integration of a H_2 selective membrane influences CO conversion (Le Chatelier's principle) i.e. the concentration of CO_2 produced via the WGS reaction is increased. As well known, CO_2 is a weakly oxidizing gas, therefore a reoxidation along the channel in micro reactor could not be observed. However a weak Rh – O contribution was noticeable during the WGS reaction as discussed above.

Figure 5.12 shows Uras signal and average values for WGS CO conversion (retentate side) and the MS signals for the produced H_2 (permeate side) in the outlet gas streams of the micro-structured membrane reactor coated with ca. 100 mg of 10.5 wt% Rh/CeO_2 at 350°C ($\approx$GHSV=30,000 mL / g h). Also in this case, the retentate (Figure 5.12 top) gas composition was analyzed using an Infrared spectrometer (Hermann & Braun Uras 10 E) and the permeate (Figure 5.12 bottom), gas composition was followed simultaneously using MS during XAS measurements. Average values for CO conversion were calculated over 50 min (scan duration). The number for X_{CO} in the Figure 5.12 shows the range of the average values. As expected, CO conversion increased due to the increased thickness of the catalyst layer in the micro-structured membrane reactor from 76% for $\approx$50 mg of catalyst to 83% for $\approx$100 mg of catalyst. Note that the 50 mg portion of the catalyst was used before and the additional 50 mg catalyst was fresh. In this case, also the CO conversion increased with increasing S/C ratio.
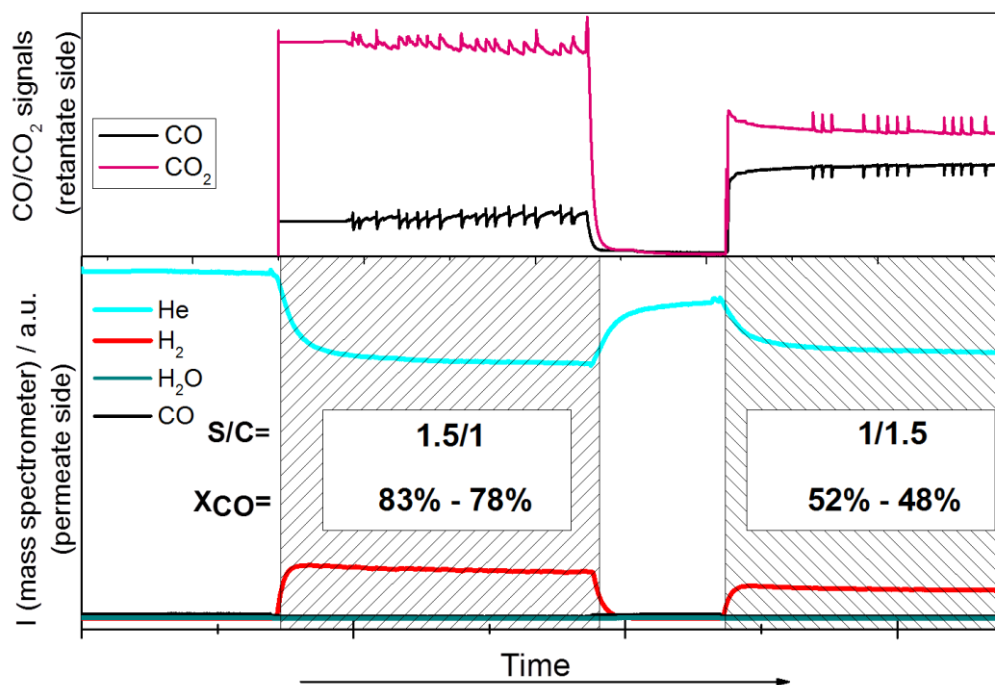
Figure 5.12: Traces of different MS signal of the gas outlet of the micro-structured membrane reactor at different S/C ratios with signals for the swap gas He (m/e = 4), the produced H_2 (m/e = 2) and the educts CO (m/e = 28) and H_2O (m/e = 18) (permeate side; bottom) and Uras signal for CO and CO_2 (retantate side; top). CO conversion was calculated $\left(\frac{[CO_2]}{[CO]+[CO_2]}\right)$ at the outlet of the retentate side (top).

Since with this set-up H_2 extraction could be monitored *in situ* during synchrotron based XAS measurements, Pd K-edge spectra were also recorded under the same WGS reaction conditions as during the Rh K-edge experiments. In this membrane microreactor a commercial ultrathin hydrogen selective Pd membrane with a thickness of 16 µm was used. These Pd membranes are the oldest membranes studied for gas permeation and separation and still show the highest hydrogen permeability [213]. For characterization of Pd membranes with respect to morphology, thickness, grain size and types and amount of impurities the following techniques are commonly used: scanning electron microscopy (SEM), energy dispersive X-ray analysis (EDX), X-ray diffraction (XRD), X-ray photoelectron spectroscopy (XPS), and transmission electron microscopy (TEM) [73]. The most critical point for practical application of Pd membranes in membrane reactors is the chemical stability of these membranes [213]. The chemical stability issues include also poisoning by reaction gas mixture, which affects the H_2 permeation [214]. Therefore, *in situ* characterization of membranes by EXAFS can contribute to further development of membranes.
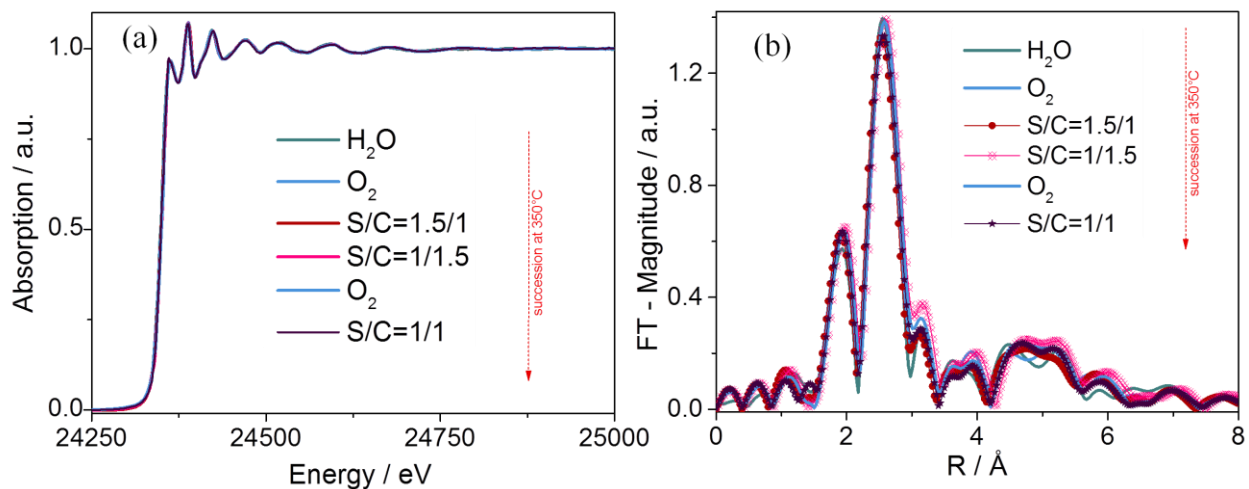
Figure 5.13: (a) Comparison of Pd K-edge XANES/EXAFS data and (b) corresponding k^2–weighted Fourier transformed EXAFS data of the Pd membrane foil in the membrane microreactor at 350°C in different reaction gas atmospheres.

First the Pd membrane foil was studied in different oxidizing atmospheres (H_2O and O_2) at 350 °C. Figure 5.13 shows that the Pd species do not undergo any change to an oxidized state in water vapor or O_2. This implies that the Pd membrane foil shows a high degree of stability. Also applying different water gas shift reaction conditions (S/C=1.5/1; 1/1; 1/1.5) does not lead to

changes in Pd oxidation state. Furthermore, the Pd – Pd bond lengths and the number of Pd neighboring atoms in the lattice do not significantly change during permeation of hydrogen through the membrane.

Table 5.7: Structural parameters obtained from fitting of Pd K-edge EXAFS data (set parameter: amplitude factor $(S_0^2) = 0.71$ (±0.08). varied parameters: N: coordination number, r: interatomic distance; σ^2: Debye-Waller factor. χ_ν^2: goodness of fit).

Bond	Shell	N	r [Å]	$\sigma^2 \, 10^{-3}$ [Å^2]	χ_ν^2
H$_2$O					
Pd – Pd	1st	12.9 (±2.11) [a]	2.76 (±0.006) [a]	10.9 (±1.6) [a]	189
O$_2$					
Pd – Pd	1st	11.8 (±2.02) [a]	2.75 (±0.001) [a]	10.2 (±1.5) [a]	250
S/C = 1.5/1					
Pd – Pd	1st	12.3 (±1.87) [a]	2.75 (±0.005) [a]	10.6 (±1.4) [a]	194
S/C = 1/1.5					
Pd – Pd	1st	11.9 (±1.73) [a]	2.74 (±0.007) [a]	10.2 (±1.3) [a]	125
O$_2$					
Pd – Pd	1st	12.0 (±1.65) [a]	2. 74 (±0.008) [a]	10.4 (±1.3) [a]	137
S/C = 1/1					
Pd – Pd	1st	12.4 (±1.33) [a]	2.74 (±0.007) [a]	10.7 (±1.0) [a]	87

[a] adjusted parameter

The Fourier Transformed spectra provide an insight into the corresponding radial atomic distribution around the Pd absorber atoms. Figure 5.13b shows Pd K-edge EXAFS data and the pseudo radial distribution function of the Pd membrane foil under 5% water vapor, then under 5% O$_2$ and after exposure to WGS conditions (S/C=1.5/1; 1/1.5; 1/1). On an atomic level the structure of the membrane, determined by *in situ* EXAFS, does not change. Detailed information about the chemical environment of the Pd absorber atom was obtained by fitting these Pd EXAFS

data. Figure A.15 (Appendix) presents the experimentally refined k^2–weighted Fourier transformed EXAFS spectra and Table 5.7 presents the respective refined structural parameters. The model used to fit the experimental data is a Pd foil. In the bulk Pd foil, the absorbing Pd atom is surrounded by 12 neighbors at a distance 2.75 Å in the first shell. The atomic distance of Pd – Pd remains the same as in the bulk state. Interestingly, the Pd – Pd distances do not change during WGS reactions. Moreover, the coordination numbers remains close to 12 which is the coordination number for Pd in bulk state. Clearly, the membrane is stable throughout the different conditions and during *in situ* H_2 extraction.

5.2.3 Conclusion

The studies in this work demonstrate various new challenges and new perspectives for identifying structure-performance relationships during the separation of product gases from the reaction gas mixture. New insights into catalysts and membranes under reaction conditions, in this case for the WGS reaction, were gained using a micro-structured membrane reactor specially designed for X-ray absorption spectroscopic studies. The geometry and window materials of the microreactor make it suitable for X-ray based experiments. Additionally, the membrane, catalyst layer and window (reactor wall) for the X-ray beam are sufficiently transparent for acquisition of high quality XAS data. Still the reactor was mechanically/chemically stable and gas tight at high temperature. In principle, spatially resolved studies are possible and it would be intriguing to follow variations in catalyst structure along the micro channels as a result of concentration or temperature gradients and to obtain spatially resolved structural information at several positions. Since the experiments have to be performed under reaction conditions and information about the oxidation state is required, the micro-structured membrane reactor was heated to high temperature (about 400 or 500 °C).

First the Pd alloy membrane foil in the new reactor without and with catalyst was characterized. Additionally, in this study three different amounts of catalyst were used (720 mg, 100 mg and 50 mg). The results showed that with 720 mg catalyst in all channels, the membrane reactor allows to acquire high XAS quality data at the Rh and Pd K-edge (in a k-range up to 15 Å^{-1}) in transmission mode. Further experiments showed that for 50 mg and 100 mg catalyst in the channels the spectra recorded in transmission mode show a low signal-to-noise ratio. Therefore,

spectra of the catalysts layers were measured in fluorescence mode. Also in this case, 100 mg catalyst in the channels resulted in significantly higher XANES and EXAFS data quality compared to 50 mg catalyst in the channels.

In this newly designed micro-structured membrane reactor a 10.5 wt.% Rh/CeO_2 catalyst and a commercial ultrathin hydrogen selective Pd alloyed membrane foil were investigated under WGS reaction conditions at atmospheric pressure. *In situ* XAS data at Pd K-edge were collected during catalytic activity measurements. They evidence a direct correlation between structure and *in situ* H_2 extraction. The results confirm that the membrane remained stable and did not undergo any structural changes during WGS reaction while it was active. In particular, these studies will be beneficial in the future as reference experiments and the infrastructure built up for this project will allow to perform more advanced experiments for further development of membranes.

The combination of X-ray absorption spectroscopy and on-line catalytic tests provided an insight into the structure-performance relationships of a flame made 10.5 wt.% Rh/CeO_2 catalyst under different WGS reaction conditions in the micro-structured membrane reactor. Several WGS experiment showed that under WGS reaction conditions the Rh species are in a reduced state. A concentration gradient along the channels can be expected due to CO conversion and H_2 removal the from the gas mixture. Spatially resolved studies in this work show that such a concentration gradient has no remarkable effect on the catalyst structure at different positions along the channels. XANES spectra recorded at two different positions indicate that under both WGS reaction conditions the catalyst was reduced. On the other hand, a weak $Rh - O$ contribution was noticeable during the WGS reaction. Integration of a H_2 selective membrane has an influence on CO conversion (Le Chatelier's principle) i.e. the concentration of CO_2 produced via the WGS reaction increased when flowing the reaction gas mixture. As well known, CO_2 is a weakly oxidizing gas, therefore a complete reoxidation along the channel in reactor could not be observed. Further results showed that decomposition of Rh species at high temperature occurred during heating up to 350 °C (or 400 °C) in He. Furthermore, reoxidation of the 10.5 wt.% Rh/CeO_2 catalyst was possible in 5% O_2/He after the WGS reaction. H_2O as oxidant could be used only after decomposition of Rh species in He at high temperature. Detailed information about the chemical environment of the Rh absorber atoms was obtained by EXAFS data fitting. The experimental results obtained at the SNBL beamline (Experiment I) showed that the Rh

particle size and coordination number changed with temperature and gas atmospheres. At room temperature in He and at 150 °C in He and in CO/H_2O the Rh species were oxidized and the coordination number of Rh was about 4 corresponding to the a particle size of 1.5 nm. At high temperature (170 – 290 °C) the coordination number was 9 and the particle size was 2.2 nm. However, further experiments (Experiment III) showed that the coordination number of Rh was very low (CN=6) when the CO concentration increased (5% in experiment I, 10% in experiment III).

5.3 Reaction Relevant Rh Structure under WGS Reaction Conditions

In this part of work, the flame spray made 10.5 wt.% and 4.3 wt.% Rh/CeO_2 catalysts were investigated in the quartz capillary micro reactor (in section 3.4.2) by XAS at synchrotron light source under different WGS reaction conditions. The aim of these studies was to investigate the difference in catalysts structure with and without H_2 separation. In addition, the challenge of these studies was to use high concentrations of CO (4% and 8%) and H_2O (6% and 12%) at high temperature in a micro quartz capillary. Deng et al. [215] studied gold-ceria samples (200 mg) in 5% CO, 3% H_2O at a total flow of 10 mL/min in WGS reaction test at 100 and 200 °C using *in situ* XAS techniques. Tibilleti et al. [216] investigated the nature of the active form of gold on ceria-zirconia support for WGS reaction, using a gas mixture 2% CO, 2.5% CO_2, 7.5% H_2O and 8.1% H_2 in N_2 at a total flow of 100 mL/min (m_{cat}=150 mg).

5.3.1 Experimental part

Flame spray made 10.5 wt.% and 4.3 wt.% Rh/CeO_2 catalysts were investigated under different WGS reaction conditions in a capillary micro reactor. 25.2 mg of 10.5 wt.% Rh/CeO_2 catalyst was filled into the capillary (outer diameter 1.5 mm, wall thickness 20 μm) between quartz wool plugs. In this study, the influence of two different WGS reaction conditions on 10.5 wt.% Rh/CeO_2 catalyst were studied under the same condition as applied to the micro-structured membrane reactor (Table 5.8) Capillary experiments under WGS-3 reaction condition could not

be carried out because the H_2O ($\dot{V}_{H2O}$=24 mL/min corresponds to m_{H2O}=1.08 g/h) vapor flow was too high, leading to obvious vibrations in the catalyst bed. In the case of the 4.3 wt.% Rh/CeO_2 catalyst, the effect of different feed gas compositions and temperature on the catalyst structure was investigated (Figure 5.14). The first series of XAS spectra were recorded at room temperature, first under He, then in 8% CO/He. Afterwards the capillary reactor was heated to 200 °C in 8% CO/He. Further series of XAS spectra were recorded at 200 °C in 8% CO/He, 12% H_2O/He, and CO/H_2O (8% CO, 12% H_2O and 80% He), respectively. Afterwards the capillary reactor was heated to 300 °C and 400 °C in the WGS gas mixture. Finally the reactor was cooled to room temperature and further XAS spectra were recorded.

Table 5.8: Water gas shift reaction conditions for the 10.5 wt.% Rh/CeO_2 at BM25 Beamline (same conditions as in Table 5.1, section 5.2.1).

WGS reaction conditions	S/C ratio	$\dot{V}_{total}$ [mL/min]	$\dot{V}_{CO}$ [mL/min]	$\dot{V}_{H2O}$ [mL/min]	m_{H2O} [g/h]	$\dot{V}_{He}$ [mL/min]
1	1.5	50	4	6	0.27	40
2	1.5	50	2	3	0.14	45
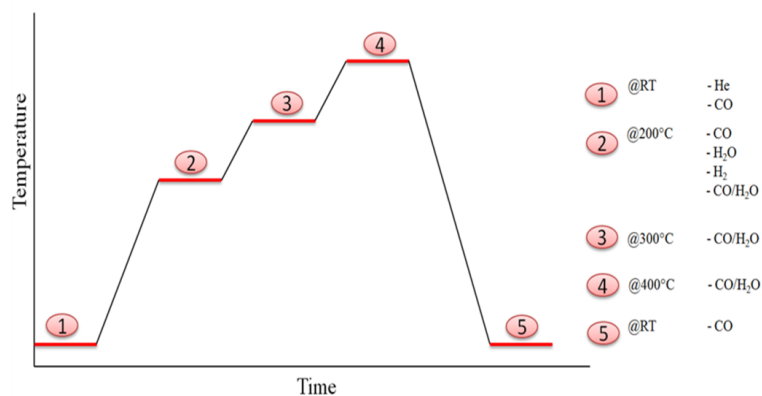
Figure 5.14: Sequence of treatments for the 4.3 wt.% Rh/CeO_2 catalyst in the quartz capillary micro reactor at the BM25 beamline. EXAFS spectra were recorded at each temperature plateau.

Moreover, the FSP made 10.5 wt.% and 4.3 wt.% Rh/CeO_2 catalysts were studied during temperature programmed reduction (TPR). First the catalysts were activated in a 5% H_2/He flow (total flow 50 mL/min) while heating up to 450 °C at 5 °C/min and recording XANES spectra in rapid continuous scanning mode. EXAFS spectra (step scanning mode) were recorded at temperature plateaus at 450, 350, 200 and 100 °C in a 5% H_2/He (total flow 50 mL/min), respectively. Afterwards the gas was switched to pure CO (20 mL/min), the sample was cooled down to room temperature and EXAFS spectra were recorded in CO.

5.3.2 Results and Discussion

Figure 5.15a shows Rh K-edge XANES spectra of 10.5 wt.% Rh/CeO_2 catalyst recorded *in situ* at room temperature in He, at 400 °C in He and at 400 °C under WGS-1 and WGS-2 conditions. At room temperature in He the catalyst is in an oxidized state. The decrease in white line intensity after heating to 400 °C in He indicates that Rh oxide was reduced to metallic Rh, which is also clear from the edge energy shift in the XANES spectra. The same effect was also observed for the same catalyst in the micro-structured membrane reactor studies. In conclusion, the 10.5 wt% Rh/CeO_2 catalyst is in an oxidized state at room temperature and partially decomposes at higher temperature to metallic Rh. Additionally, Figure 5.15a shows that this catalyst is in a reduced state under both WGS reaction conditions. Figure 5.15b shows the k^3–weighted Fourier transformed EXAFS data of the catalyst at room temperature, at 400 °C in He and at 400 °C in the WGS reaction gas mixtures. These curves provide a qualitative impression of the atomic environment around the Rh absorber atoms, since they are related to the radial distribution of neighboring atoms around the absorbing atoms. The k^3–weighted EXAFS data was fitted using Rh metal and Rh_2O_3 as structural models. The Fourier transformed EXAFS data with corresponding theoretical fits are shown in Figure A.16 and Table 5.9.
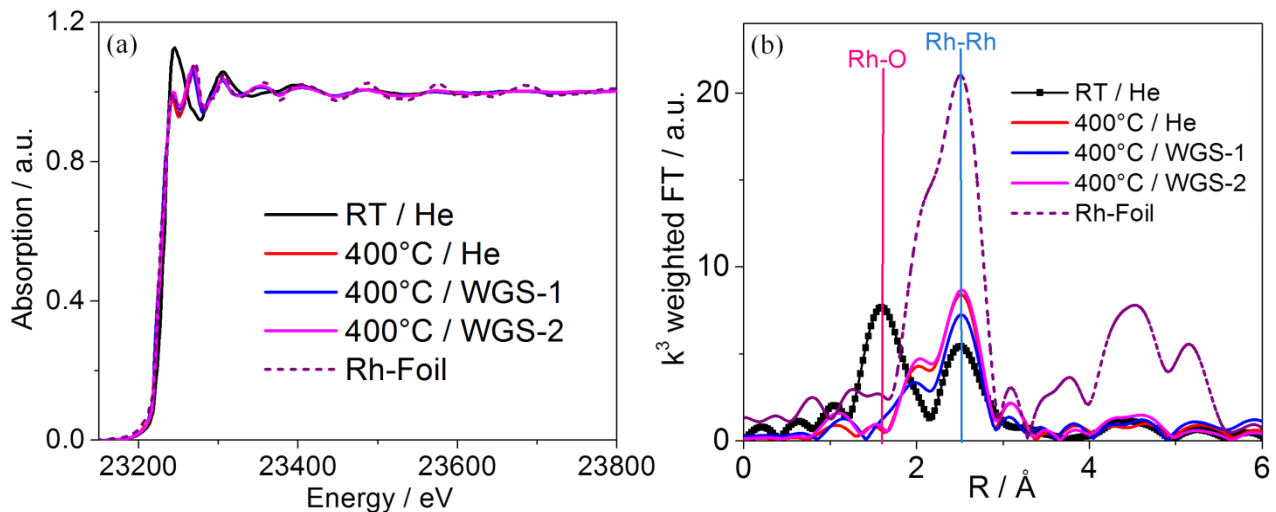
Figure 5.15: (a) Rh K-edge XANES spectra and (b) k^3–weighted Fourier transformed data of the 10.5 wt.% Rh/CeO_2 catalyst recorded at room temperature, at 400°C in He and at 400 °C under WGS reaction conditions (WGS-1: $\dot{V}_{CO}$=4 mL/min, $\dot{V}_{H2O}$=6 mL/min, $\dot{V}_{He}$=40 mL/min WGS-2: $\dot{V}_{CO}$=2 mL/min, $\dot{V}_{H2O}$=3 mL/min, $\dot{V}_{He}$=45 mL/min).

Table 5.9: Structural parameters obtained from fitting of Rh K-edge EXAFS data (10.5 wt.% Rh/CeO$_2$) (set parameter: amplitude factor $(S_0^2) = 0.85 \pm 0.06$. varied parameter: N: coordination number, r: interatomic distance; σ^2: Debye-Waller factor. χ_v^2: goodness of fit).

Reaction conditions	Rh – O			Rh – Rh			
	N	r [Å]	$\sigma^2\ 10^{-3}$ [Å^2]	N	r [Å]	$\sigma^2\ 10^{-3}$ [Å^2]	χ_v^2
RT/He	4.2 (±0.7)	2.03 (±0.01)	6.9 (±1.2)	3.9 (±1.4)	2.69 (±0.01)	7.0 (±2.1)	99
400°C/He	—	—	—	8.1 (±1.0)	2.68 (±0.01)	10.1 (±0.9)	54
400°C/WGS-1 (8% CO, 12% H$_2$O, 80% He)	—	—	—	7.7 (±1.6)	2.69 (±0.01)	10.8 (±1.4)	264
400°C/WGS-2 (4% CO, 6% H$_2$O, 90% He)	—	—	—	7.3 (±0.9)	2.68 (±0.01)	9.1 (±0.7)	37

Clearly at room temperature the EXAFS signal is dominated by four oxygen neighbors at a distance of 2.03 Å, which is consistent with the distance in Rh$_2$O$_3$ (2.01 Å). However, the coordination number is smaller than the number of oxygen neighbors in Rh$_2$O$_3$. This might be caused by substitution of Rh ions for the surface Ce^{4+} ions, which are coordinated only by four O^{2-} ions [212], as discussed already in section 5.2.2.1. At 400 °C in He the data show only Rh – Rh backscattering with a CN of 8. At this temperature there was no detectable Rh – O backscattering, whereas the EXAFS data of this catalyst in micro-structured membrane reactor at 350 °C in He, Rh – O showed a weak contribution at the inlet as well as at the outlet of the reactor (Table 5.6). Under WGS reactions in the EXAFS data, the catalyst in capillary revealed a Rh – Rh shell with a coordination number around 8 at a distance of 2.69 Å corresponding to a particle size of 1.5 nm. In Table 5.6 (previous studies 5.2.2.3), a weak Rh – O contribution was noticeable during the WGS reactions at 350 °C in micro-structured membrane reactor and the CN of Rh was 6 corresponding to a particle size of 1 nm. Deng et al. [215] observed that the Au – Au coordination number increased with increasing reaction temperature, from 6.5±2.4 at 100 °C to

8.7±1.5 at 200 °C with a gas mixture of 5%CO / 3%H₂O in He. In this case, the Rh – Rh coordination number is controlled either by temperature or by the reactor type.
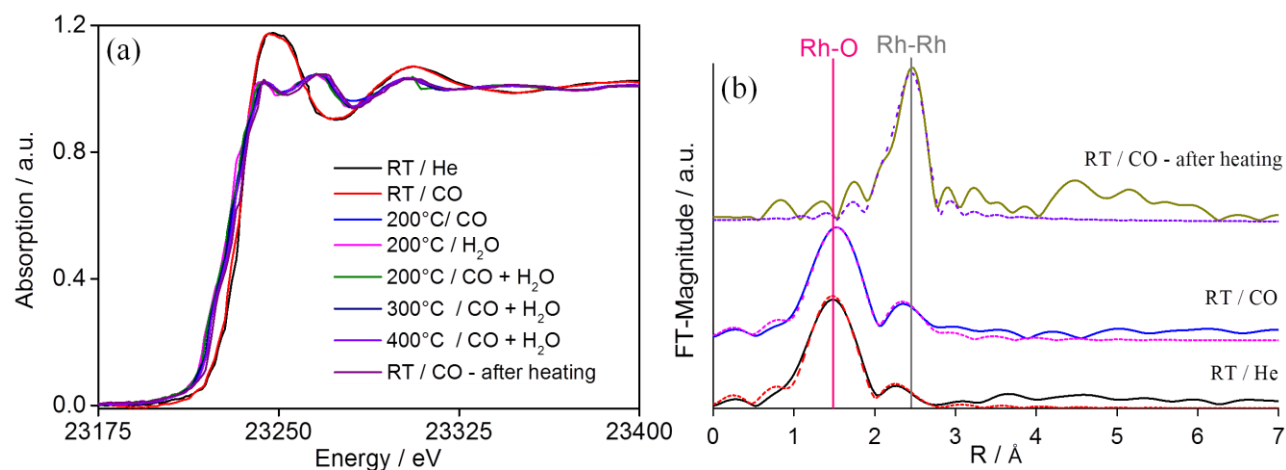
Figure 5.16: (a) Rh K-edge XANES spectra of the 4.3 wt.% Rh/CeO₂ catalyst recorded at room temperature in He and in CO, at 200°C in CO, in H₂O, at 200°C, 300°C and 400°C in CO+H₂O. (b) k^3–weighted Fourier transformed EXAFS data of the 4.3 wt.% Rh/CeO₂ catalyst at RT under He and in CO, and at RT in CO after *in situ* reaction. The fitting curves obtained from analysis using Artemis software are shown as experimental: solid lines, fitting: dash lines.

Table 5.10: Structural parameters obtained from fitting of Rh K edge EXAFS (4.3 wt.% Rh/CeO₂) (set parameter; amplitude factor (S_0^2) = 0.85 ±0.06. varied parameters: N: coordination number, r: interatomic distance; σ^2: Debye-Waller factor. χ_ν^2: goodness of fit).

Reaction conditions	Rh – O			Rh – Rh			χ_ν^2
	N	r [Å]	$\sigma^2 10^{-3}$ [Å²]	N	r [Å]	$\sigma^2 10^{-3}$ [Å²]	
RT/He	6.1 (±0.8) [a]	2.01 (±0.01) [a]	5.2 (±1.5) [a]	1	2.71 (±0.02) [a]	7.3 (±2.7) [a]	81
RT/CO	5.8 (±0.9) [a]	2.01 (±0.01) [a]	5.1 (±1.5) [a]	1	2.68 (±0.02) [a]	2.4 (±1.5) [a]	37
RT/CO after heating	–	–	–	3.9 (±0.7) [a]	2.72 (±0.04) [a]	5.8 (±1.1) [a]	10

[a] varied parameter. [b] fixed parameter

The local coordination of Rh in the 4.3 wt.% Rh/CeO_2 the catalyst was also studied at RT under He and in CO, at 200°C in CO, and H_2O and at 200, 300 and 400 °C under WGS reaction conditions (8% CO, 12% H_2O and 80% He, flow 50 mL/min) and finally at RT in CO after the WGS reaction. The detailed reaction process is shown in Figure 5.14. Normalized XANES spectra recorded under these conditions are shown in Figure 5.16a. The XANES results show a decrease in the white line intensity under different condition. The decreased white line intensity implies that the O-rich environment no longer exists. At higher temperatures the sample is in a reduced state, which is confirmed by the edge energy and XANES features. The noise in the EXAFS data is high at higher temperature, so fitting of the EXAFS data was not possible. Due to the poor signal to noise ratio, only the EXAFS data at room temperature in He and in CO before and after exposure to WGS reaction conditions could be fitted, as shown in Figure 5.16b. Structural parameters were derived from curve fitting of k^3–weighted EXAFS data in R-space and the fit results are summarized in Table 5.10. The coordination number of Rh – O is around 6 with a distance 2.01 Å in He as well as in CO at room temperature (Table 5.10). These coordination numbers are similar to coordination numbers and Rh – O distance in Rh_2O_3. In the second shell, a Rh – Rh contribution was observed, but the coordination number cannot be determined. In case of 10.5 wt.% Rh/CeO_2 catalyst, the Rh – O coordination number was around 4 in He at room temperature (Table 5.9). This implies that the oxide Rh particles in 4.3 wt.% Rh/CeO_2 catalyst was much larger compared to 10.5 wt.% Rh/CeO_2 and there is no evidence for substitution of Rh ions by the surface Ce ions. However, after WGS reaction the coordination number CN=4 of the Rh – Rh shell was significantly smaller than that of the Rh metal, which corresponds to a particle size < 1 nm.

The flame made 10.5 wt.% and 4.3 wt.% Rh/CeO_2 catalysts were further studied, using different characterization methods such as XRD, BET, TPR and TEM. Figure 5.17 shows XRD patterns of the flame made 10.5 wt.% and 4.3 wt.% Rh/CeO_2 catalyst. The materials shows reflections corresponding to the fluorite type of ceria (2θ = 28.6°, 33.0°, 47.5°, 56.5°, 59.1°) and reflection of Rh at 2θ = 41.3°. For 4.3 wt.% Rh/CeO_2 the reflection at 41.3° is so weak that it can hardly be distinguished from the background. The diffractograms were further analyzed using the Scherrer equation (section 3.2.1). The CeO_2 crystallite size for 10.5 wt.% Rh/CeO_2 catalyst was calculated as 9.9 nm (2θ=28.6°), 8.6 nm (2θ=33.0°) and the Rh crystallite size was 28 nm (2θ=41.3°). In the case of 4.3 wt.% Rh/CeO_2 catalyst, the CeO_2 crystallite size was calculated as 7.5 nm (2θ=28.6),

6.3 nm ($2\theta=33.0°$). The specific surface area determined by BET, amounted to 142 $m^2 g^{-1}$ for 4.3 wt.% Rh/CeO_2 and 114 $m^2 g^{-1}$ for 10.5 wt.% Rh/CeO_2 compared to two previously investigated flame made 1.9 wt.% and 3.1 wt.% Rh/CeO_2 catalysts with crystallite sizes of 11 and 17 nm (reflection at $2\theta=28.6°$) and surface areas of 125 and 105 $m^2 g^{-1}$, respectively [112]. In summary, the flame made catalysts exhibit high surface area and a high degree of crystallinity independent of metal loading.
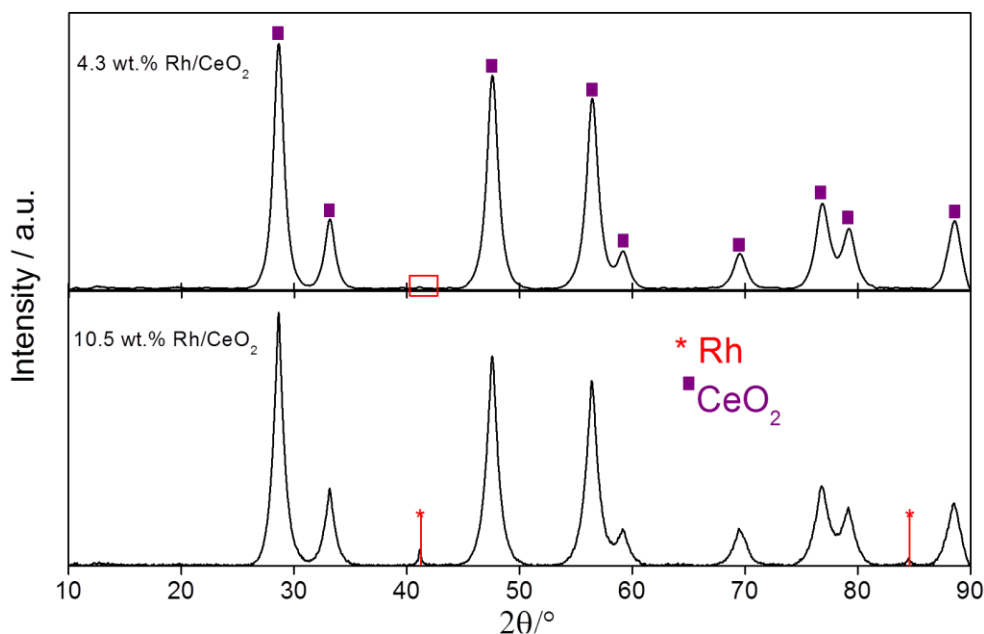
Figure 5.17: XRD patterns of flame made 10.5 wt.% Rh/CeO_2 (bottom) and 4.3 wt.% Rh/CeO_2 (top) catalysts with characteristic ceria reflections (2θ = 28.6°, 33.0°, 47.5°, 56.5°, 59.1°) and a weak Rh reflection for 10.5 wt% at 2θ = 41.1°.

Figure 5.18 shows Rh K-edge XANES spectra of the flame made 10.5 wt.% Rh/CeO_2 catalyst recorded during heating from room temperature to 450°C in 5% H_2/He (50 mL/min) as in ref. [112] and section 4.1.3.2. Figure 5.18a shows a decrease in white line intensity at approx. 97 °C indicating reduction of rhodium. The sample is almost completely reduced at ca. 114 °C. According to linear combination fitting results 50% of the Rh atoms are in a reduced state at about 99 °C (Figure 5.18b). The LCF results show also a second step increase during reduction at higher temperature. This indicates that some Rh species are much more difficult to reduce which could be related to diffusion of H_2 within the CeO_2 support. This is in good agreement with the TEM image of this catalyst in Figure 5.18c, which reveals that only some of the Rh species are

accessible (blue dotted arrow in image section). Apparently the adjacent particles (CeO$_2$) have grown together and formed regular sintering bridges support (CeO$_2$) (red solid frame in image section). It seems that some of these Rh species are located between these sintering bridges, which can make the H$_2$ access difficult. This step in reduction could be also caused by some substitution Rh ions in the surface lattice (CH=4 at RT in He, Table 5.9), as mentioned before.
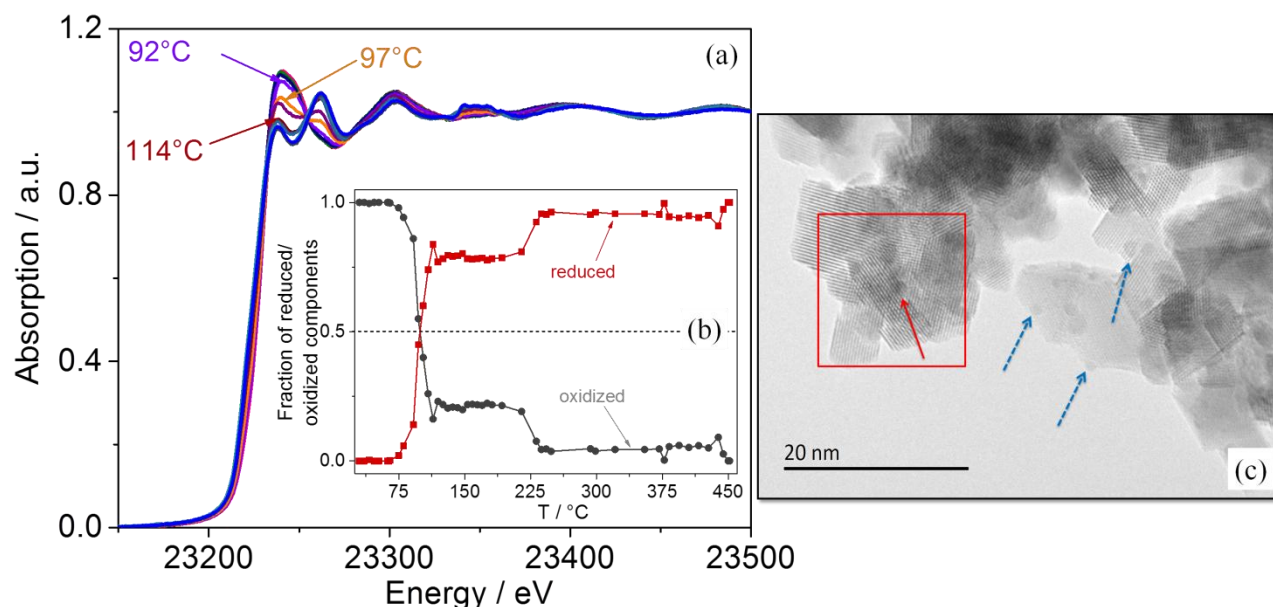
Figure 5.18: (a) Rh K-edge XANES spectra of the 10.5 wt.% Rh/CeO$_2$ catalyst recorded during temperature programmed reduction, (b) changes in relative concentrations of oxidized and reduced Rh species during TPR obtained from linear combination fitting. (c).TEM image of the ceria supported 10.5 wt.% Rh catalyst after water gas shift reaction, recorded at Dalian Institute of Chemical Physic (DICP), Chinese Academy of Sciences (CAS) in Dalian/China. Accessible Rh species: blue dotted arrow, difficult accessible Rh species: red solid frame in image section (c).

After TPR the flame made 10.5 wt.% Rh/CeO$_2$ catalyst was cooled down stepwise from 450 °C to 350, 200 and 100 °C in H$_2$, and EXAFS spectra were recorded at each temperature plateau. At 100 °C the gas flow was switched from 5% H$_2$ in He (50 mL/min) to pure CO (20 mL/min) and the reactor cooled down to room temperature. k^2–weighted EXAFS data and corresponding fit results for different temperatures are shown in Figure A.17. Structural parameters resulting from EXAFS data analysis are shown in Table A.3. At 450, 350, 200 and 100 °C in H$_2$/He the mean Rh – Rh distance for the first shell was ca. 2.67 Å and for the second shell 3.77 Å. The structural disorder in both shells increases with increasing temperature. At room temperature in CO the

Rh –Rh distance for the first shell was 2.68 Å with a coordination number of 7 (±0.6). On the other hand, a previous study (in section 4.1.3.2 and ref. [112]) showed that *in situ* reduction produced metallic clusters with 8.7±0.7 Rh atoms in H_2 at room temperature for a 3.1 wt.% Rh/CeO_2 catalyst. EXAFS spectra recorded after the activation of the catalyst showed that the Rh particle size, which was estimated from this coordination number using a method developed by Jentys [152] was ca. 2 nm in the case of 10.5 wt.% Rh/CeO_2. Furthermore, TEM images (Figure 5.18c) of the 10.5 wt.% Rh/CeO_2 catalyst indicate Rh particle sizes around 1.5 nm, which is in good agreement with the particle size obtained from the coordination numbers.
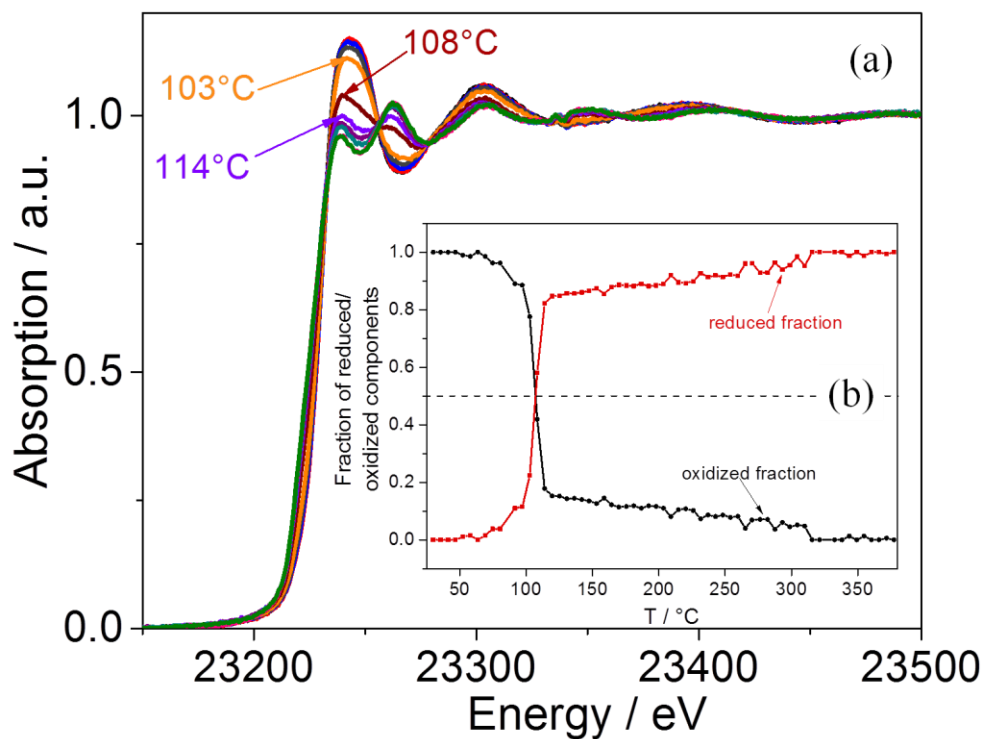
Figure 5.19: (a) Rh K-edge XANES spectra of the 4.3 wt.% Rh/CeO_2 catalyst recorded during temperature programmed reduction, (b) changes in relative concentrations of oxidized and reduced Rh species during TPR obtained from linear combination fitting.

Figure 5.19a shows Rh K-edges XANES spectra of the 4.3 wt.% Rh/CeO_2 catalyst in 5% H_2/He (50 mL/min). The decrease in white line intensity at approx. 108 °C indicates that the noble metal oxides are reduced at this temperature. The relative concentrations of oxidized and reduced species were determined by linear combination fitting of the XANES data using the first and last spectrum of the TPR series as reference spectra. These fitting results are shown in Figure 5.19b.

The concentration of oxidized Rh species abruptly changed at 95 °C and the sample was almost completely reduced at ca. 107 °C. Compared to the LCF results for the 10.5 wt.% Rh/CeO_2 catalyst, the change of 10.5 wt.% Rh/CeO_2 catalyst in relative concentrations of oxidized and reduced Rh species shows a stepwise increasing in the reduction, whereas the change for 4.3 wt.% Rh/CeO_2 catalyst is continuous. This indicates that some Rh species in the 4.3 wt.% Rh/CeO_2 are much easier to reduce which could be related to diffusion of H_2 within the CeO_2 support, as mentioned before. After TPR the catalyst was cooled down stepwise from 450 °C to 350, 200 and 100 °C in H_2, and EXAFS spectra were recorded at each temperature plateau. At 100 °C the gas flow was switched from 5% H_2 in He (50 mL/min) to pure CO (20 mL/min) and the reactor cooled down to room temperature following the same experimental process as for 10.5 wt.% Rh/CeO_2 catalyst. k^2–weighted EXAFS data and corresponding fit results for different temperatures are shown in Figure A.18. Structural parameters resulting from EXAFS data analysis are shown in Table A.4. In the case of the 4.3 wt.% Rh/CeO_2 catalyst the fitting results showed that at 450, 350, 200 and 100 °C in H_2/He a small peak labeled as $Rh - O$ appears at a distance of 2.06 Å. Upon exposure to CO at room temperature, the $Rh - O$ coordination number was 1 with a distance 2.03 Å for the first shell and the coordination number of $Rh - Rh$ for the second shell was 5 with a distance 2.69 Å (Table A.4). In summary, the 4.3 wt.% Rh/CeO_2 catalyst was partially oxidized at low temperature as well as at high temperature. In the case of 4.3 wt.% Rh/CeO_2 the particle size was estimated to be < 1 nm from this coordination number using a method developed by Jentys [152].

5.3.3 Conclusion

The flame made 10.5 wt.% and 4.3 wt.% Rh/CeO_2 catalysts were investigated in a capillary micro reactor under WGS reaction conditions and during temperature programmed reduction (TPR). At room temperature in He, the $Rh - O$ coordination number in 10.5 wt.% Rh/CeO_2 catalyst was around 4, which is smaller than the Rh coordination number in Rh_2O_3, assuming that the some of the Rh ions substituted in the surface CeO_2 lattice. *In situ* WGS reaction in the capillary micro reactor showed that the 10.5 wt.% Rh/CeO_2 catalyst was in a reduced state and there were no detectable $Rh - O$ contributions. According to the EXAFS results the Rh particle size was approx. 1.5 nm. During WGS reaction in the micro-structured membrane reactor, a

detectable Rh – O contribution still existed. The TPR result showed that the catalyst was reduced in H_2 at ca. 114 °C. However, this temperature shifted to higher temperature (170 °C) in WGS reaction gas mixture. After TPR 10.5 wt.% Rh/CeO_2 catalyst was cooled down stepwise to 100 °C in He. The mean Rh – Rh distance was 2.66 Å. At 100 °C the gas flow was switched from H_2 to CO and the reactor was cooled down to room temperature. At room temperature in CO the Rh – Rh distance was 2.68 Å with a coordination number of 7 corresponding to a particle size of ca. 2 nm. This result was consistent with TEM result (1.5 nm).

In the case of the 4.3 wt.% Rh/CeO_2 the absorbing Rh atoms were surrounded by 6 oxygen atoms at room temperature. Due to the poor signal-to-noise ratio the EXAFS data recorded under WGS reaction conditions could not be quantitatively analyzed. However, the XANES results showed that the catalyst was reduced under WGS reaction conditions. At room temperature in CO after exposure to a WGS gas mixture, the Rh – Rh coordination number was 4. This low coordination number of Rh could either be due to the small particle size (< 1 nm) or due to formation of Rh – CO species. These results were also observed for 10.5 wt.% Rh/CeO_2 during WGS reactions in the micro-structured membrane reactor (in section 5.2.2.3). The TPR results showed that the catalyst was reduced at 114 °C, at same temperature as 10.5 wt.% Rh/CeO_2 catalyst. The difference between both catalysts is that the reduction of Rh species in the 10.5 wt.% Rh/CeO_2 catalyst increased stepwise, whereas for the 4.3 wt.% Rh/CeO_2 catalyst the reduction proceeded continuously, implying that some of the Rh species in the 4.3 wt.% Rh/CeO_2 catalyst were more accessible than others. However, the EXAFS fitting results showed a weak Rh – O contribution during TPR and at room temperature in CO as well. The size of the oxidized Rh particles was < 1 nm.

PART V: FINAL REMARKS AND OUTLOOK

6 Overall Conclusions and Outlook

This thesis was conducted in the frame of the Helmholtz-CAS Joint Research Group-118 (HCJRG) on "Integrated catalytic technologies for efficient hydrogen production", which focuses on studying hydrogen-selective membranes and the integrated catalysts "at work" using advanced X-ray based techniques at synchrotron light sources under realistic operating conditions. Particularly, this thesis aimed at developing nanostructured supported noble metal catalysts for WGS reaction and improving their performance and stability. Additionally, in this thesis a micro-structured membrane reactor prototype was designed for *in situ* XAS measurements at high photon energies (Rh and Pd K-edges) with Ni (or Fe) foils as X-ray windows. This configuration corresponded to the most stable design under WGS reaction conditions. Accordingly, XAS measurements were performed at beamlines providing sufficient flux at high photon energies, mainly at the European Synchrotron Radiation Facility (ESRF, Grenoble) and only recently at the established CAT-ACT beamline at ANKA. This new reactor was designed in a collaboration between IKFT/ITCP and IMVT. More specifically, IMVT contributed with its expertise in optimization of micro reactor design and fabrication while ITCP/IKFT contributed with experience and know-how in the design of spectroscopic cells for *in situ* X-ray adsorption spectroscopic measurements including mobile set-up and experience at synchrotron radiation sources.

Since the attenuation of the transmitted X-rays decreases with increasing the thickness of the window materials, membrane foils and catalyst support, high photon energies (Rh K=23200 eV, Pt L_3=11564 eV) were preferred for the XAS experiments in the micro-structured membrane reactor. Rh based catalysts were therefore good candidates for the WGS reaction when integrated into a micro-structured membrane reactor prototype for *in situ* XAS studies. Before testing the micro-structured membrane reactor an adequate catalyst system had to be chosen. The most

important factors for developing a catalyst with a good performance are (i) high surface area, (ii) high dispersion of the active metal, (iii) small crystallite size of the support material, (iv) small particle size of the noble metal, (v) good resistance against deactivation. These requirements were met for flame made Rh/CeO$_2$ catalysts. The structure and catalytic performance of Rh/CeO$_2$ catalysts were compared with Pt/CeO$_2$ catalysts, since Pt based catalysts showed excellent performance for the WGS reaction according to literature. The experiments at the synchrotron showed that this reactor was suitable for acquiring XAS data of high quality. Additionally, after upgrading the *in situ* set-up in 2015 it was possible to record XAS data under a variety of different and reproducible reaction conditions especially water could be emphasized (new set-up allowed better control of these conditions). The influence of these reaction conditions on the catalyst structure were clearly visible in the XAS data and could be investigated systematically.

In this newly designed micro-structured membrane reactor, a 10.5 wt.% Rh/CeO$_2$ catalyst and a commercial ultrathin hydrogen selective Pd alloyed membrane foil were investigated under WGS reaction conditions at atmospheric pressure. *In situ* XAS data at the Pd K-edge were collected during catalytic activity measurements. They evidenced a direct correlation between structure of alloyed based Pd membrane and *in situ* H$_2$ extraction. The studies performed in this thesis will contribute in the future as reference experiments and the infrastructure built up for this project will allow the performance of more advanced experiments for the development of new membranes. Moreover, the combination of X-ray absorption spectroscopy and on-line catalytic tests provided an insight into the structure-performance relationships of flame made 10.5 wt.% Rh/CeO$_2$ catalysts under different WGS reaction conditions in the micro-structured membrane reactor. For this study, three different amounts of catalyst were used (720 mg, 50 mg and 100 mg). The results showed that with 720 mg catalyst in all channels the membrane reactor acquired high quality data at Rh at the EXAFS data (in a k-range up to 15 Å^{-1}) in transmission mode. Further experiments showed that for 50 mg and 100 mg catalyst in the channels the scans in transmission mode show low signal-to-noise ratio, since the catalytic layer was too thin. Therefore, the catalysts layers were measured in fluorescence mode.

Parallel to the test of a prototype micro-structured membrane reactor, novel nanostructured catalysts with high activity and stability were prepared at KIT/ITCP using Flame Spray Pyrolysis (FSP) as an advanced preparation method. These catalysts were based on noble metals (Pt, Rh), on reducible supports such as CeO$_2$. The catalysts exhibited a high specific surface area (93–

130 m^{2}g^{-1}) and a high degree of nanocrystallinity. According to the TEM results, the metallic phase consisted of highly dispersed spherical nanoparticles with relatively small diameter (2.1– 2.7 nm). The reaction conditions hardly influenced the particle size, i.e. the particles do not aggregate. Catalytic performance tests for WGS reactions showed that these catalysts were highly active.

The first test results showed that as a rather new method, FSP seemed to be a very promising method for the synthesis of high temperature WGS catalysts for membrane and micro reactors, since FSP allows the synthesis of the corresponding catalysts in one single step. Therefore, further noble metal (Pt, Rh) nanoparticles with low loading (0.3–0.9 wt.%) were synthesized on a variety of different supports (CeO$_2$, TiO$_2$, ZrO$_2$, Ce-Zr mixed oxides). This allowed the investigation of the influence of different supports and preparation techniques (single flame (SF) and double flame (DF) spray pyrolysis) on the structural and catalytic properties of a broad variety of catalysts in a systematic way. These Rh and Pt based catalysts were tested in a fixed bed reactor and in a quartz capillary micro reactor.

Single flame made catalysts exhibited higher specific surface area, smaller crystallite sizes and higher reduction temperature compared to double flame made catalysts. Flame made Pt and Rh based catalysts supported on CeO$_2$, TiO$_2$, ZrO$_2$, Ce-Zr mixed oxides showed fairly small particle sizes (1.5–3.8 nm). In case of noble metals on TiO$_2$, the SF made Rh/TiO$_2$ catalysts showed a higher reduction temperature (at 280 °C about 50% Rh species in metallic phase) compared to DF made catalyst (at 160 °C about 50% Rh species in metallic phase). Potentially, the Rh particles were encapsulated in the lattice during preparation by SF spray pyrolysis, which might need to migrate to the surface during the reduction treatment. Furthermore, the structure of noble metals on TiO$_2$ may be affected by a strong metal-support interaction. This phenomenon could be observed for the Rh/TiO$_2$, since SF and DF made Rh/TiO$_2$ catalysts exhibited higher reduction temperature compared to SF made Rh/CeO$_2$ catalysts (reduction temperature ca. 75 °C for 3.1 wt.% Rh/CeO$_2$ and 114 °C for 4.3 wt.% Rh/CeO$_2$). The titania supported Rh and Pt catalysts were tested in a fixed bed reactor and in a quartz capillary micro reactor. In general, the Pt based catalysts showed higher activity compared to the Rh based catalysts. DF made Rh based catalysts showed slightly higher CO conversion compared to SF made catalysts in the fixed bad reactor, whereas Pt based catalysts showed similar catalytic performance regardless of the flame spray process used during preparation. The low CO conversion over SF made Rh/TiO$_2$ catalysts could

be caused either by the substitution of Rh ions in the TiO_2 lattice or by SMSI. Furthermore, all catalysts were reduced prior to the WGS reaction and then tested in the quartz capillary micro reactor. The comparison of CO conversion for reduced and non-reduced catalysts showed important differences for Rh/TiO_2 catalysts, implying that the Rh particles migrated to the surface. The DF made Rh based and Pt based catalysts show similar catalytic activities before and after H_2 pretreatment. In general the activity of Rh based and Pt based catalysts for WGS reactions was related to the preparation methods and the pre-treatment conditions. The DF made Rh catalysts showed higher catalytic activity compared to SF made samples. The WGS reaction activity of Pt and Rh based catalysts is highly influenced by the nature of the supports (CeO_2, ZrO_2 and $Ce_xZr_{1-x}O_2$). The results of catalytic performance tests results in a fixed bed reactor as well as in a capillary micro reactor were in agreement, implying that the results were reproducible. The results showed that noble metal particles on CeO_2, ZrO_2 and $Ce_xZr_{1-x}O_2$ have very high WGS activity at a high steam to CO ratio ($S/C = 4$). Pt based catalysts could be considered as promising catalysts for the WGS reaction compared to Rh based catalysts. Pt based catalysts reached full CO conversion (thermodynamic equilibrium point) at low temperature (350 °C). Nano crystalline CeO_2 and $Ce_xZr_{1-x}O_2$ supported noble metal catalysts exhibited the highest activity and turnover frequency (TOF) as well as low activation energy in the WGS reaction. In the case of Pt/ZrO_2 and Rh/ZrO_2 catalysts an important difference in the CO conversion was observed depending on the synthesis method. The catalytic performance of Pt/ZrO_2 and Rh/ZrO_2 catalysts was enhanced if double flame spray pyrolysis was used as a synthesis method. The catalytic performance of Pt/TiO_2 catalysts was higher compared to Pt/CeO_2 and $Pt/Ce_xZr_{1-x}O_2$ catalysts independent of the preparation method. For instance, at 350 °C CO conversion was 81% for $SF-Pt/TiO_2$, 77% for Pt/CeO_2 catalyst and 94% $Pt/Ce_xZr_{1-x}O_2$ catalyst. Note that the loading of Pt on TiO_2 (0.4 wt.%) was lower than Pt on CeO_2 (0.94 wt.%) and $Ce_xZr_{1-x}O_2$ (0.76 wt.%).

The development and continuous improvement of catalysts requires a deeper understanding of the underlying reaction mechanisms. Particularly interesting is the interaction between the active component and the carrier. In this context, a capillary micro reactor set-up was successfully applied in synchrotron based *in situ* experiments, with simultaneously on-line gas analysis of the products acquired under demanding working conditions of the WGS reaction. Both the micro-structured membrane reactor and the capillary micro reactor gave first insight into the structure of

the noble metals on the different supports and are very valuable tools to establish structure-activity relationships as a basis for improved catalyst design (also membranes), i.e. to improve catalyst performance and stability and for assessing the perspectives of the materials for long-term application.

7 References

[1]   K. Liu, C. Song, V. Subramani, *Hydrogen and Syngas Production and Purification Technologies*, John Wiley & Sons, Inc. **2009**.

[2]   G.J. Stiegel, M. Ramezan, *Hydrogen from Coal Gasification: An economical Pathway to a Sustainable Energy Future,* International Journal of Coal Geology **2006**, 65, 173-190.

[3]   A.F. Holleman, N. Wieberg, *Inorganic Chemistry*, Walter de Gruyter & Co. **2007**.

[4]   G. Gahleitner, *Hydrogen from Renewable Electricity: An International Review of Power-to-Gas Pilot Plants for Stationary Applications,* International Journal of Hydrogen Energy **2013**, 38, 2039-2061.

[5]   M.A. Rosen, D.S. Scott, *Comparative Efficiency Assessments for a Range of Hydrogen Production Processes,* International Journal of Hydrogen Energy **1998**, 23, 653-659.

[6]   J.R. Rostrup-Nielsen, *Conversion of Hydrocarbons and Alcohols for Fuel Cells,* Physical Chemistry Chemical Physics **2001**, 3, 283-288.

[7]   S. Sharma, B.G. Pollet, *Support Materials for PEMFC and DMFC Electrocatalysts─A Review,* Journal of Power Sources **2012**, 208, 96-119.

[8]   K.R. Gunugunuri, G.S. Panagiotis, *Water Gas Shift Reaction: Research Developments and Applications*, 1st Edition, Elsevier **2015**.

[9]   D. Mendes, A. Mendes, L.M. Madeira, A. Iulianelli, J.M. Sousa, A. Basile, *The Water-Gas Shift Reaction: From Conventional Catalytic Systems to Pd-based Membrane Reactors,* Asia-Pacific Journal of Chemical Engineering **2010**, 5, 111–137.

[10]   C. Ratnasamy, J.P. Wagner, *Water Gas Shift Catalysis,* Catalysis Reviews - Science and Engineering **2009**, 51, 325-440.

[11]   J.R. Ladebeck, J.P. Wagner, *Catalyst Development for Water-Gas Shift in Handbook of Fuel Cells – Fundamentals, Technology and Applications*, *Volume 3*, Edited by W. Vielstich, A. Lamm, H. A. Gasteige, John Wiley & Sons, Ltd. **2003**, 190-201.

[12]   R. J. B. Smith, M. Loganathan, M. S. Shantha, *A Review of the Water Gas Shift Reaction Kinetics,* International Journal of Chemical Reactor Engineering **2010**, 8, 1-34.

[13]   D.S. Newsome, *The Water-Gas Shift Reaction,* Catalysis Reviews - Science and Engineering **1980**, 2, 275-318.

[14]   G.A. Khalid, *A Further Step toward H$_2$ in Automobile: Development of an Efficient Bi-Functional Catalyst for Single Stage Water Gas Shift*, The Netherlands **2008**.

[15] C. Rhodes, G.J. Hutchings, A.M. Ward, *Water-Gas Shift Reaction: Finding the Mechanistic Boundary,* Catalysis Today **1995**, 23, 43-58.

[16] J.-D. Grunwaldt, P. Kappen, B.S. Hammershoi, L. Troger, B.S. Clausen, *Fluorescence EXAFS for the in situ Study on the State of Promotors in Catalysis,* Journal of Synchrotron Radiation **2001**, 8, 572-574.

[17] T.M. Yurieva, T.P. Minyukova, *State of Copper in Cu-Zn-Al Oxide Catalysts for Methanol Synthesis,* Reaction Kinetics and Catalysis Letters **1985**, 29, 55-61.

[18] M.J.L. Ginés, N. Amadeo, M. Laborde, C.R. Apesteguía, *Activity and Structure-Sensitivity of the Water-Gas Shift Reaction over CuZnAl Mixed Oxide Catalysts,* Applied Catalysis A: General **1995**, 131, 283-296.

[19] P. Panagiotopoulou, A. Christodoulakis, D.I. Kondarides, S. Boghosian, *Particle Size Effects on the Reducibility of Titanium Dioxide and its Relation to the Water–Gas Shift Activity of Pt/TiO$_2$ Catalysts,* Journal of Catalysis **2006**, 240, 114-125.

[20] W. Ruettinger, *A New Generation of Water Gas Shift Catalysts for Fuel Cell Applications,* Journal of Power Sources **2003**, 118, 61-65.

[21] T. Bunluesin, R.J. Gorte, G.W. Graham, *Studies of the Water-Gas-Shift Reaction on Ceria-supported Pt, Pd, and Rh: Implications for Oxygen-Storage Properties,* Applied Catalysis B: Environmental **1998**, 15, 107-114.

[22] Q. Fu, S. Kudriavtseva, H. Saltsburg, M. Flytzani-Stephanopoulos, *Gold-Ceria Catalysts for Low-Temperature Water-Gas Shift Reaction,* Chemical Engineering Journal **2003**, 93, 41-53.

[23] Q. Fu, H. Saltsburg, M. Flytzani-Stephanopoulos, *Active Nonmetallic Au and Pt Species on Ceria-Based Water-Gas Shift Catalysts,* Science **2003**, 301, 935-938.

[24] R. Burch, *Gold Catalysts for Pure Hydrogen Production in the Water-Gas Shift Reaction: Activity, Structure and Reaction Mechanism,* Physical Chemistry Chemical Physics **2006**, 8, 5483-5500.

[25] X. Wang, R.J. Gorte, J.P. Wagner, *Deactivation Mechanisms for Pd/Ceria during the Water-Gas-Shift Reaction,* Journal of Catalysis **2002**, 212, 225-230.

[26] X. Wang, R.J. Gorte, *The Effect of Fe and Other Promoters on the Activity of Pd/Ceria for the Water-Gas Shift Reaction,* Applied Catalysis A: General **2003**, 247, 157-162.

[27] L.W. Gary Jacobs, Uschi Graham, Dennis Sparks, and Burtron H. Davis, *Low-Temperature Water-Gas Shift: In-Situ DRIFTS-Reaction Study of a Pt/CeO$_2$ Catalyst for*

Fuel Cell Reformer Applications, The Journal of Physical Chemistry B **2003**, 107, 10398-10404.

[28]   G. Jacobs, L. Williams, U. Graham, G.A. Thomas, D.E. Sparks, B.H. Davis, *LowTemperature Water-Gas Shift: In Situ DRIFTS-Reaction Study of Ceria Surface Area on the Evolution of Formates on Pt/CeO$_2$ Fuel Processing Catalysts for Fuel Cell Applications,* Applied Catalysis A: General **2003**, 252, 107-118.

[29]   O. Thinon, F. Diehl, P. Avenier, Y. Schuurman, *Screening of Bifunctional Water-Gas Shift Catalysts,* Catalysis Today **2008**, 137, 29-35.

[30]   G.G. Olympiou, C.M. Kalamaras, C.D. Zeinalipour-Yazdi, A.M. Efstathiou, *Mechanistic Aspects of the Water-Gas Shift Reaction on Alumina-Supported Noble Metal Catalysts: In Situ DRIFTS and SSITKA-Mass Spectrometry Studies,* Catalysis Today **2007**, 127, 304-318.

[31]   D. Andreeva, V. Idakiev, T. Tabakova, L. Ilieva, P. Falaras, A. Bourlinos, A. Travlos, *Low-Temperature Water-Gas Shift Reaction over Au/CeO$_2$ Catalysts,* Catalysis Today **2002**, 72, 51-57.

[32]   G. Jacobs, E. Chenu, P.M. Patterson, L. Williams, D. Sparks, G. Thomas, B.H. Davis, *Water-Gas Shift: Comparative Screening of Metal Promoters for Metal/Ceria Systems and Role of the Metal,* Applied Catalysis A: General **2004**, 258, 203-214.

[33]   S. Hilaire, X. Wang, T. Luo, R.J. Gorte, J. Wagner, *A Comparative Study of Water-Gas-Shift Reaction over Ceria Supported Metallic Catalysts,* Applied Catalysis A: General **2001**, 215, 271-278.

[34]   T. Shido, Y. Iwasawa, *Reactant-Promoted Reaction Mechanism for Water-Gas Shift Reaction on Rh-Doped CeO$_2$,* Journal of Catalysis **1993**, 141, 71-81.

[35]   Y. Sato, K. Terada, S. Hasegawa, T.o. Miyao, S. Naito, *Mechanistic Study of Water–Gas-Shift Reaction over TiO$_2$ Supported Pt–Re and Pd–Re Catalysts,* Applied Catalysis A: General **2005**, 296, 80-89.

[36]   H. Iida, A. Igarashi, *Characterization of a Pt/TiO$_2$ (rutile) Catalyst for Water Gas Shift Reaction at Low-Temperature,* Applied Catalysis A: General **2006**, 298, 152-160.

[37]   H. Iida, A. Igarashi, *Structure Characterization of Pt-Re/TiO$_2$ (rutile) and Pt-Re/ZrO$_2$ Catalysts for Water Gas Shift Reaction at Low-Temperature,* Applied Catalysis A: General **2006**, 303, 192-198.

[38] S.Y. Choung, M. Ferrandon, T. Krause, *Pt-Re Bimetallic Supported on CeO$_2$-ZrO$_2$ Mixed Oxides as Water–Gas Shift Catalysts,* Catalysis Today **2005**, 99, 257-262.

[39] W. Ruettinger, X. Liu, R.J. Farrauto, *Mechanism of Aging for a Pt/CeO$_2$-ZrO$_2$ Water Gas Shift Catalyst,* Applied Catalysis B: Environmental **2006**, 65, 135-141.

[40] F. Boccuzzi, A. Chiorino, M. Manzoli, D. Andreeva, T. Tabakova, L. Ilieva, V. Iadakiev, *Gold, Silver and Copper Catalysts Supported on TiO$_2$ for Pure Hydrogen Production,* Catalysis Today **2002**, 75, 169-175.

[41] H. Kušar, S. Hočevar, J. Levec, *Kinetics of the Water-Gas Shift Reaction over Nanostructured Copper-Ceria Catalysts,* Applied Catalysis B: Environmental **2006**, 63, 194-200.

[42] G. Jacobs, E. Chenu, P.M. Patterson, L. Williams, D. Sparks, G. Thomas, B.H. Davis, *Water-Gas Shift: Comparative Screening of Metal Promoters for Metal/Ceria Systems and Role of the Metal,* Applied Catalysis A: General **2004**, 258, 203-214.

[43] P. Panagiotopoulou, D.I. Kondarides, *Effect of the Nature of the Support on the Catalytic Performance of Noble Metal Catalysts for the Water-Gas Shift Reaction,* Catalysis Today **2006**, 112, 49-52.

[44] G. Zhou, P.R. Shah, T. Montini, P. Fornasiero, R.J. Gorte, *Oxidation Enthalpies for Reduction of Ceria Surfaces,* Surface Science **2007**, 601, 2512-2519.

[45] A. Trovarelli, *Catalytic Properties of Ceria and CeO$_2$-Containing Materials,* Catalysis Reviews - Science and Engineering **1996**, 38, 439-520.

[46] M. Haruta, N. Yamada, T. Kobayashi, S. Iijima, *Gold Catalysts Prepared by Coprecipitation for Low-Temperature Oxidation of Hydrogen and of Carbon Monoxide,* Journal of Catalysis **1989**, 115, 301-309.

[47] M. Haruta, S. Tsubota, T. Kobayashi, H. Kageyama, M.J. Genet, B. Delmon, *Low-Temperature Oxidation of CO over Gold Supported on TiO$_2$, α-Fe$_2$O$_3$, and Co$_3$O$_4$,* Journal of Catalysis **1993**, 144, 175-192.

[48] H.N. Evin, G. Jacobs, J. Ruiz-Martinez, G.A. Thomas, B.H. Davis, *Low Temperature Water Gas Shift: Alkali Doping to Facilitate Formate C–H Bond Cleaving over Pt/Ceria Catalysts—An Optimization Problem,* Catalysis Letters **2008**, 120, 166-178.

[49] H.N. Evin, G. Jacobs, J. Ruiz-Martinez, U.M. Graham, A. Dozier, G. Thomas, B.H. Davis, *Low Temperature Water Gas Shift/Methanol Steam Reforming: Alkali Doping to*

Facilitate the Scission of Formate and Methoxy C–H Bonds over Pt/Ceria Catalyst, Catalysis Letters **2008**, 122, 9-19.

[50] P. Panagiotopoulou, D.I. Kondarides, *Effects of Alkali Promotion of TiO_2 on the Chemisorptive Properties and Water Gas Shift Activity of Supported Noble Metal Catalysts,* Journal of Catalysis **2009**, 267, 57-66.

[51] X. Zhu, M. Shen, L.L. Lobban, R.G. Mallinson, *Structural Effects of Na Promotion for High Water Gas Shift Activity on Pt–Na/TiO_2,* Journal of Catalysis **2011**, 278, 123-132.

[52] X. Zhu, T. Hoang, L.L. Lobban, R.G. Mallinson, *Significant Improvement in Activity and Stability of Pt/TiO_2 Catalyst for Water Gas Shift Reaction Via Controlling the Amount of Na Addition,* Catalysis Letters **2009**, 129, 135-141.

[53] J.H. Pazmiño, M. Shekhar, W.D. Williams, M.C. Akatay, J.T. Miller, W.N. Delgass, F.H. Ribeiro, *Metallic Pt as Active Sites for the Water Gas Shift Reaction on Alkali-Promoted Supported Catalysts,* Journal of Catalysis **2012**, 286, 279-286.

[54] J.M. Pigos, C.J. Brooks, G. Jacobs, B.H. Davis, *Low Temperature Water Gas Shift: Characterization of Pt-Based ZrO_2 Catalyst Promoted with Na Discovered by Combinatorial Methods,* Applied Catalysis A: General **2007**, 319, 47-57.

[55] J.M. Pigos, C.J. Brooks, G. Jacobs, B.H. Davis, *Low Temperature Water Gas Shift: The effect of Alkali Doping on the CH Bond of Formate over Pt/ZrO_2 Catalysts,* Applied Catalysis A: General **2007**, 328, 14-26.

[56] Y. Zhai, D. Pierre, R. Si, W. Deng, P. Ferrin, A.U. Nilekar, G. Peng, J.A. Herron, D.C. Bell, H. Saltsburg *et al*, *Alkali-Stabilized Pt-OH_x Species Catalyze Low Temperature Water Gas Shift Reactions,* Science **2010**, 329, 1633-1636.

[57] E. Chenu, G. Jacobs, A.C. Crawford, R.A. Keogh, P.M. Patterson, D.E. Sparks, B.H. Davis, *Water-gas shift: an Examination of Pt Promoted MgO and Tetragonal and Monoclinic ZrO_2 by In Situ DRIFTS,* Applied Catalysis B: Environmental **2005**, 59, 45-56.

[58] C.V. Ovesen, P. Stoltze, J.K. Nørskov, C.T. Campbell, *A Kinetic Model of the Water Gas Shift Reaction,* Journal of Catalysis **1992**, 134, 445-468.

[59] C.V. Ovesen, B.S. Clausen, B.S. Hammershøi, G. Steffensen, T. Askgaard, I. Chorkendorff, J.K. Nørskov, P.B. Rasmussen, P. Stoltze, P. Taylor, *A Microkinetic Analysis of the Water–Gas Shift Reaction under Industrial Conditions,* Journal of Catalysis **1996**, 158, 170-180.

[60]   T. van Herwijnen, W.A. de Jong, *Kinetics and Mechanism of the CO shift on CuZnO,* Journal of Catalysis **1980**, 63, 83-93.

[61]   R. Jain, A.S. Poyraz, D.P. Gamliel, J. Valla, S.L. Suib, R. Maric, *Comparative Study for Low Temperature Water-Gas Shift Reaction on Pt/Ceria Catalysts: Role of Different Ceria Supports,* Applied Catalysis A: General **2015**, 507, 1-13.

[62]   C. Vignatti, M.S. Avila, C.R. Apesteguı´a, T.F. Garetto, *Catalytic and DRIFTS Study of the WGS Reaction on Pt-Based Catalysts,* International Journal of Hydrogen Energy **2010**, 35, 7302-7312.

[63]   A.A. Gokhale, J.A. Dumesic, M. Mavrikakis, *On the Mechanism of Low-Temperature Water Gas Shift Reaction on Copper,* Journal of the American Chemical Society **2008**, 130, 1402-1414.

[64]   A. Brunetti, E. Drioli, G. Barbieri, *Medium/High Temperature Water Gas Shift Reaction in a Pd-Ag Membrane Reactor: an Experimental Investigation,* RSC Advances **2012**, 2, 226-233.

[65]   S. Adhikari, S. Fernando, *Hydrogen Membrane Separation Techniques,* Industrial & Engineering Chemistry Research **2006**, 45, 875-881.

[66]   S. Sircar, T.C. Golden, *Purification of Hydrogen by Pressure Swing Adsorption,* Separation Science and Technology **2000**, 35, 667-687.

[67]   F. Marcello De, L. Marrelli, G. Iaquaniello, *Membrane Reactors for Hydrogen Production Processes***,** Springer **2011**.

[68]   R. Dittmeyer, V. Höllein, K. Daub, *Membrane Reactors for Hydrogenation and Dehydrogenation Processes Based on Supported Palladium,* ournal of Molecular Catalysis A: Chemical **2001**, 173, 135-184.

[69]   G. Barbieri, A. Brunetti, A. Caravella, E. Drioli, *Pd-based Membrane Reactors for One-Stage Process of Water Gas Shift,* RSC Advances **2011**, 1, 651-661.

[70]   E. Drioli, A. Brunetti, G. Di Profio, G. Barbieri, *Process Intensification Strategies and Membrane Engineering,* Green Chemistry **2012**, 14, 1561-1572.

[71]   F. Gallucci, E. Fernandez, P. Corengia, M. van Sint Annaland, *Recent Advances on Membranes and Membrane Reactors for Hydrogen Production,* Chemical Engineering Science **2013**, 92, 40-66.

[72]   S. Yun, S.T. Oyama, *Correlations in Palladium Membranes for Hydrogen Separation: A Review,* Journal of Membrane Science **2011**, 375, 28-45.

[73]   S.N. Paglieri, J.D. Way, *Innovations in Palladium Membrane Research,* Separation & Purification Reviews **2002**, 31, 1-169.

[74]   H. Kurokawa, Y. Shirasaki, I. Yasuda, *Energy-Efficient Distributed Carbon Capture in Hydrogen Production from Natural Gas,* Energy Procedia **2011**, 4, 674-680.

[75]   P. Pfeifer, *Application of Catalysts to Metal Microreactor Systems* in *Chemical Kinetic*, Edited by V. Patel, InTech, **2012**, 325-344.

[76]   T. Boeltken, A. Wunsch, T. Gietzelt, P. Pfeifer, R. Dittmeyer, *Ultra-Compact Microstructured Methane Steam Reformer with Integrated Palladium Membrane for on-site Production of Pure Hydrogen: Experimental Demonstration,* International Journal of Hydrogen Energy **2014**, 39, 18058-18068.

[77]   G. Kolb, *Review: Microstructured Reactors for Distributed and Renewable Production of Fuels and Electrical Energy,* Chemical Engineering and Processing: Process Intensification **2013**, 65, 1-44.

[78]   G. Germani, P. Alphonse, M. Courty, Y. Schuurman, C. Mirodatos, *Platinum/Ceria/Alumina Catalysts on Microstructures for Carbon Monoxide Conversion,* Catalysis Today **2005**, 110, 114-120.

[79]   O. Goerke, P. Pfeifer, K. Schubert, *Water Gas Shift Reaction and Selective Oxidation of CO in Microreactors,* Applied Catalysis A: General **2004**, 263, 11-18.

[80]   E.F. Gallei, M. Hesse, E. Schwab, *Preparation of Solid Catalysts* in *Handbook of Heterogeneous Catalysis*, *Volume 1*, Edited by G. Ertl, H. Knozinger, F. Schüth, J. Weitkamp, Weinheim, Wiley-VCH Verlag GmbH& Co. KGaA **2008**, 57-66.

[81]   R. Strobel, S.E. Pratsinis, *Flame Synthesis of Supported Platinum Group Metals for Catalysis and Sensors,* Platinum Metals Review **2009**, 53, 11-20.

[82]   W.Y. Teoh, R. Amal, L. Madler, *Flame spray pyrolysis: An EnablingTechnology for Nanoparticles Design and Fabrication,* Nanoscale **2010**, 2, 1324-1347.

[83]   H.K. Kammler, L. Mädler, S.E. Pratsinis, *Flame Synthesis of Nanoparticles,* Chemical Engineering & Technology **2001**, 24, 583-569.

[84]   S.E. Pratsinis, *Flame Aerosol Synthesis of Ceramic Powders,* Progress in Energy and Combustion Science **1998**, 24, 197-219.

[85]   R. Strobel, S.E. Pratsinis, *Flame Aerosol Synthesis of Smart Nanostructured Materials,* Journal of Materials Chemistry **2007**, 17, 4743-4756.

[86]   T. Rudin, K. Wegner, S.E. Pratsinis, *Uniform Nanoparticles by Flame-Assisted Spray Pyrolysis (FASP) of Low Cost Precursors,* Journal of Nanoparticle Research **2011**, 13, 2715-2725.

[87]   R. Strobel, A. Alfons, S.E. Pratsinis, *Aerosol Flame Synthesis of Catalysts,* Advanced Powder Technology **2006**, 17, 457-480.

[88]   M. Sokolowski, A. Sokolowska, A. Michalski, B. Gokieli, *The "In-Flame-Reaction" Method for Al_2O_3 Aerosol Formation,* Journal of Aerosol Science **1977**, 8, 219-230.

[89]   C.R. Bickmore, K.F. Waldner, D.R. Treadwell, R.M. Laine, *Ultrafine Spinel Powders by Flame Spray Pyrolysis of a Magnesium Aluminum Double Alkoxide,* Journal of the American Ceramic Society **1996**, 79, 1419-1423.

[90]   L. Mädler, H.K. Kammler, R. Mueller, S.E. Pratsinis, *Controlled Synthesis of Nanostructured Particles by Flame Spray Pyrolysis,* Journal of Aerosol Science **2002**, 33, 369-389.

[91]   R. Mueller, R. Jossen, H.K. Kammler, S.E. Pratsinis, M.K. Akhtar, *Growth of Zirconia Particles Made by Flame Spray Pyrolysis,* AIChE Journal **2004**, 50, 3085-3094.

[92]   H. Schulz, L. Mädler, R. Strobel, R. Jossen, S.E. Pratsinis, T. Johannessen, *Independent Control of Metal Cluster and Ceramic Particle Characteristics During One-step Synthesis of Pt/TiO_2,* Journal of Materials Research **2005**, 20, 2568-2577.

[93]   G.L. Chiarello, I. Rossetti, L. Forni, *Flame-Spray Pyrolysis Preparation of Perovskites for Methane Catalytic Combustion,* Journal of Catalysis **2005**, 236, 251-261.

[94]   R. Strobel, W.J. Stark, L. Mädler, S.E. Pratsinis, A. Baiker, *Flame-Made Platinum/Alumina: Structural Properties and Catalytic Behaviour in Enantioselective Hydrogenation,* Journal of Catalysis **2003**, 213, 296-304.

[95]   W.Y. Teoh, L. Mädler, D. Beydoun, S.E. Pratsinis, R. Amal, *Direct (one-step) Synthesis of TiO_2 and Pt/TiO_2 Nanoparticles for Photocatalytic Mineralisation of Sucrose,* Chemical Engineering Science **2005**, 60, 5852-5861.

[96]   R. Strobel, L. Mädler, M. Piacentini, M. Maciejewski, A. Baiker, S.E. Pratsinis, *Two-Nozzle Flame Synthesis of $Pt/Ba/Al_2O_3$ for NO_x Storage,* Chemistry of Materials **2006**, 18, 2532-2537.

[97]   M. Høj, D.K. Pham, M. Brorson, L. Mädler, A.D. Jensen, J.-D. Grunwaldt, *Two-Nozzle Flame Spray Pyrolysis (FSP) Synthesis of $CoMo/Al_2O_3$ Hydrotreating Catalysts,* Catalysis Letters **2013**, 143, 386-394.

[98]   M. Tepluchin, M. Casapu, A. Boubnov, H. Lichtenberg, D. Wang, S. Kureti, J.-D. Grunwaldt, *Fe and Mn-Based Catalysts Supported on γ-Al$_2$O$_3$ for CO Oxidation under O$_2$-Rich Conditions,* ChemCatChem **2014**, 6,1763-1773.

[99]   F.M.F. de Groot, A. Knop-Gericke, T. Ressler, *X-ray Absorption Near Edge Spectroscopy* in *In-Situ Spectroscopy of Catalysts*, Edited by B. M. Weckhuysen, American Scientific Publishers **2004**, 105-122.

[100]   C. Scott, *XAFS for Everyone*, Taylor & Francis Group **2013**.

[101]   M. Newville, *Fundamentals of XAFS,* Consortium for Advanced Radiation Sources, University of Chicago, Chicago, IL **2004**.

[102]   G. Bunker, *EXAFS*, United States of America by Cambridge University Press, 1st Edition, New York, **2010**.

[103]   J.-D. Grunwaldt, A.I. Frenkel, *Synchrotron Studies of Catalysts: From XAFS to QEXAFS and Beyond,* Synchrotron Radiation News **2009**, 22, 2-4.

[104]   J.A. Van Bokhoven, T. Ressler, F.M.F. De Groot, A. Knop-Gericke, *Extended X-ray Absorption Fine-Structure Spectroscopy* in *In-situ Spectroscopy of Catalysts*, Edited by B. M. Weckhuysen, American Scientific Publishers **2004**, 123-144.

[105]   M. Bauer, H. Bertagnolli, *X-Ray Absorption Spectroscopy – the Method and Its Applications* in *Methods in Physical Chemistry*, Edited by R. Schäfer, P. C. Schmidt, Wiley-VCH Verlag GmbH & Co. KGaA **2012**, 231-269.

[106]   B.M. Weckhuysen, *In-situ Spectroscopy of Catalysts* in *In-Situ Spectroscopy of Catalysts*, Edited by B. M. Weckhuysen **2004**, 1-10.

[107]   J.D. Grunwaldt, *In Situ Analysis of Heterogeneous Catalysts in Chemical Energy Conversion* in *Chemical Energy Storage*, Edited by R. Schlögl, Walter de Gruyter GmbH&Co.KG **2013**, 311-324.

[108]   J.-D. Grunwaldt, A. Baiker, *Axial Variation of the Oxidation State of Pt-Rh/Al$_2$O$_3$ during Partial Methane Oxidation in a Fixed-Bed Reactor: An In Situ X-ray Absorption Spectroscopy Study,* Catalysis Letters **2005**, 99, 5-12.

[109]   J.-D. Grunwaldt, L. Basini, B.S. Clausen, *In Situ EXAFS Study of Rh/Al$_2$O$_3$ Catalysts for Catalytic Partial Oxidation of Methane,* Journal of Catalysis **2001**, 200, 321-329.

[110]   J.-D. Grunwaldt, N. van Vegten, A. Baiker, *Insight into the Structure of Supported Palladium Catalysts during the Total Oxidation of Methane,* Chemical Communications **2007**, 4635-4637.

[111] W.J. Stark, S.E. Pratsinis, A. Baiker, *Heterogeneous Catalysis by Flame-Made Nanoparticles,* CHIMIA International Journal for Chemistry **2002**, 56, 485-489.

[112] G. Cavusoglu, D. Miao, H. Lichtenberg, H.W.P. Carvalho, H. Xu, A. Goldbach, J.-D. Grunwaldt, *Structure and Activity of Flame Made Ceria Supported Rh and Pt Water Gas Shift Catalysts,* Applied Catalysis A: General **2015**, 504, 381-390.

[113] C. Weidenthaler, *Pitfalls in the Characterization of Nanoporous and Nanosized Materials,* Nanoscale **2011**, 3, 792-810.

[114] R.E. Dinnebier, S.J.L. Billinge, *Principles of Powder Diffraction* in *Powder Diffraction-Theory and Practice*, Edited by R. E. Dinnebier, S. J. L. Billinge, The Royal Society of Chemistry **2008**, 1-19.

[115] A. Le Bail, *The Profile of a Bragg Reflection for Extracting Intensities* in *Powder Diffraction-Theory and Practice*, Edited by R. E. Dinnebier, S. J. L. Billinge, The Royal Society of Chemistry **2008**, 134-165.

[116] I. Chorkendorff, J.W. Niemantsverdriet, *Concepts of Modern Catalysis and Kinetics*, WILEY-VCH Verlag GmbH & Co. KGaA **2003**.

[117] G. Bergeret, P. Gallezot, *Particle Size and Dispersion Measurements* in *Handbook of Heterogeneous Catalysis*, *Volume 1*, Edited by G. Ertl, H. Knozinger, F. Schüth, J. Weitkamp, Weinheim, Wiley-VCH Verlag GmbH & Co. KGaA **2008**, 738-763.

[118] A.V. Neimark, K.S.W. Sing, M. Thommes, *Surface Area and Porosity* in *Handbook of Heterogeneous Catalysis*, *Volume 1*, Edited by G. Ertl, H. Knozinger, F. Schüth, J. Weitkamp, Weinheim, Wiley-VCH Verlag GmbH& Co. KGaA **2008**, 721-737.

[119] J.A. Anderson, M. Fernández-García, A. Martínez-Arias, *Determination of Dispersion and Crystallite Sizes for Supported Metal Catalysts* in *Supported Metals in Catalysis*, 2nd edn, London, Imperial College Pres **2012**, 41-79.

[120] V. Perrichon, L. Retailleau, P. Bazin, M. Daturi, J.C. Lavalley, *Metal Dispersion of CeO_2–ZrO_2 Supported Platinum Catalysts Measured by H_2 or CO chemisorption,* Applied Catalysis A: General **2004**, 260, 1-8.

[121] T. Tanabe, Y. Nagai, T. Hirabayashi, N. Takagi, K. Dohmae, N. Takahashi, S.I. Matsumoto, H. Shinjoh, J.N. Kondo, J.C. Schouten, H.H. Brongersma, *Low Temperature CO Pulse Adsorption for the Determination of Pt particle Size in a Pt/Cerium-Based Oxide Catalyst,* Applied Catalysis A: General **2009**, 370, 108-113.

[122] N.W. Hurst, S.J. Gentry, A. Jones, B.D. McNicol, *Temperature Programmed Reduction,* Catalysis Reviews **1982**, 24, 233-309.

[123] R. Frahm, *New Method for Time Dependent X-ray Absorption Studies,* Review of Scientific Instruments **1989**, 60, 2515-2518.

[124] M. Newville, *IFEFFIT : interactive XAFS analysis and FEFF fitting,* Journal of Synchrotron Radiation **2001**, 8, 322-324.

[125] P.W. Albers, *Bulk Chemical Composition* in *Handbook of Heterogeneous Catalysis*, Edited by G. Ertl, H. Knozinger, F. Schüth, J. Weitkamp, Weinheim, Wiley-VCH Verlag GmbH & Co. KGaA **2008**, 1000-1013.

[126] R. Dittmeyer et al. , J.-D. Grunwaldt et al. , *Integration of thin Amorphous Membrane by Laser Welding* (publication in progress).

[127] http://henke.lbl.gov/optical_constants/, Berkeley, California .

[128] A. Zimina, K. Dardenne, M.A. Denecke, J.D. Grunwaldt, E. Huttel, H. Lichtenberg, S. Mangold, T. Pruessmann, J. Rothe, R. Steininger *et al*, *The CAT-ACT Beamline at ANKA: A new High Energy X-ray Spectroscopy Facility for CATalysis and ACTinide Research,* Journal of Physics: Conference Series **2016**, 712, 012019.

[129] J.-D. Grunwaldt, M. Caravati, S. Hannemann, A. Baiker, *X-ray Absorption Spectroscopy under Reaction Conditions: Suitability of Different Reaction Cells for Combined Catalyst Characterization and Time-Resolved Studies,* Physical Chemistry Chemical Physics **2004**, 6, 3037-3047.

[130] J.-D. Grunwaldt, B.S. Clausen, *Combining XRD and EXAFS with On-line Catalytic Studies for In Situ Characterization of Catalysts,* Topics in Catalysis **2002**, 18, 37-43.

[131] T. Gunter, H.W.P. Carvalho, D.E. Doronkin, T. Sheppard, P. Glatzel, A.J. Atkins, J. Rudolph, C.R. Jacob, M. Casapu, J.-D. Grunwaldt, *Structural Snapshots of the SCR Reaction Mechanism on Cu-SSZ-13,* Chemical Communications **2015**, 51, 9227-9230.

[132] A.M. Ruppert, B.M. Weckhuysen, *Active Phase – Support Interactions* in *Handbook of Heterogeneous Catalysis*, Edited by G. Ertl, H. Knozinger, F. Schüth, J. Weitkamp, Wiley-VCH Verlag GmbH& Co. KGaA **2008**, 1178-1187.

[133] J. Kašpar, P. Fornasiero, N. Hickey, *Automotive Catalytic Converters: Current Status and some Perspectives,* Catalysis Today **2003**, 77, 419-449.

[134] R.M. Heck, R.J. Farrauto, *Automobile Exhaust Catalysts,* Applied Catalysis A: General **2001**, 221, 443–457.

[135] J.M. Christensen, D. Deiana, J.-D. Grunwaldt, A.D. Jensen, *Ceria Prepared by Flame Spray Pyrolysis as an Efficient Catalyst for Oxidation of Diesel Soot,* Catalysis Letters **2014**, 144, 1661-1666.

[136] A. Trovarelli, *Catalytic Properties of Ceria and CeO_2-Containing Materials,* Catalysis Reviews **1996**, 38, 439-520.

[137] M. Yashima, *Cyrstal and Electronic Structures, Structural Disorder, Phase Transformation and Phase Diagram of Ceria-Zirconia and Ceria-based Materials* in *Catalysis by Ceria and Related Materials*, 2nd Edition, Edited by A. Trovarelli, P. Fornasiero, Imperial College Press **2013**, 1-45.

[138] H.C. Yao, Y.F.Y. Yao, *Ceria in Automotive Exhaust Catalysts,* Journal of Catalysis **1984**, 86, 254-265.

[139] A. Trovarelli, G. Dolcetti, C. de Leitenburg, J. Kaspar, P. Finetti, A. Santoni, *Rh-CeO_2 Interaction Induced by High-Temperature Reduction. Characterization and Catalytic Behaviour in Transient and Continuous Conditions,* Journal of the Chemical Society, Faraday Transactions **1992**, 88, 1311-1319.

[140] G. Kim, *Ceria-Promoted Three-Way Catalysts for Auto Exhaust Emission Control,* Industrial & Engineering Chemistry Product Research and Development **1982**, 21, 267-274.

[141] T. Shido, Y. Iwasawa, *Regulation of Reaction Intermediate by Reactant in the Water-Gas Shift Reaction on CeO_2, in Relation to Reactant-Promoted Mechanism,* Journal of Catalysis **1992**, 136, 493-503.

[142] L. Mädler, W.J. Stark, S.E. Pratsinis, *Flame-Made Ceria Nanoparticles,* Journal of Materials Research **2002**, 17, 1356-1362.

[143] A. Luengnaruemitchai, S. Osuwan, E. Gulari, *Comparative studies of Low-Temperature Water–Gas Shift Reaction over Pt/CeO_2, Au/CeO_2, and Au/Fe_2O_3 Catalysts,* Catalysis Communications **2003**, 4, 215-221.

[144] G. Jacobs, L. Williams, U. Graham, G.A. Thomas, D.E. Sparks, B.H. Davis, *Low Temperature Water-Gas Shift: In Situ DRIFTS-Reaction Study of Ceria Surface Area on the Evolution of Formates on Pt/CeO_2 Fuel Processing Catalysts for Fuel Cell Applications,* Applied Catalysis A: General **2003**, 252, 107-118.

[145] B. Liu, A. Goldbach, H. Xu, *Sour Water-Gas shift Reaction over Pt/CeO_2 Catalysts,* Catalysis Today **2011**, 171, 304-311.

[146] C. Diagne, H. Idriss, A. Kiennemann, *Hydrogen Production by Ethanol Reforming over Rh/CeO₂–ZrO₂ Catalysts,* Catalysis Communications **2002**, 3, 565-571.

[147] M.J. Beier, B. Schimmoeller, T.W. Hansen, J.E.T. Andersen, S.E. Pratsinis, J.-D. Grunwaldt, *Selective Side-chain Oxidation of Alkyl Aromatic Compounds Catalyzed by Cerium Modified Silver Catalysts,* J Journal of Molecular Catalysis A: Chemical **2010**, 331, 40-49.

[148] S. Bernal, J.J. Calvino, M.A. Cauqui, J.M. Gatica, C. López Cartes, J.A. Pérez Omil, J.M. Pintado, *Some Contributions of Electron Microscopy to the Characterisation of the Strong Metal–Support Interaction Effect,* Catalysis Today **2003**, 77, 385-406.

[149] G. Jacobs, S. Ricote, U.M. Graham, P.M. Patterson, B.H. Davis, *Low Temperature Water Gas Shift: Type and Loading of Metal Impacts forward Decomposition of Pseudo-Stabilized Formate over Metal/Ceria Catalysts,* Catalysis Today **2005**, 106, 259-264.

[150] J.-D. Grunwaldt, B. Kimmerle, S. Hannemann, A. Baiker, P. Boye, C.G. Schroer, *Parallel Structural Screening of Solid Materials,* Journal of Materials Chemistry **2007**, 17, 2603-2606.

[151] H. Roh, Jeong, D., Kim, K. et al., *Single Stage Water-Gas Shift Reaction Over Supported Pt Catalysts,* Catalysis Letters **2011**, 141, 95-99.

[152] A. Jentys, *Estimation of Mean Size and Shape of Small Metal Particles by EXAFS,* Physical Chemistry Chemical Physics **1999**, 1, 4059-4063.

[153] C.B. Roldan, O.M. Alcántara, L.K. Ono, F. Behafarid, S. Mostafa, J.R. Croy, K. Paredis, G. Shafai, T.S. Rahman, L. Li *et al*, *Thermodynamic Properties of Pt Nanoparticles: Size, Shape, Support, and Adsorbate Effects,* Hysical Review B **2011**, 84, 245438.

[154] Y. Nagai, T. Hirabayashi, K. Dohmae, N. Takagi, T. Minami, H. Shinjoh, S. Matsumoto, *Sintering Inhibition Mechanism of Platinum Supported on Ceria-Based Oxide and Pt-Oxide–Support Interaction,* Journal of Catalysis **2006**, 242, 103-109.

[155] A. Boubnov, S. Dahl, E. Johnson, A.P. Molina, S.B. Simonsen, F.M. Cano, S. Helveg, L.J. Lemus-Yegres, J.-D. Grunwaldt, *Structure–Activity Relationships of Pt/Al₂O₃ Catalysts for CO and NO oxidation at Diesel Exhaust Conditions,* Applied Catalysis B: Environmental **2012**, 126, 315-325.

[156] C. Wheeler, A. Jhalani, E.J. Klein, S. Tummala, L.D. Schmidt, *The Water–Gas-Shift Reaction at Short Contact Times,* Journal of Catalysis **2004**, 223, 191-199.

[157] P. Piermartini, T. Schuhmann, P. Pfeifer, G. Schaub, *Water Gas Shift in Microreactors at Elevated Pressure: Platinum-Based Catalyst Systems and Pressure Effects,* Topics in Catalysis **2011**, 54, 967-976.

[158] H. Meland, T. Johannessen, B. Arstad, H.J. Venvik, M. Rønning, A. Holmen, *Preparation of Low Lemperature Water-Gas Shift Catalysts by Flame Spray Pyrolysis* in *Studies in Surface Science and Catalysis, Volume 162*, Elsevier **2006**, 985-992.

[159] G.B. Raupp, J.A. Dumesic, *Adsorption of Carbon Monoxide, Carbon Dioxide, Hydrogen, and Water on Titania Surfaces with Different Oxidation States,* The Journal of Physical Chemistry **1985**, 89, 5240-5246.

[160] Y. Zhou, D.E. Doronkin, M. Chen, S. Wei, J.-D. Grunwaldt, *Interplay of Pt and Crystal Facets of TiO$_2$: CO Oxidation Activity and Operando XAS/DRIFTS Studies,* ACS Catalysis **2016**, 6, 7799-7809.

[161] J.-D. Grunwaldt, A. Baiker, *Gold/Titania Interfaces and Their Role in Carbon Monoxide Oxidation,* The Journal of Physical Chemistry B **1999**, 103, 1002-1012.

[162] M. Calatayud, A. Markovits, M. Menetrey, B. Mguig, C. Minot, *Adsorption on Perfect and Reduced Surfaces of Metal Oxides,* Catalysis Today **2003**, 85, 125-143.

[163] S. Akbar, P. Dutta, C. Lee, *High-Temperature Ceramic Gas Sensors: A Review,* International Journal of Applied Ceramic Technology **2006**, 3, 302-311.

[164] G.L. Haller, D.E. Resasco, *Metal–Support Interaction: Group VIII Metals and Reducible Oxides* in *Advances in Catalysis*, *Volume 36*, Edited by D. D. Eley, H. Pines, P. B. Weisz, Academic Press **1989**, 173-235.

[165] Z. Jiang, Y. Yang, W. Shangguan, Z. Jiang, *Influence of Support and Metal Precursor on the State and CO Catalytic Oxidation Activity of Platinum Supported on TiO$_2$,* The Journal of Physical Chemistry C **2012**, 116, 19396-19404.

[166] D.A.H. Hanaor, C.C. Sorrell, *Review of the Anatase to Rutile Phase Transformation,* Journal of Materials Science **2011**, 46, 855-874.

[167] N. Wetchakun, B. Incessungvorn, K. Wetchakun, S. Phanichphant, *Influence of Calcination Temperature on Anatase to Rutile Phase Transformation in TiO$_2$ Nanoparticles Synthesized by the Modified Sol–Gel Method,* Materials Letters **2012**, 82, 195-198.

[168] H. Sakurai, A. Ueda, T. Kobayashi, M. Haruta, *Low-Temperature Water-Gas Shift Reaction over Gold Deposited on TiO$_2$,* Chemical Communications **1997**, 271-272.

[169] P. Panagiotopoulou, D.I. Kondarides, *Effect of Morphological Characteristics of TiO₂-Supported Noble Metal Catalysts on their Activity for the Water-Gas Shift Reaction,* Journal of Catalysis **2004**, 225, 327-336.

[170] K.G. Azzam, I.V. Babich, K. Seshan, L. Lefferts, *Bifunctional Catalysts for Single-Stage Water–Gas Shift Reaction in Fuel Cell Applications.: Part 1. Effect of the Support on the Reaction Sequence,* Journal of Catalysis **2007**, 251, 153-162.

[171] K.G. Azzam, I.V. Babich, K. Seshan, L. Lefferts, *A Bifunctional Catalyst for the Single-Stage Water–Gas Shift Reaction in Fuel Cell Applications. Part 2. Roles of the Support and Promoter on Catalyst Activity and Stability,* Journal of Catalysis **2007**, 251, 163-171.

[172] S.J. Tauster, S.C. Fung, R.L. Garten, *Strong Metal-Support Interactions. Group 8 Noble Metals Supported on Titanium Dioxide,* Journal of the American Chemical Society **1978**, 100, 170-175.

[173] J. van de Loosdrecht, A.M. van der Kraan, A.J. van Dillen, J.W. Geus, *Metal-Support Interaction: Titania-Supported and Silica-Supported Nickel Catalysts,* Journal of Catalysis **1997**, 170, 217-226.

[174] Y. Li, Y. Fan, H. Yang, B. Xu, L. Feng, M. Yang, Y. Chen, *Strong Metal-Support Interaction and Catalytic Properties of Anatase and Rutile Supported Palladium Catalyst Pd/TiO₂,* Chemical Physics Letters **2003**, 372, 160-165.

[175] H.K. Grossmann, T. Grieb, F. Meierhofer, M.J. Hodapp, D. Noriler, A. Gröhn, H.F. Meier, U. Fritsching, K. Wegner, L. Mädler, *Nanoscale Mixing during Double-Flame Spray Synthesis of Heterostructured Nanoparticles,* Journal of Nanoparticle Research **2015**, 17, 1-16.

[176] O.I. Arabi–Katbi, S.E. Pratsinis, P.W. Morrison Jr, C.M. Megaridis, *Monitoring the Flame Synthesis of TiO₂ Particles by In-Situ FTIR Spectroscopy and Thermophoretic Sampling,* Combustion and Flame **2001**, 124, 560-572.

[177] M. Minnermann, H.K. Grossmann, S. Pokhrel, K. Thiel, H. Hagelin-Weaver, M. Bäumer, L. Mädler, *Double Flame Spray pyrolysis as a Novel Technique to Synthesize Alumina-Supported Cobalt Fischer–Tropsch Catalysts,* Catalysis Today **2013**, 214, 90-99.

[178] G. Cavusoglu, H. Lichtenberg, A. Gaur, A. Goldbach, J.D. Grunwaldt, *Flame Made Ceria Supported Noble Metal Catalysts for Efficient H₂ Production via the Water Gas Shift Reaction,* Journal of Physics: Conference Series **2016**, 712, 012065.

[179] W.J. Stark, J.-D. Grunwaldt, M. Maciejewski, S.E. Pratsinis, A. Baiker, *Flame-Made Pt/Ceria/Zirconia for Low-Temperature Oxygen Exchange,* Chemistry of Materials **2005**, 17, 3352-3358.

[180] D. Miao, A. Goldbach, H. Xu, *Platinum/Apatite Water-Gas Shift Catalysts,* ACS Catalysis **2016**, 6, 775-783.

[181] E. Riedel, *Anorganische Chemie*, *Volume* 6, Berlin Walter de Gruyter **2004**.

[182] K.G. Azzam, I.V. Babich, K. Seshan, L. Lefferts, *Single Stage Water Gas Shift Conversion over Pt/TiO₂—Problem of Catalyst Deactivation,* Applied Catalysis A: General **2008**, 338, 66-71.

[183] R.J. Gorte, S. Zhao, *Studies of the Water-Gas-Shift Reaction with Ceria-Supported Precious Metals,* Catalysis Today **2005**, 104, 18-24.

[184] T. Murota, T. Hasegawa, S. Aozasa, H. Matsui, M. Motoyama, *Production Method of Cerium Oxide with High Storage Capacity of Oxygen and its Mechanism,* Journal of Alloys and Compounds **1993**, 193, 298-299.

[185] M. Ozawa, M. Kimura, A. Isogai, *The application of Ce-Zr Oxide Solid Solution to Oxygen Storage Promoters in Automotive Catalysts,* Journal of Alloys and Compounds **1993**, 193, 73-75.

[186] A. Trovarelli, F. Zamar, J. Llorca, C. de Leitenburg, G. Dolcetti, J.T. Kiss, *Nanophase Fluorite-Structured CeO₂–ZrO₂ Catalysts Prepared by High-Energy Mechanical Milling,* Journal of Catalysis **1997**, 169, 490-502.

[187] A. Trovarelli, C. de Leitenburg, G. Dolcetti, *Design better Cerium-Based Oxidation Catalysts,* Chem Tech **1997**, 27, 32-37.

[188] P. Fornasiero, G. Balducci, R. Di Monte, J. Kašpar, V. Sergo, G. Gubitosa, A. Ferrero, M. Graziani, *Modification of the Redox Behaviour of CeO₂ Induced by Structural Doping with ZrO2,* Journal of Catalysis **1996**, 164, 173-183.

[189] C. de Leitenburg, A. Trovarelli, J. Llorca, F. Cavani, G. Bini, *The Effect of Doping CeO₂ with Zirconium in the Oxidation of Isobutane,* Applied Catalysis A: General **1996**, 139, 161-173.

[190] W.J. Stark, L. Madler, M. Maciejewski, S.E. Pratsinis, A. Baiker, *Flame Ssynthesis of Nanocrystalline Ceria-Zirconia: Effect of Carrier Liquid,* Catalysis Communications **2003**, 588, 588-589.

[191] D. Miao, G. Cavusoglu, H. Lichtenberg, J. Yu, H. Xu, J.-D. Grunwaldt, A. Goldbach, *Water-Gas Shift Reaction over Platinum/Strontium Apatite Catalysts,* Applied Catalysis B: Environmental **2017**, 202, 587-596.

[192] R. Strobel, F. Krumeich, S.E. Pratsinis, A. Baiker, *Flame-derived Pt/Ba/: Influence of Support on Thermal Deterioration and Behavior as Storage-Reduction Catalysts,* Journal of Catalysis **2006**, 243, 229-238.

[193] N. Hotz, M.J. Stutz, S. Loher, W.J. Stark, D. Poulikakos, *Syngas Production from Butane using a Flame-Made $Rh/Ce_{0.5}Zr_{0.5}O_2$ Catalyst,* Applied Catalysis B: Environmental **2007**, 73, 336-344.

[194] F. Menegazzo, F. Pinna, M. Signoretto, V. Trevisan, F. Boccuzzi, A. Chiorino, M. Manzoli, *Quantitative Determination of Sites Able to Chemisorb CO on Au/ZrO_2 Catalysts,* Applied Catalysis A: General **2009**, 356, 31-35.

[195] D.-W. Jeong, H.S. Potdar, J.-O. Shim, W.-J. Jang, H.-S. Roh, *H_2 Production from a Single Stage Water Gas Shift Reaction over Pt/CeO_2, Pt/ZrO_2, and $Pt/Ce_{(1-x)}Zr_{(x)}O_2$ Catalysts,* International Journal of Hydrogen Energy **2013**, 38, 4502-4507.

[196] R. Mueller, R. Jossen, S.E. Pratsinis, M. Watson, M.K. Akhtar, *Zirconia Nanoparticles Made in Spray Flames at High Production Rates,* Journal of the American Ceramic Society **2004**, 87, 197-202.

[197] R.C. Garvie, *The Occurrence of Metastable Tetragonal Zirconia as a Crystallite Size Effect,* The Journal of Physical Chemistry **1965**, 69, 1238-1243.

[198] T. Chraska, A.H. King, C.C. Berndt, *On the size-dependent Phase Transformation in Nanoparticulate Zirconia,* Materials Science and Engineering: A **2000**, 286, 169-178.

[199] W.J. Stark, L. Mädler, S.E. Pratsinis, *Flame Made Metal Oxides* in, vol. US 7,211,236 B2, Google Patents, **2007**.

[200] C. Padeste, N.W. Cant, D.L. Trimm, *Reactions of Ceria Supported Rhodium with Hydrogen and Nitric Oxide Studied with TPR/TPO and XPS Techniques,* Catalysis Letters **1994**, 28, 301-311.

[201] K. Yaccato, R. Carhart, A. Hagemeyer, A. Lesik, P. Strasser, A.F. Volpe Jr, H. Turner, H. Weinberg, R.K. Grasselli, C. Brooks, *Competitive CO and CO_2 Methanation over Supported Noble Metal Catalysts in High Throughput Scanning Mass Spectrometer,* Applied Catalysis A: General **2005**, 296, 30-48.

[202] T. Iizuka, Y. Tanaka, K. Tanabe, *Hydrogenation of CO and CO$_2$ over Rhodium Catalysts Supported on Various Metal Oxides,* Journal of Catalysis **1982**, 76,1-8.

[203] C.M. Kalamaras, S. Americanou, A.M. Efstathiou, *"Redox" vs "Associative Formate with -OH Group Regeneration" WGS Reaction Mechanism on Pt/CeO$_2$: Effect of Platinum Particle Size,* Journal of Catalysis **2011**, 279, 287-300.

[204] G. Jacobs, S. Ricote, B.H. Davis, *Low Temperature Water-Gas Shift: Type and Loading of Metal Impacts Decomposition and Hydrogen Exchange Rates of Pseudo-Stabilized Formate over Metal/Ceria Catalysts,* Applied Catalysis A: General **2006**, 302, 14-21.

[205] S. Ricote, G. Jacobs, M. Milling, Y. Ji, P.M. Patterson, B.H. Davis, *Low Temperature Water–Gas Shift: Characterization and Testing of Binary Mixed Oxides of Ceria and Zirconia Promoted with Pt,* Applied Catalysis A: General **2006**, 303, 35-47.

[206] C.I. Vignatti, M.S. Avila, C.R. Apesteguía, T.F. Garetto, *Study of the Water-Gas Shift Reaction over Pt Supported on CeO$_2$–ZrO$_2$ Mixed Oxides,* Catalysis Today **2011**, 171, 297-303.

[207] C.M. Kalamaras, D.D. Dionysiou, A.M. Efstathiou, *Mechanistic Studies of the Water–Gas Shift Reaction over Pt/Ce$_x$Zr$_{1-x}$O$_2$ Catalysts: The Effect of Pt Particle Size and Zr Dopant,* ACS Catalysis **2012**, 2, 2729-2742.

[208] K.-R. Hwang, S.-K. Ihm, S.-C. Park, J.-S. Park, *Pt/ZrO$_2$ Catalyst for a Single-Stage Water-Gas Shift Reaction: Ti Addition Effect,* International Journal of Hydrogen Energy **2013**, 38, 6044-6051.

[209] X. Liu, W. Ruettinger, X. Xu, R. Farrauto, *Deactivation of Pt/CeO$_2$ Water-Gas Shift Catalysts due to Shutdown/Startup Modes for Fuel Cell Applications,* Applied Catalysis B: Environmental **2005**, 56, 69-75.

[210] J.-D. Grunwaldt, J.B. Wagner, R.E. Dunin-Borkowski, *Imaging Catalysts at Work: A Hierarchical Approach from the Macro- to the Meso- and Nano-Scale,* ChemCatChem **2013**, 5, 62-80.

[211] J.-D. Grunwaldt, C.G. Schroer, *Hard and soft X-ray Microscopy and Tomography in Catalysis: Gridging the Different Time and Length Scales,* Chemical Society Reviews **2010**, 39, 4741-4753.

[212] A. Gayen, K.R. Priolkar, P.R. Sarode, V. Jayaram, M.S. Hegde, G.N. Subbanna, S. Emura, *Ce1-xRhxO2-δ Solid Solution Formation in Combustion-Synthesized Rh/CeO$_2$*

Catalyst Studied by XRD, TEM, XPS, and EXAFS, Chemistry of Materials **2004**, 16, 2317-2328.

[213] H. Gao, Y.S. Lin, Y. Li, B. Zhang, *Chemical Stability and Its Improvement of Palladium-Based Metallic Membranes,* Industrial & Engineering Chemistry Research **2004**, 43, 6920-6930.

[214] H. Li, A. Goldbach, W. Li, H. Xu, *PdC Formation in ultra-thin Pd Membranes during Separation of H_2/CO Mixtures,* Journal of Membrane Science **2007**, 299, 130-137.

[215] W. Deng, A.I. Frenkel, R. Si, M. Flytzani-Stephanopoulos, *Reaction-Relevant Gold Structures in the Low Temperature Water-Gas Shift Reaction on Au-CeO$_2$,* The Journal of Physical Chemistry C **2008**, 112, 12834-12840.

[216] D. Tibiletti, A.A. Fonseca, R. Burch, Y. Chen, J.M. Fisher, A. Goguet, C. Hardacre, P. Hu, D. Thompsett, *DFT and In Situ EXAFS Investigation of Gold/Ceria−Zirconia Low-Temperature Water Gas Shift Catalysts: Identification of the Nature of the Active Form of Gold,* The Journal of Physical Chemistry B **2005**, 109, 22553-22559.

Appendix

1) Investigation of Structure and Activation of Ceria Supported Catalysts
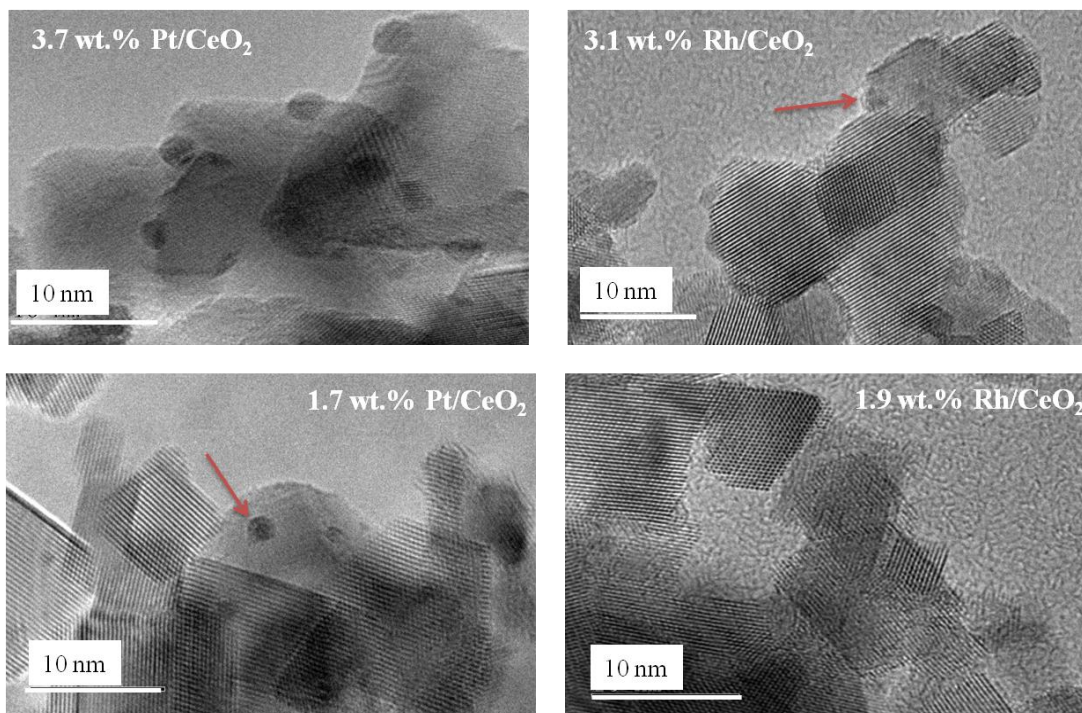
Figure A.1: TEM images of ceria supported noble metal catalysts: 3.7 wt.% Pt/CeO_2, 3.1 wt.% Rh/CeO_2, 1.7 wt.% Pt/CeO_2, and 1.9 wt.% Rh/CeO_2 before water gas shift reaction (fresh samples). TEM images recorded at Dalian Institute of Chemical Physic (DICP), Chinese Academy of Sciences (CAS) in Dalian/China.
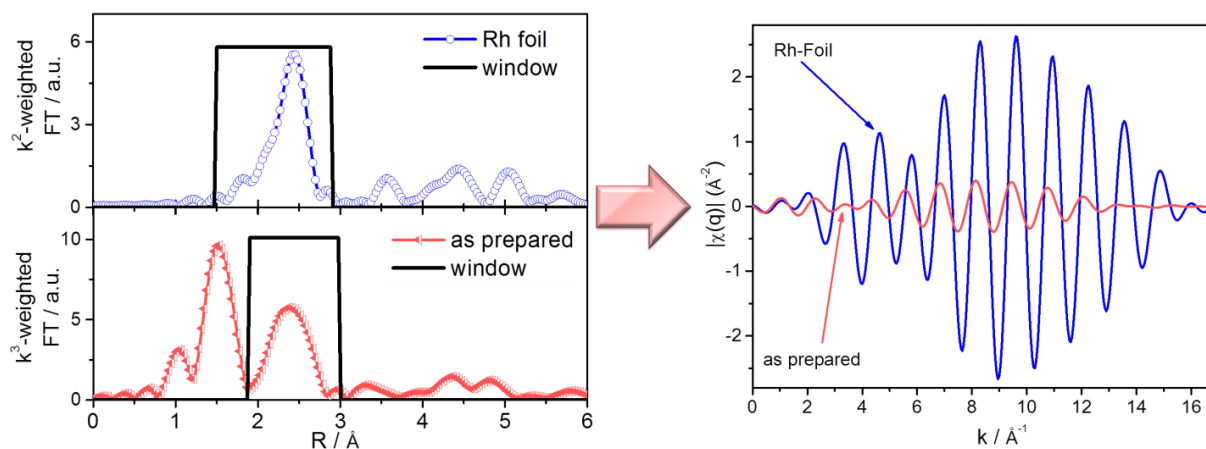
Figure A.2: Selection of second shell of Rh/CeO_2-as prepared, and selection of first shell of Rh-foil, for backward Fourier Transformation for comparison of backscattering of 2nd shell of Rh/CeO_2 and 1st shell of Rh-Foil.
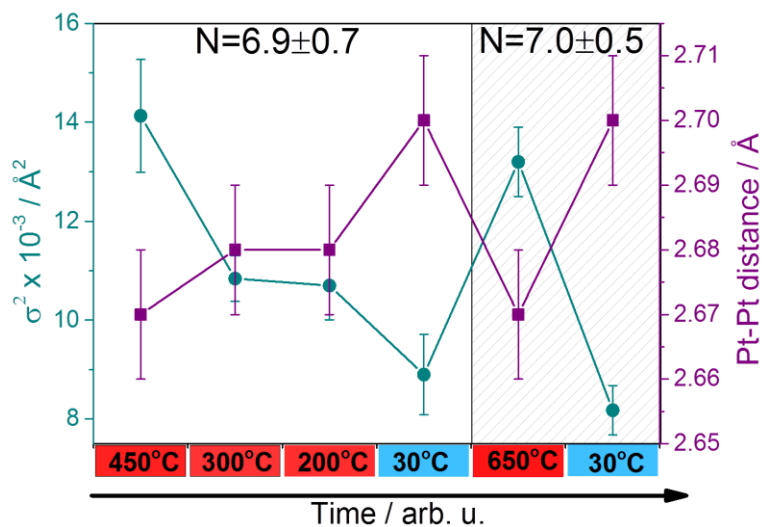
Figure A.3: Temperature-dependent Pt-Pt-bond length and Debye-Waller-Factor of 3.7 wt.% Pt/CeO$_2$ catalyst.
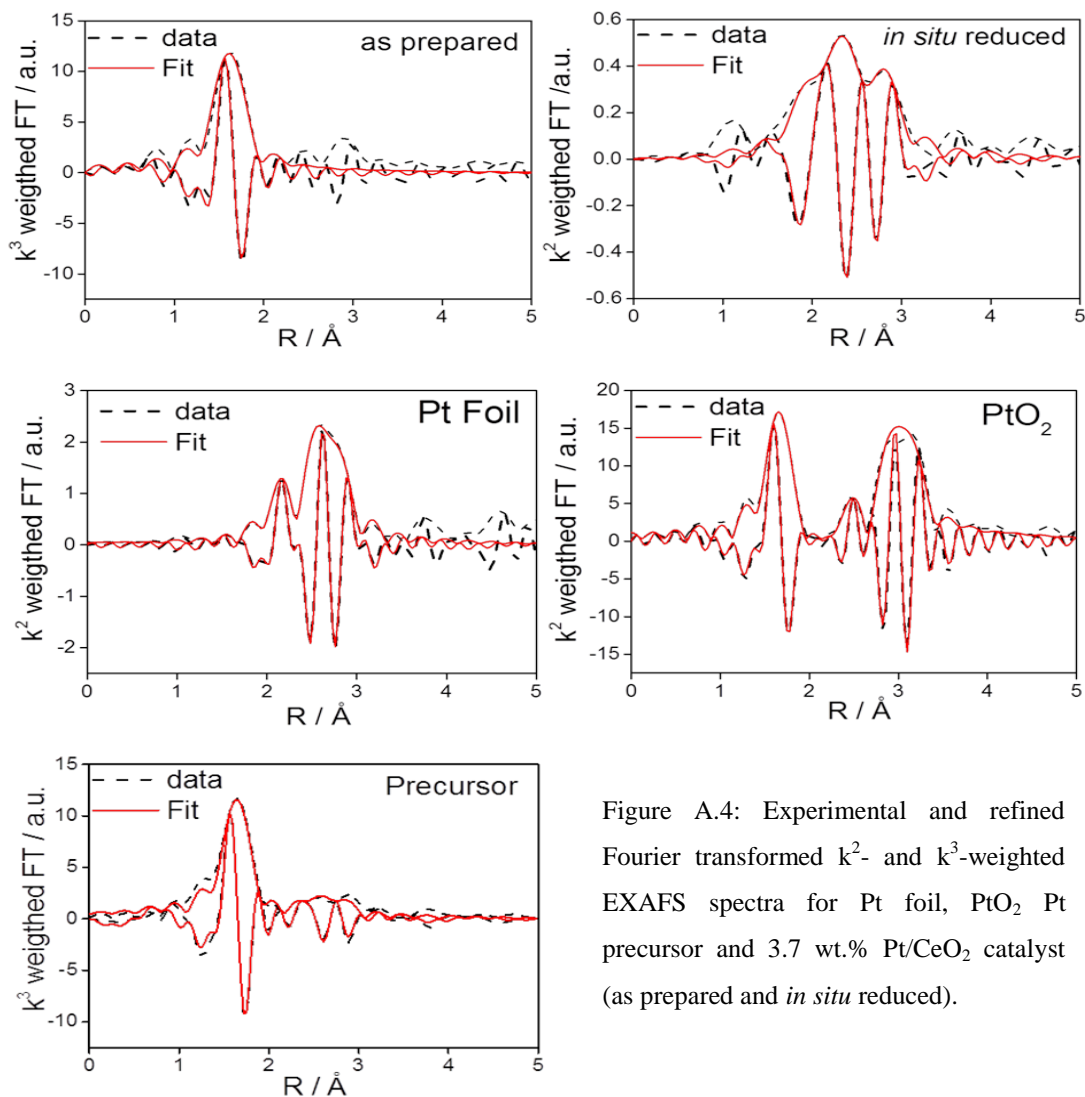
Figure A.4: Experimental and refined Fourier transformed k^2- and k^3-weighted EXAFS spectra for Pt foil, PtO$_2$ Pt precursor and 3.7 wt.% Pt/CeO$_2$ catalyst (as prepared and *in situ* reduced).

2) Investigation of Titania Supported Noble Metal Catalysts
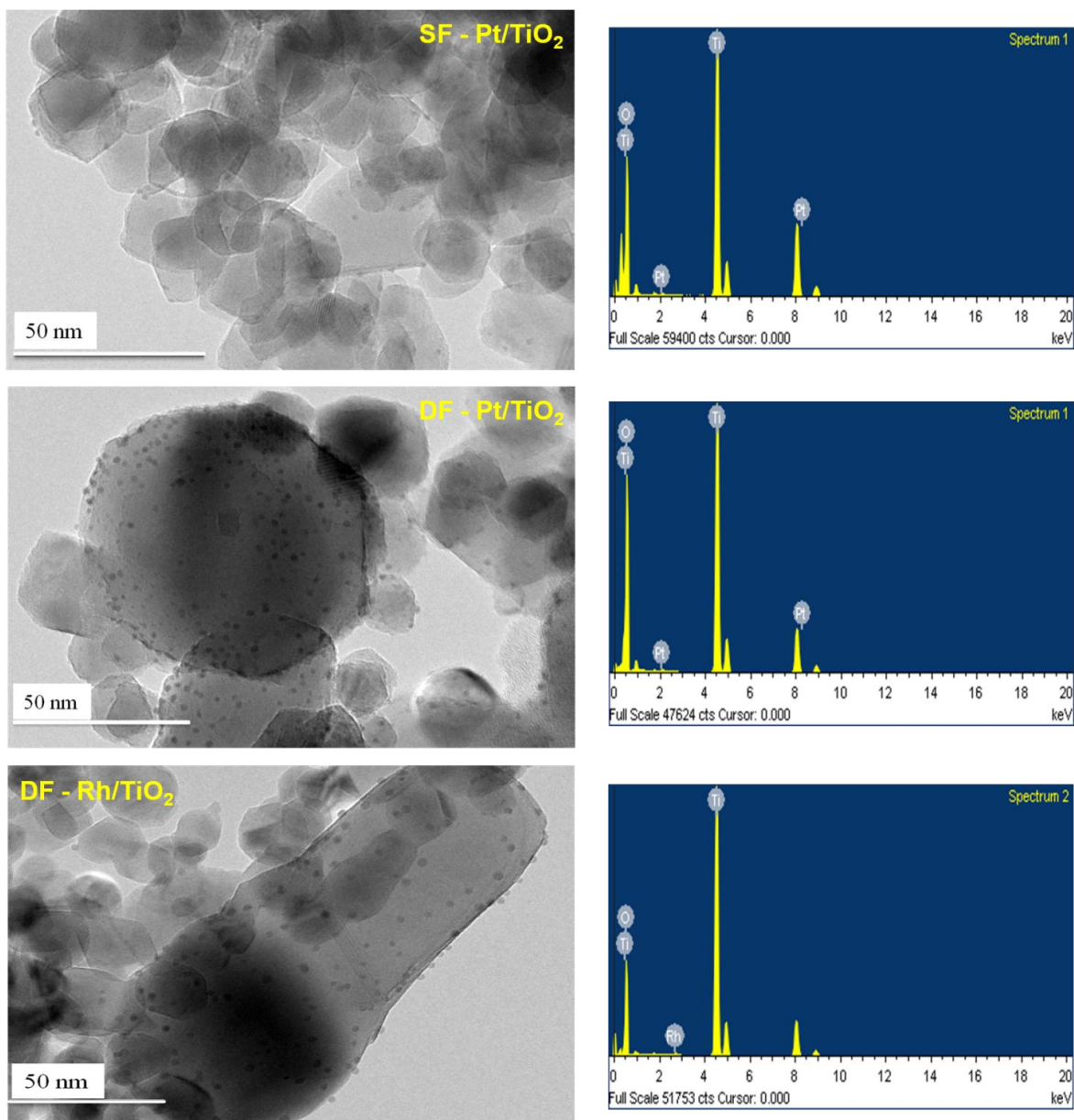
Figure A.5: TEM images of TiO_2 supported Pt nanoparticles made by single flame (SF), and double flame (DF) spray pyrolysis and Rh nanoparticles made by double flame spray pyrolysis (DF). The corresponding EDX spectrums (on the right) reveal a high dispersion of Pt and Rh nanoparticles on TiO_2. TEM images recorded at Dalian Institute of Chemical Physic (DICP), Chinese Academy of Sciences (CAS) in Dalian/China.
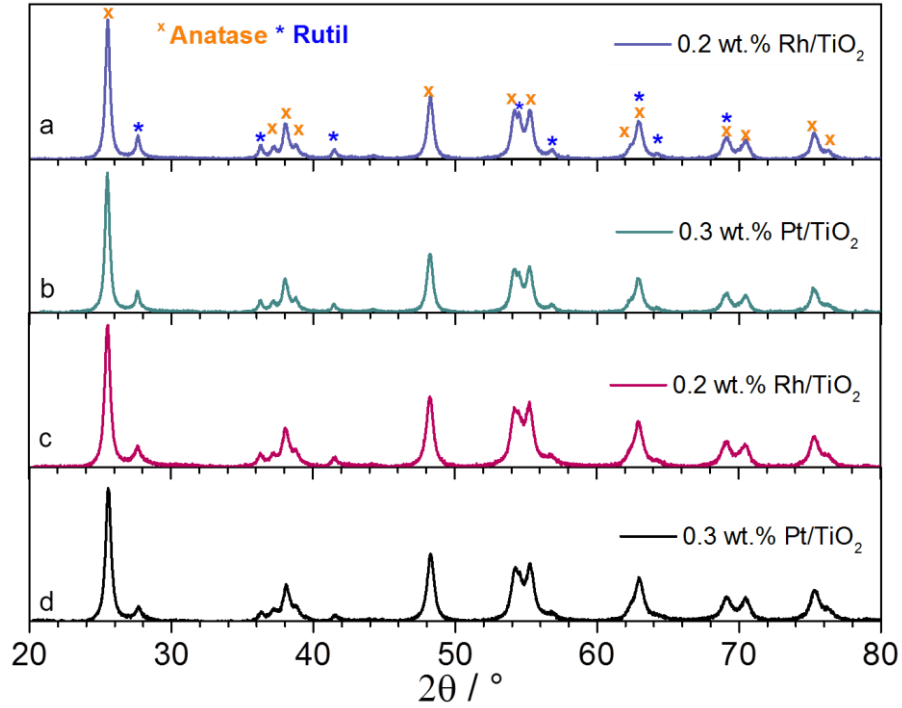
Figure A.6: XRD diffraction pattern of double flame spray made Rh (a) and Pt (b) as well as single flame spray made Rh (c) and Pt (d) supported on TiO_2.

Table A.1: The crystalline sizes of TiO_2 anatase at 25.5° and rutile at 27.5° for TiO_2 supported Pt and Rh.

	Sample	$d_{Anatase}$ [nm]	d_{Rutile} [nm]
Single flame	0.3 wt.% Pt/TiO_2	17	5
	0.2 wt.% Rh/ TiO_2	17	5
Double flame	0.3 wt.% Pt/TiO_2	21	8
	0.2 wt.% Rh/ TiO_2	21	8

3) Screening of Ceria, Zirconia and Ceria-Zirconia Supported Noble Metal Catalysts
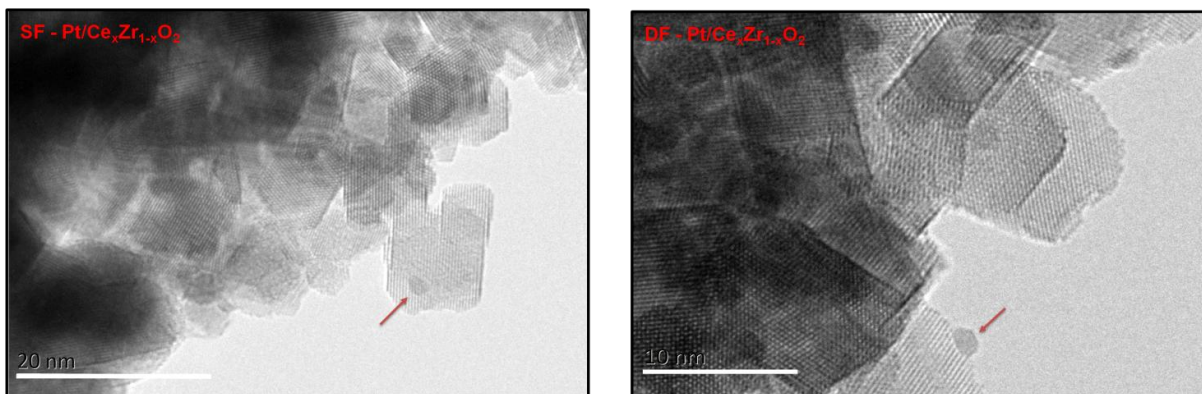
Figure A.7: TEM images of $Ce_xZr_{1-x}O_2$ supported Pt nanoparticles made by single flame (SF), and double flame (DF) spray pyrolysis, recorded at Dalian Institute of Chemical Physic (DICP), Chinese Academy of Sciences (CAS) in Dalian/China.
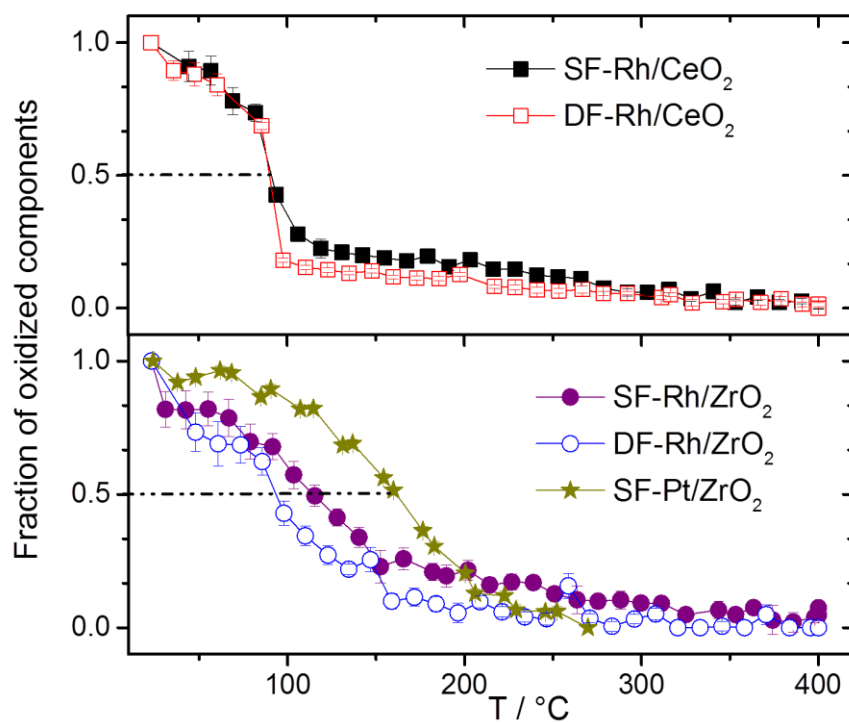
Figure A.8: Comparison of changes in relative concentrations of oxidized Rh and Pt species on CeO_2 (top) and on ZrO_2 (bottom) prepared by SF and DF during TPR obtained from linear combination fitting of XANES spectra.
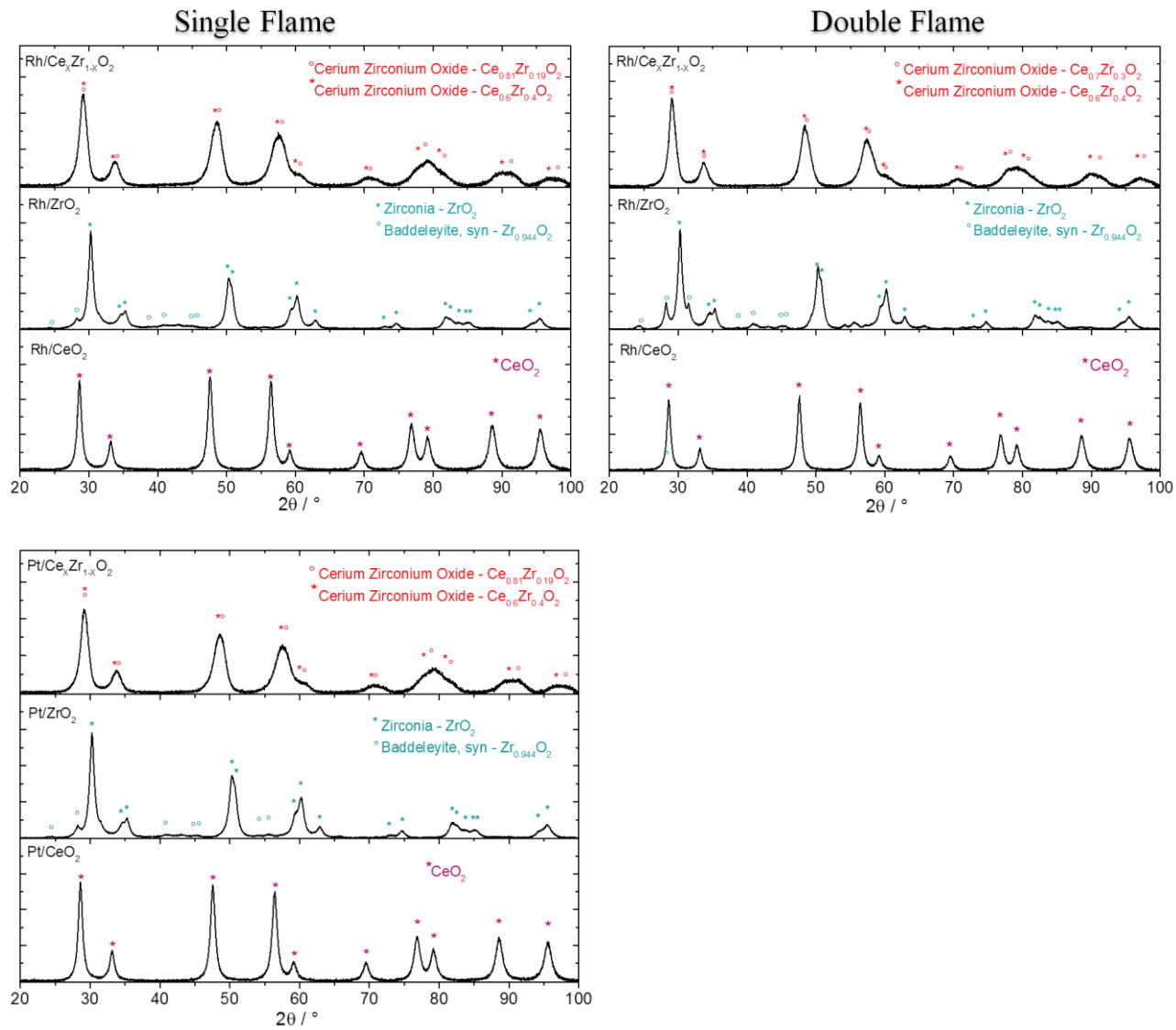
Figure A.9: XRD diffraction pattern of single (right) and double (left) flame spray made samples of CeO_2, ZrO_2 and $Ce_xZr_{1-x}O_2$ supported Pt and Rh, respectively.
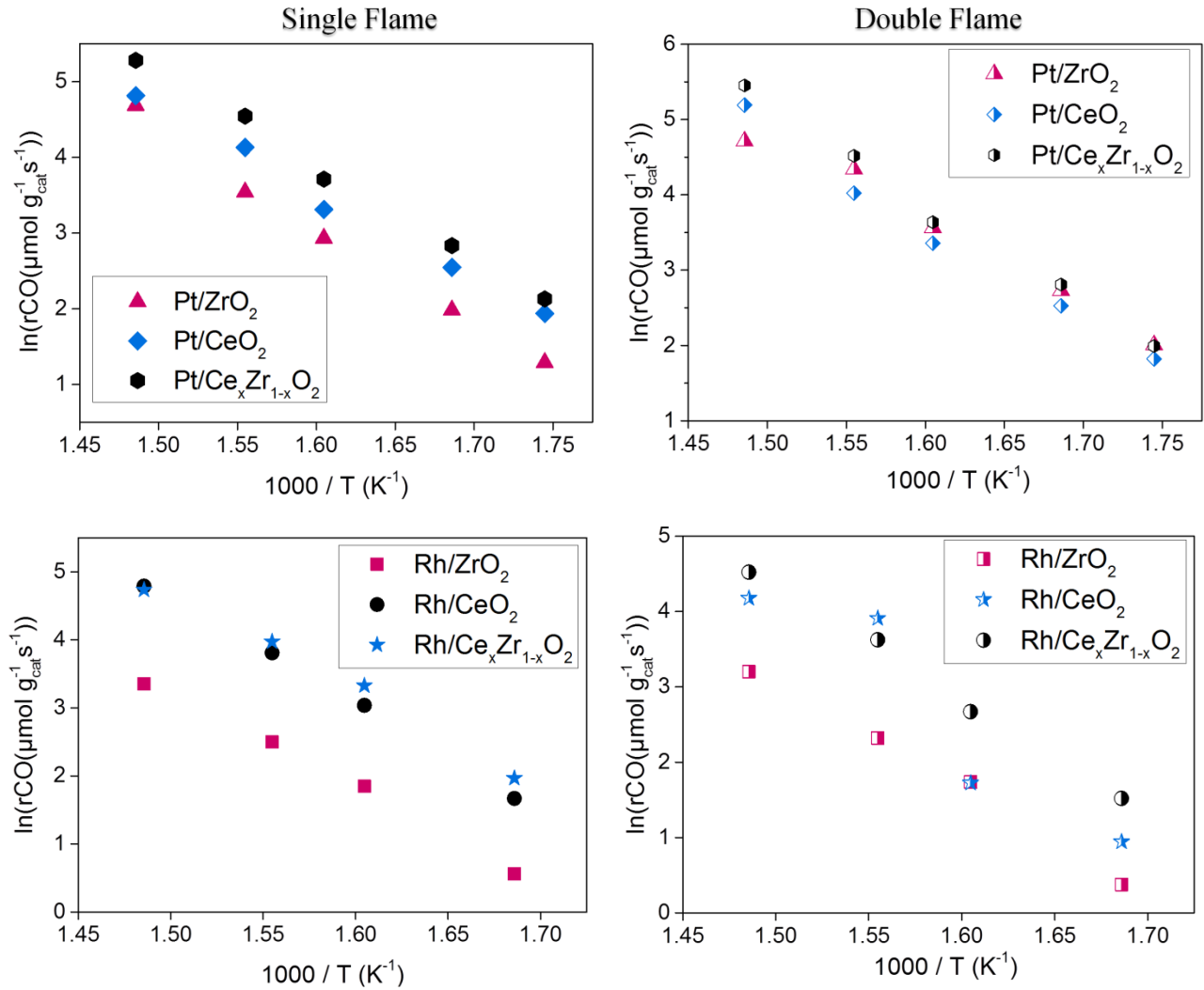
Figure A.10: WGS reaction rates over Pt/ZrO_2, Pt/CeO_2, $Pt/Ce_xZr_{1-x}O_2$ (top) and Rh/ZrO_2, Rh/CeO_2, $Rh/Ce_xZr_{1-x}O_2$ (bottom) prepared by SF (left) and DF (right).

Table A.2: Overview of the average light-off temperatures of the catalysts during the activity measurements. The temperature is corresponding for 50% of CO conversion.

Catalysts			Loading [wt.%]	$T_{50\%}$ [°C]	
				S/C=2	S/C=4
Pt	CeO_2	SF	0.94	276	270
		DF	0.90	276	261
	ZrO_2	SF	0.84	276	271
		DF	0.95	290	281
	$Ce_xZr_{1-x}O_2$	SF	0.81	287	280
		DF	0.76	284	285
Rh	CeO_2	SF	0.70	325	321
		DF	0.70	328	307
	ZrO_2	SF	0.94	—	—
		DF	0.89	377	364
	$Ce_xZr_{1-x}O_2$	SF	0.89	330	322
		DF	0.70	330	317
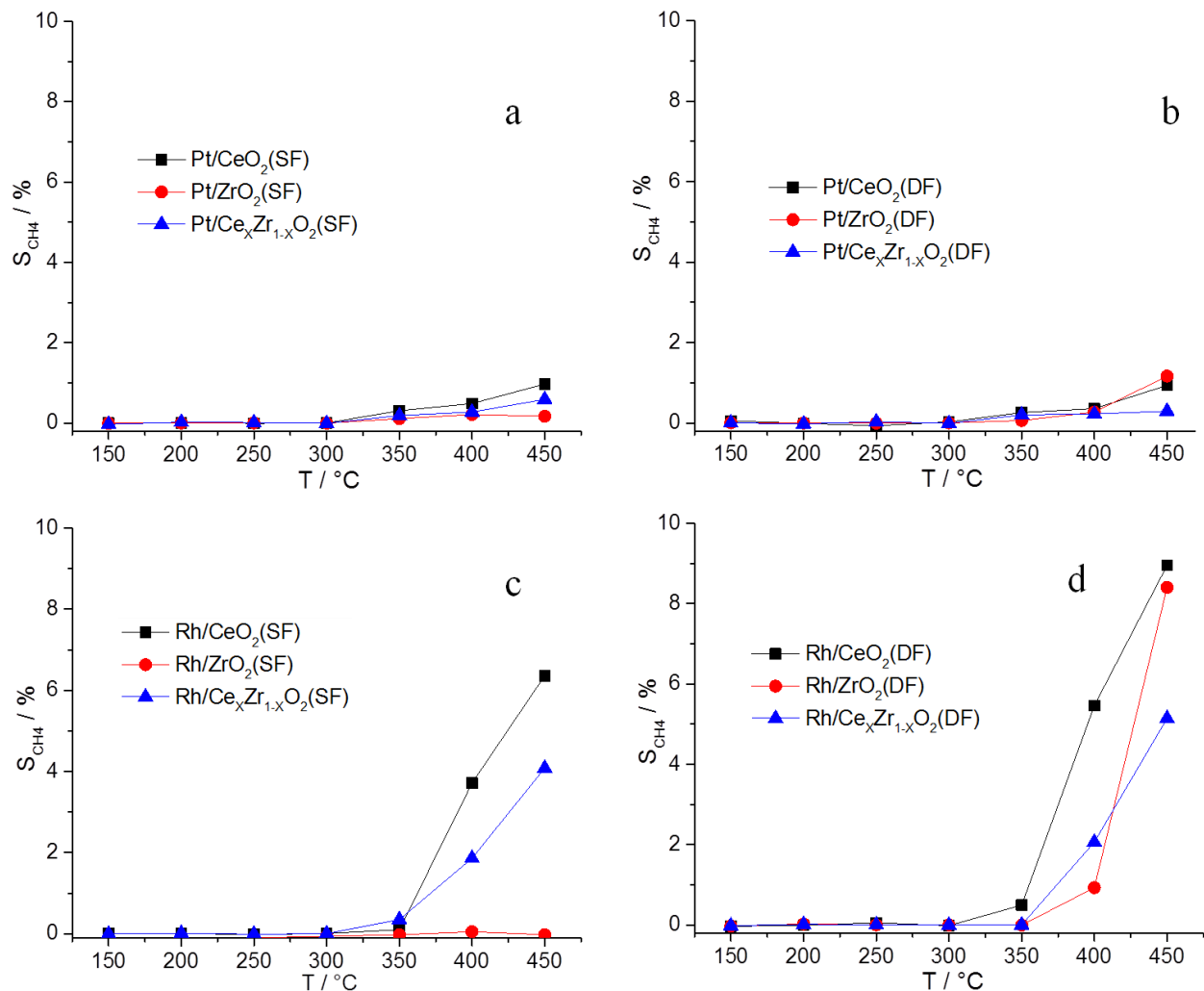
Figure A.11: Methane formation during water gas shift experiments over Pt/CeO₂, Pt/ZrO₂, Pt/Ce$_x$Zr$_{1-x}$O₂ SF (a) and DF (b), and over Rh/CeO₂, Rh/ZrO₂, Rh/Ce$_x$Zr$_{1-x}$O₂ SF (c) and DF (d) at S/C ratio of 2.
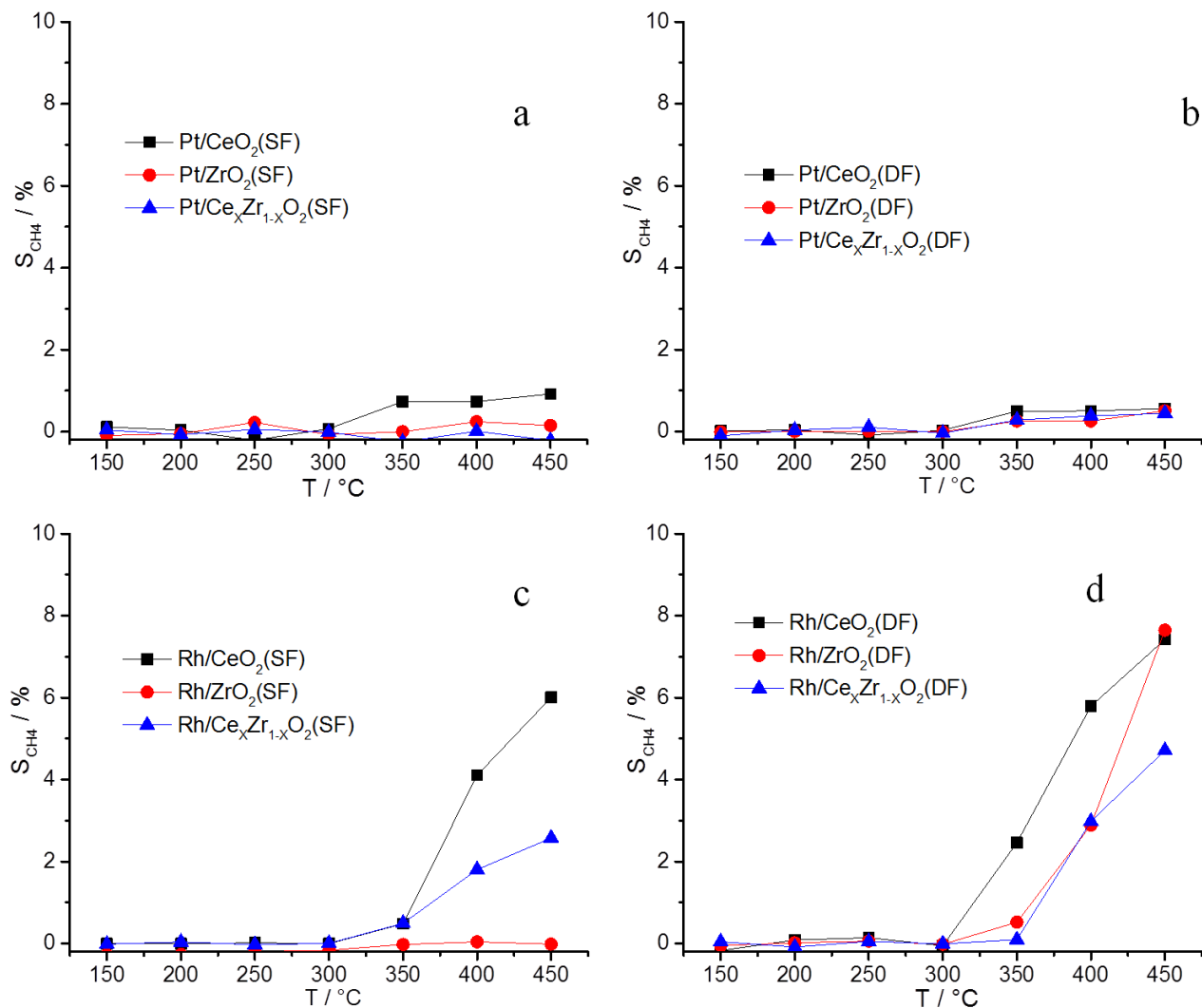
Figure A.12: Methane formation during water gas shift experiments over Pt/ CeO_2, Pt/ ZrO_2, Pt/$Ce_xZr_{1-x}O_2$ SF (a) and DF (b), and over Rh/ CeO_2, Rh/ ZrO_2, Rh/$Ce_xZr_{1-x}O_2$ SF (c) and DF (d) at S/C ratio of 4.

4) *Testing a specially Designed Micro-Structured Membrane Reactor at the Synchrotron*
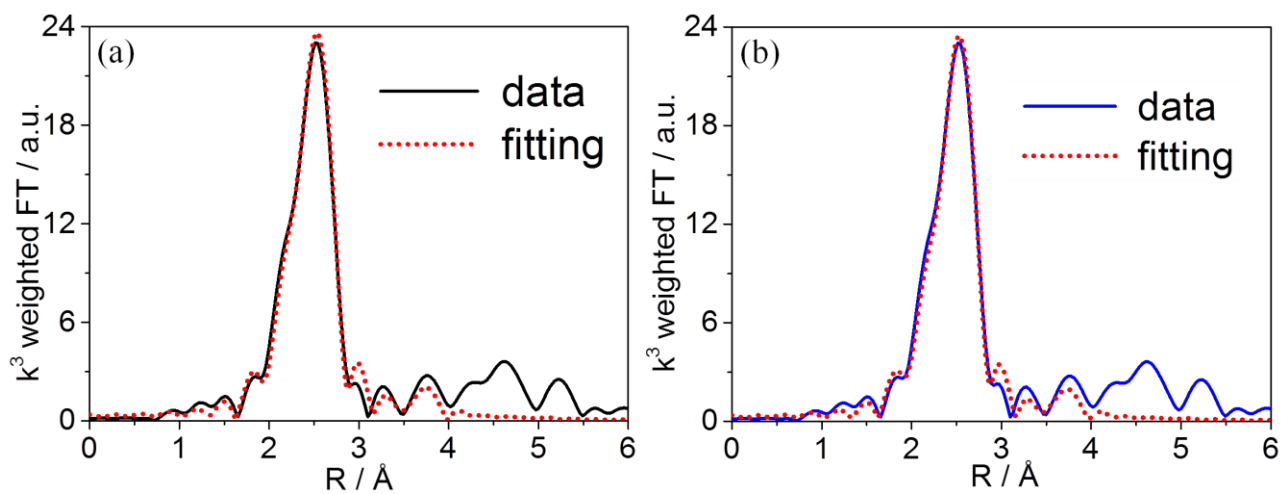
Figure A.13: Experimental and refined Fourier transformed k^3-weighted EXAFS data for Pd membrane foil, at room temperature in He before (a) and after (b) applying water gas shift reaction
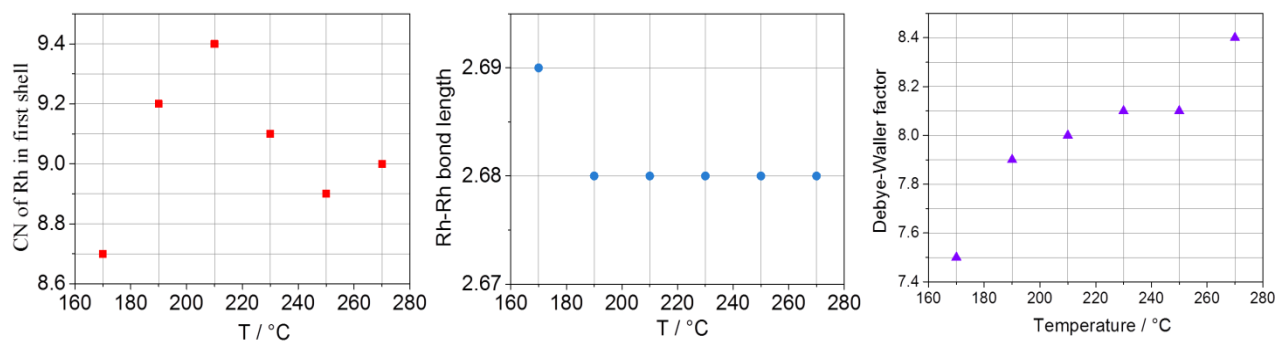
Figure A.14: Plotted coordination number, Rh – Rh bond length and Debye-Waller-factor versus temperature.
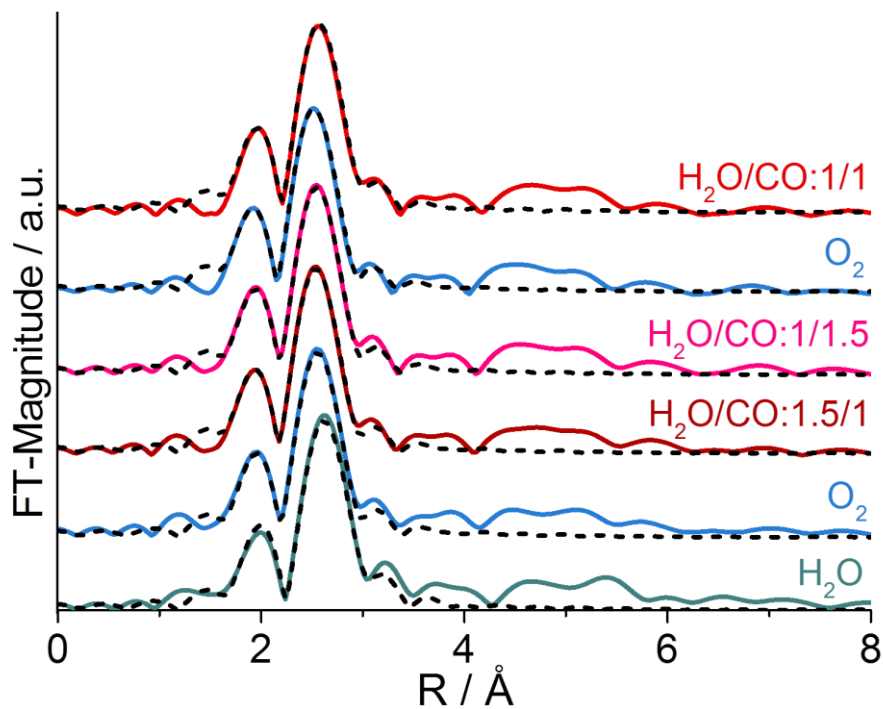
Figure A.15: k^2–weighted Fourier transformed data of Pd membrane foil at 350 °C in H_2O, O_2 and different WGS reaction conditions. Fitted data derived from analysis in Artemis (experimental – solid lines, fitting – dashed lines).

5) *Reaction Relevant Rh Structure under WGS Reaction Conditions*
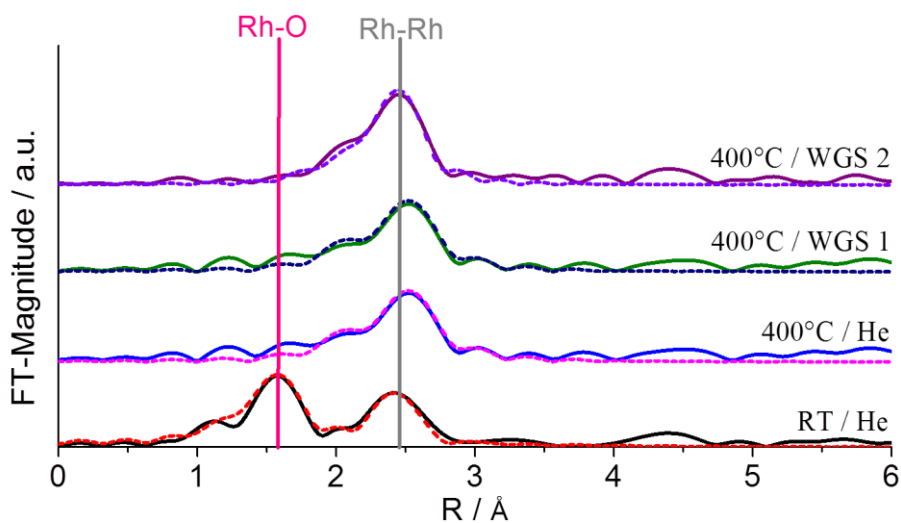
Figure A.16: k^3–weighted Fourier transformed data of 10.5 wt.% Rh/CeO$_2$ catalyst at RT, at 400°C under He and at 400°C in WGS reaction conditions (capillary micro reactor). (WGS-1: $\dot{V}_{CO}$=4 mL/min, $\dot{V}_{H2O}$=6 mL/min, $\dot{V}_{He}$=40 mL/min WGS-2: $\dot{V}_{CO}$=2 mL/min, $\dot{V}_{H2O}$=3 mL/min, $\dot{V}_{He}$=45 mL/min).
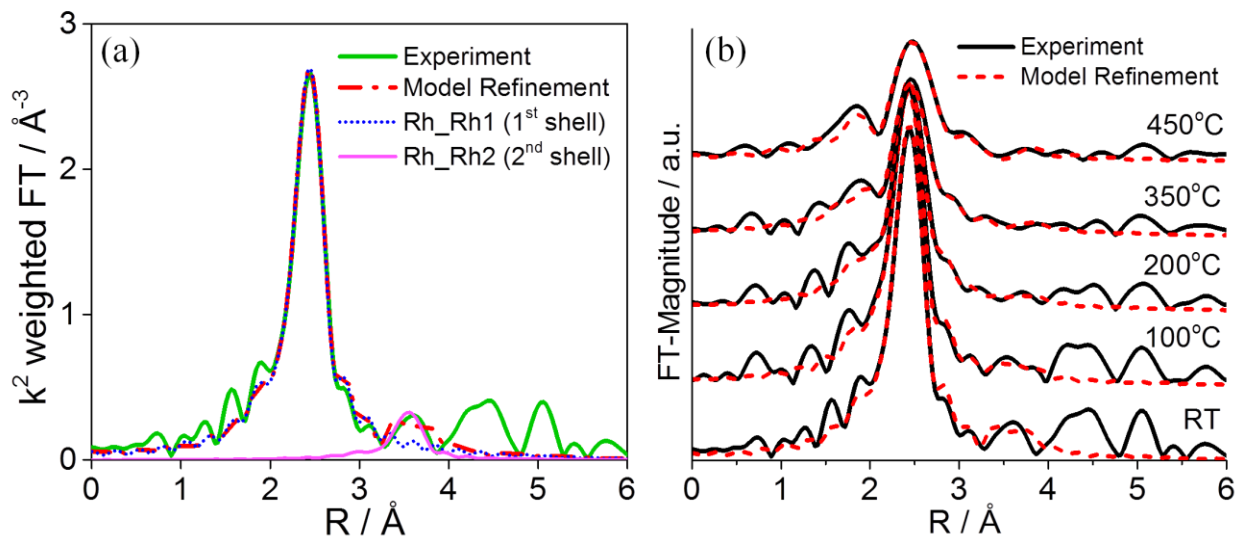
Figure A.17: (a) k^2–weighted Rh K-edge Fourier transformed EXAFS data of 10.5 wt.% Rh/CeO$_2$ catalyst after TPR at room temperature in CO and (b) fitted derived from data curves analysis using Artemis (solid lines black experimental data, dash lines red fitted data at 450, 350, 200 and 100 °C in H$_2$ and at room temperature in CO).

Table A.3: Structural parameters for the atomic environment around the Rh absorber atoms obtained from refined EXAFS data (Figure A.17) (450, 350, 200 and 100 °C in H$_2$, room temperature in CO).

Temperature [°C]	Shell	Atom	N	r [Å]	σ^2 10^{-3} [Å^2]
450	1st	Rh		2.66 ($\pm$0.01)	11.0 ($\pm$0.4)
	2nd	Rh	—	3.75 ($\pm$0.04)	17.7 ($\pm$4.7)
350	1st	Rh		2.66 ($\pm$0.01)	9.6 ($\pm$0.4)
	2nd	Rh	—	3.75 ($\pm$0.04)	16.3 ($\pm$4.9)
200	1st	Rh		2.67 ($\pm$0.01)	7.1 ($\pm$0.3)
	2nd	Rh	—	3.77 ($\pm$0.04)	14.4 ($\pm$4.4)
100	1st	Rh		2.67 ($\pm$0.01)	5.7 ($\pm$0.3)
	2nd	Rh	—	3.79 ($\pm$0.04)	12.0 ($\pm$5.0)
RT	1st	Rh	7.0$\pm$0.6	2.68 ($\pm$0.01)	5.1 ($\pm$0.4)
	2nd	Rh	4.4$\pm$2.5	3.80 ($\pm$0.04)	9.3 ($\pm$3.5)
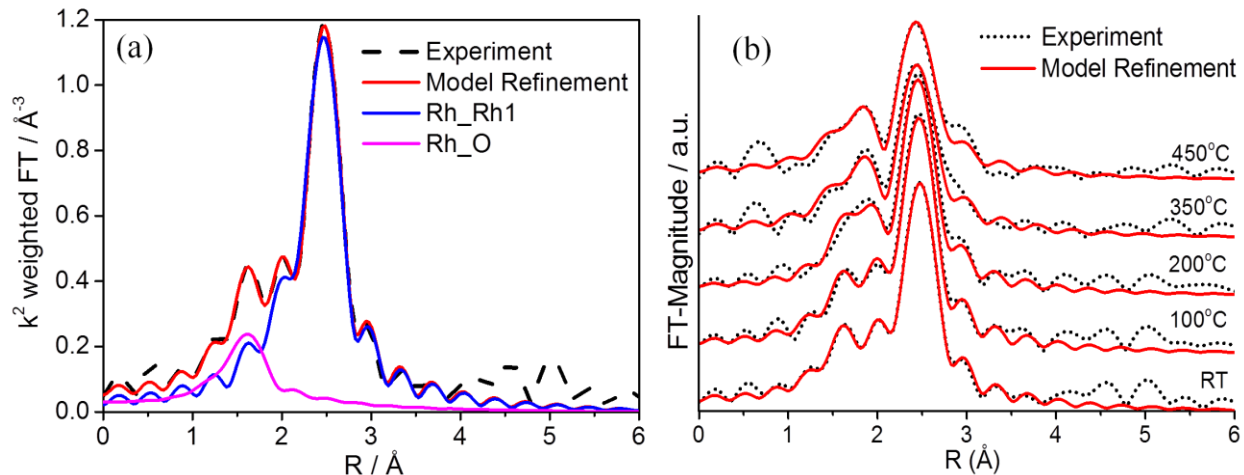
Figure A.18: a) k^2–weighted Rh K-edge Fourier transformed EXAFS data of 4.3 wt.% Rh/CeO$_2$ catalyst after TPR at room temperature in CO and (b) fitted derived from data curves analysis using Artemis (solid lines black experimental data, dash lines red fitted data at 450, 350, 200 and 100 °C in H$_2$ and at room temperature in CO).

Table A.4: Structural parameters for the atomic environment around the Rh absorber atoms obtained from refined EXAFS data (Figure A.18) (450, 350, 200 and 100 °C in H$_2$, room temperature in CO).

Temperature [°C]	Shell	Atom	N	r [Å]	σ^2 10^{-3} [Å^2]
450	1st	O	—	2.07 (±0.04)	13.1 (±0.6)
	2nd	Rh		2.63 (±0.04)	170.3 (±0.5)
350	1st	O	—	2.06 (±0.05)	11.2 (±0.1)
	2nd	Rh		2.63 (±0.01)	9.5 (±0.5)
200	1st	O	—	2.08 (±0.01)	4.3 (±2.8)
	2nd	Rh		2.66 (±0.01)	8.0 (±0.4)
100	1st	O	—	2.05 (±0.02)	6.4 (±2.1)
	2nd	Rh		2.68 (±0.01)	7.2 (±0.1)
RT	1st	O	1.1±0.2	2.03 (±0.01)	5.1 (±0.1)
	2nd	Rh	5.0±0.9	2.69 (±0.01)	7.3 (±1.2)

List of Abbreviations

Abbreviation	Name
ANKA	Angströmquelle Karlsruhe (synchrotron in Karlruhe)
DF	Double Flame
EDX	Energy Dispersive X-ray Spectroscopy
ESRF	European Synchrotron Radiation Facility (synchrotron in Grenoble)
EXAFS	Extended X-ray Absorption Fine Structure
FSP	Flame Spray Pyrolysis
FWHM	Full Width Half Maximum
GC	Gas Chromatography
GHSV	Gas hourly space velocity
HTS	High Temperature Shift
ICP-OES	Inductively coupled plasma optical emission spectroscopy
IKFT	Institute of Catalysis Research and Technology
IMVT	Institute for Micro Process Engineering
ITCP	Institute for Chemical Technology and Polymer Chemistry
IWI	Incipient Wetness Impregnation
KIT	Karlsruhe Institute of Technology
LCF	Linear Combination Fitting
LTS	Low Temperature Shift
LO	Light-Off
MS	Mass Spectrometry
S/C	Steam to carbon ratio
SF	Single Flame

Abbreviation	*Name*
TEM	Transmission Electron Microscopy
TPR	Temperature Programmed Reduction
WGS	Water Gas Shift
wt.%	Weight percent
XANES	X-ray Absorption Near edge Structure
XRD	X-ray diffraction

List of Publications

Publications:

"Structure and Activity of Flame Made Ceria Supported Rh and Pt Water Gas Shift Catalysts" G. Cavusoglu, D. Miao, H. Lichtenberg, H. W. P. Carvalho, H. Xu, A. Goldbach, J.-D. Grunwaldt, Applied Catalyst A: General **504** (2015), 381 – 390
Results from this publication are presented in chapter 4.1.

"Investigation of Single and Double Flame Made Noble Metal Catalysts Supported on TiO$_2$ for the Water-Gas Shift Reaction" G. Cavusoglu, D. Miao, H. Lichtenberg, A. Goldbach, J.-D. Grunwaldt (publication in progress)
Results from this publication are presented in chapter 4.2.

"Flame Made Ce$_x$Zr$_{1-x}$O$_2$ (0 $\leq x \leq$ 1) Supported Noble Metal Catalysts for High Temperature Water-Gas Shift Reaction" G. Cavusoglu, F. Maurer, H. Lichtenberg, A. Goldbach, J.-D. Grunwaldt (publication in progress)
Results from this publication are presented in chapter 4.3.

"In situ Characterization of Catalysts and Membranes in a Microchannel under High Temperature Water Gas Shift Reaction Conditions" G. Cavusoglu, F. Dallmann, H. Lichtenberg, A. Goldbach, R. Dittmeyer, J.-D. Grunwaldt Journal of Physics: Conference Series **712** (2016) 012054
Results from this publication are presented in chapter 5.2.2.1.

"Flame Made Ceria Supported Noble Metal Catalysts for Efficient H$_2$ Production via the Water Gas Shift Reaction" G. Cavusoglu, H. Lichtenberg, A. Gaur, A. Goldbach, J.-D. Grunwaldt, Journal of Physics: Conference Series **712** (2016) 012065
Results from this publication are presented in chapter 5.3.

"Water-Gas Shift Reaction over Platinum/Strontium Apatite Catalysts" D. Miao, G. Cavusoglu, H. Lichtenberg, J. Yu, H. Xu, J.-D. Grunwaldt, A. Goldbach, Applied Catalysis B: Environmental **202** (2017) 587 – 596

Oral presentations:

➤ Sino-German Workshop on Nanostructured Materials for Hydrogen Production 9th – 10th December 2013(Dalian/China)

➤ Sino-German Workshop on Membrane Reactors for Hydrogen Production and Chemical Energy Storage 1st – 2nd July 2014 (Nanjing/China)

➤ Summer school organized by Helmholtz Research School Energy-Related Catalysis: 28th July – 1st August 2014 (Hofheim am Taunus)

➤ Winter school organized by Helmholtz-CAS Joint Research Group (HCJRG) „Integrated catalytic technologies for efficient hydrogen production" 2015 9th–11th January (Zugspitze)

➤ Sino-German Workshop on *in situ* Spectroscopy on Catalysts and Membranes 28th – 29th August 2015 (Karlsruhe/Germany)

Poster:

➤ *"Nanostructured Catalytic Materials and their Integration in Microchannel Reactors"* Seungcheol Lee, <u>Gülperi Cavusoglu</u>, Programme Storage and Cross-linked Infrastructures (SCI), Karlsruhe

➤ *"Flame Made Ceria Supported Pt Catalysts for Water Gas Shift Reaction"* <u>Gülperi Cavusoglu</u>, Henning Lichtenberg, Jan-Dierk Grunwaldt, ANKA User Meeting, Karlsruhe

➤ *"Flame Made Ceria Supported Noble Metal Catalysts for Efficient H_2 Production via the Water Gas Shift Reaction"* <u>Gülperi Cavusoglu</u>, Henning Lichtenberg, Andreas Goldbach, Jan-Dierk Grunwaldt, 7th International Conference on Green and Sustainable Chemistry (GSC-6), Tokyo

➤ *"Characterization of Catalysts and Membrane in Microreactor under WGS Reaction Conditions at the Synchrotron"* <u>Gülperi Cavusoglu</u>, Felix Dallmann, Henning Lichtenberg, Andreas Goldbach, Roland Dittmeyer, Jan-Dierk Grunwaldt, XAFS16 , Karlsruhe

➤ *"Flame Made Ceria Supported Noble Metal Catalysts for Efficient H_2 Production via the Water Gas Shift Reaction"* <u>Gülperi Cavusoglu</u>, Henning Lichtenberg, Andreas Goldbach, Jan-Dierk Grunwaldt